Modeling of electromechanical interactions in architected media in the framework of generalized continua

Nagham Mawassy

THÈSE de doctorat en cotutelle

Pour obtenir le grade de:

DOCTEUR DE L'UNIVERSITÉ DE LORRAINE ET DE L'UNIVERSITÉ LIBANAISE

Mention: Mécanique des Matériaux

École doctorale: C2MP et EDST

Présentée par:

Nagham Mawassy

Intitulée :

Modeling of electromechanical interactions in architected media in the framework of generalized continua

---

Thèse soutenue à:

Nancy, le 14/06/2023

Devant le jury composé de:

Claude Boutin	Pr., ENTPE, Université de Lyon	Rapporteur
Michel Devel	Pr., FEMTO-ST, Université de Franche- Comté	Rapporteur
Ausrine Bartasyte	Pr., FEMTO-ST, Université de Franche- Comté	Présidente
Khaled Khalil	Pr., ECAM-Rennes	Examinateur
Hilal Reda	Dr., Lebanese University	Examinateur
Jean-François Ganghoffer	Pr., LEM3, Université de Lorraine	Directeur de thèse
Hassan Lakiss	Pr., Islamic University of Lebanon	Directeur de thèse

Acknowledgments

First of all, I would like to thank Claude Boutin and Michel Devel for accepting to be the reviewers of my thesis. As well, I would like to thank Ausrine Bartasyte and Khaled Khalil for being a part of my thesis jury as examinators.

I would like to express my deepest gratitude to my thesis supervisor Jean-François Ganghoffer, from whom I learned alot. His expertise and insights have inspired me to think critically and creatively about my research, and his dedication to helping me succeed has been truly remarkable.

I want to thank my supervisor Hassan Lakiss for believing in me, and giving me this opportunity to pursue my PhD.

Special thanks to Hilal Reda whose invaluable guidance, support, and encouragement throughout my research journey has been instrumental in the successful completion of this thesis. His expertise, patience, and insightful feedback have been invaluable and have helped me to develop as a researcher.

I would also like to thank my colleague Seyed Ehsan ALAVI for his help in my thesis. As well, I would like to thank Yves Vallet for solving my ABAQUS problems :) and Emilie Wiedemann-Fodé for being my french teacher.

I would like to express my warm thanks to my parents, my sister, my brothers, and my cousin for their support throughout my PhD journey. Their belief in me has been a constant source of inspiration and motivation. This achievement would not have been possible without you.

Also, I would like to express my heartfelt gratitude to my friends for their unwavering support and encouragement during my PhD journey. Their presence, understanding, and encouragement have consistently motivated and inspired me. I am grateful for the countless conversations, shared laughs, and moments of respite that we have shared. Thank you for being there for me through thick and thin.

Nagham

Abstract/Résumé

Modeling of electromechanical interactions in architected media in the framework of generalized continua

Abstract

The objective of the thesis is to address in a theoretical and numerical way the homogenization of periodic architected and composite media with multiphysical behavior, in the context of generalized continua. The manuscript is thus decomposed into two parts that explicitly cover these issues.

The first part of the manuscript deals with the homogenization of periodic and quasi-periodic media towards a strain gradient effective continuum. A discrete homogenization method is applied for architected periodic materials, leading to the elaboration of higher order effective properties in the form of analytical expressions depending on the edge length of the unit cell. The use of a strain gradient formulation allows the quantification of the edge effects (surface effects in 3D) of architected materials. Moreover, a quasi-periodic homogenization is developed from a volumetric expression of the energy and relying on the notion of shape derivative to determine the quasi-periodic effective properties based on the periodic domain being transformed.

The second part of the manuscript integrates multiphysical aspects in the homogenization approaches towards generalized continua. The theory of piezoelectric and flexoelectric homogenization is elaborated in the context of periodic homogenization, employing a variational formulation in combination with the extended Hill macro-homogeneity condition. This is followed by numerical applications for the homogenization of piezoelectric composites and architected materials as well as wave propagation analysis. Moreover, homogenization towards Cosserat (micropolar) effective continuum is addressed for the magnetoelastic heterogeneous solids.

Keywords: Homogenization, Piezoelectricity, Flexoelectricity, Magnetoelasticity, Strain Gradient Medium, Effective Cosserat Medium, Quasi-periodicity.

Modélisation des interactions électromécaniques dans les milieux architecturés par la mécanique des milieux continus généralisés

Résumé

La thèse a pour objectif d'aborder de façon théorique et numérique l'homogénéisation de milieux architecturés et composites périodiques présentant un comportement multiphysique, dans le contexte des milieux continus généralisés. Le manuscrit est donc décomposé en deux parties qui couvrent explicitement ces questions.

La première partie du manuscrit traite l'homogénéisation des milieux périodiques et quasi-périodiques vers un continuum effectif à gradient de déformation. Une méthode d'homogénéisation discrète est appliquée pour les matériaux périodiques architecturés, conduisant à l'élaboration des propriétés effectives d'ordre supérieur sous forme d'expressions analytiques dépendant de la longueur du bord de la cellule unité. Le recours à une formulation à gradient de déformation permet de quantifier les effets de bord (les effets de surface en 3D) de matériaux architecturés. En outre, une homogénéisation quasi-périodique est développée à partir d'une expression volumétrique de l'énergie et en s'appuyant sur la notion de dérivée de forme pour déterminer les propriétés effectives quasi-périodiques basées sur le domaine périodique transformé.

La deuxième partie du manuscrit intègre des aspects multiphysiques dans les approches d'homogénéisation vers les continuums généralisés. La théorie de l'homogénéisation piézoélectrique et flexoélectrique est élaborée dans le contexte de l'homogénéisation périodique, en employant une formulation variationnelle en combinaison avec la condition de macro-homogénéité de Hill étendue. Ceci est suivie par des applications numériques pour l'homogénéisation des composites piézoélectriques et des matériaux architecturés ainsi que pour l'analyse de la propagation des ondes. En outre, l'homogénéisation vers le continuum effectif de Cosserat (micropolaire) est abordée pour les solides hétérogènes magnétoélastiques.

Mots clés: Homogénéisation, Piézoélectricité, Flexoélectricité, Magnétoélasticité, Milieux à gradient de déformation, Milieu effectif de Cosserat, Quasi-périodicité.

Contents

List of figures

List of tables

Chapter 1

General introduction

Multiphysical aspects refer to the interplay of multiple physical phenomena that occur simultaneously in a system or material. These phenomena can include mechanical, thermal, electrical, magnetic, chemical, and biological processes. Among different multiphysical phenomena, electromechanical and magneto-mechanical couplings, that relate respectively the electrical, and magnetic fields with mechanical fields, have been attracting alot of attention. The next subsections will be dealing with these two aspects.

1.1 Piezoelectricity and flexoelectricity

Electroactive materials have the ability to convert mechanical energy into electric energy and vice versa, making them widely used in modern technologies (as shown in Fig. 1.1 [1]). Energy harvesting is a primary application of these materials, which involves generating electrical power from mechanical sources like vibrations from machines, wind, ocean waves, and movements of the human body, among others [1]. Another application of electroactive materials is to convert the mechanical energy into electric energy which is used widely in sensors and measuring devices. On the other hand, applying electric fields to these materials can produce precisely controlled mechanical forces that can be used for actuation in various fields, such as motors, robotics, biomedical devices, and personal electronics, among others.

Piezoelectricity is a widely recognized and frequently utilized form of electromechanical coupling, where electric polarization $\boldsymbol{p}$ and mechanical strains $\boldsymbol{\varepsilon}$ are coupled linearly as follows:

$$p_l = d_{lij}\varepsilon_{ij}$$

wherein $\boldsymbol{d}$ is the piezoelectric tensor. Piezoelectric ceramics exemplify this phenomenon, where these materials become polarized when subjected to deformation and deform when an electric field is applied. Fig. 1.2(a) [2] explains using an ion-model how piezoelectricity arises when subjected to tension or compression, where the electric dipole moment changes due to a shift between the negative and positive ion centers of gravity. Piezoelectricity is limited to non-centrosymmetric dielectric crystals.

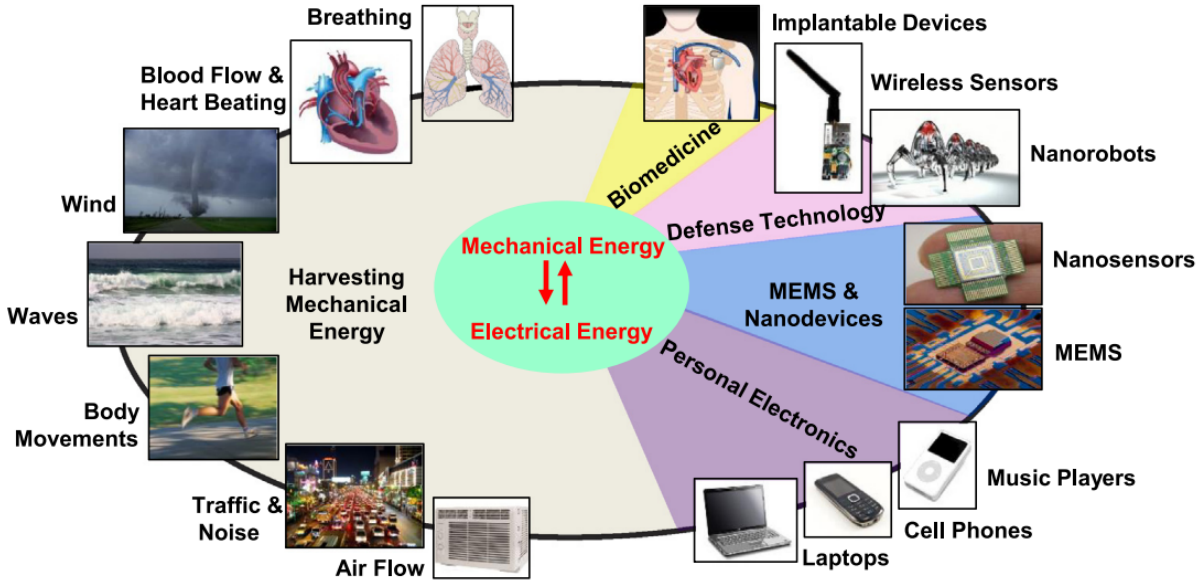

Figure 1.1 Energy harvesting sources (left) and applications of sensing and actuating (right) that can be used for piezoelectric devices [1].

On a smaller scale such as micro and nano-levels, there are other effects that need to be considered. One of these electromechanical couplings that has received less attention and is a main subject of this thesis is *flexoelectricity* [3].

Flexoelectricity involves the coupling between strain gradients and electric polarization [4,5]. The direct flexoelectric effect refers to the polarization of a material resulting from non-uniform deformation such as bending or twisting [6]. This effect can be mathematically represented as:

$$p_l = f_{lijk}\frac{\partial \varepsilon_{ij}}{\partial x_k}$$

with $\boldsymbol{f}$ being the flexocoupling tensor. As shown in Fig. 1.2(b) [2], when the crystal undergoes bending, a non-zero dipole is generated even if the structure is centrosymmetric.

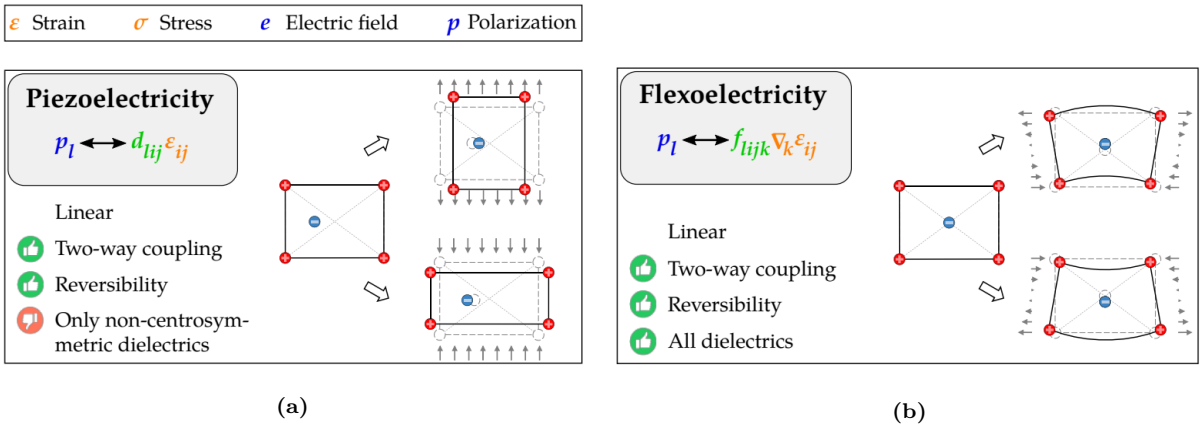

(a) **(b)**

Figure 1.2 Schematic presentation of Piezoelectricity (a), and flexoelectricity (b) in dielectric crystals [2].

Flexoelectricity appears to be a promising phenomenon for modern technologies due to its advantageous properties such as reversibility, and two-way coupling. However, and as shown in Fig. 1.3 [3], it has only recently started gaining attention. This is because the flexoelectric material constants are usually very small, which requires sufficiently large strain gradients to trigger a significant flexoelectric effect.

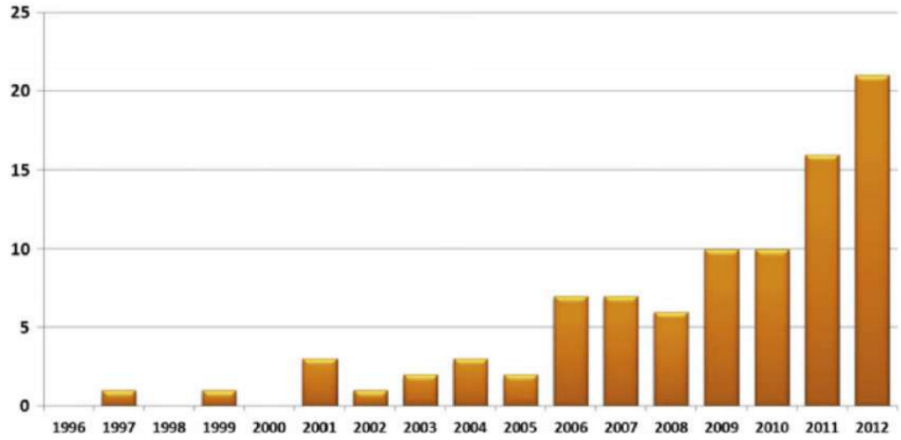

Figure 1.3 Evolution of the number of research publications on flexoelectricity[3].

After the theoretical predictions made by Mashkevich and Tolpygo [7], Bursian and Zaikovskii [8] were the first to observe the flexoelectric effect through experimental means in 1968. Since then, it has been found in various materials such as biomaterials which include viruses [9], and cellular membranes [10, 11], soft materials including polymers [12–17] and liquid crystals [18, 19], as well as atomically-thin nanomaterials such as carbon nanotubes [20] or graphene [21].

The flexoelectric effect is widespread in nature. This can be shown in the noteworthy biological examples such as the mammalian hearing mechanism (see Fig. 1.4 [22]). Hair cells serve as the main sensory receptors in the auditory system, converting the mechanical vibrations of sound into detectable electric signals. While there is still some uncertainty about the underlying mechanism, one plausible explanation is that the stereocilia found in inner hair cells may be responsible for flexoelectricity [10, 22–24].

Another interesting application of flexoelectricity in biology was found to be in the human bone self-healing (see Fig. 1.5 [25]). According to [25], micro-cracks present in bones produce significant strain gradients, which cause an electric field to develop in the area surrounding the affected region due to the flexoelectric properties of the bone mineral hydroxyapatite.

This electric stimulus generated by the cracks is strong enough to prompt osteoblasts to become active in the damaged regions, thereby initiating the process of repairing the micro-cracks.

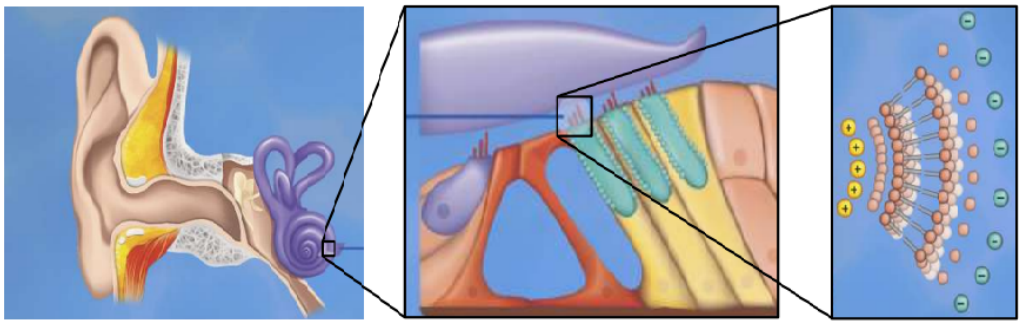

Figure 1.4 The flexoelectricity in the hearing mechanism of mammals is described, where hair bundles comprised of multiple stereocilia connected by thin fibers are organized in rows of decreasing height. Bending the hair bundle towards the tallest or shortest row causes the cellular inner environment to become more positively or negatively charged, respectively. This bending process leads to a voltage difference across the thickness of the stereocilia membrane due to the flexoelectric response of the cellular membrane [22].

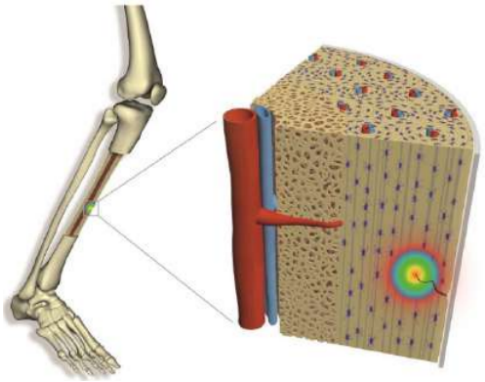

Figure 1.5 Flexoelectricity in human bones; significant strain gradients can be observed around micro-cracks in the bone mineral leading to a gradient-induced electricity (i.e., flexoelectricity) in the vicinity of these defects which is also significant [25].

1.2 Magnetoelasticity

Besides the studies done on the different electromechanical coupling effects, many were focusing on the *magnetoelastic* coupling which refers to the interconnection between the magnetic and elastic fields [26]. The magnetoelastic coupling is apparent in different materials, such as magnetostrictive materials. These materials belong to the broader category of smart materials that can alter their properties, shape, or dimensions when exposed to an external field (magnetic field).

One of the applications of magnetostrictive materials that exemplifies the concept of magnetoelasticity is the acoustomagnetic tags used by shops to prevent shoplifting (see Fig. 1.6 [26] [27]). Typically, they comprise a thin, amorphous metal strip with magnetostrictive properties that respond to an external magnetic field through vibrations.

The detectors emit a magnetic signal that matches the resonance frequency of the metal strip in the tag, inducing a vibration in it that leads to a modification of its magnetization. The detectors react to this alteration with an AC voltage, which ultimately triggers the alarm.

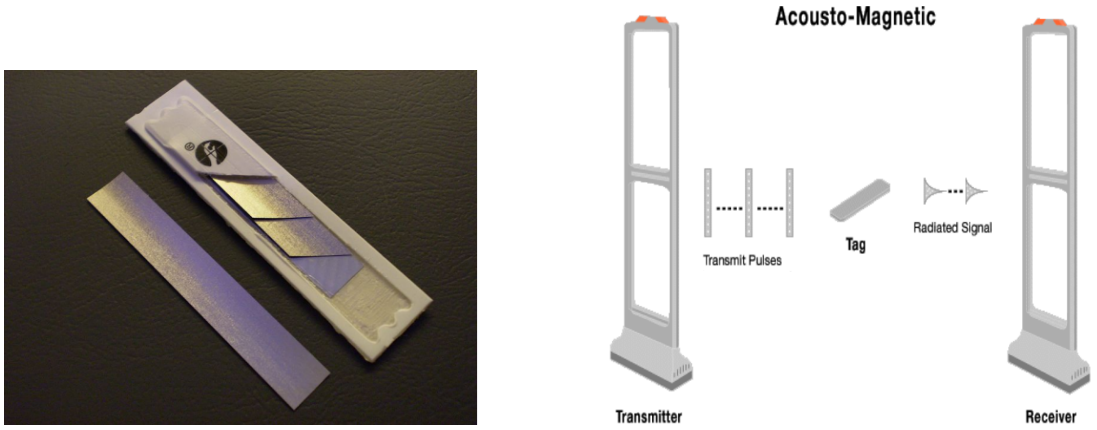

(a) (b)

Figure 1.6 (a) Acoustomagnetic tag with the its magnetic strips [26], (b) System of detection of the tag[27].

Furthermore, magnetoelasticity is present in magnetoelastic sensors (MES), which are extensively studied for their wide range of applications, particularly in the biomedical field. MES rely on the inverse of the magnetoelastic effect whereby exposure to mechanical stress results in a corresponding alteration in their magnetic permeability [28]. Various applications of this approach have been reported, such as monitoring bone plate strain as shown in Fig. 1.7(a) [29] , and monitoring force exertion on artificial bone (Fig. 1.7(b) [30]) [31].

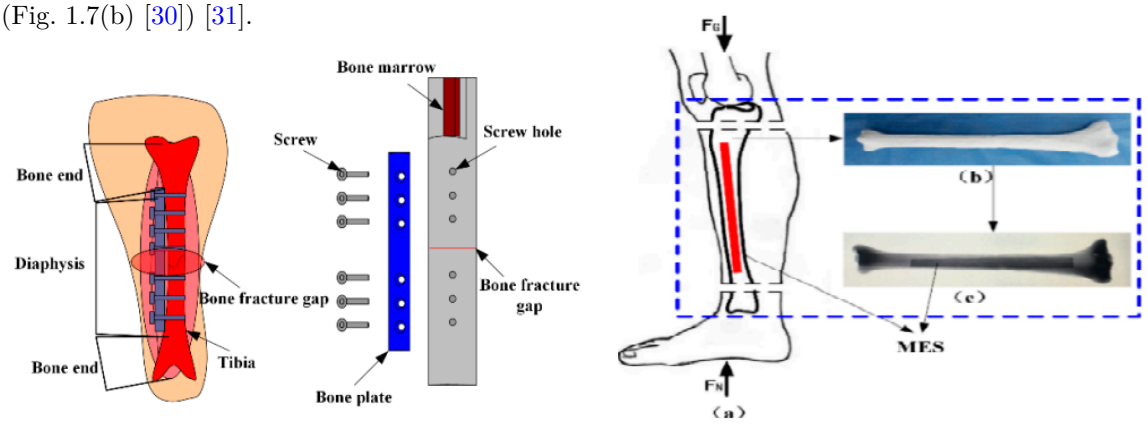

(a) (b)

Figure 1.7 (a) The repair model of sheep tibia, (b) application of the artificial bone [30].

1.3 Composites and architected materials: the foundation of different applications

The development of novel material with unique properties has led to significant advancements in engineering. *Composites* and *architected materials* are two such materials that have revolutionized the field of materials engineering and have become the base materials in many multiphysical applications because of their ability to offer high mechanical performance (such as strength, energy absorption capacity, acoustic and thermal insulation properties), while maintaining a low weight.

Over the past 35 years, there has been a growing interest in piezoelectric composites due to their application in various fields of engineering [32]. This has led to the creation of novel mechanical structures that are used in advanced technological devices [33,34]. The diverse uses of piezoelectric composites have accelerated the progress of mathematical, experimental, and computational models that pertain to the analysis of these materials' properties [35–37].

The term "architected materials" was first introduced in [38] as a means to connect the methods of topology optimization [39], which are used to design lightweight, high-performance, and aesthetically pleasing materials, with the field of structural engineering. By modifying the inner topology of architected materials, it becomes possible to achieve novel behaviors of the effective medium without even changing the chemical composition of the base materials.

This technological development has become possible thanks to the fast advancements of additive-manufacturing techniques. One key property is Poisson's ratio, which is sometimes used as a metric for material properties. Materials with a negative Poisson's ratio, known as *auxetic materials*, have exceptional dynamic and static properties, such as high resistance to shock and impact, and the capability to mitigate sound waves and vibrations. Such materials can also show promising electromechanical properties in comparison to the bulk material as elaborated in [40–42]. Fig. 1.8 [43] shows a collection of periodic architected materials with either positive or negative Poisson's ratios.

Architected materials (and composites) intended for use in engineering applications are typically characterized by a unit cell, which is considered as the fundamental building block of the material and is used to construct the entire structure with the concept of periodicity.

Starting from the mechanical behaviour at the level of the unit cell, by incorporating the microstructural information, one can reach the desired properties at the mesoscopic or macroscopic scales. It is crucial to create predictive micromechanical models that can help understand how the current microstructure affects mechanical responses on both the mesoscopic and macroscopic levels. These models will allow the connection between different scales and establish the relationship between the equivalent properties and both the structure's mechanical and geometrical properties.

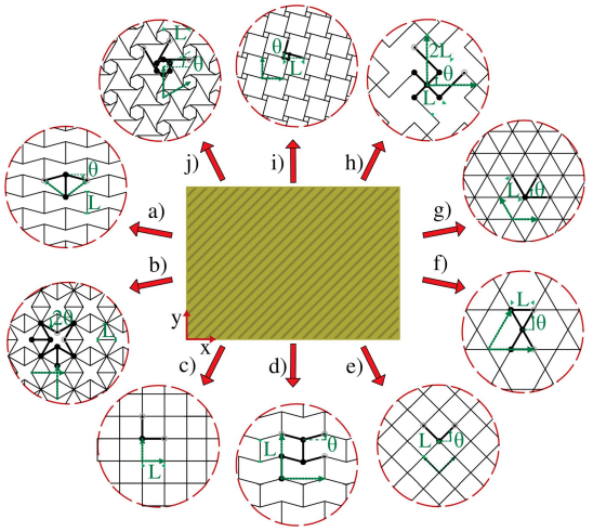

Figure 1.8 2D architected materials: (a)Hexagon, (b) star-shaped re-entrant, (c) rectangular,(d) semi-entrant, (e, f, g) diamond, kagome, triangular-saped, chiral lattices: (h) chiral diamond , (i) tetrachiral , (j) hexachiral [43].

1.4 Mechanics of generalized continua and enriched continuum models

Classical continuum mechanics uses only the first gradient of the displacement field to measure a body's deformations, disregarding higher-order displacement gradients. However, this approach is inherently size-independent, whereas materials may display non-local behaviors and exhibit a size dependency at a small scale due to their discrete nature, according to [44]. The validity of first-order Cauchy-based theories is limited to situations where there is a clear separation of scales, but they fail when dealing with small structural sizes, such as in MEMS, where the micro and macro structures become comparable in size. This failure occurs in scenarios where the wavelength of the loading is comparable to the size of the microstructure, or when deformation becomes localized within narrow bands due to strain softening. The width of these bands depends on microstructural length scales such as the size and distance between internal defects. Classical continuum theories, which lack internal length scales, are incapable of describing these localization phenomena adequately. Moreover, finite element (FE) simulations often exhibit a spurious mesh dependency, preventing them from accurately resolving the width of the localization bands.

Additionally, classical continuum mechanics is limited and cannot fully explain many mechanical and physical phenomena [45]. In the context of multiphysical phenomena, for instance electromagnetism, the presence of an electromagnetic source term leads to a non-symmetric stress tensor, thus requiring to extend the framework of Cauchy mechanics (that relies on a symmetrical stress tensor) to the context of so-called generalized continua [46]. The occurrence of couple body forces motivates the recourse

to a micropolar description of the magneto-mechanical response. The displacement of mobile electric charges within crystals due to e.g. bending leads to a polarization, a phenomenon deserving the name flexoelectricity. Flexoelectric solids couple the gradient of strain to the electric field and reciprocally the gradient of the electric field will induce a stress. The occurrence of multiphysical phenomena has led many authors to develop different generalized continuum models, including *Cosserat* [47–50], *strain gradient* [51] and *micromorphic* ones [52], an overview of these theories being exposed in [46].

Homogenization towards generalized continua (beyond Cauchy) aims to address the limitations of a strict scale separation and broaden the range of validity of the continuum approach beyond the restricted assumption of the scale separation [53, 54]. The definition of a generalized continuum can be extended through two main approaches, based on the classification into two main categories, namely the higher-order and higher-gradient continua, as shown in the illustration in the Fig. 1.9 [55].

Higher-order continua introduces further degrees of freedom, such as the Cosserat medium developed by the Cosserat brothers [56] and the micromorphic medium which is considered the most advanced generalized continuum theory [53, 54, 57–60]. In Cosserat elasticity, local rotations are included as additional degrees of freedom [56]. In the micropolar theory, interactions between material points through a surface element involve a force vector and a moment vector. This theory defines the "force-stress" tensor and the "couple-stress" tensor, respectively, as force per unit area and moment per unit area. The momentum balance indicates that the stress tensor in micropolar media is not symmetrical as in classical theory due to the imbalance of local moments produced by the microstructure. The non-symmetric stress tensor can be separated into two parts: a symmetrical part that leads to deformation of the macro-element, and a skew-symmetric part that contributes to the rigid rotation of the microstructure relative to the material.

On the other hand, *higher-gradient continua* involve incorporating higher gradients of the primary kinematic variable (such as strain or displacement) or internal variables (such as plasticity or damage) as additional variables in the formulation [61–66]. Of the various effective substitution media available (such as micromorphic, Cosserat strain-gradient, etc.), the strain gradient elastic continuum proposed by Mindlin [53] and Mindlin and Eshel [67] has several benefits, as highlighted in [68]. This model is capable of representing emergent properties without the need for the micromorphic medium, which has a greater number of inherent parameters [69], and can be constructed using asymptotic homogenization [62, 70, 71]. There has been a significant amount of research on the topic of strain gradient homogenization for over 40 years [55, 66, 71–73]. This research has covered a range of materials, including auxetic architected materials [74], composites with periodic or random microstructures [75], and random fibrous media [76]. Boutin [62] and Smyshlyaev and Cherednichenko [63], demonstrated the convergence of the asymptotic expansion of the solution, and then Tran et al. [71] developed a more systematic method for determining the strain gradient elastic moduli based also on asymptotic expansions of the fields.

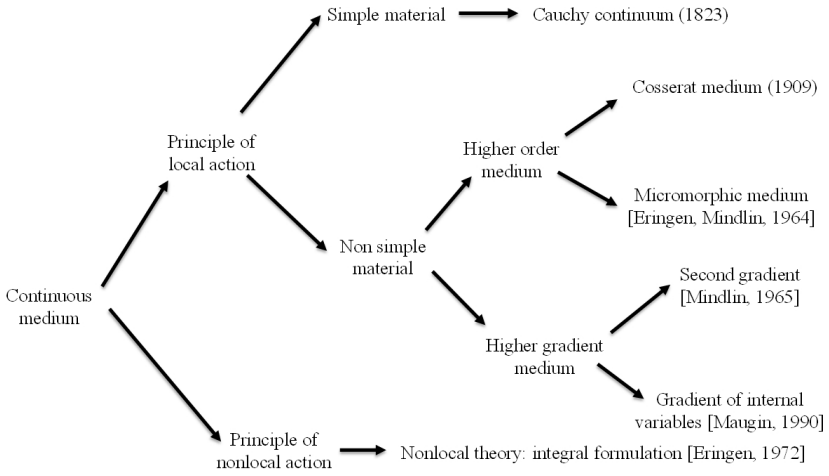

Figure 1.9 Illustration showing the classification of generalized continua into higher order and higher-grade media [55].

The existence of a couple $\boldsymbol{C}$ per unit volume in electromagnetic materials has often been suggested as a reason to take into account non-symmetric stress tensors [46];

$$\boldsymbol{C} = \boldsymbol{P} \times \boldsymbol{E} + \boldsymbol{M} \times \boldsymbol{H}$$

wherein $\boldsymbol{P}$ and $\boldsymbol{M}$ are respectively the electric polarization and magnetization per unit volume; $\boldsymbol{E}$ and $\boldsymbol{H}$ are the electric and magnetic fields respectively. This idea was the primary motivation behind the introduction of the generalization of continuum mechanics and the need of *enriched continuum theories* [77, 78]. In some cases of electroelastic and magnetoelastic couplings (which are known as the couplings of energetic origin), the standard balance equations of mechanics are not altered while only the energy balance equation changes. However, in more drastic consequences, electromagnetic materials possess an electric or magnetic microstructure that, despite its microscopic nature, affects the mechanical behavior and results in a non-symmetric stress tensor in the equation of moment of momentum that acquires additional contributions.

Approaches that tend to model magneto-mechanical interactions, show an analogy with the formulations of the Cosserat generalized continuum by introducing the concepts of spin and couple stress [46, 79]; the resulting equation is in the canonical form of the balance equation of angular momentum in Cosserat or micropolar continua but with all terms having a magnetic origin [80].

Besides the need of *enriched continuum theories* when dealing with multiphysics, these media are needed in situations to capture the influence of spatially rapid fluctuations at the mesoscopic and macroscopic levels. Enriched constitutive laws may be necessary in two scenarios. Firstly, when the chosen volume element is not representative in a statistical sense, such that individual carriers of the microstructure are excited and averaging cannot be performed. Secondly, when topological effects generate internal deformation modes that are not captured by a first gradient elastic theory. As we move to smaller scales, such as the micro or nanoscale, surface effects that were previously neglected in Cauchy elasticity

become dominant over volumetric ones, leading to the emergence of new behaviors at these scales. Enriched continuum theories incorporate a relaxation of the local action assumption and introduce spatial interactions and internal material-dependent length scales to consider the effect of neighboring points when formulating constitutive equations.

In the early sixties, most generalized continuum models were purely formal and not based on actual microstructures. Consequently, constitutive laws were developed in a phenomenological manner, without the need to recourse to micromechanical methods. However, the situation changed significantly in the early nineties with the development of new classes of materials such as composites, cellular solids (foams), and architected materials, as well as advancements in computational power and fabrication techniques like additive manufacturing. This prompted a growing interest in the mechanical and mathematical communities to understand the relation between emergent enriched behaviors at the level of an effective continuum and microscopic deformation modes.

1.5 Homogenization approaches in linear elasticity

To obtain the material properties of a structure on the level of the homogenized substitution medium, multiscale or experimental analyses can be performed. However, conducting fully resolved simulations can be computationally expensive, particularly when using full-scale finite element models [81]. Additionally, measuring the mechanical properties of such structures through experimentation can be challenging since the overall anisotropy must be considered. Furthermore, when there is no clear scale separation, enriched continuum theories that involve many more constitutive parameters than Cauchy elasticity theory may be necessary. Therefore, it is more practical to conduct *homogenization* towards effective models of the microstructure as a first step which can be used to do computations at the macrostructural level [82].

In recent decades, *homogenization* theory has been considered an essential tool in analyzing the behavior of highly heterogeneous materials like composites which consist of multiple constituents that differ significantly in their properties. Several homogenization techniques depend on identifying a representative volume element (RVE), which assumes that the RVE's structure is present almost everywhere throughout the structure: this means that there is a hidden pseudo-periodicity. The theory of *periodic homogenization* has a significant role in explaining the overall homogenized behavior. This assumption allows for precise mathematical results of the homogenized behavior. Sanchez-Palencia [83] was the initial developer of these methods, primarily using multi-scale asymptotic approaches. The mathematician J.L. Lions and his team [84] subsequently advanced these methods from a more mathematical viewpoint. However, in the context of periodic homogenization, many of the most effective and practical concepts are attributed to L. Tartar [85] .

For periodic composites, a commonly used method in the literature is to construct equivalent substitution media for the repetitive unit cell at an intermediate scale. This approach provides a good balance between accuracy and numerical efficiency for performing structural computations. Therefore, the

effective properties obtained from appropriate homogenization schemes are influenced by the geometrical and mechanical microstructural parameters of the composite constituents. However, this classical homogenization approach depends on a precise scale separation assumption, which is known as the Hill-Mandel macro-homogeneity condition [86–88].

Homogenization refers to a *mathematical theory* that deals with partial differential equations with rapidly varying coefficients at the microscopic scale of individual phases in heterogeneous composites, that are substituted at the macroscopic level with PDEs that have slowly oscillating coefficients. This allows to establish a relation between the physical behavior of heterogeneous materials at the macroscopic level and the behavior that takes place at the microscopic level. During the 1970s, homogenization evolved into a specialized research field within applied mathematics [84, 89–91], and a variety of approaches were introduced, including the asymptotic expansion method [83, 84, 92–94], G-convergence [95], H-convergence [85, 96, 97], Γ-convergence [98], and two-scale convergence [99], with applications in areas such as composite materials [100, 101] or the determination of the macroscopic limit of microscopic systems.

Homogenization methods can handle multifield phenomena like coupled electromechanical and electromagnetic effects, providing a quantitative understanding of the impact of microscale parameters on the overall multiphysical composite response. Theoretical works devoted to the computation of the effective behavior of piezoelectric composites started with Grekov et al. [102], followed by many others [103–105] who utilized multiscale asymptotic expansion. Later on, the method of oscillating functions was used for computing the homogenized response of stratified piezoelectric material [106].

1.5.1 A reduced modeling technique: the discrete homogenization

One can differentiate between two types of homogenization methods: continuous homogenization that is traditionally used for composites and discrete homogenization that utilizes reduced, discrete models for the structural elements that define the unit cell, such as a collection of beams or bars.

Discrete homogenization is a suitable method for modeling low-density lattice materials because their internal structural elements can be modeled as a collection of beams or rods, at a lower numerical cost compared to continuous homogenization approaches. They consider indeed a finite number of degrees of freedom (DOF in short) and can provide closed-form expressions for homogenized moduli [107, 108].

Among the discrete homogenization approaches, the so-called *continualization methods* presented in [109] have attracted a lot of attention in the literature. Continualization methods of periodic lattices rely on the idea of replacing discrete equations of motion by continuum differential equations to compute the static and dynamic effective qualities at a continuous level [110]. These approaches rely on two fundamental steps: (i) replacing discrete kinematics DOF with field variables that vary continuously in time and space, and then (ii) expressing the microscopic DOF within nearby UCs through a Taylor series expansion versus the chosen continuous DOF. The Lagrangian formulation emerged in the literature as

a strategy about twenty years ago. It can be used as an alternative to the strong form description of the lattice statics or dynamics [111–113]. By truncating the Taylor series at the first-order, an effective Cauchy continuum can be obtained, where only the first displacement gradient is significant.

1.6 Limitations in the literature

Despite the notable achievements of generalized continuum models in describing the mechanical behavior of microstructured solid bodies at a continuum level, they are not yet capable of accurately predicting their mechanical response.

1.6.1 Edge and size effects of lattice materials

When the macroscopic size of the sample is reduced into a microstructural size (size of a unit cell), new deformation mechanisms of the microstructure become apparent, expressed as interfacial and surface effects at the sub-micron scale. Most material classes demonstrate such size effects when the volume element being considered is too small for averaging towards a continuous medium that is meaningful. Size reduction may lead to stronger materials, which occurs for monocrystalline materials, ceramics, or composites. By designing architected materials at the nanoscale, it is possible to separate interdependent properties such as weight and strength. This allows designers to push the performance limits of existing materials.

Some experimental results on cellular solids, done on the macroscopic scale, have shown a size effect due to the relative size of the specimen and the unit cell size [114–116]. Nevertheless, it is widely recognized that Cauchy effective models are incapable of capturing the effects arising from these microstructural length scales of materials [114,117–119]. Size effects observed in lattice materials are typically categorized into two main types. The first type occurs due to the the edge of the macrodomain that is crossed by a truncated unit cell near the surface of the specimen [114, 116–119]. The second effect, known as the micropolar effect, arises from the inadequacy of classical continuum theory in describing macroscopic properties, such as flexural rigidity, when the lattice material's unit cell size is not small enough compared to the size of structural sample [120]. These limitations of classical homogenization methods can be overcome by using enriched effective continua, such as generalized continua including either additional degrees of freedom, such as rotation or higher gradients of fields such as displacement.

1.6.2 Quasi-periodic homogenization: the absence of strict periodicity

Quasi-periodic composites have a distinct feature that sets them apart from periodic composite materials: their unit cell does not repeat in an exact periodic pattern throughout the structure. Instead, the unit cell gradually changes along one or more periodicity directions, known as grading directions. This characteristic has led to the development of functionally graded materials (FGM), which are characterized

by a spatial variation of the geometry (and occasionally the material properties) of the microstructure within the unit cell. Fig. 1.10 [121] demonstrates this concept, using inclusion-based composite as an example.

One can use functionally graded materials (FGMs) with specific spatial gradients in thermal or mechanical properties for various engineering applications, such as thermal barrier coatings or contact surfaces [122]. When the grading in FGMs is too rapid compared to the size of the heterogeneities in the structure, *classical homogenization* methods become no longer applicable, which prohibits the definition of a statistically homogeneous representative volume element [121].

In such cases, the grading of the geometry cannot be neglected at the microscopic level, and any representative volume element must also be graded at the micro level. However, if the unit cell of a heterogeneous structure varies smoothly in space, the grading within adjacent unit cells can be disregarded, so that a given unit cell does not detect that its neighboring cells have a distinct microstructure. This feature leads to consider the homogenized behaviour locally without considering variations in the microgeometry of successive unit cells. Only the macro grading is taken into account to address the fact that homogenized material properties vary between unit cells in the macro-domain. In such situations, the initially heterogeneous structure can be modeled as a graded macroscopic material based on a field of homogenized properties that vary slowly at the macroscale. For example, layered materials with a graded microstructure can be approximated by an equivalent FGM with continuously varying properties at the macroscale [122–124]. This involves replacing the unit cell with a homogeneous Cauchy type material (with behavior remaining purely local in space), but with macroscopically varying properties (while ignoring the microstructural variation at the microlevel).

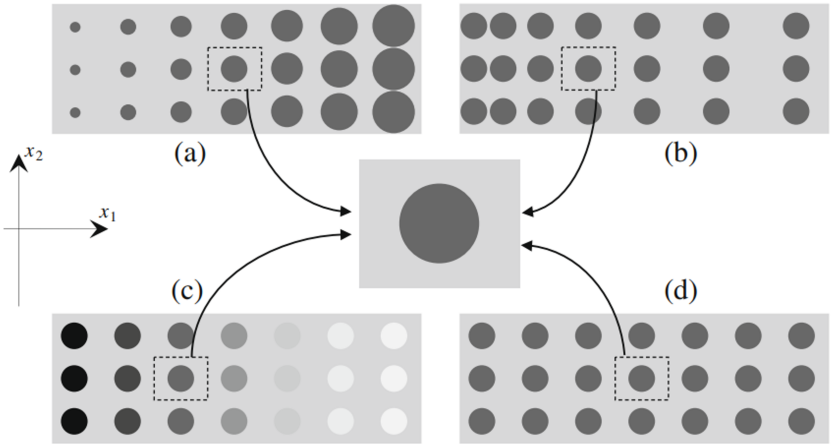

Figure 1.10 Illustration showing the quasi-periodic domain obtained from a periodic one with changing (a) the inclusion size, (b) the inclusion spacing, and (c) the material properties [121].

1.6.3 Difficulties in determining flexoelectric properties

Determining the flexoelectric tensor experimentally is a difficult task due to several factors. Firstly, the measurements require high-resolution equipment capable of detecting such small values. Additionally, it is challenging to isolate the flexoelectric effect from other physical phenomena in experiments. Moreover, the flexoelectric tensor has a high number of independent components, adding to the complexity of the experimental quantification [2].

Mathematical and computational models face another challenge due to the non-local nature of flexoelectricity, which involves strain or polarization gradients. As a result, analytical solutions are limited to simple 1D or 2D geometries. In such cases, numerical methods can be used as alternative strategies but they usually have some limitations or inefficiencies [2]. While many approaches aimed to model flexoelectricity from a phenomenological point of view [7, 51, 125, 126], few contributions deal with homogenization approaches to determine flexoelectric properties [127, 128].

1.7 Addressed scientific issues and methodology

Developing enriched continuum models of solids with a microstructure, especially composites and architected materials, requires addressing multiple scientific challenges outlined previously in the mechanical and multiphysical areas. To address these scientific issues, this thesis introduces several innovative aspects, which are outlined below:

- A new discrete homogenization model of periodic lattice materials is developed to upscale the microstructural information towards an effective strain gradient continuum at the macroscopic level;
- The scaling laws of the computed strain gradient moduli versus the absolute edge lengths of periodic architected materials are derived in a 2D context and are confirmed based on a different method involving the notion of shape derivative;
- An extended second strain gradient formulation of surface effects is proposed, generalizing Mindlin's approach to surface elasticity;
- New homogenization schemes of quasi-periodic microstructures are proposed in the context of strain gradient theory;
- A novel homogenization method of heterogeneous piezoelectric microstructures is developed relying on variational principles articulated with Hill lemma to evaluate the piezoelectric effective moduli in the region of small strains;
- The piezoelectric homogenization is then extended to determine the flexoelectric properties, thereby accounting for higher-gradient effects;
- A numerical algorithm is proposed and applied for the determination of piezoelectric and flexoelectric properties of different types of composites, architected materials and wave propagation;

- A variational based homogenization method for magnetoelastic composite materials is established using Hill lemma, towards Cosserat effective media, in a small strains framework.

1.8 Thesis outline

The thesis aims to bring some new developments in the field of homogenization of heterogeneous materials prone to multiphysical phenomena, focusing on piezoelectricity and magnetoelasticity. Moreover, while homogenization of periodic media have deserved a lot of contributions in the relevant literature, fewer works consider micromechanical approaches to upscale the response of quasi-periodic media in the context of higher gradient theories. The content of the manuscript accordingly reflects these two aspects tackled into the thesis; it is divided into two parts that cover explicitly the two aforementioned scientific issues.

Part I of the manuscript deals with the homogenization of periodic and quasi-periodic media towards a strain gradient effective continuum. This is shown, precisely, in **chapter 2** where a discrete homogenization method is applied for periodic architected materials leading to the elaboration of the higher order effective properties as closed form expressions depending on the edge length of the window of analysis. Whereas, in **chapter 3**, the idea of mapping any unit cell of the quasi-periodic domain to a parent periodic (fixed) unit cell is introduced through a quasi-periodic homogenization. This homogenization is developed starting from a volumetric expression of the energy and relying on the notion of shape derivative to determine the effective quasi-periodic properties.

Part II of the manuscript accounts for multiphysical aspects in the homogenization approaches towards generalized continua. This appears clearly in **chapter 4** where the theory of piezoelectric and flexoelectric homogenization is elaborated and followed by numerical applications for the homogenization of piezoelectric composites and architected materials as well as wave propagation analysis in **chapter 5**. Moreover, homogenization towards Cosserat (micropolar) effective continuum is addressed in **chapter 6** for magnetoelastic heterogeneous solids.

Finally, in the general **conclusion**, we summarize the main findings and novelties of the research and list the proposals for future developments.

Part I

Homogenization of periodic and quasi-periodic media towards strain gradient effective continua

Chapter 2

Analysis of surface effects based on first and second strain gradient mechanics

Summary

This chapter provides an analysis of surface effects (edge effects in 2D) in the mechanical response of architected materials modeled in the framework of strain gradient mechanics. The classical and strain gradient properties are evaluated by relying on a dedicated discrete homogenization method to upscale the microstructural information towards an effective strain gradient continuum at the macroscopic level. The formulation of the strain gradient model formulated via Hill extended macrohomogeneity condition allows a proper surface expression of the effective strain gradient kinematic and static variables. The scaling law of the strain gradient moduli with the edge contribution is obtained from their closed-form expressions versus the lattice microstructural parameters, and recoursing to the notion of shape derivative. The sensitivity of the strain gradient moduli to the surface effects (through edge contribution here) is evaluated, showing that absolute size effects are well captured by strain gradient moduli. The energetic formulation of a second strain gradient continuum allows to revisit the notion of anisotropic surface energy, thereby providing a generalization of Mindlin's model [129] of surface energy.

2.1 Introduction

It is well known that absolute size effects cannot be captured by standard elasticity theory based on the sole displacement gradient as a kinematic descriptor [130] since this theory is devoid of any internal length scale. The generalized continuum theories developed in the early sixties together with homogenization methods had the main objective to extend the range of validity of the classical Cauchy theory of elasticity beyond the strict assumption of scale separation [131]. Higher-order micro-continuum theories have been developed to account for the microstructure effects within heterogeneous solid bodies by introducing either additional degrees of freedom - like the Cosserat medium [132] or the micromorphic medium [133] - or additional higher-order gradients, as for the second gradient continuum [134, 135], both strategies leading to new material constants in addition to the conventional ones [129, 136–148]. Those theories introduce additional intrinsic parameters and internal length scales to correlate the microstructure to kinematic and static variables at the macroscopic level of an enriched continuum [149,150]. Higher-order continuum theories trace back to the works of the Cosserat brothers [151], followed by Toupin [134] and Mindlin [129,148]; they found a proper generalized formulation in subsequent works by Germain [152] and Sedov [153] using the virtual power method accounting for an enriched set of kinematic variables. Recent advances in the literature have seen many homogenization approaches either towards second gradient continuum [154–156] or Cosserat and micromorphic continua such as in [157–159]

Moreover, it is well established that unusual and novel properties of nanomaterials emerge from their surface/interfacial properties. One well-known consequence of surface properties is the appearance of size effects, traducing the dependency of the effective mechanical properties on the absolute size of the considered specimen, as exemplified in [160–164]. The analysis of surface phenomena and the formulation of models used in the context of surface-related mechanics originates in the pioneering works of Laplace [165, 166], Young [167], and Poisson [168], who introduced surface tension for fluids and formulated the corresponding boundary-value problems. Later on, Gibbs generalized the notion of surface tension for solids [169]. An account of the recent state of the art in the theory of capillarity can be found in [170,171]. Gurtin and Murdoch [172,173] elaborated a model of surface elasticity for elastic solids prone to large deformations; an elastic membrane is attached to the surface, with the stress resultant tensor within the membrane deserving the interpretation of surface stresses. This so-called Gurtin–Murdoch model predicts the size effects observed for nanosized materials [174–176], for which surface properties dominate over bulk properties.

The different models that incorporate surface effects involve enhanced constitutive equations including a description of the surface behavior, introducing a surface stress tensor constitutively related to a surface strain measure. More general surface models beyond the Gurtin-Murdoch model have been developed in the literature [177–185], like a Cosserat surface for material interfaces [186]. These extended models include additional material parameters [187–193], the determination of which is most of the time challenging.

Lattice materials are a type of structural and functional material with tunable mechanical and multiphysical properties that are increasingly being used in engineering applications due to their broad range of qualities that traditional materials cannot meet. As a type of porous material with reticulated structures, lattice materials are frequently developed with a periodic microstructure, allowing the identification of a repeated unit cell (UC in short). This property enables the efficient design of structures with excellent mechanical properties that can be manufactured using additive manufacturing techniques on the level of nanoscale [194].

Many works in the literature were devoted to predict the effective properties of lattice materials, each attempting to upscale the microscopic lattice level behavior to that of an effective continuum with homogenized properties. When such analyses are performed, two critical issues must be taken into account: first, the appropriate continuum theory for the substituted homogeneous medium, which is dependent on the inner lattice architecture and deformation mechanisms; and second, the ability of evaluating the scaling of classical and higher-order mechanical properties concerning for appropriate microstructural parameters. Measurements or recoursing to multiscale analyses can both be used to determine the structural response of an effective substitution medium. Fully resolved simulations, on the other hand, are almost always computationally too expensive [195]. Multiscale homogenization methods, on the other hand, can effectively relate calculated effective continuum-based properties of a supposed effective medium to microstructural lattice-based geometrical and mechanical parameters [196].

When compared to continuous homogenization approaches, discrete homogenization techniques use reduced, discrete type models for the structural elements of the lattice, characterizing the UC as a collection of bars or beams. As well, discrete homogenization is suitable for low-density lattice materials and architected materials because of their inner structural elements that can be naturally described as rods or beams at a low computational cost. These discrete modeling methods offer a benefit of taking into account a limited number of degrees of freedom (DOF) at the microscale and may also yield to analytical formulations for the effective moduli in certain situations [107, 108]. Continualization methods introduced in [109] are a class of the discrete homogenization methods that have gained notable attention in the literature. The methodology is further detailed in [197], and it will be used in the current work.

In this chapter, we adopt a strain gradient formulation for periodic architected materials with the main objective to analyze the contribution of surface effects (mainly edge effects that can lead to absolute size effects) based on strain gradient models of lattice materials constructed from homogenization methods.

The novel aspects investigated in this chapter are the following ones:

- A new discrete homogenization method adequate for architected media endowed with a discrete topology towards strain gradient effective continua is developed.
- The scaling laws of the computed strain gradient moduli versus the absolute edge lengths of periodic architected materials are derived in a 2D context.
- The dependency of the strain gradient effective moduli on the absolute edge length is confirmed by the computation of their shape derivative dependency.

- An extended second strain gradient formulation of surface effects is proposed, generalizing Mindlin's approach to surface elasticity.

The outline of the chapter is as follows: a discrete homogenization method of 2D lattice materials towards an effective strain gradient continuum is exposed in section 2.2. Thereby, the strain gradient elastic properties of architectured materials (exemplified by hexagons and square geometries) are evaluated in closed form versus the unit cell lattice microstructural parameters, focusing on the square and hexagonal unit cells. Based on this knowledge, the absolute size dependency of strain gradient moduli versus the edge length is evaluated (section 2.2). The sensitivity of the strain gradient moduli to geometrical parameters of the unit cell is evaluated in the same section 2.2. The shape derivative of the effective moduli is evaluated in section 2.3 as an alternative for analyzing absolute size effects caused by an edge contribution. An anisotropic notion of surface energy is derived in section 2.4 from a second strain gradient formulation, thereby providing a generalization of Mindlin's model. Conclusion is provided in section 2.5.

A few words regarding notations are in order. Vectors and higher-order tensors are denoted with boldface symbols. The bracket $\langle f(\boldsymbol{y})\rangle_Y := \frac{1}{|Y|}\int\limits_Y f(\boldsymbol{y})dV_y$ denotes the volume average of any quantity, here the scalar-valued function $f(\boldsymbol{y})$ over the domain of a reference lattice unit cell Y, with infinitesimal integration volume dV_y. The partial derivative of a scalar function $f\,(x)$ is denoted alternatively $\partial_x f$or $\frac{\partial f}{\partial x}$. The second order identity tensor is denoted $\boldsymbol{I}$. The gradient and divergence of a second order tensor $\boldsymbol{A}$ are successively denoted by the quantities $\boldsymbol{A}\otimes\nabla_x$ and $\boldsymbol{A}.\nabla_x$. The transpose of the second order tensor is denoted with a superscript 'T', so for instance $\boldsymbol{A}^T$.

2.2 Derivation of the strain gradient mechanics as a function of the length of lattice unit cell

In this section, we provide a more theoretical basis of the surface effects captured by strain gradient moduli by first deriving a surface formulation of Hill macrohomogeneity condition [74] to highlight the dependency of strain gradient moduli on a lattice length parameter. In the second part, the analytical expressions of the strain gradient moduli are derived through a discrete method of homogenization to show explicitly their dependency on the unit cell edge length.

2.2.1 Surface formulation of Hill macro-homogeneity condition

At the microscopic scale, the material is assumed to obey linear elasticity, so that the symmetrical Cauchy satisfies the following BVP posed over the UC with anti-periodic traction conditions (with no body force

tensor):

$$\begin{cases} \boldsymbol{\sigma} \cdot \nabla_y = \mathbf{0} \ \text{ in } Y \\ \boldsymbol{\sigma}.\boldsymbol{n} = \boldsymbol{t} \quad on\ \partial Y \\ \boldsymbol{\sigma} = \boldsymbol{C} : \boldsymbol{\varepsilon} \end{cases} \tag{2.1}$$

With $\boldsymbol{\sigma}$ being the symmetrical Cauchy stress, $\boldsymbol{n}$ the unit-length exterior normal vector, $\boldsymbol{t}$ the traction vector, $\boldsymbol{C}$ the fourth-order microscopic rigidity tensor, and $\boldsymbol{\varepsilon}$ the second-order strain tensor. We evaluate the virtual work of internal forces, the scalar-valued integral $\int_Y \boldsymbol{\sigma} : (\boldsymbol{\omega} \otimes \nabla_y) dV$, for a virtual velocity of the following form $\boldsymbol{\omega}(\boldsymbol{x}, \boldsymbol{\xi}) = \boldsymbol{E}(\boldsymbol{x}) \cdot \boldsymbol{\xi} + \frac{1}{2}\boldsymbol{K}(\boldsymbol{x}) \cdot (\boldsymbol{\xi} \otimes \boldsymbol{\xi})$, characteristic of the homogeneous strain gradient continuum, with $\boldsymbol{\xi} := \boldsymbol{y} - \boldsymbol{x}$, $\boldsymbol{E}$, and $\boldsymbol{K} = \boldsymbol{E} \otimes \nabla_x$ defining respectively the relative microposition, the strain, and strain gradient. Then, by converting volume integrals into surface integrals, a surface formulation of the Hill-Mandel macro-homogeneity condition is reached in the context of strain gradient mechanics [198]; this is explained in more technical details in Eq. A.4 of Appendix A:

$$\begin{aligned} \int_Y \boldsymbol{\sigma} : (\boldsymbol{\omega} \otimes \nabla_y) dV &= \frac{1}{|Y|} \sum_{i=1,2} \left(\left(\boldsymbol{E}(\boldsymbol{x}) \cdot \boldsymbol{Y}^i \right) \otimes \boldsymbol{N}^i \right) : \sum_{j=1,2} \left(\int_{\partial Y} (\boldsymbol{\sigma} \cdot \boldsymbol{n})\, ds \otimes \boldsymbol{Y}^j \right) + \\ &+ \sum_{i=1,2} \left(\left(\boldsymbol{K}(\boldsymbol{x}) \cdot \boldsymbol{Y}^i \right) \otimes \boldsymbol{N}^i \right) \therefore \sum_{j=1,2} \left(\frac{1}{2\,|Y|} \int_{\partial Y} (\boldsymbol{\sigma} \cdot \boldsymbol{n})\, ds \right) \otimes \boldsymbol{Y}^j \otimes \boldsymbol{Y}^j \\ &= \langle \boldsymbol{\sigma} \rangle_Y : \boldsymbol{E} + \langle \boldsymbol{\xi} \otimes \boldsymbol{\sigma} \rangle_Y \therefore \boldsymbol{K} = \boldsymbol{\Sigma} : \boldsymbol{E} + \boldsymbol{S} \therefore \boldsymbol{K} \\ &\Rightarrow \boldsymbol{\Sigma} := \langle \boldsymbol{y} \otimes \boldsymbol{t} \rangle_{\partial Y} = \frac{1}{|Y|} \sum_{j=1,2} \left(\int_{\Gamma_j} \boldsymbol{t} ds_y \otimes \underset{\sim}{\boldsymbol{Y}}^j \right) \\ &\Rightarrow \boldsymbol{S} := \frac{1}{2} \langle \boldsymbol{y} \otimes \boldsymbol{y} \otimes \boldsymbol{t} \rangle_{\partial Y} = \frac{1}{|Y|} \sum_{j=1,2} \frac{1}{2} \left(\int_{\Gamma_j} \boldsymbol{t} ds_y \otimes \underset{\sim}{\boldsymbol{Y}}^j \otimes \underset{\sim}{\boldsymbol{Y}}^j \right) \end{aligned} \tag{2.2}$$

in which $\boldsymbol{N}^i$ denote the macroscopic unit exterior normal. The upscaling of the microscopic virtual work leads to the macroscopic virtual work, expressing the duality product $\boldsymbol{\Sigma} : \boldsymbol{E} + \boldsymbol{S} \therefore \boldsymbol{K}$ of the macroscopic stress and hyperstress tensors with the macrostrain and macrostrain gradient tensors. Accordingly, the macroscopic Cauchy stress and hyperstress tensors express as unit cell volume averages of the microscopic Cauchy stress tensor weighted by the microposition vector, as expressed in the first set of the last two equalities in Eq. 2.2. Alternatively and at the macroscale, the classical and higher order stress tensors are expressed (second set of equalities in the last two relations of Eq. 2.2) as dyadic products of the surface average of the traction over the UC boundary, viz. the integral term $\int_{\partial Y} \left(\underset{\sim}{\boldsymbol{\sigma}} \cdot \underset{\sim}{\boldsymbol{n}} \right) ds_y$ with the periodicity vectors $\left\{ \underset{\sim}{\boldsymbol{Y}}^j \right\}$ associated to a given unit cell of a periodic heterogeneous domain shown in Fig. 2.1.

The periodicity vectors $\left\{ \underset{\sim}{\boldsymbol{Y}}^j \right\}$in previous relations relate material points under the periodicity conditions that hold for the unit cell shown in Fig. 2.1. Material points crossing the outer UC boundary are associated by pairs (from left to right boundaries and bottom top boundaries successively), with Γ_1, Γ_2 denoting the 'internal' boundaries, respectively the left vertical and bottom horizontal edges for the considered 2D rectangular unit cell domain.

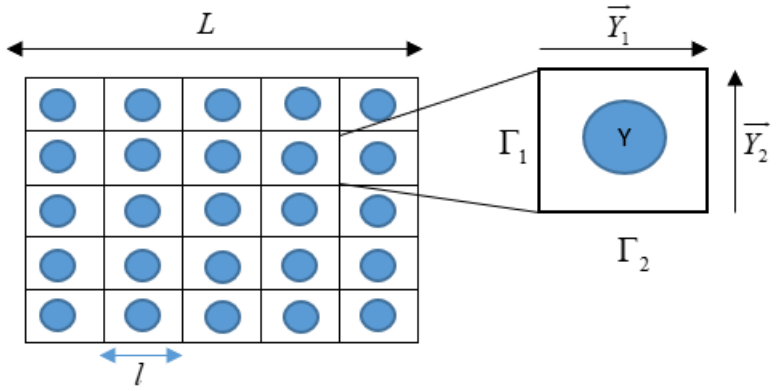

Figure 2.1 Periodic unit cell of a periodic material and definition of the internal boundaries and periodicity vectors.

While Cauchy stress and strains each involve one periodicity vector, this is not the case for the higher-order terms, where the presence of the periodicity vectors in the higher-order strain and stress tensors is unbalanced: $\underline{\boldsymbol{Y}}^j$ appears indeed twice in the hyperstress (the second term on the right-hand side of previous relation), but only once in the conjugated higher-order strain tensor. These facts have the consequence that Cauchy moduli do not depend on any absolute length, in contrast to strain gradient moduli. As it is well-known, the ratio of strain gradient to Cauchy moduli leads to the elaboration of internal lengths quantifying the strength of strain gradient interactions, so the intensity of interactions between neighboring unit cells. Beyond these internal lengths, strain gradient moduli may intrinsically depend on some absolute size through some geometrical length parameters.

We aim in the present chapter to investigate the dependency of the strain gradient formulation of architected media on the absolute size and to identify the relevant geometrical parameter of interest. For this purpose, we will elaborate a discrete homogenization method to derive the effective strain gradient moduli of periodic lattice materials, from the response of an identified repetitive unit cell.

2.2.2 Discrete homogenization of lattice materials

The effective (in a homogenized sense) properties of a strain gradient effective medium are derived from the periodic lattice material through a discrete homogenization method. The first step of the discrete homogenization method lies in the periodic repetition of an elementary unit cell made up of beams connected at nodes to define an infinite network in the plane or in 3D space. This discrete homogenization is developed based on a Taylor-series expansion of the kinematic variables [199–201]. To set the stage, a homogeneous isotropic beam element obeying Bernoulli beam theory is adopted for each of the struts building the investigated architected materials. The homogenization method is exemplified by the case of the topology of the hexagon, parameterized with the two lengths L and h, the thickness parameter t and the angular variable θ, as shown in Fig. 2.2. The second lattice material of interest in this work is the square lattice of linear length L and thickness t represented in Fig. 2.3. Referring to Fig. 2.2

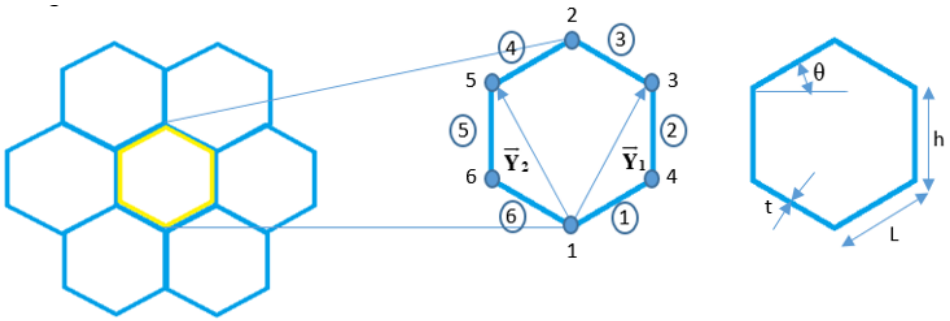

Figure 2.2 Hexagon unit cell with periodicity vectors and geometrical parameters (nodes and beam numbering).

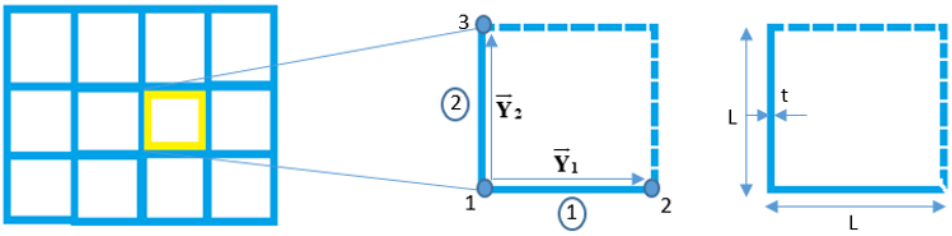

Figure 2.3 Square unit cell with periodicity vectors and its geometrical parameters (nodes and beam numbering).

and Fig. 2.3, there exists a dependency between the nodes of the unit cell according to the periodicity vectors for each of the two lattices. This dependency is determined according to Eq. B.7 and illustrated in Table 2.1 and Table 2.2 for the UC building the hexagonal and square lattices respectively.

Table 2.1 Dependency Relations of the Hexagon UC nodes

Independent node	Dependent node	$\overrightarrow{Y}_1$	$\overrightarrow{Y}_2$
1	3	1	0
1	5	0	1
2	4	0	-1
2	6	-1	0

Table 2.2 Dependency Relations of the Square UC nodes

Independent node	Dependent node	$\overrightarrow{Y}_1$	$\overrightarrow{Y}_2$
1	2	1	0
1	3	0	1

These dependency relations are utilized to generate the transformation matrix, which allows reducing the set of kinematic variables to the minimum independent ones and the lattice equilibrium to its periodic form: a dependency between the nodes of the UC takes place according to the following two relations for the kinematic variables and forces, successively the two relations:

$$\boldsymbol{q}_{\text{dependent}} = \boldsymbol{T}\, \boldsymbol{q}_{\text{independent}} \tag{2.3}$$

$$\boldsymbol{f}_{\text{independent}} = \boldsymbol{T}^{T} \boldsymbol{f}_{\text{dependent}} = 0 \tag{2.4}$$

wherein $\boldsymbol{q}_{\text{dependent}}$, $\boldsymbol{T}$, $\boldsymbol{q}_{\text{independent}}$ are successively the vectors of degrees of freedom (DOF in short) of the dependent nodes, the transformation matrix, and the vector of the DOF's of the independent nodes. The vectors $\boldsymbol{f}_{\text{dependent}}$ and $\boldsymbol{f}_{\text{independent}}$ are the nodal forces of the dependent and independent nodes respectively.

In the present 2D situation, the vectors or nodal DOFs expand as follows for the hexagonal UC to be more specific, with the first index referring to the node number (Fig. 2.2 and Fig. 2.3), and the second index indicating the direction (x or y):

$$\boldsymbol{q}^{\mathrm{T}}_{\text{dependent}} = \begin{bmatrix} u_{1x} & u_{1y} & u_{2x} & u_{2y} & u_{3x} & u_{3y} & u_{4x} & u_{4y} & u_{5x} & u_{5y} & u_{6x} & u_{6y} \end{bmatrix}$$
$$\boldsymbol{q}^{\mathrm{T}}_{\text{independent}} = \begin{bmatrix} u_{1x} & u_{1y} & u_{2x} & u_{2y} \end{bmatrix}$$

The detailed computations leading to the expression of the microscopic homogeneous displacement field in 2D versus the macroscopic strain and strain gradient tensors are to be found in [198]:

$$\boldsymbol{u}\left(\boldsymbol{x},\boldsymbol{y}\right) = \begin{vmatrix} u_x = u_{0x} + E_{11}x + E_{12}y + K_{111}\dfrac{x^2}{2} + K_{112}xy - K_{221}\dfrac{y^2}{2} + \left(K_{122}+K_{212}\right)\dfrac{y^2}{2}, \\ u_y = u_{0y} + E_{21}x + E_{22}y - K_{112}\dfrac{x^2}{2} + \left(K_{121}+K_{211}\right)\dfrac{x^2}{2} + K_{221}xy + K_{222}\dfrac{y^2}{2} \end{vmatrix} \tag{2.5}$$

wherein the vector $\boldsymbol{u}_0\left(\boldsymbol{x}\right) = \left(u_{0x}, u_{0y}\right)$ describes a rigid body motion. This expression will be used for the derivation of the strain gradient effective moduli based on the proposed discrete homogenization method.

The infinitesimal displacement field of a periodic node in any lattice material can be formulated according to Eq. 2.5, resulting in the following formulation of the UC discrete DOF's versus the continuous

kinematic variables of the adopted effective second gradient medium.

$$
\begin{bmatrix} u_{1x} \\ u_{1y} \\ u_{2x} \\ u_{2y} \\ u_{3x} \\ u_{3y} \\ u_{4x} \\ u_{4y} \\ u_{5x} \\ u_{5y} \\ u_{6x} \\ u_{6y} \end{bmatrix} = \begin{bmatrix} 1 & 0 & 0 & 0 \\ 0 & 1 & 0 & 0 \\ 0 & 0 & 1 & 0 \\ 0 & 0 & 0 & 1 \\ 1 & 0 & 0 & 0 \\ 0 & 1 & 0 & 0 \\ 0 & 0 & 1 & 0 \\ 0 & 0 & 0 & 1 \\ 1 & 0 & 0 & 0 \\ 0 & 1 & 0 & 0 \\ 0 & 0 & 1 & 0 \\ 0 & 0 & 0 & 1 \end{bmatrix} \begin{bmatrix} u_{1x} \\ u_{1y} \\ u_{2x} \\ u_{2y} \end{bmatrix}
$$

$$
+ \begin{bmatrix}
0 & 0 & 0 & 0 & 0 & 0 & 0 & 0 & 0 \\
0 & 0 & 0 & 0 & 0 & 0 & 0 & 0 & 0 \\
0 & 0 & 0 & 0 & 0 & 0 & 0 & 0 & 0 \\
0 & 0 & 0 & 0 & 0 & 0 & 0 & 0 & 0 \\
(x_3-x_1) & 0 & (y_3-y_1) & \frac{(x_3-x_1)^2}{2} & (x_3-x_1)(y_3-y_1) & -\frac{(y_3-y_1)^2}{2} & 0 & 0 & (y_3-y_1)^2 \\
0 & (y_3-y_1) & (x_3-x_1) & 0 & -\frac{(x_3-x_1)^2}{2} & (x_3-x_1)(y_3-y_1) & \frac{(y_3-y_1)^2}{2} & (x_3-x_1)^2 & 0 \\
(x_4-x_2) & 0 & (y_4-y_2) & \frac{(x_4-x_2)^2}{2} & (x_4-x_2)(y_4-y_2) & -\frac{(y_4-y_2)^2}{2} & 0 & 0 & (y_4-y_2)^2 \\
0 & (y_4-y_2) & (x_4-x_2) & 0 & -\frac{(x_4-x_2)^2}{2} & (x_4-x_2)(y_4-y_2) & \frac{(y_4-y_2)^2}{2} & (x_4-x_2)^2 & 0 \\
(x_5-x_1) & 0 & (y_5-y_1) & \frac{(x_5-x_1)^2}{2} & (x_5-x_1)(y_5-y_1) & -\frac{(y_5-y_1)^2}{2} & 0 & 0 & (y_5-y_1)^2 \\
0 & (y_5-y_1) & (x_5-x_1) & 0 & -\frac{(x_5-x_1)^2}{2} & (x_5-x_1)(y_5-y_1) & \frac{(y_5-y_1)^2}{2} & (x_5-x_1)^2 & 0 \\
(x_6-x_2) & 0 & (y_6-y_2) & \frac{(x_6-x_2)^2}{2} & (x_6-x_2)(y_6-y_2) & -\frac{(y_6-y_2)^2}{2} & 0 & 0 & (y_6-y_2)^2 \\
0 & (y_6-y_2) & (x_6-x_2) & 0 & -\frac{(x_6-x_2)^2}{2} & (x_6-x_2)(y_6-y_2) & \frac{(y_6-y_2)^2}{2} & (x_6-x_2)^2 & 0
\end{bmatrix}
\begin{bmatrix} E_{xx} \\ E_{yy} \\ E_{xy} \\ K_{xxx} \\ K_{xxy} \\ K_{yyx} \\ K_{yyy} \\ K_{xyx} \\ K_{xyy} \end{bmatrix}
\tag{2.6}
$$

The stiffness system of a UC that has b elements connected between j nodes is of the following expression:

$$\boldsymbol{K}_s \boldsymbol{q} = \boldsymbol{f} \tag{2.7}$$

where $\boldsymbol{K}_s \in R^{j \times j}$ is the stiffness matrix of the structure that relates the applied force vector, $\boldsymbol{f} \in R^j$ to the nodal deformation vector, $\boldsymbol{q} \in R^j$ (corresponding to $\boldsymbol{q}_{\text{dependent}}$ in Eqs. 2.3). Eqs. 2.3 and 2.4 are substituted into the stiffness system of the UC, Eq. 2.7, to derive its periodic reduced form as follows ($\tilde{\boldsymbol{q}}$ and $\tilde{\boldsymbol{f}}$ correspond to the independent vectors in Eqs. 2.3 and 2.4)

$$\widetilde{\boldsymbol{K}}_s \tilde{\boldsymbol{q}} = \tilde{\boldsymbol{f}} \tag{2.8}$$

where $\widetilde{\boldsymbol{K}}_s$ is the reduced stiffness matrix of the UC, expressed versus the original stiffness matrix as follows:

$$\widetilde{\boldsymbol{K}}_s = \boldsymbol{T}^T \boldsymbol{K}_s \boldsymbol{T} \tag{2.9}$$

Substituting Eq. 2.4 and 2.6 in Eq. 2.7 results in the following set of algebraic equations

$$\widetilde{\boldsymbol{K}}_s \, \tilde{\boldsymbol{q}} + \boldsymbol{T}^{\boldsymbol{T}} \boldsymbol{K}_s \bar{\boldsymbol{A}} \bar{\boldsymbol{\varepsilon}} = \tilde{\boldsymbol{f}} \tag{2.10}$$

that are solved for the independent microscopic displacement field versus the macro kinematic variables of the strain gradient continuum. $\bar{\boldsymbol{A}}$ and $\bar{\boldsymbol{\varepsilon}}$ are respectively the matrix to create continuous nodal displacement, and the vector of kinematic variables of the continuum model. These expressions are then substituted along with Eqs. 2.3, 2.4, and 2.6 into the expression of strain energy Eq. 2.11 to get the continuous expression of the strain gradient strain energy density:

$$W_s = \frac{1}{2} q^T \boldsymbol{K}_s q = \frac{1}{2} \left[\boldsymbol{T}\tilde{q} + \bar{\boldsymbol{A}}\bar{\boldsymbol{\varepsilon}}\right]^T \boldsymbol{K}_s \left[\boldsymbol{T}\tilde{q} + \bar{\boldsymbol{A}}\bar{\boldsymbol{\varepsilon}}\right] \tag{2.11}$$

The nodal forces and deformations formulated in the previous section are used to derive the effective mechanical properties using Hill-Mandel macro-homogeneity condition, which can be written, according to [198], as:

$$\boldsymbol{W}_s\left(\boldsymbol{E}, \boldsymbol{K}\right) = \frac{1}{2}(\boldsymbol{\Sigma}_{ij} : \boldsymbol{E}_{ij} + \boldsymbol{S}_{ijk} \therefore \boldsymbol{K}_{ijk}) = \langle \boldsymbol{w}_{\boldsymbol{\mu}} \rangle \tag{2.12}$$

The stress and hyperstress are formally expressed as the partial derivative of the macroscopic strain energy density with respect to the conjugated kinematic variables:

$$\boldsymbol{\Sigma}_{ij} = \frac{\partial \boldsymbol{W}_s}{\partial \boldsymbol{E}_{ij}}, \quad \boldsymbol{S}_{ijk} = \frac{\partial \boldsymbol{W}_s}{\partial \boldsymbol{K}_{ijk}} \tag{2.13}$$

Then, according to the general constitutive law in Eq. 2.14 (considering a 2D formulation with the following correspondence of indices: i, j, k, l=x,y)

$$\begin{aligned} \boldsymbol{\Sigma}_{ij} &= \boldsymbol{C}_{ijkl} : \boldsymbol{E}_{kl} + \boldsymbol{B}_{ijklm} \therefore \boldsymbol{K}_{klm} \\ \boldsymbol{S}_{ijk} &= \boldsymbol{B}_{ijkpq}{}^{\boldsymbol{T}} : \boldsymbol{E}_{pq} + \boldsymbol{A}_{ijkpqr} \therefore \boldsymbol{K}_{pqr} \end{aligned} \tag{2.14}$$

the effective strain gradient homogenized properties appear in component form in the effective strain gradient constitutive law:

$$\begin{aligned} \begin{Bmatrix} \Sigma_{xx} \\ \Sigma_{yy} \\ \Sigma_{xy} \end{Bmatrix} &= \begin{bmatrix} C_{11} & C_{12} & 0 \\ C_{12} & C_{22} & 0 \\ 0 & 0 & C_{33} \end{bmatrix} \begin{Bmatrix} E_{xx} \\ E_{yy} \\ E_{xy} \end{Bmatrix} + \begin{bmatrix} B_{11} & B_{12} & B_{13} & B_{14} & B_{15} & B_{16} \\ B_{21} & B_{22} & B_{23} & B_{24} & B_{25} & B_{26} \\ B_{31} & B_{32} & B_{33} & B_{34} & B_{35} & B_{36} \end{bmatrix} \begin{bmatrix} K_{xxx} \\ K_{xxy} \\ K_{yyx} \\ K_{yyy} \\ K_{xyx} \\ K_{xyy} \end{bmatrix} \\ \begin{Bmatrix} S_{xxx} \\ S_{xxy} \\ S_{yyx} \\ S_{yyy} \\ S_{xyx} \\ S_{xyy} \end{Bmatrix} &= \begin{bmatrix} B_{11} & B_{21} & B_{31} \\ B_{12} & B_{22} & B_{32} \\ B_{13} & B_{23} & B_{33} \\ B_{14} & B_{24} & B_{34} \\ B_{15} & B_{25} & B_{35} \\ B_{16} & B_{26} & B_{36} \end{bmatrix} \begin{Bmatrix} E_{xx} \\ E_{yy} \\ E_{xy} \end{Bmatrix} + \begin{bmatrix} A_{11} & A_{12} & A_{13} & A_{14} & A_{15} & A_{16} \\ A_{21} & A_{22} & A_{23} & A_{24} & A_{25} & A_{26} \\ A_{31} & A_{32} & A_{33} & A_{34} & A_{35} & A_{36} \\ A_{41} & A_{42} & A_{43} & A_{44} & A_{45} & A_{46} \\ A_{51} & A_{52} & A_{53} & A_{54} & A_{55} & A_{56} \\ A_{61} & A_{62} & A_{63} & A_{64} & A_{65} & A_{66} \end{bmatrix} \begin{bmatrix} K_{xxx} \\ K_{xxy} \\ K_{yyx} \\ K_{yyy} \\ K_{xyx} \\ K_{xyy} \end{bmatrix} \end{aligned} \tag{2.15}$$

wherein [C], [B], and [A] are respectively the homogenized Cauchy, coupling and strain gradient tensors. The same procedure is to be followed for the square unit cell by applying the periodicity relations according

to Table 2.2.

The non-zero effective moduli for the hexagon and square lattices are determined as closed-form expressions of the microscopic parameters of the UCs shown in Fig. 2.2 and Fig. 2.3. (see Table C.1 and Table C.2 in Appendix C). The coupling matrix [B] is found to be zero for the hexagonal UC as expected due to its centrosymmetric features.

The predictions of the employed discrete homogenization method are compared to the predictions of an alternative discrete homogenization method developed in [202] summarized in the Appendix D. A good agreement is obtained in Fig. 2.4 between the values of effective strain gradient parameters obtained from both methods as a function of θ of a hexagonal unit cell (with a maximum relative difference around 5%).

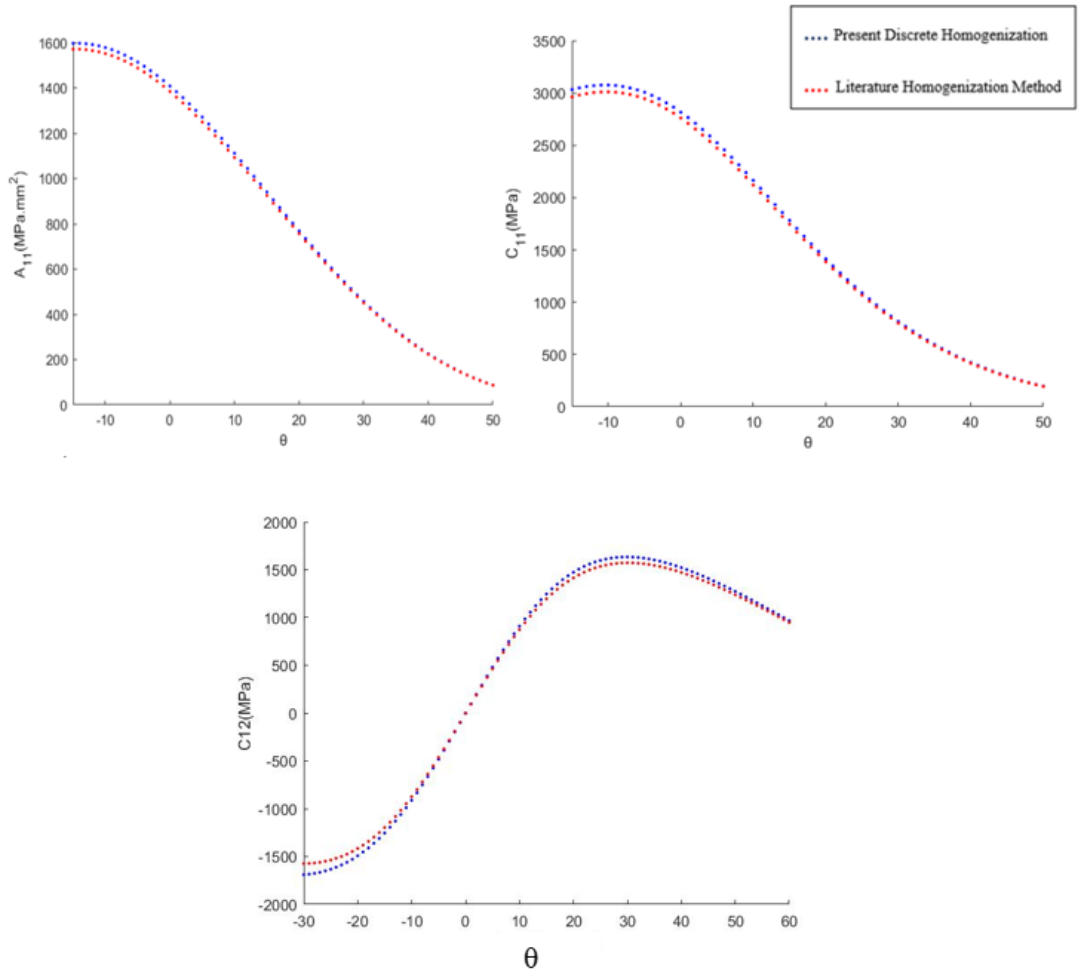

Figure 2.4 Homogenized Cauchy and strain gradient tensile moduli obtained computed from the present discrete homogenization method and the method in literature [202] versus θ for the hexagonal UC .

We subsequently investigate the ability of the identified strain gradient mechanical model to capture absolute size effects.

2.2.3 Absolute size dependency of strain gradient moduli

In order to determine the expected absolute edge length dependency of the effective strain gradient moduli, a selection of first and strain gradient moduli obtained on previous section (their analytical expressions are in Appendix C) is plotted versus the edge length of the hexagon and square unit cells. We vary the unit cell shape in a self-similar manner, such a way that the volume fraction remains constant. The volume fraction of material can be determined by adjusting the microstructural parameters from the following relation:

$$V_f^* = \left(1 - \frac{V_{void}}{V_{cell}}\right) \tag{2.16}$$

The volume fraction of material is set in this section for all UC configurations to be equal to 0.4. The mechanical properties are selected for aluminum, with E=69000 MPa, $\nu = 0.3$, and b=1mm (outward plane thickness), with the angular variable set to be $\theta = 30^\circ$ for the regular hexagon.

As shown in Fig. 2.5 and Fig. 2.6, the Cauchy effective moduli for the hexagon and square unit cells remain constant when the dimensions of the unit cell vary; this finding is consistent with the fact that Cauchy elasticity is devoid of any intrinsic length, and they remain unchanged for self-similar UC shapes sharing the same relative volume fraction of material. In contrast to this, the strain gradient effective moduli show a quadratic increase with the unit cell edge length for both considered unit cells.

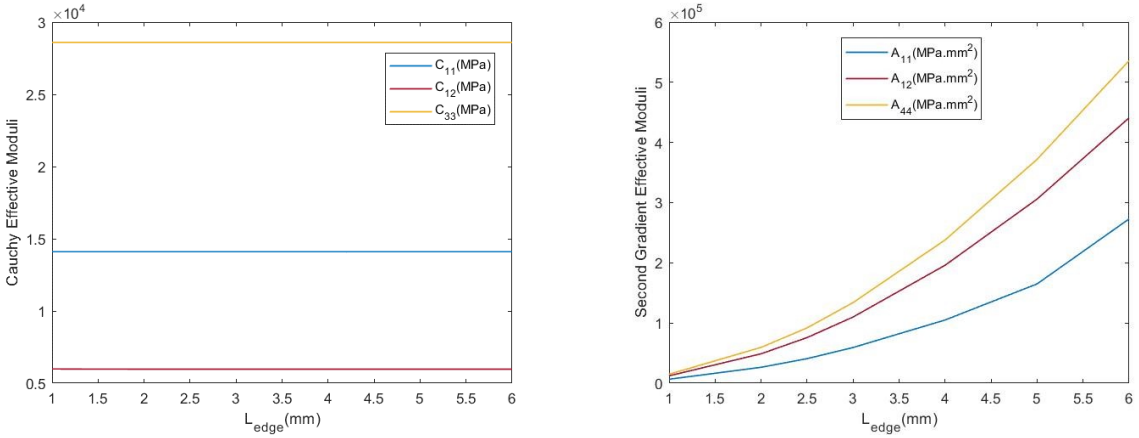

Figure 2.5 Cauchy (a) and strain gradient moduli (b) as a function of the unit cell edge length for the regular hexagonal unit cell.

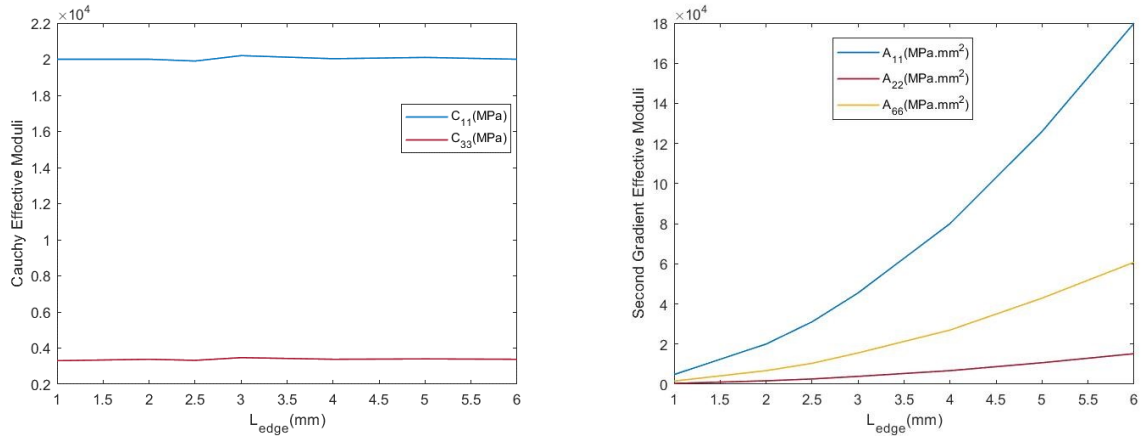

Figure 2.6 Cauchy (a) and strain gradient moduli (b) as function of the unit cell edge length for the square unit cell.

2.2.4 Sensitivity of the effective strain gradient moduli to lattice geometrical parameters

In this paragraph, an analysis is performed to study the sensitivity of the effective moduli to the geometrical parameters of the unit cell. For the hexagonal unit cell, the chosen design variables are the dimentionless ratio t/L and the angular variable θ with the ranges $t/L \in [0.04, 0.2]$ and $\theta \in [-15, 50]$. In all subsequent analyses, the out-of-plane thickness is set to be $b = 1$ mm and the ratio L/h is fixed at a constant unity value. The mechanical properties (Young modulus and Poisson's ratio) of the base material of the unit cell are $E = 69000$ MPa and $\nu = 0.3$.

Fig. 2.7 shows the contour plots of the strain gradient modulus A_{11}, the Cauchy modulus C_{11}, and the associated internal length $l_x = \sqrt{\frac{A_{11}}{C_{11}}}$, respectively, as a function of the geometrical variables t/L and θ. The values of A_{11} and C_{11} increase as the angular variable θ decreases. This shows that the re-entrant hexagon, defining an auxetic configurations (it has a negative Poisson's ratio) has higher values of the effective strain gradient moduli compared to the regular hexagon with positive Poisson's ratio values. The internal length l_x shows the highest values for the hexagonal UC compared to the rectangular and even the re-entrant UC; for both the extension and shear modes, the internal length values reaches about 70% of the UC linear size for configuration angles around 40°. For auxetic hexagonal configurations, the internal length in the uniaxial extension mode reaches similar values of 71%, with the internal length in shear reaching lower values of about 40% of the UC linear size (Fig. 2.8).

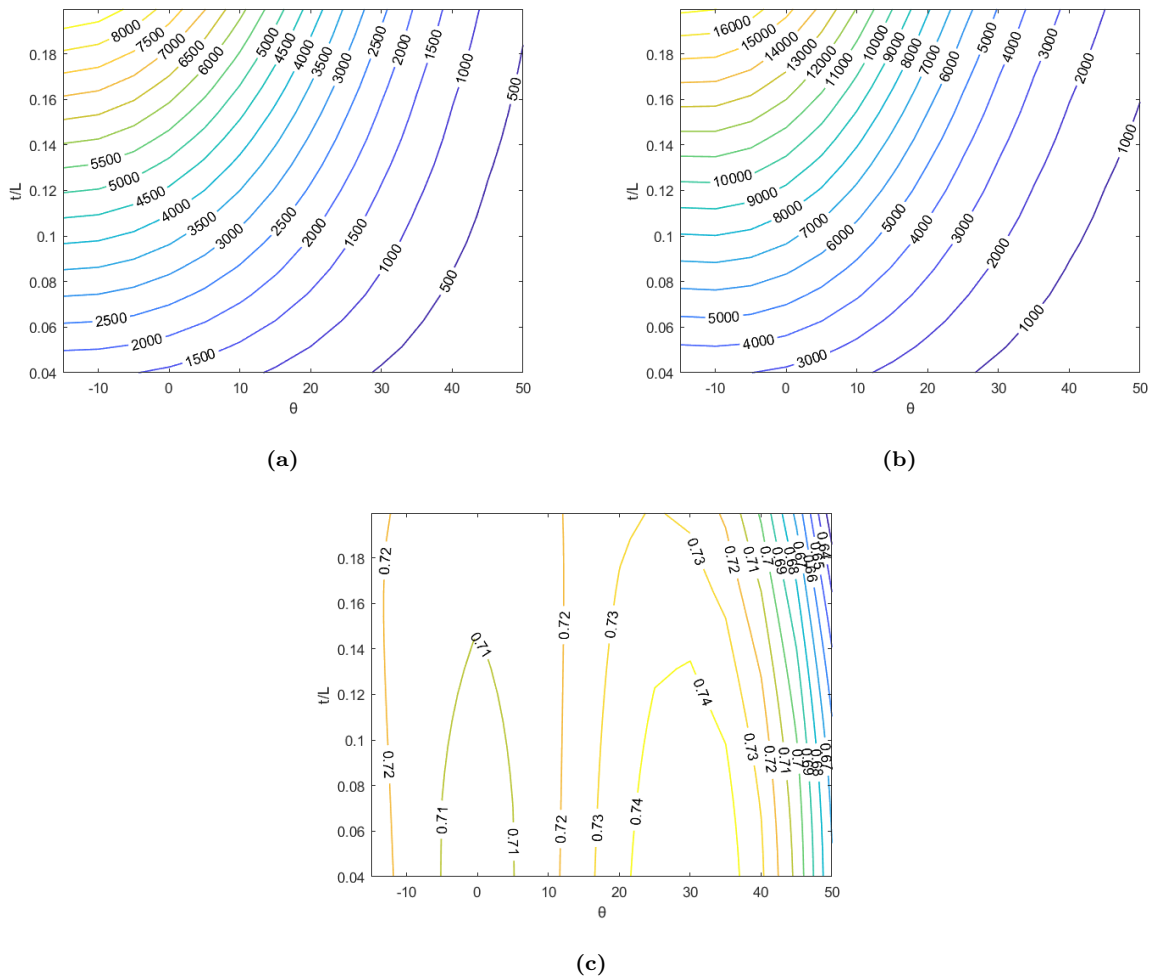

Figure 2.7 Contour plots of effective moduli for the hexagonal lattice (a) A_{11},(b) C_{11}, and internal length (c) l_x as a function of the geometrical lattice parameters t/L and θ

Fig. 2.8 reflects the shear modes, showing the contour plots of the effective moduli A_{55}, C_{33} and internal shear length l_{xy}. The effective strain modulus A_{55} increases with the ratio t/L for the three considered lattice materials, but the highest values are attained for the hexagon. However, the Cauchy modulus C_{33} shows the highest values for the re-entrant unit cell, while the internal length l_{xy} reaches its highest values for the hexagon at low values of the slenderness ratio t/L.

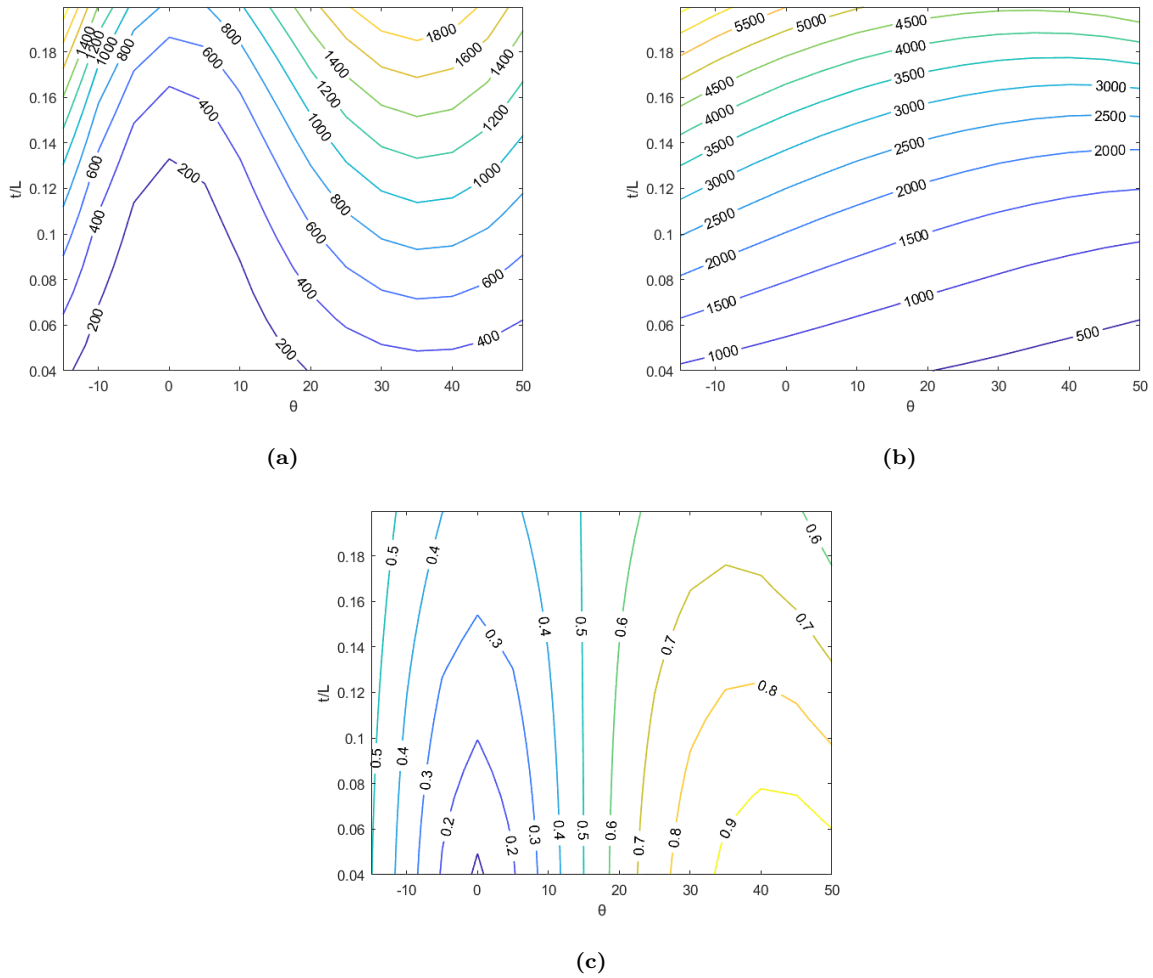

Figure 2.8 Contour plots of effective moduli of the hexagonal lattice (a) A_{55} (b) C_{33}, and internal length l_{xy} (c) as a function of the geometrical parameters t/L and θ

In the next section, we use a different method to analyze the absolute edge length dependency of the effective strain gradient moduli, relying on the evaluation of the sensitivity of these moduli to a variation of their shape, to induce a variation of unit cell area (edge length in the considered 2D situation). More specifically, the variation the unit cell edge length over self-similar unit cell shapes is achieved by imposing a suitable shape velocity field to the UC internal and external edges defining the UC boundaries.

2.3 Shape sensitivity of the strain gradient moduli

To quantify the sensitivity of the effective strain gradient moduli of the considered architected materials to the variation of the periodic unit cell boundary, thusly versus the total amount of edge length of the lattice UC in the considered 2D context, we rely on the notion of shape derivative of the strain energy for an effective medium of purely strain gradient type. Indeed, for such self-similar shapes, the Cauchy effective moduli will remain the same. Concerning this objective to quantify the absolute edge length dependency of the effective strain gradient moduli, the basic underlying physical idea is that surface effects

in 3D (or edge effects for 2D geometries) arise as a suitable measure of the resistance of an interface or surface to change of its shape or size (area in 3D, length in 2D) due to the 'deformation' (in the sense of design variation) of the enclosed domain.

2.3.1 Shape derivative of the energy within the framework of strain gradient mechanics

Consider initially a domain Y with boundary ∂Y subjected to a perturbation, so that the new domain occupied by the unit cell becomes : $Y_\tau := \{\boldsymbol{y}_\tau = \boldsymbol{y} + \tau \boldsymbol{V}_S, \boldsymbol{y} \in Y\}$, with τ a small scalar parameter used to parameterize the domain and $\boldsymbol{V}_S := \delta \boldsymbol{X}_{|\partial Y}$ the shape velocity field representing the change of UC boundary, so it is an input field for modifying the unit cell design [203]. The unit exterior normal vector to the domain filled with material is denoted $\boldsymbol{N}$ here and in the sequel. The shape velocity field vector $\boldsymbol{V}_S$ can be decomposed into a normal part $V_{S,N}\boldsymbol{N}$ and a tangential contribution $\boldsymbol{V}_{S,T}$, this last part being known not to contribute to the shape derivative [204]:

$$\begin{vmatrix} \boldsymbol{V}_S = \boldsymbol{V}_{S,T} + V_{S,N}\boldsymbol{N} \\ V_{S,N} := \boldsymbol{V}_S.\boldsymbol{N} \\ \boldsymbol{V}_{S,T}.\boldsymbol{N} = 0 \end{vmatrix} \tag{2.17}$$

in which the scalar projection $V_{S,N}$ represents the magnitude of the normal shape velocity.

The shape derivative D_s of the cost function J defined on the set of domains Y_τ parameterized with τ parameter is elaborated as the following limit [204]:

$$D_s J = \lim_{\tau \to 0} \frac{J(Y_\tau) - J(Y)}{\tau} \tag{2.18}$$

in which $Y := Y_{\tau=0}$ denotes the initial unperturbed domain. Selecting the total potential energy as the cost function, its shape derivative is then expressed after some derivations over the homogenized domain according to [204] as:

$$D_s J = \int_{\partial Y} \boldsymbol{N}.\boldsymbol{\Sigma}_{Eshelby}.\delta \boldsymbol{X}\, d(\partial Y) \tag{2.19}$$

wherein J is defined as the difference of the internal energy of the homogeneous continuum V_x and the work of external forces acting on it:

$$J(Y_\tau) := W_{in} - W_{ext} \tag{2.20}$$

The second order tensor therein $\boldsymbol{\Sigma}_{Eshelby} := w_\mu \boldsymbol{I} - \boldsymbol{\varepsilon}^T.\boldsymbol{\sigma}$ is the Eshelby stress acting at the microscopic level of the lattice unit cell. Thus, we get from Eq. 2.19 and for the more specific choice of a purely normal shape velocity field the expression of the shape derivative of the total potential energy

$$D_s J = \int_{\partial Y} \boldsymbol{N}.\boldsymbol{\Sigma}_{Eshelby}.\boldsymbol{N} V_{S,N}\, d(\partial Y) = \int_{\partial Y} \boldsymbol{\Sigma}_{NN} V_{S,N}\, d(\partial Y) \tag{2.21}$$

Thereby, the normal component of Eshelby stress $\boldsymbol{\Sigma}_{NN} := \boldsymbol{N}.\boldsymbol{\Sigma}_{Eshelby}.\boldsymbol{N}$ in short can be viewed as the driving force acting to change the shape of the domain, possibly at the expense of an extra energy cost

associated with the concomitant increase of the domain area (in 3D) or edge (in 2D). Note that the physical unit of the previous integral is that of energy (in Joules).

The surface integral on the right-hand side of Eq. 2.21 defines a surface density of mechanical energy acting on the unit cell boundary :

$$\begin{aligned}
&\int_{\partial Y} \boldsymbol{\Sigma}_{NN} V_{S,N} d(\partial Y) = \int_{\partial Y} \left(w_\mu(\boldsymbol{\varepsilon}) - \boldsymbol{\varepsilon}.\boldsymbol{\sigma}\right) V_{S,N} d(\partial Y) \\
&\left| \begin{aligned} &\boldsymbol{\varepsilon} = \boldsymbol{A}^K \therefore \boldsymbol{K}, \\ &\boldsymbol{\sigma} = \boldsymbol{c}_\mu : \varepsilon = \boldsymbol{c}_\mu : \boldsymbol{A}^K \therefore \boldsymbol{K} \end{aligned} \right. \\
&\Rightarrow \int_{\partial Y} \boldsymbol{\Sigma}_{NN} V_{S,N} d(\partial Y) = \frac{1}{2} \int_{\partial Y} \left(\boldsymbol{A}^K \therefore \boldsymbol{K} : \boldsymbol{c}_\mu : \boldsymbol{A}^K \therefore \boldsymbol{K}\right) V_{S,N} d(\partial Y) - \int_{\partial Y} \boldsymbol{N}.\left(\boldsymbol{A}^K \therefore \boldsymbol{K}.\boldsymbol{c}_\mu : \boldsymbol{A}^K \therefore \boldsymbol{K}\right).\boldsymbol{N} V_{S,N} d(\partial Y)
\end{aligned} \tag{2.22}$$

wherein $\boldsymbol{A}^K$ is the strain gradient localization operator (fifth-order tensor) relating the microscopic strain to the macroscopic strain gradient tensor acting over the unit cell. In deriving the set of relations of Eq. 2.22, we have assumed that the unit cell is subjected to a pure strain gradient kinematic loading (the macrostrain tensor is chosen to be nil).

In a subsequent step, Clapeyron theorem is used to express the total potential energy, elaborated as the difference of internal mechanical energy W_{in} and work of external forces W_{ext} expressed over the homogeneous unit cell V_x, in terms of the strain energy density, which is the quantity of interest for the shape sensitivity analysis to follow. It follows that the total potential energy can be fully expressed in terms of the internal mechanical energy, considering that the macroscopic energy density is independent of the macroscopic spatial position within the homogeneous unit cell:

$$\left| \begin{aligned} &W_{in} := \frac{1}{2} \int_{V_x} \left(\boldsymbol{C}^{\boldsymbol{hom}} : \boldsymbol{E} : \boldsymbol{E} + \boldsymbol{A}^{\boldsymbol{hom}} \therefore \boldsymbol{K} \therefore \boldsymbol{K}\right) dV_x \\ &Clapeyron\ theorem \Rightarrow J(Y_\tau) := -W_{in} \end{aligned} \right. \tag{2.23}$$

The work of external forces for the strain gradient medium includes (beyond the classical Cauchy type contributions) double forces, as well as edge and corner contributions [205]; it will however not be written here, since it does not contribute to the analysis of absolute edge effects to follow.

The previous relation allows evaluating the sensitivity of the strain gradient elastic energy to the area variation induced by the shape velocity field applied over the unit cell boundaries:

$$\frac{\boldsymbol{D_s} J}{DA} = -\frac{\boldsymbol{D_s}\left(\frac{1}{2}|V_x| \left\langle \boldsymbol{C}^{\boldsymbol{hom}} : \boldsymbol{E} : \boldsymbol{E} + \boldsymbol{A}^{\boldsymbol{hom}} \therefore \boldsymbol{K} \therefore \boldsymbol{K} \right\rangle_{V_x}\right)}{DA} = \frac{\int_{\partial Y} \boldsymbol{N}.\boldsymbol{\Sigma}_{Eshelby}.\boldsymbol{N} V_{S,N} d(\partial Y)}{\iint_{\partial Y} V_{S,N} d\theta} \tag{2.24}$$

The volume $|V_x|$ (area in 2D) of the unit cell has been introduced in the previous relation as a way to express the macroscopic energy in terms of a volume integral to subsequently perform integration by part (considering that the macroscopic energy density does not depend on spatial position), viz.

$$|V_x| \left\langle \boldsymbol{C}^{\boldsymbol{hom}} : \boldsymbol{E} : \boldsymbol{E} + \boldsymbol{A}^{\boldsymbol{hom}} \therefore \boldsymbol{K} \therefore \boldsymbol{K} \right\rangle_{V_x} = \int_{V_x} \left(\boldsymbol{C}^{\boldsymbol{hom}} : \boldsymbol{E} : \boldsymbol{E} + \boldsymbol{A}^{\boldsymbol{hom}} \therefore \boldsymbol{K} \therefore \boldsymbol{K}\right) dV_x \tag{2.25}$$

Due to the normalization of the right-hand side by the shape velocity field, the left-hand side (and the right-hand side) in Eq. 2.24 becomes independent of it, especially in the more specific case for which a uniform shape velocity field is applied.

While the previous evaluation of the Eshelby stress relies on the microscopic fields evaluated within the unit cell (via FE simulations employing periodicity boundary conditions), the macroscopic approach replacing the heterogeneous UC with an effective strain gradient continuum will next be considered in order to perform a shape sensitivity analysis of the homogenized strain gradient moduli.

The sensitivity of the effective continuum strain gradient macroscopic energy to a variation of the unit cell internal and external boundary motion is captured by the shape derivative of the strain energy density of the effective continuum within the framework of strain gradient mechanics, articulated with Hill macrohomogeneity condition. Thereby, it extends the evaluation done in [206] for a Cauchy medium in which only the first displacement gradient is of importance. Using the Clapeyron theorem, the shape derivative of the effective moduli will be deduced from the shape derivative of the internal macroscopic energy as in Eq. 2.24, wherein the surface integral is expressed over the entire unit cell boundary.
The connection between the microscopic displacement entering into the Eshelby stress and the macroscopic kinematic loadings over the unit cell, tensors $\boldsymbol{E}, \boldsymbol{K}$, is formulated by writing the UC boundary value problem for the displacement fluctuation as follows:

$$\left|\begin{array}{l} -\, div_y \left(C_\mu : \varepsilon \left(\boldsymbol{u}_{E,K}\right)\right) = \boldsymbol{0} \\ \sigma_\mu := C_\mu : \varepsilon \left(\boldsymbol{u}_{E,K}\right) = 0 \text{ on } \partial Y \\ \boldsymbol{u}_{E,K} = \boldsymbol{E}(\boldsymbol{x}).\boldsymbol{y} + \dfrac{1}{2}\boldsymbol{K}(\boldsymbol{x}) : (\boldsymbol{y} \otimes \boldsymbol{y}) + \tilde{\boldsymbol{u}}_{E,K}\left(\boldsymbol{y}\right) \\ \boldsymbol{u}_{E,K} \text{ Y-periodic} \end{array}\right. \tag{2.26}$$

in which $\tilde{\boldsymbol{u}}_{E,K}\left(\boldsymbol{y}\right)$ denotes the displacement fluctuation induced by the macroscopic kinematic loading applied over the unit cell, namely the macroscopic strain and strain gradient tensors $\boldsymbol{E}, \boldsymbol{K}$ respectively. Thereby, the shape derivative of the classical and strain gradient moduli can be evaluated based on the expression of the microscopic displacement versus the macroscopic kinematic loadings and its periodic fluctuation obtained by solving the corresponding unit cell BVP in Eq. 2.26.

Especially, the sensitivity of the strain gradient moduli to a variation of the edge contribution of material at a fixed volume fraction (obtained in the previous section by generating self-similar shapes of the unit cell) - thus the Cauchy effective moduli remain unchanged - can be evaluated from the general relation of Eq. 2.24, selecting a displacement field in which a strain gradient kinematic control is applied over the unit cell, thus of the form ($\boldsymbol{E} = \boldsymbol{0},\ \boldsymbol{K} \neq \boldsymbol{0}$):

$$\boldsymbol{u}_{0,K} = \frac{1}{2}\boldsymbol{K} : (\boldsymbol{y} \otimes \boldsymbol{y}) + \tilde{\boldsymbol{u}}_{0,K}\left(\boldsymbol{y}\right) \tag{2.27}$$

We consequently evaluate in this context the shape sensitivity of the effective strain gradient moduli, based on the relation arising as a direct consequence of Eq. 2.24 and after a few straightforward computations

$$D_s\left(\frac{1}{2}\left|V_x\right|\left\langle \boldsymbol{K} \therefore \boldsymbol{A} \therefore \boldsymbol{K}\right\rangle_{V_x}\right) = -\int_{\partial Y} \boldsymbol{N}.\boldsymbol{\Sigma}_{Eshelby}.\delta\boldsymbol{X}\, d\left(\partial Y\right) \tag{2.28}$$

The surface density on the right-hand side of Eq. 2.28 can be interpreted as a kind of surface energy due to mechanical fields (a driving force).

Applying unit strain gradient tensor fields, viz. $\boldsymbol{K}^{ijk} = \boldsymbol{e}_i \otimes \boldsymbol{e}_j \otimes \boldsymbol{e}_k$, $\boldsymbol{K}^{lmn} = \boldsymbol{e}_l \otimes \boldsymbol{e}_m \otimes \boldsymbol{e}_n$, allows computing the shape derivative of the strain gradient moduli from Eq. 2.28. Previous relation Eq. 2.28 will be next exploited to compute the sensitivity of strain gradient moduli to the variation of edge length for a suitable choice of the shape velocity field, expanding the Eshelby stress from its very definition:

$$\begin{aligned}\frac{D_s\left(\frac{1}{2}\left|V_x\right|\left\langle \boldsymbol{K} \therefore \boldsymbol{A} \therefore \boldsymbol{K}\right\rangle_{V_x}\right)}{DA} &= -\frac{\int_{\partial Y} \boldsymbol{\Sigma}_{NN} V_{S,N} d\left(\partial Y\right)}{\iint_{\partial Y} V_{S,N} d\theta} \\ &= -\frac{\left\{\frac{1}{2}\int_{\partial Y}\left(\boldsymbol{A}^K \therefore \boldsymbol{K} : \boldsymbol{c}_\mu : \boldsymbol{A}^K \therefore \boldsymbol{K}\right) V_{S,N} d\left(\partial Y\right) - \int_{\partial Y} \boldsymbol{N}.\left(\boldsymbol{K} \therefore \left(\boldsymbol{A}^{K,T}.\boldsymbol{c}_\mu : \boldsymbol{A}^K\right) \therefore \boldsymbol{K}\right).\boldsymbol{N} V_{S,N} d\left(\partial Y\right)\right\}}{\iint_{\partial Y} V_{S,N} d\theta}\end{aligned} \tag{2.29}$$

wherein the boundary displacement field from Eq. 2.27 has been inserted into the right-hand side, using the strain gradient localization operator $\boldsymbol{A}^K$ introduced in Eq. 2.22.

Moreover, by introducing the surface energy γ as an intrinsic surface parameter, one can postulate the following physical balance law expressing the resistive effects of surface energy to the increase of area promoted by the strain gradient energy:

$$\mathrm{D_s}J + \int_{\partial Y} \gamma \; d\left(\partial Y\right) = 0 \Rightarrow \int_{\partial Y} \boldsymbol{\Sigma}_{NN} V_{S,N} d\left(\partial Y\right) + \int_{\partial Y} \gamma \; d\left(\partial Y\right) = 0 \tag{2.30}$$

To clarify, shape derivative evaluation leads to the identification of the surface driving force (normal projection of Eshelby stress) accompanying area (edge in 2D) increase; this can be made such that Cauchy energy will not vary in the process, whereas strain gradient surface energy will, and moreover it is traduced as a surface energy in the shape derivative expression. This strain gradient energy that promotes the increase of area is resisted by the (anisotropic) surface energy in Eq. 2.30.

In the next subsection, the shape derivative of the strain gradient macroscopic energy is utilized to evaluate the scaling of the homogenized strain gradient moduli versus the unit absolute edge length of the lattice unit cell.

2.3.2 Scaling of effective strain gradient moduli versus the absolute edge lengths based on the shape derivative

Considering a square unit cell of length L and thickness t (see Fig. 2.3), a shape velocity field is applied, of the form:

$$\boldsymbol{V}_S = \left(e\, \boldsymbol{t}\right) \boldsymbol{N} \tag{2.31}$$

wherein e is a small constant to be determined such that a constant volume fraction is maintained between the initial and modified unit cells, so that Cauchy effective moduli will not experience any sensitivity to the unit cell shape variation. By considering different configurations, applying the appropriate boundary conditions for the strain gradient continuum, and selecting e keeping a constant volume fraction, the shape velocity vector $\boldsymbol{V}_S = V_{S,N}\boldsymbol{N}$ is applied for both the internal and external boundaries of the unit

cell.

After determining the shape derivative of the strain gradient moduli for different configurations of the square unit cell at a constant volume fraction of 40% (the shape derivative represents the slope of the tangent at each point of the curve), the strain gradient tensile modulus shows a quadratic increase versus the unit cell edge length in Fig. 2.9, thereby obtaining the same scaling law obtained in section 2.2 based on the closed-form expressions of the homogenized strain gradient moduli.

In the next section, the notion of surface energy inherent to the strain gradient effective model is further elaborated.

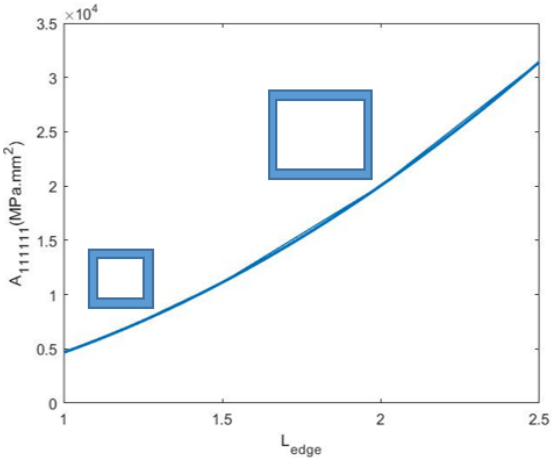

Figure 2.9 Strain gradient modulus in extension A_{111111} versus the total edge length L, obtained from self-similar square unit cells having the same Cauchy moduli based on the shape derivative method.

2.4 Contribution of strain gradient mechanics to surface energy

The homogenized strain gradient model is investigated for its ability to define the notion of an anisotropic surface energy extending the pioneering Mindlin's model [129] of surface energy. Note that Mindlin's model introduces a third gradient model to account for surface energy, since it appears that first strain gradient mechanics is not sufficient by itself to account for the notion of surface energy. In line with Mindlin's seminal work, we accordingly start writing the macroscopic strain energy density, assumed to be dependent on the macroscopic strain tensor and its first and second (macroscopic) spatial gradients together with the associated equilibrium equation $Eq.\ (2.32)_2$ in the absence of body forces [129]:

$$\left|\begin{array}{l} W_M\left(\boldsymbol{E},\boldsymbol{K},\overline{\boldsymbol{K}}\right)=\dfrac{1}{2}\left(\boldsymbol{\Sigma}:\boldsymbol{E}+\boldsymbol{S}\ \therefore\boldsymbol{K}+\overline{\boldsymbol{S}}::\overline{\boldsymbol{K}}\right), \\ \boldsymbol{\tau}\cdot\nabla_x=0 \\ \boldsymbol{\tau}=\boldsymbol{\Sigma}-\boldsymbol{S}\cdot\nabla_x+\overline{\boldsymbol{S}}:\nabla_x\otimes\nabla_x \\ \boldsymbol{E}=\boldsymbol{U}\otimes^s\nabla_x \\ \overline{\boldsymbol{S}}=\overline{\boldsymbol{A}}^{\text{hom}}::\overline{\boldsymbol{K}}\ ,\ \overline{\boldsymbol{K}}:=\boldsymbol{K}\otimes\nabla_x \end{array}\right. \tag{2.32}$$

wherein $\overline{\boldsymbol{S}}$, $\overline{\boldsymbol{A}}^{\text{hom}}$ and $\overline{\boldsymbol{K}} = \boldsymbol{K} \otimes \nabla_x$ are succesively the second hyperstress tensor, the third gradient moduli tensor (a eighth-order tensor), and the second strain gradient tensor (a fourth-order tensor), satisfying the constitutive laws written in *Eq.* $(2.32)_4$. Such a second strain gradient constitutive model may be obtained from the homogenization of the unit cell microstructure. Such an extension towards second strain gradient homogenization lies however outside the scope of this contribution.

Eq. $(2.32)_1$ is integrated over the unit cell domain to set the average strain energy of the homogeneous substitution medium as follows, considering that the macroscopic energy density does not depend on the spatial position within the homogeneous unit cell domain:

$$W_M = \frac{1}{|V_x|} \int\limits_{V_x} W_M \left(\boldsymbol{E}, \boldsymbol{K}, \overline{\boldsymbol{K}} \right) dV_x = \frac{1}{2\,|V_x|} \int\limits_{V_x} \left(\boldsymbol{\Sigma} : \boldsymbol{E} + \boldsymbol{S} \therefore \boldsymbol{K} + \overline{\boldsymbol{S}} :: \overline{\boldsymbol{K}} \right) dV_x \tag{2.33}$$

Integrating Eq. 2.33 by parts and taking into consideration the equilibrium equation *Eq.* $(2.32)_{2,3}$ leads after lengthy but straightforward computations (accounting for the index symmetries of the involved tensors) to the following surface integral formulation of the effective strain energy:

$$|V_x|\, W_M = \frac{1}{2} \left\{ \int\limits_{\partial V_x} \boldsymbol{N}.\boldsymbol{\tau}.\boldsymbol{U}\ \mathrm{dS} + \int\limits_{\partial V_x} \boldsymbol{N}.\left(\boldsymbol{S} - \overline{\boldsymbol{S}} \cdot \nabla_x \right) : (\boldsymbol{U} \otimes \nabla_x)\ \mathrm{dS} + \int\limits_{\partial V_x} \boldsymbol{N}.\overline{\boldsymbol{S}} \therefore (\boldsymbol{U} \otimes \nabla_x \otimes \nabla_x)\, \mathrm{dS} \right\} \tag{2.34}$$

The first term on the right-hand side of Eq. 2.34 is a Cauchy contribution that will not lead to any surface contributions. In the derivations to follow, we will focus on the terms involving the third gradient contributions. The second integral term in Eq. 2.34 rewrites in index format:

$$\int\limits_{\partial V_x} N_i \left(S_{ijk} - \overline{S}_{ijkl,l} \right) U_{j,k} \mathrm{dS} = \int\limits_{\partial V_x} \underbrace{N_i \left(A^{\text{hom}}_{ijkpqr} K_{pqr} \right) U_{j,k}}_{(1)} - \underbrace{N_i \left(\overline{A}_{ijklmnpq} \overline{K}_{mnpq,l} \right) U_{j,k}}_{(2)} \mathrm{dS}, \tag{2.35}$$

The first part of the right-hand side of Eq. 2.35 allows recovering a variant of Mindlin's surface energy when selecting identical pairs of indices $\{j = k$ and p=q$\}$, leading in turn to the isotropic part of the strain gradient tensor of moduli A^{hom}. More specifically, it leads to a kinematic invariant obtained after integrating by part the first surface integral on the right-hand side of Eq. 2.36:

$$\begin{aligned} (1) &= \int\limits_{\partial V_x} N_i \left(A^{\text{hom}}_{ijkpqr} E_{pq,r} \right) U_{j,k} \mathrm{dS} = \frac{1}{2} \int\limits_{\partial V_x} N_i A^{\text{hom}}_{ijkpqr} \left(U_{p,qr} + U_{q,pr} \right) U_{j,k} \mathrm{dS} \\ &= \frac{1}{2} \int\limits_{\partial V_x} N_i A^{\text{hom}}_{ikkppr} \left(U_{p,pr} + U_{p,pr} \right) U_{k,k} \mathrm{dS} \\ &\to \frac{1}{2} \int\limits_{\partial V_x} N_i A^{\text{hom}}_{ikkppr} (U \cdot \nabla_x)_{,r} \left(U \cdot \nabla_x \right)\ \mathrm{dS} = \frac{1}{4} \int\limits_{\partial V_x} \boldsymbol{N} \cdot \boldsymbol{A}^{\text{hom}}_{\{(2,3),(4,5)\}} \cdot (\boldsymbol{U} \cdot \nabla_x)^{2} \otimes \nabla_x \mathrm{dS} \end{aligned} \tag{2.36}$$

wherein we define the following second order tensor by index contractions $\left(\boldsymbol{A}^{\text{hom}}_{\{(2,3),(4,5)\}} \right)_{ij} = \boldsymbol{A}^{\text{hom}}_{ikkppj}$. The last surface integral in Eq. 2.36 bears a strong similarity with Mindlin's isotropic formulation of surface energy depending on the first invariant of the macroscopic strain tensor; it represents the normal projection of the gradient of the kinematic invariant $(\boldsymbol{U} \cdot \nabla_x)^2$ representing the square of the local volume change. The difference however is that the obtained density involves instead the square of the local

volumetric change as a true kinematic invariant (the trace of the macroscopic strain tensor); in contrast to this, Mindlin's original formulation is linear in this last contribution.

The last integral in Eq. 2.34 can be rewritten in index format as follows:

$$\begin{aligned}\int_{\partial V_x} N_i \overline{S}_{ijkl} U_{m,np} \mathrm{dS} &= \int_{\partial V_x} N_i \left(\overline{A}_{ijklmnpq} \overline{K}_{mnpq}\right) U_{m,np} \mathrm{dS} \cong \int_{\partial V_x} N_i \left(\overline{A}_{ijklmnpq} K_{mnp,q}\right) U_{m,np} \mathrm{dS} \\ &\cong \frac{1}{2} \int_{\partial V_x} N_i \overline{A}_{ijklmnpq} (K_{mnp} \therefore K_{mnp})_{,q} \mathrm{dS}\end{aligned} \tag{2.37}$$

Selecting identical indices $\{j = m, k = n, l = p\}$ in Eq. 2.37 leads to the following higher-order invariant of the strain gradient tensor, the quadratic term $(\boldsymbol{K} \therefore \boldsymbol{K})$, involving a reduced form of the third gradient moduli tensor:

$$\frac{1}{2} \int_{\partial V_x} \boldsymbol{N} \cdot \overline{\boldsymbol{A}}^{\mathrm{hom}}_{\{(2,3,4),(5,6,7)\}} \cdot [(\boldsymbol{K} \therefore \boldsymbol{K}) \otimes \nabla_x] dS \tag{2.38}$$

wherein we use the notation $\left(\overline{\mathbf{A}}^{\mathrm{hom}}_{\{(2,3,4),(5,6,7)\}}\right)_{ij} = \overline{\mathbf{A}}^{\mathrm{hom}}_{imnpmnpj}$ to denote the components of a second order tensor obtained by contracting the enclosed triplets of indices. Thereby, we have derived a higher-order surface term depending on a higher kinematic invariant, providing a generalization of Mindlin's original formulation of surface energy and introducing moreover an additional degree of anisotropy encapsulated into the contracted Cauchy and strain gradient moduli involved in the two relations of Eq. 2.36 and Eq. 2.38 respectively. Observe that the two obtained densities in Eq. 2.36 and Eq. 2.38 have the physical units of energy per unit area in 3D, and energy per unit length in 2D. Note that the surface energy densities in Eqs. 2.36 and 2.38 can lead to other terms representative of surface energies (especially those built from kinematic invariants), which will however not be analyzed in this chapter.

2.5 Conclusion

This chapter exposes a discrete homogenization method for periodic architected materials towards a strain gradient continuum formulation, providing the effective classical and strain gradient moduli as closed-form expressions of the lattice microstructural parameters. It provides an analysis of edge effects (surface effects in 3D) in the mechanical response of architected materials modeled in the framework of strain gradient mechanics. While Cauchy moduli do not capture surface properties, a theoretical and numerical examination yielded the scaling law of the strain gradient moduli with the edge contribution of surface material, showing a quadratic variation with the absolute edge length. To reach this objective, the extended Hill macrohomogeneity condition for strain gradient media has been formulated from purely surface mechanical fields over the unit cell boundary. The same scaling law has been obtained from a shape sensitivity analysis of the internal macroscopic energy, whereby strain gradient kinematic tensors have been applied over self-similar unit cells with varying amount of edge lengths.

In the last part of the chapter, based on a second strain gradient effective continuum model formulation, the notion of surface energy has been formulated in an anisotropic manner, relying on the identification of

two surface integral contributions involving kinematic invariants of the macroscopic first strain gradient and second strain gradient tensors.

Chapter 3

Higher gradient homogenization methods of quasi-periodic media

Summary

This chapter introduces quasi-periodic homogenization schemes for quasi-periodic media, those without periodicity, but that can be mapped to a parent periodic medium. Quasi-periodic homogenization relies on the conceptual idea of mapping a non-periodic domain to a reference periodic one through a point mapping of material points within the domain of an identified unit cell. The theoretical background of quasi-periodic homogenization introduced in the first part of this chapter relies on expressing the microscopic position of micropoints within a physical unit cell as a sum of the macroscopic position (the center of area of the unit cell) and the relative position of micropoints with respect to the center of area. This decomposition parameterized by the small-scale parameter entails a corresponding additive decomposition of the tangent map defining the geometrical transformation of the periodic UC into the quasi-periodic one in terms of an additive decomposition into macroscopic and microscopic contributions. The quasi-periodic homogenized effective moduli are then determined, starting from the average of the microscopic energy, those being expressed in terms of the periodic moduli and a perturbation term, both expressed in a volumetric format as surface integrals over the reference unit cell domain in a 2D context. In the second part of this chapter, a surface formulation of the quasi-periodic moduli is derived, based on the notion of shape derivative of the total potential energy stored within the unit cell. This approach relies on introducing a shape velocity field at the boundary of the periodic unit cell to model the change of its design, driven by the normal projection of Eshelby stress onto both the internal and external boundaries of the unit cell. This second scheme offers comparatively to the first one a simpler way to compute the quasi-periodic moduli as it only requires the evaluation of the mechanical fields on the unit cell boundaries. Application of the proposed homogenization schemes are done for inclusion-based composites showing a gradient of size.

3.1 Introduction

Quasi-periodic composites differ from periodic composite materials in that their unit cell does not repeat exactly in a periodic manner throughout the structure. Instead, the unit cell gradually changes along one or more periodicity directions, which are known as grading directions. Due to this feature, a class of materials called functionally graded materials (FGM) has emerged, and it is characterized by a spatial variation of the geometry, and sometimes even the material properties, of the microstructure within the unit cell. The spatial variation within FGMs can take place in a single direction, (as is the case with stratified materials) in a discrete or continuous manner.

When a composite has a unit cell that varies smoothly in space, the grading within neighboring unit cells can be ignored. This means that a given unit cell does not perceive any differences in microstructure from neighboring ones. As a consequence, the homogenized behavior can be determined locally without considering the differences in the microgeometry of successive unit cells. The grading is only considered at the macro-level to account for the variation of homogenized material properties from one-unit cell to another in the macrodomain [122–124].

On the contrary, in situations where the grading across unit cells is too fast, the variation of unit cell geometry must be considered at the microscale. This means that higher order terms are expected to appear when performing the asymptotic homogenization. Because of this microscopic variation, the overall effective behavior of the composite may no longer be purely local, and nonlocal mechanical behaviors may emerge proportional to the rate of grading. According to [121], classical homogenization methods are not applicable to FGMs because the minimum size of the RVE is larger than the size of a statistically homogeneous RVE. This requires considering the grading within the RVE, which is also graded. There has been very little effort devoted to the homogenization of quasi-periodic media in the literature, especially when considering higher order terms in asymptotic expansion methods. [207] studied the first-order homogenization of quasi-periodic structures, while [208] developed a second-order solution by adding correctors computed from the first-order solution, but no corrections accounting for quasi-periodicity is present in the first order equation. In the field of dynamics, [209] and [210] developed a non-periodic homogenization of the wave equation for seismic applications, but their higher-order solution was incomplete. [211] developed a second gradient model for composites with material property gradation, but without variation in geometry. They used asymptotic expansions up to the second order combined with a variational approach to derive the higher-order macroscopic energy, assuming that the properties within the unit cell depend on the position of the cell within the composite. The resulting energy includes the gradient of a characteristic microstructure parameter and the strain gradient as a new kinematic variable. As opposite to most homogenization methods for FGMs that account for the grading only at the macrolevel by replacing the homogeneous effective properties with a field of material properties varying at the macroscale, [121] accounted for the grading at the micro-level through the development of a second gradient effective constitutive law.

There are two ways to derive quasi-periodic properties. The first approach involves a unit cell $Y = Y(x)$ that varies with the macroscopic position $\boldsymbol{x}$, allowing the expression of the microscopic moduli tensor in the form $\boldsymbol{C}^{\varepsilon}(\boldsymbol{x}) = \boldsymbol{C}\left(\boldsymbol{x}, \frac{\varphi(\boldsymbol{x})}{\varepsilon}\right)$, wherein $\varphi(\boldsymbol{x})$ is a smooth diffeomorphism. This indicates that the quasi-periodic variable is transformed by the diffeomorphism $\varphi(\boldsymbol{x})$ into a periodic counterpart and that $\boldsymbol{C}$ is still periodic in the second variable [212]. The mapping of the periodic unit cell by $\varphi^{-1}(\boldsymbol{x})$ is also dependent on the macroposition in this case. The second approach involves the transformation of the boundary value problem (BVP) formulated on the quasi-periodic domain onto on a periodic domain using a change of parameterization as demonstrated in [213]. By adopting this approach, a periodic BVP is still constructed with a modified apparent microscopic moduli tensor, which can be further elaborated versus the small-scale parameter. In [213], the hypothesis of a quasi-affine geometric transformation enables the unit cell BVP to be expressed as a periodic one, through the extraction of a term that depends only on the macroscale variable. This involves disregarding any gradation within the adjacent unit cells and assuming that any changes in the effective properties are a result of variations solely in the unit cell geometry at the macroscale. However, in this chapter we will be dealing with a new homogenization scheme of quasi-periodic media to determine the quasi-periodic moduli relying on the shape derivative of the total potential energy leading to a surface formulation of the moduli.

This chapter is organized as follow: a general method that relies on a physical viewpoint of micropoints located within the UC is developed in section 3.2 towards quasi-periodic media to determine a volumetric formulation of the quasi-periodic moduli. In section 3.3, a shape derivative approach is adopted in view of a surface formulation of the energy and of the ensuing quasi-periodic moduli. The unit cell micro grading is potentially the source of an emergent higher gradient behavior, so that we expand our homogenization scheme towards the incorporation of the second displacement gradient. Thereby, the quasi-periodic moduli are expanded versus the asymptotic small parameter, so that a ranking of the different contributions entering these moduli traducing both the second gradient enhancement and the quasi-periodic perturbation of the reference periodic unit cell is obtained. section 3.4 is devoted to numerical illustrations of the established quasi-periodic homogenization schemes, considering inclusion-based composites showing a gradient of their inclusion size. We conclude in section 3.5 by a summary of the main theoretical developments and results and by few perspectives of developments in the field of multiphysical behavior of functionally graded materials.

A few notes about the notations in use are in order. Boldface symbols stand in for vectors and tensors. The transpose of a tensor is written with a superscript notation, for instance $\boldsymbol{B}^{\boldsymbol{T}}$. The gradient of a tensor field $\boldsymbol{A}(\boldsymbol{y})$ with respect to the spatial position $\boldsymbol{y}$ for example) is denoted $\boldsymbol{A}(\boldsymbol{y}) \otimes \nabla_y$ (with $\otimes$ the tensor product) and its divergence is obtained as the trace of the gradient, $\boldsymbol{A}(\boldsymbol{y}).\nabla_y$. The symmetrized dyadic product is denoted $\otimes^s$. The dot product therein represents the inner product in the space of Cartesian tensors. The simple, double and triple contractions of tensors are written $.$, $:$, $\therefore$ respectively, so that it holds $\boldsymbol{A}.\boldsymbol{B} = A_k B_k$, $\boldsymbol{C}:\boldsymbol{D}=\mathrm{C}_{ij} D_{ij}$, $\boldsymbol{U} \therefore \boldsymbol{V}=\mathrm{U}_{ijk} V_{ijk}$, with $(\boldsymbol{A}, \boldsymbol{B})$, $(\boldsymbol{C}, \boldsymbol{D})$, $(\boldsymbol{U}, \boldsymbol{V})$ pairs of first order, second order and third order tensors respectively. The symbol $\boxtimes$ represents the square tensor

product defined in index format as $\left(\boldsymbol{A}_M^{-1} : \boldsymbol{E} : \boldsymbol{A}_M\right)_{ij} = \left(\boldsymbol{A}_M^{-1}\right)_{ip} \boldsymbol{E}_{pq} (\boldsymbol{A}_M)_{qj} = \left(\boldsymbol{A}_M^{-1}\right)_{ip} (\boldsymbol{A}_M)^T_{jq} \boldsymbol{E}_{pq} = \left(\boldsymbol{A}_M^{-1} \boxtimes \boldsymbol{A}_M^T\right)_{ijpq} \boldsymbol{E}_{pq} = \left(\left(\boldsymbol{A}_M^{-1} \boxtimes \boldsymbol{A}_M^T\right) : \boldsymbol{E}\right)_{ij}$ for the purpose of factoring our tensor $\boldsymbol{E}$ on the right side. Alternatively, in order to factor our $\boldsymbol{E}$ on the left-hand side, the previous evaluation can be written in the form $\left(\boldsymbol{A}_M^{-1} : \boldsymbol{E} : \boldsymbol{A}_M\right)_{ij} = \left(\boldsymbol{A}_M^{-1}\right)_{ip} \boldsymbol{E}_{pq} (\boldsymbol{A}_M)_{qj} = \boldsymbol{E}_{pq} \left(\boldsymbol{A}_M^{-T}\right)_{pi} (\boldsymbol{A}_M)_{jq} = \boldsymbol{E}_{pq} \left(\boldsymbol{A}_M^{-T} \boxtimes \boldsymbol{A}_M\right)_{pqij} = \left(\boldsymbol{E} : \left(\boldsymbol{A}_M^{-T} \boxtimes \boldsymbol{A}_M\right)\right)_{ij}$

3.2 Volumetric formulation of quasi-periodic moduli

This section starts with an overview on mapping a periodic domain to reach a quasi-periodic one. We then aim to relate the quasi-periodic moduli to the ones in the periodic domain through homogenization and express them in the form of volume integrals.

3.2.1 From periodic to quasi-periodic domains

Here and in the sequel, variables attached to the periodic domain are denoted with an overhead tilde, whereas those living in the quasi-periodic domain are written without tilde.

Starting from the periodic parent unit cell $\tilde{Y}$, one can move into the quasi-periodic unit cell Y such that the relation between both domains is $Y = \varphi\left(\tilde{Y}\right) \Leftrightarrow \tilde{Y} = \varphi^{-1}\left(Y\right)$, where φ is the point mapping that allows the transition between the coordinate systems by mapping the points of the periodic domain to the quasi-periodic one $\tilde{\boldsymbol{x}} \mapsto \boldsymbol{x} = \varphi(\tilde{\boldsymbol{x}})$ (Fig. 3.1). Noting that this geometrical transformation of coordinates will have an impact on both macroscopic and microscopic scales. Different definitions will be introduced next starting from this mapping.

Moreover, Fig. 3.1 shows the periodic domain $\widetilde{\Omega}$ (a) with the corresponding unit cell (UC) on the right side on which we define the microscopic $\underline{\widetilde{\boldsymbol{y}}}$ and macroscopic $\underline{\tilde{\boldsymbol{x}}}$ position vectors. For the quasi-periodic domain Ω (b), the microscopic and macroscopic position vectors will be denoted as $\underline{\boldsymbol{y}}$ and $\underline{\boldsymbol{x}}$ respectively (they are not shown on the figure but they have the same scheme as the one corresponding to the periodic UC without tilde).

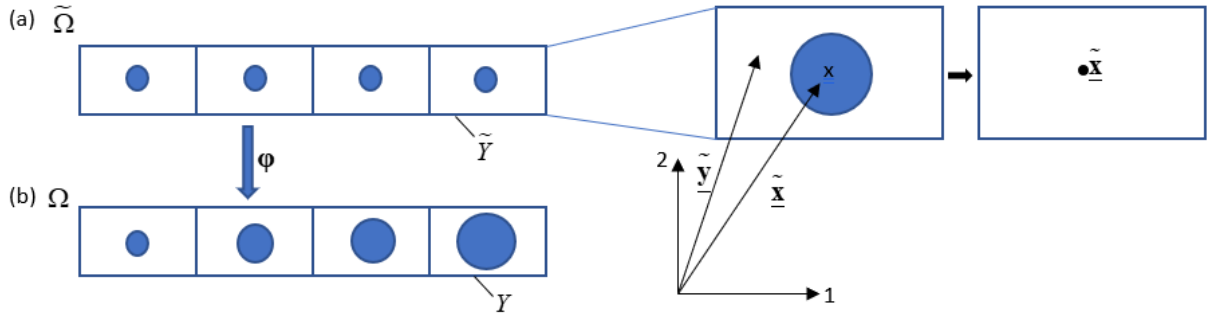

Figure 3.1 Illustration of the transformation introduced which is defined by a mapping $\boldsymbol{\varphi}$ between (a) the periodic domain $\widetilde{\Omega}$ and (b) the quasi-periodic domain Ω. The periodic unit cell on the right hand side shows the microscopic $\underline{\widetilde{\boldsymbol{y}}}$ and macroscopic $\underline{\tilde{\boldsymbol{x}}}$ position vectors.

'Small' vectors from the periodic domain $\tilde{\Omega}$ are mapped to 'small' vectors in the quasi-periodic domain Ω through a tangent mapping of the point mapping defined as $\boldsymbol{A}(\tilde{\boldsymbol{x}}) := \boldsymbol{\varphi}(\widetilde{\boldsymbol{x}}) \otimes \nabla_{\widetilde{\boldsymbol{x}}}$. Lets call

$$\boldsymbol{A} := \boldsymbol{\varphi}(\tilde{\boldsymbol{x}}) \otimes \nabla_{\widetilde{\boldsymbol{x}}} = \boldsymbol{x} \otimes \nabla_{\widetilde{\boldsymbol{x}}} \Leftrightarrow A^i_{.j} = \frac{\partial x^i}{\partial \tilde{x}^j} = A^i_{.j}(\tilde{\boldsymbol{x}}) \tag{3.1}$$

The tangent mapping admits an inverse that maps vectors from quasi-periodic to periodic domain written in components format:

$$\frac{\partial \tilde{x}^p}{\partial x^q} = \tilde{x}^p_{.,q} \equiv \left(A^{-1}\right)^p_{.q}(\boldsymbol{x}) \tag{3.2}$$

The transformation rules of vectors and tensors are next exposed, in the context of the coordinate transformations arising from the mapping from periodic to quasi-periodic domains. The volume element transforms as:

$$\begin{aligned} &d\boldsymbol{x} = \boldsymbol{\varphi}(\tilde{\boldsymbol{x}}) \otimes \nabla_{\widetilde{\boldsymbol{x}}} . d\tilde{\boldsymbol{x}} \rightarrow dV_x = \det\left(\boldsymbol{\varphi}(\tilde{\boldsymbol{x}}) \otimes \nabla_{\widetilde{\boldsymbol{x}}}\right) dV_{\tilde{x}} = J dV_{\tilde{x}} \\ &J := \det\left(\boldsymbol{\varphi}(\tilde{\boldsymbol{x}}) \otimes \nabla_{\widetilde{\boldsymbol{x}}}\right) \end{aligned} \tag{3.3}$$

The transformation laws of tensors and vectors, considering a general non-affine change of coordinates, are elaborated as a prerequisite for the quasi-periodic homogenization to be developed later. This will entail the relation between the microscopic strain and stress tensors and their corresponding macroscale counterparts, paying attention to their covariant and contravariant character respectively.

In both periodic and quasi-periodic domains, the basis vectors are defined as tangents at each point to coordinate lines serving as curvilinear coordinates. Let's denote the tangent basis vectors as $\tilde{\boldsymbol{g}}_k, \boldsymbol{g}_k$ on the untransformed and transformed domains, respectively, (see Fig. 3.2). It is essential to figure

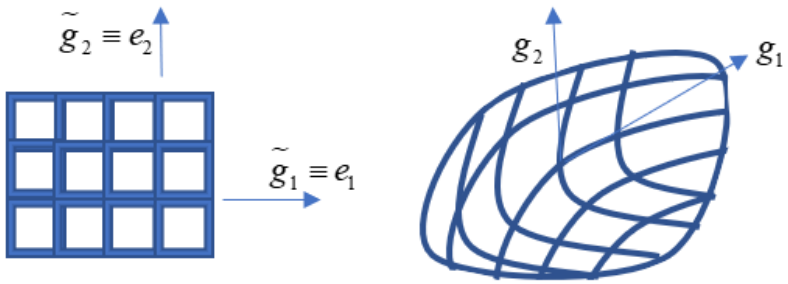

Figure 3.2 Figures showing the tangent basis vectors in (left) an initial non-deformed and (right) deformed configurations; $(e_1, e_2)$are the basis vectors of a cartesian coordinate system.

out the variance of tensors because the transformation rule of covariant and contravariant tensors is different [214]. Covariant tensors transform like the basis vectors by using the transition matrix, while contravariant tensors are those transforming in an opposite way to the basis vectors, by using the inverse of the transition matrix. Contravariant tensors (resp. covariant) have their components denoted with upper indices (resp. lower indices).

The tangent vectors constructing the natural basis transform between the two configurations are as

follows:

$$\begin{aligned}\tilde{\boldsymbol{g}}_h &:= \frac{\partial \boldsymbol{y}}{\partial \tilde{y}^h} = \frac{\partial \boldsymbol{y}}{\partial y^j}.\frac{\partial y^j}{\partial \tilde{y}^h} = \frac{\partial y^j}{\partial \tilde{y}^h}\boldsymbol{g}_j \Leftrightarrow \boldsymbol{g}_j = \widetilde{\boldsymbol{g}}_k \frac{\partial \tilde{y}^k}{\partial y^j} \equiv \widetilde{\boldsymbol{g}}_k \left(A^{-1}\right)^k_{.j} \\ d\boldsymbol{v}_i &= \frac{dv^i}{dy^l} dy^l \boldsymbol{g}_i \Rightarrow \tilde{\boldsymbol{g}}_k d\tilde{y}^k = \frac{\partial y^j}{\partial \tilde{y}^k}\boldsymbol{g}_j \frac{\partial \tilde{y}^k}{\partial y^p} dy^p \equiv \delta_{jp}\boldsymbol{g}_j dy^p = \boldsymbol{g}_q dy^q\end{aligned} \tag{3.4}$$

The rule of summation of repeated indices in a monomial is implicitly adopted here and in the sequel; in a pair of such repeated indices, one index appears in lower position, and the other index in upper position.

Note that the variation of the components of a tensor or a vector from the periodic to the quasi-periodic domain can be equivalently expressed as an active or a passive transformation. In the passive viewpoint, a vector field remains invariant whereas the observer viewpoint is changing, so that it holds $\tilde{\boldsymbol{v}} = \boldsymbol{v} = v^j \boldsymbol{g}_j$. In the active viewpoint (meaning that the material points within the reference domain are mapped to a new domain like a deformation), the vector is described as a covariant vector, which means that its components transform in the same way as the covariant base vectors; therefore, the components of the vector remain the same in both domains, whereas the tangent vectors defining the natural basis do change:

$$\begin{aligned}&\boldsymbol{g}^i = \boldsymbol{A}^{-T}.\tilde{\boldsymbol{g}}^i \\ &\boldsymbol{v} = v_i \boldsymbol{g}^i = \boldsymbol{A}^{-T}.\tilde{\boldsymbol{v}} = \tilde{v}_j \boldsymbol{A}^{-T}.\tilde{\boldsymbol{g}}^j = \tilde{v}_j \boldsymbol{g}^j \Rightarrow v_j = \tilde{v}_j\end{aligned} \tag{3.5}$$

Considering in this chapter the active viewpoint leads to the expression of the displacement field (in tensor format) in terms of its covariant representation. Thus, the strain is elaborated as a mixed tensor when considered as a single scale-dependent field from the onset:

$$\begin{aligned}&\tilde{\boldsymbol{u}}\left(\tilde{\boldsymbol{y}}\right) \otimes \nabla_{\tilde{\boldsymbol{y}}} = \tilde{u}^i_{,j} \tilde{\boldsymbol{g}}_i \otimes \tilde{\boldsymbol{g}}^j,\ \boldsymbol{u}\left(\boldsymbol{y}\right) \otimes \nabla_{\boldsymbol{y}} = u^i{}_{,j} \boldsymbol{g}_i \otimes \boldsymbol{g}^j \\ &\boldsymbol{g}^i.\boldsymbol{g}_j = \delta^i_{.j} = \tilde{\boldsymbol{g}}^i.\tilde{\boldsymbol{g}}_j\end{aligned} \tag{3.6}$$

Previous relations introduce the primal bases, the set of tangent vectors $\boldsymbol{g}_i, \tilde{\boldsymbol{g}}_i$, and the reciprocal (dual) bases $\boldsymbol{g}^i, \tilde{\boldsymbol{g}}^i$ in quasi-periodic and periodic domains. The last identity of Eq. 3.6 shows the product relation of the set of primal basis vectors with the dual bases. The stress $\boldsymbol{\sigma}$ and strain $\boldsymbol{\varepsilon} = \boldsymbol{u}\left(\boldsymbol{y}\right) \otimes \nabla_{\boldsymbol{y}}$ tensors are expressed as mixed variant second order tensors, with the transformations as follows:

$$\begin{aligned}&\tilde{\boldsymbol{\sigma}} = \tilde{\sigma}^{\cdot q}_{p} \tilde{\boldsymbol{g}}^p \otimes \tilde{\boldsymbol{g}}_q,\ \boldsymbol{\sigma} = \sigma^{\cdot q}_{p} \boldsymbol{g}^p \otimes \boldsymbol{g}_q \\ &\left|\begin{aligned}&\boldsymbol{u}\left(\boldsymbol{y}\right) \otimes \nabla_{\boldsymbol{y}} = \boldsymbol{A}.\tilde{\boldsymbol{u}}\left(\tilde{\boldsymbol{y}}\right) \otimes \nabla_{\tilde{\boldsymbol{y}}}.\boldsymbol{A}^{-1}, \\ &\boldsymbol{\sigma}\left(\boldsymbol{y}\right) = \boldsymbol{A}^{-T}.\tilde{\boldsymbol{\sigma}}.\boldsymbol{A}^T\end{aligned}\right.\end{aligned} \tag{3.7}$$

As a consequence of the previous transformation equations of quasi-periodic stress and strain, it is shown from straightforward algebraic evaluations that the microscopic energy density remains invariant between the periodic and quasi-periodic domains:

$$w_\mu\left(\boldsymbol{y}\right) := \frac{1}{2}\boldsymbol{\sigma} : \boldsymbol{\varepsilon} = \frac{1}{2} Tr(\boldsymbol{\sigma}^T.\boldsymbol{\varepsilon}) = \frac{1}{2}\sigma^{\cdot j}_{i}\varepsilon^{\cdot i}_{j} = \frac{1}{2}\tilde{\sigma}^{\cdot j}_{i}\tilde{\varepsilon}^{\cdot i}_{j} = \frac{1}{2}\tilde{\boldsymbol{\sigma}} : \tilde{\boldsymbol{\varepsilon}} = \tilde{w}_\mu\left(\tilde{\boldsymbol{y}}\right) \tag{3.8}$$

For the development of the quasi-periodic homogenization theory, an approach relying on physical viewpoint of micropoints located within the UC is introduced in the following subsection.

3.2.2 Homogenization of quasi-periodic media: volumetric approach

In this section, a homogenization technique is developed with the underlying assumption of the smoothness of the design change. The main concept of this method is to magnify the unit cell from the physical domain where it exists to set a problem onto a fixed domain called the zoomed unit cell, which becomes independent of the small-scale parameter. The small parameter is denoted $\eta = \frac{\ell}{L}$ and it is defined as the ratio of a unit cell size (ℓ) to a characteristic macroscopic dimension of the macrodomain (L), as pictured in Fig. 3.3. A new spatial variable is introduced, elaborated as the relative position of micropoints with respect to center of area $\tilde{\boldsymbol{\xi}} = \tilde{\boldsymbol{y}} - \tilde{\boldsymbol{x}}$. The two variables $\tilde{\boldsymbol{x}}$, and $\eta\tilde{\boldsymbol{\xi}}$ (Fig. 3.3 [212]) are considered independent because they represent two different and separated scales. Any mechanical field defined over the η-dependent UC in the physical domain will depend on these two independent variables. The vectors $\boldsymbol{x}_m$, and $\tilde{\boldsymbol{x}}_m$ in Fig. 3.3 are defined as the generic microscopic positions in the quasi-periodic and periodic dimensionless domains respectively.

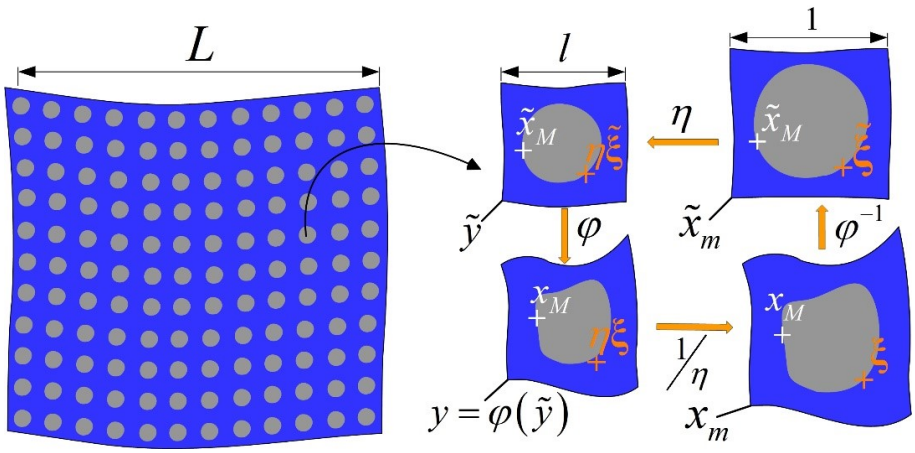

Figure 3.3 Schematic representation of periodic material (left), definition of micropoints within the physical and zoomed non-dimensional UCs of the periodic (right top row), and quasi-periodic domains (right bottom row).

These position vectors are in turn decomposed additively into the macroscopic position of the center of the area $\boldsymbol{x}, \tilde{\boldsymbol{x}}$ and the relative position of micropoints $\tilde{\boldsymbol{\xi}}, \boldsymbol{\xi}$ in the physical quasi-periodic and periodic unit cells, respectively, as follows:

$$\begin{aligned} \tilde{\boldsymbol{x}}_m = \tilde{\boldsymbol{x}}_M + \widetilde{\boldsymbol{\xi}} \Rightarrow \begin{vmatrix} \tilde{\boldsymbol{x}} = \tilde{\boldsymbol{x}}_M, \\ \tilde{\boldsymbol{y}} = \tilde{\boldsymbol{x}}_M + \eta\widetilde{\boldsymbol{\xi}} \end{vmatrix}, \\ \tilde{\boldsymbol{y}} = \tilde{\boldsymbol{x}} + \eta\widetilde{\boldsymbol{\xi}} \mapsto \boldsymbol{y}\left(\widetilde{\boldsymbol{x}}, \widetilde{\boldsymbol{y}}\right) = \boldsymbol{x} + \eta\boldsymbol{\xi} \end{aligned} \tag{3.9}$$

The two last equations in Eq. 3.9 represent the positions in the physical periodic and quasi-periodic UCs.

One then writes the following differential relations of the position vectors between the periodic and quasi-periodic domains:

$$\begin{cases} d\boldsymbol{x} = \boldsymbol{\varphi}_{\widetilde{x}}\left(\widetilde{\boldsymbol{x}}\right) \otimes \nabla_{\widetilde{\boldsymbol{x}}}.d\widetilde{\boldsymbol{x}} \\ \eta d\boldsymbol{\xi} = \eta\boldsymbol{\xi}\left(\widetilde{\boldsymbol{x}},\widetilde{\boldsymbol{y}}\right) \otimes \nabla_{\widetilde{\boldsymbol{x}}}.d\widetilde{\boldsymbol{x}} + \boldsymbol{\xi}\left(\widetilde{\boldsymbol{x}},\widetilde{\boldsymbol{y}}\right) \otimes \nabla_{\widetilde{\boldsymbol{\xi}}}.d\left(\eta\widetilde{\boldsymbol{\xi}}\right) \end{cases} \tag{3.10}$$

Eq. 3.10 leads to the following global tangent map $\boldsymbol{A}\left(\widetilde{\boldsymbol{x}},\widetilde{\boldsymbol{y}}\right)$ mapping the vector $\begin{pmatrix} d\boldsymbol{x} & \eta d\boldsymbol{\xi} \end{pmatrix}$, which includes the macroscopic and microscopic positions in the quasi-periodic domain, into its counterparts in the periodic domain, the infinitesimal vector $\begin{pmatrix} d\widetilde{\boldsymbol{x}} & \eta d\widetilde{\boldsymbol{\xi}} \end{pmatrix}$

$$\begin{pmatrix} d\boldsymbol{x} \\ \eta d\boldsymbol{\xi} \end{pmatrix} = \begin{pmatrix} \boldsymbol{\varphi}_{\widetilde{x}}\left(\widetilde{\boldsymbol{x}}\right) \otimes \nabla_{\widetilde{\boldsymbol{x}}} & 0 \\ \eta\boldsymbol{\xi}\left(\widetilde{\boldsymbol{x}},\widetilde{\boldsymbol{y}}\right) \otimes \nabla_{\widetilde{\boldsymbol{x}}} & \boldsymbol{\xi}\left(\widetilde{\boldsymbol{x}},\widetilde{\boldsymbol{y}}\right) \otimes \nabla_{\widetilde{\boldsymbol{\xi}}} \end{pmatrix} . \begin{pmatrix} d\widetilde{\boldsymbol{x}} \\ \eta d\widetilde{\boldsymbol{\xi}} \end{pmatrix} = \boldsymbol{A}\left(\widetilde{\boldsymbol{x}},\widetilde{\boldsymbol{y}}\right) . \begin{pmatrix} d\widetilde{\boldsymbol{x}} \\ \eta d\widetilde{\boldsymbol{\xi}} \end{pmatrix} \tag{3.11}$$

The center of coordinates is chosen at the center of area of the RVE (short-cut for representative volume element), so that the relative position coincides with the microscopic position $\left(\tilde{\boldsymbol{\xi}} = \tilde{\boldsymbol{y}}, \text{ and } \boldsymbol{\xi} = \boldsymbol{y}\right)$. According to Eq. 3.11 the tangent map $\boldsymbol{A}\left(\widetilde{\boldsymbol{x}},\widetilde{\boldsymbol{y}}\right)$ can be decomposed additively versus the small-scale parameter as:

$$\boldsymbol{A}\left(\tilde{\boldsymbol{x}},\tilde{\boldsymbol{y}}\right) = \boldsymbol{A}_M\left(\tilde{\boldsymbol{x}}\right) + \eta\boldsymbol{A}_m\left(\tilde{\boldsymbol{x}},\tilde{\boldsymbol{y}}\right) \tag{3.12}$$

where $\boldsymbol{A}_M\left(\widetilde{\boldsymbol{x}}\right) = \begin{pmatrix} \boldsymbol{\varphi}_{\widetilde{x}}\left(\widetilde{\boldsymbol{x}}\right) \otimes \nabla_{\widetilde{\boldsymbol{x}}} & 0 \\ 0 & \boldsymbol{y} \otimes \nabla_{\widetilde{\boldsymbol{y}}} \end{pmatrix}$ and $\boldsymbol{A}_m\left(\widetilde{\boldsymbol{x}},\widetilde{\boldsymbol{y}}\right) = \begin{pmatrix} 0 & 0 \\ \boldsymbol{y} \otimes \nabla_{\widetilde{\boldsymbol{x}}} & 0 \end{pmatrix}$ represent successively the macroscopic and microscopic contributions to the tangent map. The macroscopic tangent mapping $\boldsymbol{A}_M\left(\widetilde{\boldsymbol{x}}\right)$ acts at the macroscopic scale and it maps tangent vectors at the center of area from the periodic to the quasi-periodic UCs. On the contrary, the microscopic tangent mapping $\boldsymbol{A}_m\left(\widetilde{\boldsymbol{x}},\widetilde{\boldsymbol{y}}\right)$ operates on the tangent vectors of any micropoint in the periodic UC and maps them to their corresponding tangent vectors at micropoints located within the quasi-periodic UC. More precisely, the tangent map and its inverse as well as their corresponding determinants can be written as expansion versus the small-scale parameter as:

$$\begin{aligned} &\boldsymbol{A}\left(\tilde{\boldsymbol{x}},\tilde{\boldsymbol{y}}\right) = \boldsymbol{A}_M\left(\tilde{\boldsymbol{x}}\right) + \eta\boldsymbol{A}_m\left(\tilde{\boldsymbol{x}},\tilde{\boldsymbol{y}}\right) = \boldsymbol{A}_M\left(\tilde{\boldsymbol{x}}\right) . \left(\boldsymbol{I} + \eta\boldsymbol{A}_M(\tilde{\boldsymbol{x}})^{-1}.\boldsymbol{A}_m\left(\tilde{\boldsymbol{x}},\tilde{\boldsymbol{y}}\right)\right), \\ &\Rightarrow \det\boldsymbol{A} = \det\left(\boldsymbol{A}_M\right)\left(1 + \eta Tr\left({\boldsymbol{A}_M}^{-1}.\boldsymbol{A}_m\right)\right) + o\left(\eta\right) \\ &\Rightarrow \boldsymbol{A}(\tilde{\boldsymbol{x}},\tilde{\boldsymbol{y}})^{-1} = \left(\boldsymbol{I} + \eta\boldsymbol{A}_M^{-1}\left(\tilde{\boldsymbol{x}}\right).\boldsymbol{A}_m\left(\tilde{\boldsymbol{x}},\tilde{\boldsymbol{y}}\right)\right)^{-1}.\boldsymbol{A}_M^{-1}\left(\tilde{\boldsymbol{x}}\right) \\ &\cong \left(\boldsymbol{I} - \eta\boldsymbol{A}_M^{-1}\left(\tilde{\boldsymbol{x}}\right).\boldsymbol{A}_m\left(\tilde{\boldsymbol{x}},\tilde{\boldsymbol{y}}\right)\right).\boldsymbol{A}_M^{-1}\left(\tilde{\boldsymbol{x}}\right) = \boldsymbol{A}_M^{-1}\left(\tilde{\boldsymbol{x}}\right) - \eta\boldsymbol{A}_M^{-1}\left(\tilde{\boldsymbol{x}}\right).\boldsymbol{A}_m\left(\tilde{\boldsymbol{x}},\tilde{\boldsymbol{y}}\right).\boldsymbol{A}_M^{-1}\left(\tilde{\boldsymbol{x}}\right) + o\left(\eta\right) \\ &\det\left(\boldsymbol{A}^{-1}\right) = \det\left(\boldsymbol{A}_M^{-1} - \eta\boldsymbol{A}_M^{-1}.\boldsymbol{A}_m.\boldsymbol{A}_M^{-1}\right) \cong \det\left(\boldsymbol{A}_M^{-1}\right)\left(1 - \eta Tr\left(\boldsymbol{A}_M^{-1}.\boldsymbol{A}_m\right)\right) + o\left(\eta\right) \end{aligned} \tag{3.13}$$

Before proceeding with further developments of the relations related to quasi-periodic homogenization, it is necessary to highlight the smoothness conditions of the point mapping. This means that the mapping should induce a slow variation of the considered design of the unit cell. Thus, according to Eq. 3.12 which gives a geometrical information about the change of design, the microscopic and macroscopic mappings $\boldsymbol{A}_m\left(\tilde{\boldsymbol{x}},\tilde{\boldsymbol{y}}\right), \boldsymbol{A}_M\left(\tilde{\boldsymbol{x}}\right)$ should have a limited magnitude which is to be validated *aposteriori* from computational results.

$$\|\boldsymbol{A}_M\| << 1 \ ; \ \|\boldsymbol{A}_m\| << 1$$

To check the smoothness of a selected mapping, a geometrical length is defined after considering the higher gradient decomposition of the tangent mapping (can be also applied to microscopic mapping) according to a first order Taylor series expansion between two neighboring macropoints, namely centers of area of two neighboring unit cells:

$$\begin{aligned} &\boldsymbol{A}_M\left(\tilde{\boldsymbol{x}}+\Delta\tilde{\boldsymbol{x}}\right)=\boldsymbol{A}_M\left(\tilde{\boldsymbol{x}}\right)+\boldsymbol{A}_M\left(\tilde{\boldsymbol{x}}\right)\otimes\nabla_{\tilde{\boldsymbol{x}}}.\boldsymbol{L}^{geo}+o\left(\|\boldsymbol{L}^{geo}\|\right)\\ &\Rightarrow\boldsymbol{L}^{geo}\cong\left(\boldsymbol{A}_M\left(\tilde{\boldsymbol{x}}+\Delta\tilde{\boldsymbol{x}}\right)-\boldsymbol{A}_M\left(\tilde{\boldsymbol{x}}\right)\right).\left(\boldsymbol{A}_M\left(\tilde{\boldsymbol{x}}\right)\otimes\nabla_{\tilde{\boldsymbol{x}}}\right)^{-1}\end{aligned} \tag{3.14}$$

The criterion of a smooth design variation can be formulated by comparing the geometrical length to the size of the unit cell (ℓ) as:

$$\frac{L_i^{geo}}{\ell}>>1\Rightarrow L_i^{geo}>>\ell=\eta L \tag{3.15}$$

Therefore, the geometrical characteristic length associated with a smooth geometrical transformation should be asymptotically larger than the unit cell size such that quasi-periodic moduli can be defined in relation to the small-scale parameter.

As a first step of homogenization, we write the boundary value problem (BVP in short) of linear elasticity in periodic media. At the microscopic level of the single UC, the material satisfies the following equations of first gradient linear elasticity:

$$\begin{cases}\widetilde{\boldsymbol{\sigma}}\cdot\nabla_{\widetilde{y}}+\widetilde{\boldsymbol{b}}=\boldsymbol{0}\ \ in\ \ \widetilde{Y}\\ \widetilde{\boldsymbol{\sigma}}\cdot\widetilde{\boldsymbol{n}}=\widetilde{\boldsymbol{t}}\quad on\ \partial\widetilde{Y}\\ \widetilde{\boldsymbol{\sigma}}=\widetilde{\boldsymbol{C}}_{\mu}:\widetilde{\boldsymbol{\varepsilon}},\\ \widetilde{\boldsymbol{\varepsilon}}=\widetilde{\boldsymbol{A}}^{E}:\widetilde{\boldsymbol{E}}\end{cases} \tag{3.16}$$

wherein $\widetilde{\boldsymbol{\sigma}}$ is the symmetrical Cauchy stress, $\widetilde{\boldsymbol{b}}$ is the body force vector, $\widetilde{\boldsymbol{n}}$ is the normal vector, $\widetilde{\boldsymbol{t}}$ is the traction vector, and $\widetilde{\boldsymbol{C}}_{\mu}$ is the fourth order microscopic rigidity tensor in the periodic domain. $\widetilde{\boldsymbol{A}}^{E}$ is a fourth-order strain localization operator that relates the periodic micro $\widetilde{\boldsymbol{\varepsilon}}$ and macro $\widetilde{\boldsymbol{E}}$ strains.

The transformation of the strain tensor is then expressed using Eq. 3.7 and by substituting therein the expressions of Eq. 3.13:

$$\boldsymbol{\varepsilon}\left(\boldsymbol{y}\right)=\boldsymbol{A}.\widetilde{\varepsilon}.\boldsymbol{A}^{-1}=\left(\boldsymbol{A}_M\left(\tilde{\boldsymbol{x}}\right)+\eta\boldsymbol{A}_m\left(\tilde{\boldsymbol{x}},\tilde{\boldsymbol{y}}\right)\right).\widetilde{\varepsilon}.\left(\boldsymbol{A}_M^{-1}\left(\tilde{\boldsymbol{x}}\right)-\eta\boldsymbol{A}_M^{-1}\left(\tilde{\boldsymbol{x}}\right).\boldsymbol{A}_m\left(\tilde{\boldsymbol{x}},\tilde{\boldsymbol{y}}\right).\boldsymbol{A}_M^{-1}\left(\tilde{\boldsymbol{x}}\right)\right) \tag{3.17}$$

Let's recall the general transformation rule from the quasi-periodic to the periodic domains of the integral of an arbitrary scalar-valued density, using the definition of the volume average $\langle(.)\rangle_{\tilde{Y}}=\frac{1}{\left|\tilde{Y}\right|}\int\limits_{\tilde{Y}}(.)\,\mathrm{d}\tilde{Y}$:

$$\left\langle\tilde{h}\left(\tilde{\boldsymbol{y}}\right)\right\rangle_{\tilde{Y}}:=\frac{1}{\left|\tilde{Y}\right|}\int\limits_{\tilde{Y}}\tilde{h}\left(\tilde{\boldsymbol{y}}\right)d\tilde{V}_y=\frac{1}{\left|\tilde{Y}\right|}\int\limits_{Y}h\left(\boldsymbol{y}\right)\det\left(\boldsymbol{A}^{-1}\right)\left(\boldsymbol{y}\right)dV_y=\frac{|Y|}{\left|\tilde{Y}\right|}\frac{1}{|Y|}\int\limits_{Y}h\left(\boldsymbol{y}\right)\det\left(\boldsymbol{A}^{-1}\right)\left(\boldsymbol{y}\right)dV_y \tag{3.18}$$

wherein the ratio $\frac{|Y|}{\left|\tilde{Y}\right|}$ is the area change under coordinate transformation defined from the macroscopic tangent map as:

$$\det(\boldsymbol{A}_M)\left(\tilde{\boldsymbol{x}}\right)=\frac{|Y|}{\left|\tilde{Y}\right|}\Rightarrow\det(\boldsymbol{A}_M^{-1})\left(\tilde{\boldsymbol{x}}\right)=\frac{\left|\tilde{Y}\right|}{|Y|} \tag{3.19}$$

To proceed with the determination of the quasi-periodic moduli, we formulate the average microscopic strain energy density in the periodic domain using Eq. 3.18 and Eq. 3.19 :

$$\langle w_\mu(\boldsymbol{\varepsilon})\rangle_Y = \frac{1}{2}\langle \boldsymbol{\sigma} : \boldsymbol{\varepsilon}\rangle_Y = \frac{1}{2}\frac{\left|\widetilde{Y}\right|}{|Y|}\langle(\widetilde{\boldsymbol{\sigma}} : \widetilde{\boldsymbol{\varepsilon}})\det(\boldsymbol{A})\ \rangle_{\widetilde{Y}} = \frac{1}{2}\det\left(\boldsymbol{A}_M^{-1}\right)\langle(\widetilde{\boldsymbol{\sigma}} : \widetilde{\boldsymbol{\varepsilon}})\det(\boldsymbol{A})\ \rangle_{\widetilde{Y}} \tag{3.20}$$

The periodic macroscopic strain is elaborated classically as the average of the microscopic strain, which in turn can be written according to Eq. 3.17 and Eq. 3.18 as:

$$\widetilde{\boldsymbol{E}} = \langle\widetilde{\boldsymbol{\varepsilon}}\rangle_{\widetilde{Y}} = \det(\boldsymbol{A}_M)\left\langle \boldsymbol{A}^{-1}.\boldsymbol{\varepsilon}.\boldsymbol{A}\det\left(\boldsymbol{A}^{-1}\right)\ \right\rangle_{\widetilde{Y}} \tag{3.21}$$

Substituting Eq. 3.13 into Eq. 3.21 then leads to the following expression of the macroscopic periodic strain elaborated as the volume average of the microscopic strain:

$$\begin{aligned}\widetilde{\boldsymbol{E}} = \langle\widetilde{\boldsymbol{\varepsilon}}\rangle_{\widetilde{Y}} &= \boldsymbol{A}_M^{-1}.\langle\boldsymbol{\varepsilon}\rangle_Y.\boldsymbol{A}_M + \eta\left[\boldsymbol{A}_M^{-1}.\langle\boldsymbol{\varepsilon}.\boldsymbol{A}_m\rangle_Y - \left\langle\boldsymbol{A}_M^{-1}.\boldsymbol{A}_m.\boldsymbol{A}_M^{-1}.\boldsymbol{\varepsilon}.A_M\right\rangle_Y - \left\langle\boldsymbol{A}_M^{-1}.\boldsymbol{\varepsilon}.\boldsymbol{A}_M\left(\boldsymbol{A}_M^{-1} : \boldsymbol{A}_m^T\right)\right\rangle_Y\right] \\ &+\eta^2\left[-\left\langle\boldsymbol{A}_M^{-1}.\boldsymbol{A}_m.\boldsymbol{A}_M^{-1}.\boldsymbol{\varepsilon}.\boldsymbol{A}_m\right\rangle_Y - \left\langle\left(\boldsymbol{A}_M^{-1}.\boldsymbol{\varepsilon}.\boldsymbol{A}_M\right)\left(\boldsymbol{A}_M^{-1} : \boldsymbol{A}_m^T\right)\right\rangle_Y - \left\langle\left(\boldsymbol{A}_M^{-1}.\boldsymbol{A}_m.\boldsymbol{A}_M^{-1}.\boldsymbol{\varepsilon}.\boldsymbol{A}_m\right)\left(\boldsymbol{A}_M^{-1} : \boldsymbol{A}_m^T\right)\right\rangle_Y\right] \\ &+\eta^3\left[\left\langle\left(\boldsymbol{A}_M^{-1}.\boldsymbol{A}_m.\boldsymbol{A}_M^{-1}.\boldsymbol{\varepsilon}.\boldsymbol{A}_m\right)\left(\boldsymbol{A}_M^{-1} : \boldsymbol{A}_m^T\right)\right\rangle_Y\right]\end{aligned} \tag{3.22}$$

Defining the quasi-periodic macroscopic strain at the leading order zero of η to be the average of the quasi-periodic microscopic strain $\langle\boldsymbol{\varepsilon}\rangle_Y$,(all higher order terms of η in Eq. 3.22 are neglected) leads the relation between the macroscopic strain in the periodic domain and its counterpart in the quasi-periodic domain to be approximated at first order by:

$$\widetilde{\boldsymbol{E}} \approx \boldsymbol{A}_M^{-1}.\boldsymbol{E}.\boldsymbol{A}_M \Rightarrow \boldsymbol{E} \approx \boldsymbol{A}_M.\widetilde{\boldsymbol{E}}.\boldsymbol{A}_M^{-1} \tag{3.23}$$

Substituting Eq. 3.13, Eq. 3.23, and *Eq.* $3.16_{3,4}$ in Eq. 3.20 then leads the average microscopic strain energy in the quasi-periodic domain to be expressed as:

$$\begin{aligned}&\langle w_\mu(\boldsymbol{\varepsilon})\rangle_Y = \frac{1}{2}\langle\boldsymbol{\sigma} : \boldsymbol{\varepsilon}\rangle_Y = \frac{1}{2}\det\left(\boldsymbol{A}_M^{-1}\right)\left\langle\widetilde{\boldsymbol{E}} : \left(\widetilde{\boldsymbol{A}}^{E,T} : \widetilde{\boldsymbol{C}}_\mu : \widetilde{\boldsymbol{A}}^{E}\right) : \widetilde{\boldsymbol{E}}\det(\boldsymbol{A})\ \right\rangle_{\widetilde{Y}} \\ &\approx \frac{1}{2}\det\left(\boldsymbol{A}_M^{-1}\right)\left\langle\left(\boldsymbol{A}_M^{-1}.\boldsymbol{E}.\boldsymbol{A}_M\right) : \left(\widetilde{\boldsymbol{A}}^{E,T} : \widetilde{\boldsymbol{C}}_\mu : \widetilde{\boldsymbol{A}}^{E}\right) : \left(\boldsymbol{A}_M^{-1}.\boldsymbol{E}.\boldsymbol{A}_M\right)\det(\boldsymbol{A})\right\rangle_{\widetilde{Y}} \\ &\approx \frac{1}{2}\det\left(\boldsymbol{A}_M^{-1}\right)\boldsymbol{E} : \left(\boldsymbol{A}_M^{-T}\boxtimes\boldsymbol{A}_M\right) : \left\langle\left(\widetilde{\boldsymbol{A}}^{E,T} : \widetilde{\boldsymbol{C}}_\mu : \widetilde{\boldsymbol{A}}^{E}\right)\det(\boldsymbol{A})\right\rangle_{\widetilde{Y}} : \left(\boldsymbol{A}_M^{-1}\boxtimes\boldsymbol{A}_M^T\right) : \boldsymbol{E} \\ &\approx \frac{1}{2}\det\left(\boldsymbol{A}_M^{-1}\right)\boldsymbol{E} : \left(\boldsymbol{A}_M^{-T}\boxtimes\boldsymbol{A}_M\right) : \left\langle\left(\widetilde{\boldsymbol{A}}^{E,T} : \widetilde{\boldsymbol{C}}_\mu : \widetilde{\boldsymbol{A}}^{E}\right)\det(\boldsymbol{A}_M)\left(I+\eta Tr\left(\boldsymbol{A}_M^{-1}\boldsymbol{A}_m\right)\right)\right\rangle_{\widetilde{Y}} : \left(\boldsymbol{A}_M^{-1}\boxtimes\boldsymbol{A}_M^T\right) : \boldsymbol{E} \\ &\approx \frac{1}{2}\boldsymbol{E} : \left(\boldsymbol{A}_M^{-T}\boxtimes\boldsymbol{A}_M\right) : \left\langle\left(\widetilde{\boldsymbol{A}}^{E,T} : \widetilde{\boldsymbol{C}}_\mu : \widetilde{\boldsymbol{A}}^{E}\right)\right\rangle_{\widetilde{Y}} : \left(\boldsymbol{A}_M^{-1}\boxtimes\boldsymbol{A}_M^T\right) : \boldsymbol{E} \\ &+ \frac{1}{2}\eta\boldsymbol{E} : \left(\boldsymbol{A}_M^{-T}\boxtimes\boldsymbol{A}_M\right) : \left\langle\left(\widetilde{\boldsymbol{A}}^{E,T} : \widetilde{\boldsymbol{C}}_\mu : \widetilde{\boldsymbol{A}}^{E}\right)\left(\boldsymbol{A}_M^{-1} : \boldsymbol{A}_m^T\right)\right\rangle_{\widetilde{Y}} : \left(\boldsymbol{A}_M^{-1}\boxtimes\boldsymbol{A}_M^T\right) : \boldsymbol{E} \\ &\equiv \frac{1}{2}\boldsymbol{E} : \boldsymbol{C}_\eta^{\hom}(\boldsymbol{x}) : \boldsymbol{E}\end{aligned} \tag{3.24}$$

The last relation implicitly defines the tensor of quasi-periodic homogenized moduli expressed as an asymptotic expansion versus the small-scale parameter. The previous Eq. 3.24 then leads to the expression of the quasi-periodic moduli versus the tensor of the periodic homogenized moduli as the sum of a macroscopic contribution traducing the macro-grading of the unit cell and a perturbation reflecting the

higher order micrograding of the same unit cell:

$$\boldsymbol{C}_{\eta}^{\mathrm{hom}}(\boldsymbol{x}) = \boldsymbol{C}_{0}^{\mathrm{hom}}(\boldsymbol{x}) + \eta\delta\boldsymbol{C}^{\mathrm{hom}} \text{ where}$$
$$\begin{vmatrix} \boldsymbol{C}_{0}^{\mathrm{hom}}(\boldsymbol{x}) = \left(\boldsymbol{A}_{M}^{-T} \boxtimes \boldsymbol{A}_{M}\right) : \left\langle \left(\widetilde{\boldsymbol{A}}^{E,T} : \widetilde{\boldsymbol{C}}_{\mu} : \widetilde{\boldsymbol{A}}^{E}\right) \right\rangle_{\widetilde{Y}} : \left(\boldsymbol{A}_{M}^{-1} \boxtimes \boldsymbol{A}_{M}^{T}\right) \\ \delta\boldsymbol{C}^{\mathrm{hom}} = \left(\boldsymbol{A}_{M}^{-T} \boxtimes \boldsymbol{A}_{M}\right) : \left\langle \left(\widetilde{\boldsymbol{A}}^{E,T} : \widetilde{\boldsymbol{C}}_{\mu} : \widetilde{\boldsymbol{A}}^{E}\right) \left(\boldsymbol{A}_{M}^{-1} : \boldsymbol{A}_{m}^{T}\right) \right\rangle_{\widetilde{Y}} : \left(\boldsymbol{A}_{M}^{-1} \boxtimes \boldsymbol{A}_{M}^{T}\right) \end{vmatrix} \tag{3.25}$$

The effective quasi-periodic moduli are expressed as volume averages as shown in Eq. 3.25. From a numerical point of view, they are evaluated by first solving the BVP over the periodic unit cell (Eq. 3.16) and then mapping the moduli to the quasi-periodic domain. At the (zero) leading order of η , $\boldsymbol{C}_{0}^{\mathrm{hom}}(\boldsymbol{x})$ is calculated based on the sole macroscopic contribution of the tangent map; this means that one ignores the micrograding of the unit cell and focuses on the macrograding of the geometry.

Opposite to this, at the first order of η, besides $\boldsymbol{A}_{M}$, the microscopic tangent mapping $\boldsymbol{A}_{m}^{T}$ needs to be defined at each micro-point of the volume as an input; this makes it difficult to implement numerically this homogenization schemes in situations where the new quasi-periodic shape is prescribed by a motion of the internal or / and external surfaces or interfaces of the repetitive unit cell, whereas the mapping of internal micropoints is not defined explicitly from the onset. In order to overcome this difficulty, a surface formulation of quasi-periodic homogenization is developed in the next section. It relies on the shape derivative of the average potential energy involving the sole knowledge of the fields on the unit cell internal and external (outer) boundaries.

3.3 Surface formulation of the quasi-periodic moduli using the shape derivative

This section uses the notion of shape derivative towards the objective of formulating the surface integral of the energy in both periodic and quasi-periodic domains. We have initially the periodic domain $\widetilde{Y}$ with boundary $\partial\,\widetilde{Y}$ that is subjected to a smooth perturbation of its geometry, and the point mapping $\varphi : \widetilde{\boldsymbol{y}} \rightarrow \widetilde{\boldsymbol{y}} + \eta\boldsymbol{V}_{s}$ with its associated tangent map $\boldsymbol{A}$, wherein η being a small scalar parameter used to parametrize the domain and $\boldsymbol{V}_{s}$ being the shape velocity field in $\widetilde{Y}$ representing the change of periodic UC boundary (Fig. 3.4). The new perturbed domain occupied by the unit cell becomes: $Y_{\eta} := \left\{\boldsymbol{y} = \widetilde{\boldsymbol{y}} + \eta\boldsymbol{V}_{s}, \widetilde{\boldsymbol{y}} \in \widetilde{Y}\right\}$. Thus, $\boldsymbol{V}_{s}$ is considered as an input field for modifying the design of the unit cell [203].

The advantage of this approach is that it allows the determination of the effective moduli in the perturbed domain by performing the needed computations only on the boundary of the non-perturbed domain (in its unit cell), as will be exposed in the sequel.

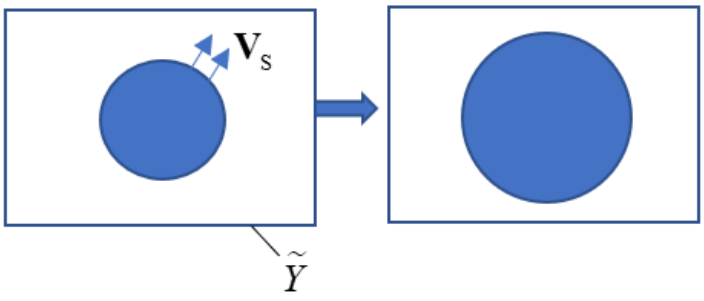

Figure 3.4 Schematic representation of the change of design of an initial periodic UC when subjected to a shape velocity field $\boldsymbol{V}_s$ on the boundaries of the inclusion.

From the volumetric approach developed previously, and for developing the surface formulations we reexpress with the energy density of Eq. 3.24 expressed as follows:

$$
\begin{aligned}
&W_M\left[Y_\eta\right] := \left\langle w_\mu\left(\boldsymbol{\varepsilon}\right)\right\rangle_Y = \frac{1}{2}\langle \boldsymbol{\sigma} : \boldsymbol{\varepsilon}\rangle_Y = \frac{1}{2}\det\left(\boldsymbol{A}_M^{-1}\right)\left\langle \widetilde{\boldsymbol{E}} : \left(\widetilde{\boldsymbol{A}}^{E,T} : \widetilde{\boldsymbol{C}}_\mu : \widetilde{\boldsymbol{A}}^{E}\right) : \widetilde{\boldsymbol{E}}\det\left(\boldsymbol{A}\right)\right\rangle_{\widetilde{Y}} \\
&= \frac{1}{2}\det\left(\boldsymbol{A}_M^{-1}\right)\widetilde{\boldsymbol{E}} : \left\langle \left(\widetilde{\boldsymbol{A}}^{E,T} : \widetilde{\boldsymbol{C}}_\mu : \widetilde{\boldsymbol{A}}^{E}\right)\det\left(\boldsymbol{A}_M\right)\left(I + \eta Tr\left(\boldsymbol{A}_M^{-1}\boldsymbol{A}_m\right)\right)\right\rangle_{\widetilde{Y}} : \widetilde{\boldsymbol{E}} \\
&= \frac{1}{2}\widetilde{\boldsymbol{E}} : \left\langle \left(\widetilde{\boldsymbol{A}}^{E,T} : \widetilde{\boldsymbol{C}}_\mu : \widetilde{\boldsymbol{A}}^{E}\right)\right\rangle_{\widetilde{Y}} : \widetilde{\boldsymbol{E}} + \frac{1}{2}\eta\widetilde{\boldsymbol{E}} : \left\langle \left(\widetilde{\boldsymbol{A}}^{E,T} : \widetilde{\boldsymbol{C}}_\mu : \widetilde{\boldsymbol{A}}^{E}\right)\left(Tr\left(\boldsymbol{A}_M^{-1}\boldsymbol{A}_m\right)\right)\right\rangle_{\widetilde{Y}} : \widetilde{\boldsymbol{E}} \\
&= \underbrace{\frac{1}{2}\widetilde{\boldsymbol{E}} : \left\langle \left(\widetilde{\boldsymbol{A}}^{E,T} : \widetilde{\boldsymbol{C}}_\mu : \widetilde{\boldsymbol{A}}^{E}\right)\right\rangle_{\widetilde{Y}} : \widetilde{\boldsymbol{E}}}_{\widetilde{W}_M\left[\widetilde{Y}\right]} + \eta\underbrace{\frac{1}{2}\widetilde{\boldsymbol{E}} : \left\langle \left(\widetilde{\boldsymbol{A}}^{E,T} : \widetilde{\boldsymbol{C}}_\mu : \widetilde{\boldsymbol{A}}^{E}\right)\left(\boldsymbol{A}_M^{-1} : \boldsymbol{A}_m^{T}\right)\right\rangle_{\widetilde{Y}} : \widetilde{\boldsymbol{E}}}_{\delta\widetilde{W}_M\left[\widetilde{Y}\right]} \\
&\Rightarrow W_M\left[Y_\eta\right] = \widetilde{W}_M\left[\widetilde{Y}\right] + \eta\delta\widetilde{W}_M\left[\widetilde{Y}\right] \\
&\Rightarrow \frac{W_M\left[Y_\eta\right] - \widetilde{W}_M\left[\widetilde{Y}\right]}{\eta} = \delta\widetilde{W}_M\left[\widetilde{Y}\right]
\end{aligned}
\tag{3.26}
$$

The last relation in Eq. 3.26, can then be written according to the definition of the derivative [204] when $\eta \to 0$, as:

$$
\frac{d}{d\eta}W_M\left[Y_\eta\right] = \delta\widetilde{W}_M\left[\widetilde{Y}\right] \tag{3.27}
$$

The total potential energy, elaborated as the difference of internal mechanical energy and work of external forces, is selected to be the cost function, viz. $J\left[Y_\eta\right] := W_{in} - W_{ext}$. According to [203], the shape derivative of the cost function J is expressed, after some derivations over the periodic domain as:

$$
\frac{d}{d\eta}\mathrm{J}\left[Y_\eta\right] = \int_{\widetilde{Y}} \boldsymbol{\Sigma}_{Eshelby} : \boldsymbol{V}_s \otimes \nabla_{\widetilde{y}} d\widetilde{Y} \tag{3.28}
$$

with $\boldsymbol{\Sigma}_{Eshelby} := w_\mu \boldsymbol{I} - \boldsymbol{\varepsilon}^T.\boldsymbol{\sigma}$ the Eshelby stress appearing as the driving force acting at the microscopic level of the unit cell to change its shape.

Clapeyron theorem is next utilized to express the total potential energy in terms of the strain energy density as the quantity of concern as shown in Eq. 3.27, viz. $J\left[Y_\eta\right] := -W_{in} = -W_M\left[Y_\eta\right]$, as demonstrated in [215]. Thus, Eq. 3.28 becomes:

$$
\frac{d}{d\eta}W_M\left[Y_\eta\right] = \delta\widetilde{W}_M\left[\widetilde{Y}\right] = -\int_{\widetilde{Y}} \boldsymbol{\Sigma}_{Eshelby} : \boldsymbol{V}_s \otimes \nabla_{\widetilde{y}} d\widetilde{Y} \tag{3.29}
$$

Since the Eshelby stress has a nil divergence [203], it is straightforward to write Eq. 3.29 as a surface integral of the form:

$$\delta\widetilde{W}_M\left[\widetilde{Y}\right] = -\int_{\partial\widetilde{Y}} \widetilde{\boldsymbol{n}}.\boldsymbol{\Sigma}_{Eshelby}.\boldsymbol{V}_s d\left(\partial\widetilde{Y}\right) \tag{3.30}$$

$\boldsymbol{V}_s$ becomes the shape velocity field to be applied on the boundaries of the UC when it is smooth enough in $\widetilde{Y}$ [203]. Eq. 3.30 shows that the volumetric quantity in Eq. 3.26 now expresses as a surface integral:

$$\begin{aligned}
&\delta\widetilde{W}_M\left[\widetilde{Y}\right] = \frac{1}{2}\widetilde{\boldsymbol{E}} : \left\langle \left(\widetilde{\boldsymbol{A}}^{E,T} : \widetilde{\boldsymbol{C}}_\mu : \widetilde{\boldsymbol{A}}^{E}\right)\left(\boldsymbol{A}_M^{-1} : \boldsymbol{A}_m^{T}\right)\right\rangle_{\widetilde{Y}} : \widetilde{\boldsymbol{E}} = -\int_{\partial\widetilde{Y}} \widetilde{\boldsymbol{n}}.\boldsymbol{\Sigma}_{Eshelby}.\boldsymbol{V}_s d\left(\partial\widetilde{Y}\right) \\
&= -\int_{\partial\widetilde{Y}} \widetilde{\boldsymbol{n}}.\left(\widetilde{w}_\mu \boldsymbol{I} - \widetilde{\boldsymbol{\varepsilon}}^T.\widetilde{\boldsymbol{\sigma}}\right).\boldsymbol{V}_s d\left(\partial\widetilde{Y}\right) = -\int_{\partial\widetilde{Y}} \widetilde{\boldsymbol{n}}.\left(\frac{1}{2}\left(\widetilde{\boldsymbol{\sigma}} : \widetilde{\boldsymbol{\varepsilon}}\right)\boldsymbol{I} - \widetilde{\boldsymbol{\varepsilon}}.\widetilde{\boldsymbol{\sigma}}\right).\boldsymbol{V}_s d\left(\partial\widetilde{Y}\right) \\
&= \frac{1}{2}\int_{\partial\widetilde{Y}} \widetilde{\boldsymbol{n}}.\left[\left(\widetilde{\boldsymbol{A}}^{E} : \widetilde{\boldsymbol{E}}\right) : \widetilde{\boldsymbol{C}}_\mu : \left(\widetilde{\boldsymbol{A}}^{E} : \widetilde{\boldsymbol{E}}\right)\right].\boldsymbol{V}_s d\left(\partial\widetilde{Y}\right) = \frac{1}{2}\int_{\partial\widetilde{Y}} \widetilde{\boldsymbol{n}}.\left[\widetilde{\boldsymbol{E}} : \left(\widetilde{\boldsymbol{A}}^{E,T} : \widetilde{\boldsymbol{C}}_\mu : \widetilde{\boldsymbol{A}}^{E}\right) : \widetilde{\boldsymbol{E}}\right].\boldsymbol{V}_s d\left(\partial\widetilde{Y}\right) \\
&\Rightarrow \frac{1}{2}\widetilde{\boldsymbol{E}} : \left\langle \left(\widetilde{\boldsymbol{A}}^{E,T} : \widetilde{\boldsymbol{C}}_\mu : \widetilde{\boldsymbol{A}}^{E}\right)\left(\boldsymbol{A}_M^{-1} : \boldsymbol{A}_m^{T}\right)\right\rangle_{\widetilde{Y}} : \widetilde{\boldsymbol{E}} = \frac{1}{2}\widetilde{\boldsymbol{E}} : \left\{\int_{\partial\widetilde{Y}} \widetilde{\boldsymbol{n}}.\left[\left(\widetilde{\boldsymbol{A}}^{E,T} : \widetilde{\boldsymbol{C}}_\mu : \widetilde{\boldsymbol{A}}^{E}\right)\right].\boldsymbol{V}_s d\left(\partial\widetilde{Y}\right)\right\} : \widetilde{\boldsymbol{E}} \\
&\Rightarrow \frac{1}{2}\widetilde{\boldsymbol{E}} : \delta\boldsymbol{C}^{\boldsymbol{hom}} : \widetilde{\boldsymbol{E}} = \frac{1}{2}\widetilde{\boldsymbol{E}} : \left\{\int_{\partial\widetilde{Y}} \widetilde{\boldsymbol{n}}.\left[\left(\widetilde{\boldsymbol{A}}^{E,T} : \widetilde{\boldsymbol{C}}_\mu : \widetilde{\boldsymbol{A}}^{E}\right)\right].\boldsymbol{V}_s d\left(\partial\widetilde{Y}\right)\right\} : \widetilde{\boldsymbol{E}}
\end{aligned} \tag{3.31}$$

Thus, the perturbed moduli $\delta\boldsymbol{C}^{\boldsymbol{hom}}$ in the previous approach rewrites as surface integral as:

$$\delta\boldsymbol{C}^{\boldsymbol{hom}} = \int_{\partial\widetilde{Y}} \widetilde{\boldsymbol{n}}.\left[\left(\widetilde{\boldsymbol{A}}^{E,T} : \widetilde{\boldsymbol{C}}_\mu : \widetilde{\boldsymbol{A}}^{E}\right)\right].\boldsymbol{V}_s d\left(\partial\widetilde{Y}\right) \tag{3.32}$$

On the other hand, for the energy density $\widetilde{W}_M\left[\widetilde{Y}\right] = \frac{1}{2}\widetilde{\boldsymbol{E}} : \left\langle \left(\widetilde{\boldsymbol{A}}^{E,T} : \widetilde{\boldsymbol{C}}_\mu : \widetilde{\boldsymbol{A}}^{E}\right)\right\rangle_{\widetilde{Y}} : \widetilde{\boldsymbol{E}}$ in Eq. 3.26, to be expressed as a surface integral, we introduce a displacement localization operator $\widetilde{\boldsymbol{H}}^{E}$ such that $\widetilde{\boldsymbol{u}} = \widetilde{\boldsymbol{H}}^{E} : \widetilde{\boldsymbol{E}}$:

$$\begin{aligned}
&\widetilde{W}_M\left[\widetilde{Y}\right] = \frac{1}{2}\widetilde{\boldsymbol{E}} : \left\langle \left(\widetilde{\boldsymbol{A}}^{E,T} : \widetilde{\boldsymbol{C}}_\mu : \widetilde{\boldsymbol{A}}^{E}\right)\right\rangle_{\widetilde{Y}} : \widetilde{\boldsymbol{E}} = \frac{1}{2}\langle \widetilde{\boldsymbol{\sigma}} : \widetilde{\boldsymbol{\varepsilon}}\rangle_{\widetilde{Y}} = \frac{1}{2}\frac{1}{\left|\widetilde{Y}\right|}\int_{\partial\widetilde{Y}} \left(\widetilde{\boldsymbol{n}}.\widetilde{\boldsymbol{\sigma}}\right).\widetilde{\boldsymbol{u}}\ \mathrm{d}\left(\partial\widetilde{Y}\right) \\
&= \frac{1}{2}\widetilde{\boldsymbol{E}} : \left\{\frac{1}{\left|\widetilde{Y}\right|}\int_{\partial\widetilde{Y}} \widetilde{\boldsymbol{A}}^{E,T} : \widetilde{\boldsymbol{C}}_\mu : \left(\widetilde{\boldsymbol{n}} \otimes \widetilde{\boldsymbol{H}}^{E}\right)\mathrm{d}\left(\partial\widetilde{Y}\right)\right\} : \widetilde{\boldsymbol{E}} = \frac{1}{2}\widetilde{\boldsymbol{E}} : \left\langle \widetilde{\boldsymbol{A}}^{E,T} : \widetilde{\boldsymbol{C}}_\mu : \left(\widetilde{\boldsymbol{n}} \otimes \widetilde{\boldsymbol{H}}^{E}\right)\right\rangle_{\partial\widetilde{Y}} : \widetilde{\boldsymbol{E}}
\end{aligned} \tag{3.33}$$

Then, previous relation underline that the Cauchy moduli can be consequently derived as a surface integral as:

$$\boldsymbol{C}_0^{\mathrm{hom}} = \left\langle \widetilde{\boldsymbol{A}}^{E,T} : \widetilde{\boldsymbol{C}}_\mu : \left(\widetilde{\boldsymbol{n}} \otimes \widetilde{\boldsymbol{H}}^{E}\right)\right\rangle_{\partial\widetilde{Y}} \tag{3.34}$$

The next subsection deals with the extension of the previous homogenization into higher order strain gradient homogenization to account for the micrograding.

3.3.1 Extension towards a strain gradient effective medium

The grading of the design at the micro-level leads expectedly to a strain gradient continuum that accounts for it (whereas a first gradient formulation is not sufficient), as mentioned in [121]. For this purpose, we introduce strain gradient localization operators $\widetilde{\boldsymbol{A}}^{k}$ and $\widetilde{\boldsymbol{H}}^{k}$, besides the strain and displacement localization operators $(\widetilde{\boldsymbol{A}}^{E}, \widetilde{\boldsymbol{H}}^{E})$, to relate respectively the microscopic strain and the microscopic displacement to the macroscopic strain gradient third-order tensor $\widetilde{\boldsymbol{K}} = \widetilde{\boldsymbol{E}} \otimes \nabla_{\widetilde{x}}$, so that the

microscopic strain and displacement can be expressed versus the macroscopic kinematic variables as

$$\begin{vmatrix} \widetilde{\boldsymbol{\varepsilon}} = \widetilde{\boldsymbol{A}}^{E} : \widetilde{\boldsymbol{E}} + \widetilde{\boldsymbol{A}}^{k} \therefore \widetilde{\boldsymbol{K}} \\ \widetilde{\boldsymbol{u}} = \widetilde{\boldsymbol{H}}^{E} : \widetilde{\boldsymbol{E}} + \widetilde{\boldsymbol{H}}^{k} \therefore \widetilde{\boldsymbol{K}} \end{vmatrix} \tag{3.35}$$

We will discard in upcoming relations the couplings between first and strain gradient behaviors by restricting to centrosymmetric designs of the UC.

Now, the strain energy densities in Eq. 3.26 will be extended to account for the strain gradient medium after inserting the relations of Eq. 3.35:

$$\begin{aligned} \widetilde{W}_M\left[\widetilde{Y}\right] &= \frac{1}{2}\widetilde{\boldsymbol{E}} : \left\langle \left(\widetilde{\boldsymbol{A}}^{E,T} : \widetilde{\boldsymbol{C}}_\mu : \widetilde{\boldsymbol{A}}^{E}\right)\right\rangle_{\widetilde{Y}} : \widetilde{\boldsymbol{E}} + \frac{1}{2}\widetilde{\boldsymbol{K}} \therefore \left\langle \left(\widetilde{\boldsymbol{A}}^{k,T} : \widetilde{\boldsymbol{C}}_\mu : \widetilde{\boldsymbol{A}}^{k}\right)\right\rangle_{\widetilde{Y}} \therefore \widetilde{\boldsymbol{K}} \\ \delta\widetilde{W}_M\left[\widetilde{Y}\right] &= \frac{1}{2}\widetilde{\boldsymbol{E}} : \left\langle \left(\widetilde{\boldsymbol{A}}^{E,T} : \widetilde{\boldsymbol{C}}_\mu : \widetilde{\boldsymbol{A}}^{E}\right)\left(\boldsymbol{A}_M^{-1} : \boldsymbol{A}_m^{T}\right)\right\rangle_{\widetilde{Y}} : \widetilde{\boldsymbol{E}} + \frac{1}{2}\widetilde{\boldsymbol{K}} \therefore \left\langle \left(\widetilde{\boldsymbol{A}}^{k,T} : \widetilde{\boldsymbol{C}}_\mu : \widetilde{\boldsymbol{A}}^{k}\right)\left(\boldsymbol{A}_M^{-1} : \boldsymbol{A}_m^{T}\right)\right\rangle_{\widetilde{Y}} \therefore \widetilde{\boldsymbol{K}} \end{aligned} \tag{3.36}$$

Following the same methodology for determining the surface formulation of the Cauchy and the perturbed Cauchy moduli, the strain gradient $\boldsymbol{A}_0^{\hom}$ and its associated perturbation $\delta\boldsymbol{A}^{\boldsymbol{hom}}$ are derived:

$$\begin{aligned} \boldsymbol{A}_0^{\hom} &= \left\langle \left(\widetilde{\boldsymbol{A}}^{k,T} : \widetilde{\boldsymbol{C}}_\mu : \widetilde{\boldsymbol{A}}^{k}\right)\right\rangle_{\widetilde{Y}} = \left\langle \widetilde{\boldsymbol{A}}^{k,T} : \widetilde{\boldsymbol{C}}_\mu : \left(\widetilde{\boldsymbol{n}} \otimes \widetilde{\boldsymbol{H}}^{k}\right)\right\rangle_{\partial\widetilde{Y}} \\ \delta\boldsymbol{A}^{\boldsymbol{hom}} &= \left\langle \left(\widetilde{\boldsymbol{A}}^{k,T} : \widetilde{\boldsymbol{C}}_\mu : \widetilde{\boldsymbol{A}}^{k}\right)\left(\boldsymbol{A}_M^{-1} : \boldsymbol{A}_m^{T}\right)\right\rangle_{\widetilde{Y}} = \int_{\partial\widetilde{Y}} \widetilde{\boldsymbol{n}}.\left[\left(\widetilde{\boldsymbol{A}}^{k,T} : \widetilde{\boldsymbol{C}}_\mu : \widetilde{\boldsymbol{A}}^{k}\right)\right].\boldsymbol{V}_s d\left(\partial\widetilde{Y}\right) \end{aligned} \tag{3.37}$$

Considering the active viewpoint, the components of the tensors $\boldsymbol{C}_0^{\hom}$, $\delta\boldsymbol{C}^{\boldsymbol{hom}}, \boldsymbol{A}_0^{\hom}$, and $\delta\boldsymbol{A}^{\boldsymbol{hom}}$ are identical in the respective bases of the periodic and quasi-periodic domain, i.e. it holds $\delta C_{ijkl}^{\hom}\Big|_{inY-bases} = \delta C_{ijkl}^{\hom}\Big|_{in\widetilde{Y}-bases}$ This leads to the components of the periodic effective first (Cauchy) and strain gradient moduli versus their periodic counterpart plus their corresponding fluctuation:

$$\begin{aligned} C_{ijkl}^{\hom}(\boldsymbol{x})\big|_{inY-bases} &= \left(C_0^{\hom}\right)_{ijkl}\Big|_{inY-bases} + \eta\ \delta C_{ijkl}^{\hom}|_{inY-bases} \\ A_{ijklmn}^{\hom}(\boldsymbol{x})\big|_{inY-bases} &= \left(A_0^{\hom}\right)_{ijklmn}\Big|_{inY-bases} + \eta\ \delta A_{ijklmn}^{\hom}|_{inY-bases} \end{aligned} \tag{3.38}$$

The following section illustrates the algorithm for the determination of the effective quasi-periodic moduli starting from the periodic unit cell domain.

3.3.2 Algorithm for determining the effective quasi-periodic moduli

The expressions of the quasi-periodic effective moduli elaborated in the previous subsection make it possible to study and solve the BVP of quasi-periodic homogenization from a corresponding BVP expressed within the UC of the reference periodic domain. First, the microscopic displacement in the periodic physical UC is introduced as a sum of a fluctuating displacement $\widetilde{\widetilde{\boldsymbol{u}}}_{\underset{\sim}{E,K}}\left(\eta\widetilde{\boldsymbol{\xi}}\right)$and a homogenized part $\widetilde{\boldsymbol{u}}^{\hom}\left(\eta\widetilde{\boldsymbol{\xi}},\widetilde{\boldsymbol{x}}\right)$. Therein, $\widetilde{\boldsymbol{u}}^{\hom}$ corresponds to a heterogeneous medium that would behave exactly as a homogeneous one and its expression is fully derived in [198] for a strain gradient medium (the parameter η appears because we are working with the physical UC). The fluctuating displacement represents the deviation of the homogeneous medium from a heterogeneous medium; it is induced by applying the macroscopic kinematic loading $\left(\widetilde{\boldsymbol{E}},\widetilde{\boldsymbol{K}}\right)$ over the periodic physical unit cell.

$$\widetilde{\boldsymbol{u}} = \widetilde{\boldsymbol{u}}^{\hom}\left(\eta\widetilde{\boldsymbol{\xi}},\widetilde{\boldsymbol{x}}\right) + \widetilde{\widetilde{\boldsymbol{u}}}_{\underset{\sim}{E,K}}\left(\eta\widetilde{\boldsymbol{\xi}}\right) = \eta\widetilde{\boldsymbol{E}}(\widetilde{\boldsymbol{x}}).\widetilde{\boldsymbol{\xi}} + \frac{1}{2}\eta^2\widetilde{\boldsymbol{K}}(\widetilde{\boldsymbol{x}}) : \left(\widetilde{\boldsymbol{\xi}} \otimes \widetilde{\boldsymbol{\xi}}\right) + \widetilde{\widetilde{\boldsymbol{u}}}_{\underset{\sim}{E,K}}\left(\eta\widetilde{\boldsymbol{\xi}}\right) \tag{3.39}$$

We revisit the equilibrium and the constitutive equations of Eq. 3.16, so that the localization problem to be solved for the displacement fluctuation writes:

$$\begin{cases} \widetilde{\boldsymbol{\sigma}}.\nabla_{\widetilde{y}} = \left(\widetilde{\boldsymbol{C}}_{\mu} : \widetilde{\boldsymbol{\varepsilon}}\left(\widetilde{\boldsymbol{u}}_{\underset{E,K}{\sim}\,\widetilde{}}\right)\right).\nabla_{\widetilde{y}} = \mathbf{0} \\ \widetilde{\boldsymbol{\sigma}} := \widetilde{\boldsymbol{C}}_{\mu} : \widetilde{\boldsymbol{\varepsilon}}\left(\widetilde{\boldsymbol{u}}_{\underset{E,K}{\sim}\,\widetilde{}}\right) \\ \widetilde{\boldsymbol{u}}_{\underset{E,K}{\sim}\,\widetilde{}} = \widetilde{\boldsymbol{u}}^{\text{hom}}\left(\eta\widetilde{\boldsymbol{\xi}}, \widetilde{\boldsymbol{x}}\right) + \widetilde{\widetilde{\boldsymbol{u}}}_{\underset{E,K}{\sim}\,\widetilde{}}\left(\eta\widetilde{\boldsymbol{\xi}}\right) \\ \widetilde{\widetilde{\boldsymbol{u}}}_{\underset{E,K}{\sim}\,\widetilde{}}\ \widetilde{\text{Y}}\text{-periodic} \end{cases} \tag{3.40}$$

Thereby, the shape derivative of the classical and strain gradient moduli can be determined based on the expression of the microscopic displacement versus the macroscopic kinematic loadings and its periodic fluctuation obtained by solving the corresponding unit cell BVP in Eq. 3.40. The algorithm for solving the BVP (using the open source code FreeFem++) and determining the effective quasi-periodic moduli is explained synthetically in Fig. 3.5.

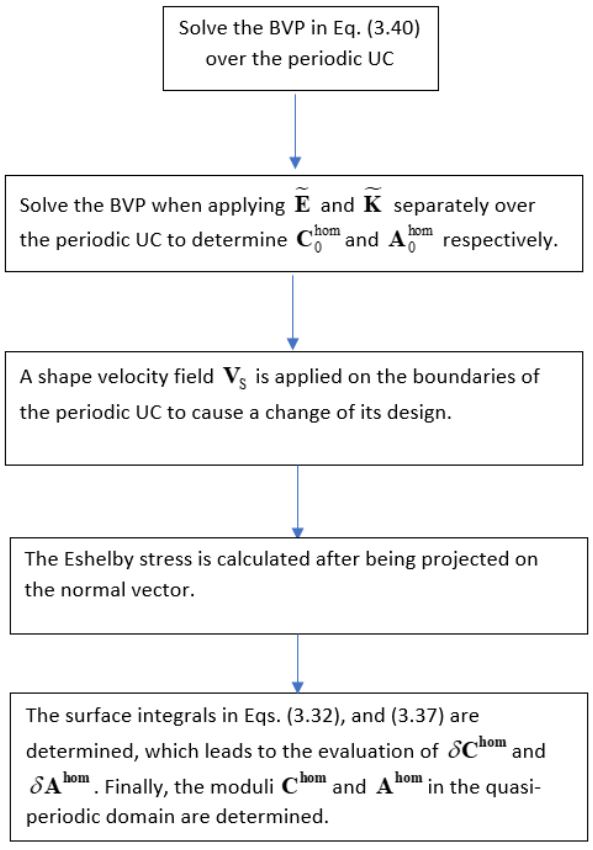

Figure 3.5 Schematic diagram for the computation of the effective quasi-periodic moduli.

3.3.3 Scale ranking of the effective quasi-periodic moduli versus the small-scale parameter

Noting that in the previous sections the fluctuating displacement and strain were neglected so the equations $\widetilde{\boldsymbol{u}} = \widetilde{\boldsymbol{u}}^{hom}$ and $\widetilde{\boldsymbol{\varepsilon}} = \widetilde{\boldsymbol{\varepsilon}}^{\text{hom}}$ hold with the associated localization operators $\left(\widetilde{\boldsymbol{H}}^{E}, \widetilde{\boldsymbol{H}}^{k}\right)$ and

$\left(\widetilde{\boldsymbol{A}}^{E},\widetilde{\boldsymbol{A}}^{k}\right)$ were considered in the derivations. These localization operators include implicitly the parameter η from which we can conclude the scaling of the effective moduli. This subsection elaborates how this scaling appears and how we can get finally an expression of the energy having η explicitly there.

In order to reach a ranking of the effective quasi-periodic moduli versus the small scale parameter, the homogeneous displacement introduced in Eq. 3.40 is first mapped into the physical unit cell, and it is elaborated along with its corresponding strain as:

$$\begin{aligned}
&\widetilde{u}_i^{\text{hom}}\left(\eta\widetilde{\boldsymbol{\xi}},\widetilde{\boldsymbol{x}}\right)=\widetilde{E}_{pq}\eta\delta_{pi}\widetilde{\xi}_q+\frac{1}{2}\eta^2\widetilde{K}_{ijk}\widetilde{\xi}_j\widetilde{\xi}_k\\
&\widetilde{\boldsymbol{u}}^{hom}\left(\eta\widetilde{\boldsymbol{\xi}},\widetilde{\boldsymbol{x}}\right)=\widetilde{\boldsymbol{H}}^{E}(\eta\widetilde{\boldsymbol{\xi}}):\widetilde{\boldsymbol{E}}(\widetilde{\boldsymbol{x}})+\widetilde{\boldsymbol{H}}^{k}(\eta\widetilde{\boldsymbol{\xi}})\therefore\widetilde{\boldsymbol{K}}(\widetilde{\boldsymbol{x}})\\
&\Rightarrow\widetilde{\varepsilon}^{\text{hom}}\left(\eta\widetilde{\boldsymbol{\xi}},\widetilde{\boldsymbol{x}}\right)=\widetilde{\boldsymbol{u}}^{hom}\otimes^{s}\nabla_{\widetilde{y}}\equiv\widetilde{\boldsymbol{A}}^{E}(\eta\widetilde{\boldsymbol{\xi}}):\widetilde{\boldsymbol{E}}(\widetilde{\boldsymbol{x}})+\widetilde{\boldsymbol{A}}^{k}(\eta\widetilde{\boldsymbol{\xi}})\therefore\widetilde{\boldsymbol{K}}(\widetilde{\boldsymbol{x}})
\end{aligned}\tag{3.41}$$

$$\begin{aligned}
&\widetilde{\boldsymbol{A}}^{E}(\eta\widetilde{\boldsymbol{\xi}})=\widetilde{\boldsymbol{H}}^{E}(\eta\widetilde{\boldsymbol{\xi}})\otimes\nabla_{\eta\widetilde{\boldsymbol{\xi}}},\ \widetilde{\boldsymbol{H}}^{E}(\eta\widetilde{\boldsymbol{\xi}})=\eta\delta_{pi}\widetilde{\xi}_q\Rightarrow\widetilde{\boldsymbol{A}}^{E}(\widetilde{\boldsymbol{\xi}})\propto\eta^0\\
&\widetilde{\boldsymbol{A}}^{k}(\eta\widetilde{\boldsymbol{\xi}})=\widetilde{\boldsymbol{H}}^{k}(\eta\widetilde{\boldsymbol{\xi}})\otimes\nabla_{\eta\widetilde{\boldsymbol{\xi}}},\ \widetilde{\boldsymbol{H}}^{k}(\eta\widetilde{\boldsymbol{\xi}})=\eta^2\frac{1}{2}\left\{\widetilde{\xi}_q\widetilde{\xi}_r\delta_{ip}\right\}\Rightarrow\widetilde{\boldsymbol{A}}^{k}(\eta\widetilde{\boldsymbol{\xi}})\propto\eta^1
\end{aligned}$$

The effective moduli are then expressed as the following integrals over the unit cell involving the strain localization operators [198]. The previously obtained ranking of the strain localization operators vs η in Eq. 3.41 determine the scale ranking of the effective moduli as well as their perturbed moduli as follows:

$$\begin{aligned}
\boldsymbol{C}_0^{\text{hom}}&=\int_{\widetilde{Y}}\widetilde{\boldsymbol{A}}^{E}(\widetilde{\boldsymbol{\xi}}):\widetilde{\boldsymbol{C}}_\mu:\widetilde{\boldsymbol{A}}^{E}(\widetilde{\boldsymbol{\xi}})dV_y\ \propto\eta^0\\
\boldsymbol{A}_0^{\text{hom}}&=\int_{\widetilde{Y}}\widetilde{\boldsymbol{A}}^{k,T}(\widetilde{\boldsymbol{\xi}}):\widetilde{\boldsymbol{C}}_\mu:\widetilde{\boldsymbol{A}}^{k}(\widetilde{\boldsymbol{\xi}})dV_y\propto\eta^2\\
\eta\delta\boldsymbol{C}^{\boldsymbol{hom}}&=\int_{\partial\widetilde{Y}}\boldsymbol{n}.\left[\left(\widetilde{\boldsymbol{A}}^{E,T}:\widetilde{\boldsymbol{C}}_\mu:\widetilde{\boldsymbol{A}}^{E}\right)\right].\boldsymbol{V}_s d\left(\partial\widetilde{Y}\right)\propto\eta^1\\
\eta\delta\boldsymbol{A}^{\boldsymbol{hom}}&=\int_{\partial\widetilde{Y}}\boldsymbol{n}.\left[\left(\widetilde{\boldsymbol{A}}^{k,T}:\widetilde{\boldsymbol{C}}_\mu:\widetilde{\boldsymbol{A}}^{k}\right)\right].\boldsymbol{V}_s d\left(\partial\widetilde{Y}\right)\propto\eta^3
\end{aligned}\tag{3.42}$$

It appears from previous relations that the first gradient effective moduli $\boldsymbol{C}_0^{\text{hom}}$ is independent of η whereas the strain gradient effective moduli $\boldsymbol{A}_0^{\text{hom}}$ is of second order of η. The perturbed moduli for both first and strain gradient terms are of one η-order higher than the corresponding unperturbed periodic moduli. Eq. 3.42 can lead to explicitly express the quasi-periodic energy in terms of η as:

$$W_M\left[Y_\eta\right]=\frac{1}{2}\widetilde{\boldsymbol{E}}:\boldsymbol{C}_0^{\text{hom}}:\widetilde{\boldsymbol{E}}+\eta\frac{1}{2}\widetilde{\boldsymbol{E}}:\delta\boldsymbol{C}^{\boldsymbol{hom}}:\widetilde{\boldsymbol{E}}+\eta^2\frac{1}{2}\widetilde{\boldsymbol{K}}\therefore\boldsymbol{A}_0^{\text{hom}}\therefore\widetilde{\boldsymbol{K}}+\eta^3\frac{1}{2}\widetilde{\boldsymbol{K}}\therefore\delta\boldsymbol{A}^{\boldsymbol{hom}}\therefore\widetilde{\boldsymbol{K}}\tag{3.43}$$

The following section considers a numerical example to determine the homogenized properties of a quasi-periodic structure.

3.4 Application of the quasi-periodic homogenization scheme

In this section, we rely on the surface formulation for the evaluation of the quasi-periodic moduli of an inclusion-based composite with variable radius as shown in Fig. 3.6. The radius of each UC is defined to change according to the relation $R(\widetilde{x}) = \widetilde{R} + \tan\beta\ \widetilde{x}$ with $\widetilde{R}$ being the radius of the initial periodic UC, $\tan\beta$ being the slope of variation of each radius with respect to the initial one (as shown in Fig. 3.6) and $\widetilde{x}$ is the position of the center of each UC (measured from the origin of coordinates).

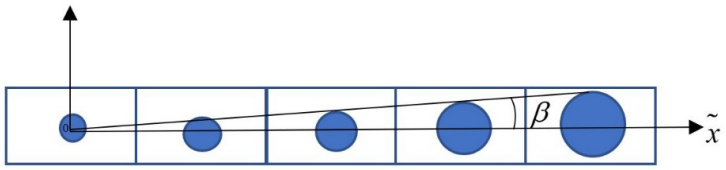

Figure 3.6 Illustration of quasi-periodic domain showing the variation of the radius with a slope of angle β.

Starting from $\widetilde{R} = 0.1$ mm (radius of the first UC), $\tan\beta$ is chosen to be 10^{-3} so that the variation between the UCs is smooth. The length of each UC is $l = 1$ mm, The mechanical properties of the constituents of the composite, carbon inclusion and epoxy matrix are listed in Table 3.1.

Table 3.1 Mechanical properties of the inclusion and matrix materials.

Mechanical properties	Inclusion (Carbon)	Matrix(epoxy)
E (MPa)	228000	1400
ν	0.26	0.3

The homogenization is done on a domain of quasi-periodic UCs in which each UC gets its homogenized Cauchy $\boldsymbol{C}^{\text{hom}}(\widetilde{\boldsymbol{x}})$,and strain gradient $\boldsymbol{A}^{\text{hom}}(\widetilde{\boldsymbol{x}})$ moduli with the associated perturbations $\delta\boldsymbol{C}^{\text{hom}}$and $\delta\boldsymbol{A}^{\text{hom}}$ respectively. The variation of some of these moduli$\left(C^{\text{hom}}_{1111}, C^{\text{hom}}_{1122}, A^{\text{hom}}_{111111}, A^{\text{hom}}_{111221}\right)$ is plotted in Fig. 7 as a function of the spatial position representing their variation with the design change. C^{hom}_{1111} represents the first moduli in the Cauchy rigidity tensor which relates the macroscopic stress to the macroscopic strain in extension, and A^{hom}_{111111} represents the first moduli in the strain gradient tensor which relates the first-term in the higher order stress (hyper-stress) tensor to the first term in the strain gradient tensor, whereas $\left(C^{\text{hom}}_{1122}, A^{\text{hom}}_{111221}\right)$ represents the shear moduli in the Cauchy rigidity tensor and strain gradient tensor respectively. It is observed in Fig. 3.7 that both the Cauchy moduli and strain gradient moduli increase as the design of unit cells changes along the spatial position $\widetilde{x}$. In Fig. 3.8, an internal length defined as $l_{xx} = \sqrt{\frac{\boldsymbol{A}^{\text{hom}}_{111111}}{\boldsymbol{C}^{\text{hom}}_{1111}}}$ is determined and illustrated versus the spatial macro position. As shown is Fig. 3.8, l_{xx} increases with the design change in a way that ensures the smoothness of design between UCs where the percentage increase of l_{xx} is small between the reference UC and the last UC.

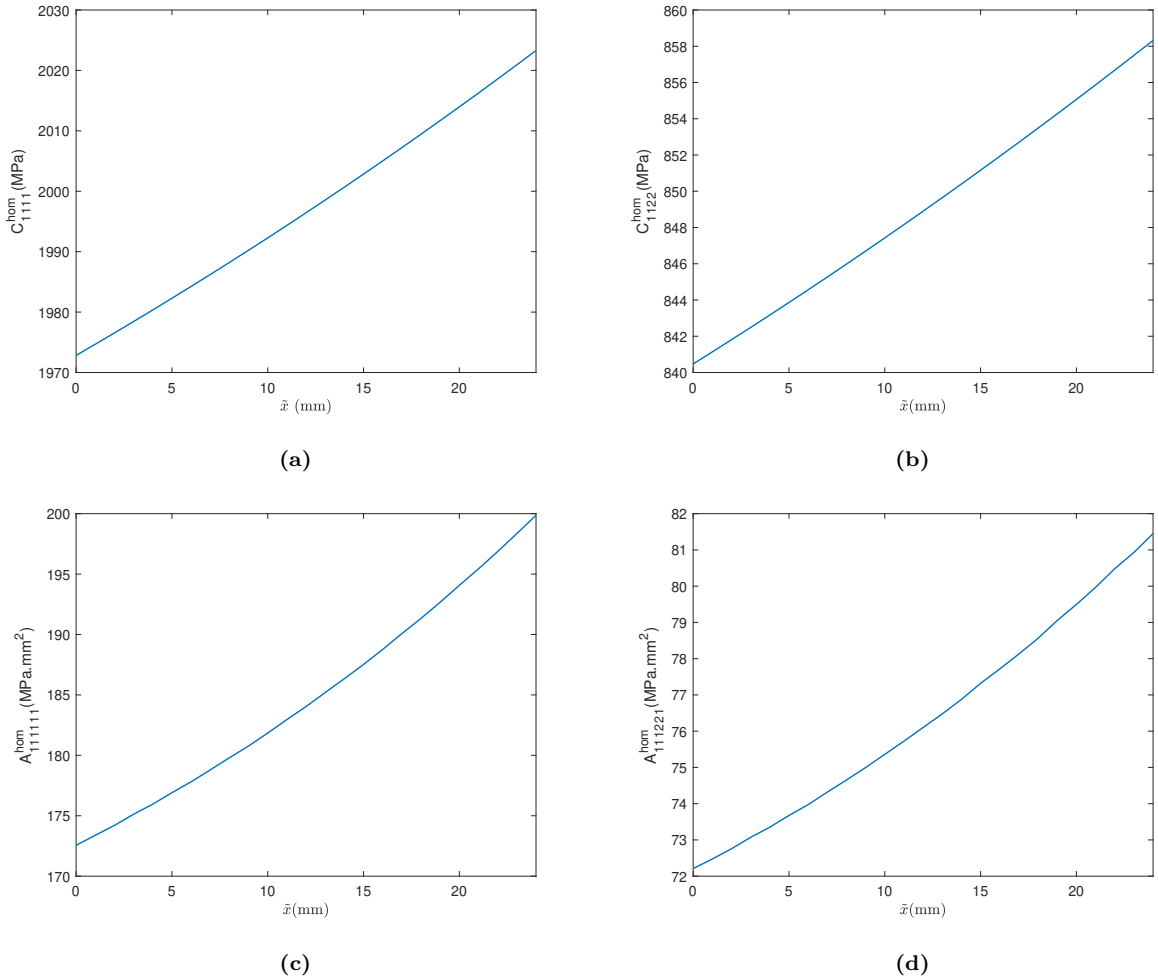

Figure 3.7 Variation of (a),(b) Cauchy moduli, and (c),(d) strain gradient moduli versus the spatial position.

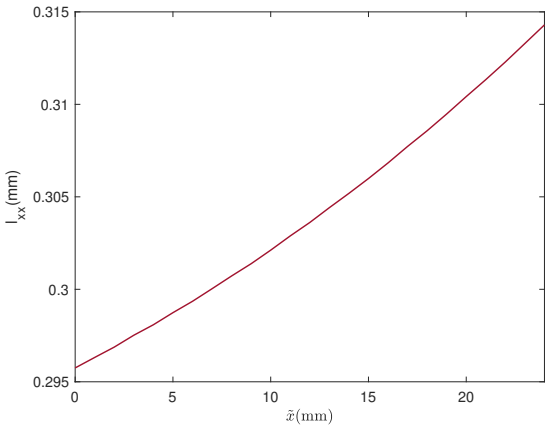

Figure 3.8 Variation of internal length l_{xx} versus spatial macro position.

To measure the importance of Cauchy and and strain gradient moduli in capturing the micrograding, the Cauchy and strain gradient energies are calculated and their percentage contributions are illustrated in Fig. 3.9 versus the spatial macro position. Fig. 3.9, shows that for UCs at position $\widetilde{x} < 290$, Cauchy

contribution is still dominant and it is capable of capturing the micrograding by $\delta \boldsymbol{C}^{\text{hom}}$. However, for UCs at position $\widetilde{x} > 290$, the contribution of strain gradient energy becomes of higher importance compared to Cauchy contribution. This reveals that at this stage Cauchy perturbation moduli is insufficient in determining the micrograding. This ensures the importance of considering strain gradient theory in accounting for microscopic variation of design through $\delta \boldsymbol{A}^{\text{hom}}$.

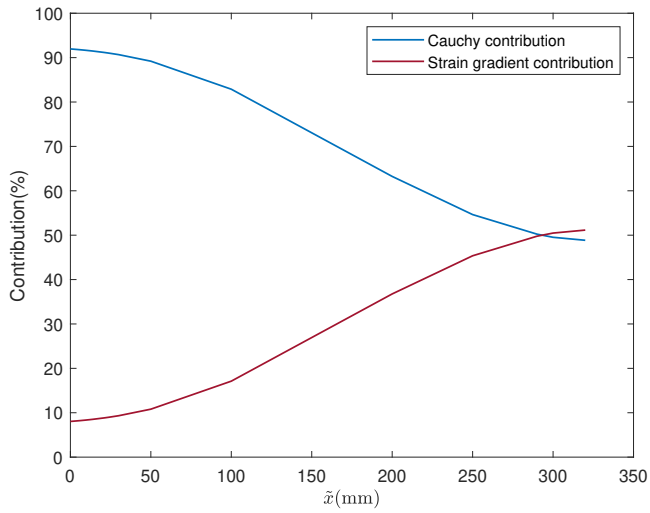

Figure 3.9 Energy contributions as a function of the macroscopic position.

The validation of the quasi-periodic homogenization is done based on the comparison of the fully resolved FE simulations and those based on the effective quasi-periodic moduli. Therefore, we consider a beam of UCs with homogenized properties and another one with heterogeneous structure that are fixed at their left boundary and subjected to a uni-axial loading (F=100N) at the right side (see Fig. 3.10). Fig. 3.11 shows the macroscopic response of both beams where the displacement in x-direction is plotted vs the force applied. The homogenized quasi-periodic model can predict the load-displacement response of a heterogeneous quasiperiodic structure with a max error of 8%.

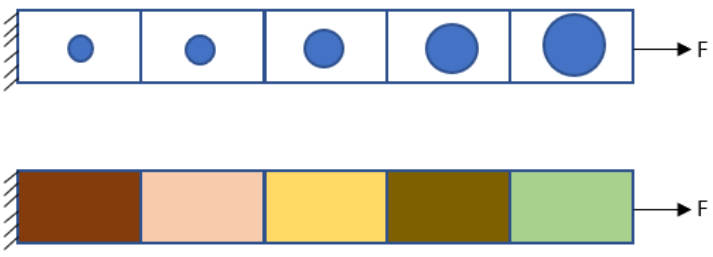

Figure 3.10 Beam with the quasi-periodic microstructure (top) and the homogenized representation (bottom).

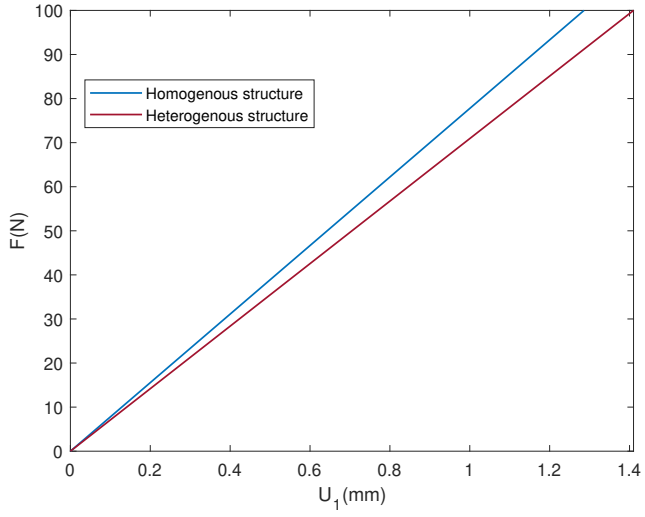

Figure 3.11 Figure showing the macroscopic response of a heterogeneous and homogeneous structure.

A post-processing scheme of the true strain gradient approach is elaborated in Appendix E, which shows, on one hand, a link between the strain $\boldsymbol{E}$ and strain gradient term $(\boldsymbol{E} \otimes \nabla_x)$ starting from macro-scale computations, and on the other hand, a dependence of the macrostress on both, strain and strain gradient. This scheme is adopted when considering the quasi-periodic macrodomain for the full-field computations. The difference in strain between the boundaries of the UC is captured by the strain gradient term $(\boldsymbol{E} \otimes \nabla_x)$ that must be taken into consideration when accounting for the UC boundary conditions. Consequently, we show in Appendix E that we will reach an enriched Cauchy medium starting from a quasi-periodic macrodomain.

3.5 Conclusion

In this chapter, we presented quasi-periodic homogenization schemes for quasi-periodic media, which do not exhibit periodicity but can be transformed into a parent periodic medium. The main results of this chapter can be summarized as follows:

- A theoretical approach of quasi-periodic homogenization is introduced, for small perturbations of the unit cell architecture according to the macro-scale, starting from the average of the microscopic energy and following the established smoothness conditions of the mapping (which means a small variation of the UC design). This enables the effective quasi-periodic moduli tensors to be linked with those of the periodic domain and the associated perturbation terms which are expressed in a volumetric format over the reference unit cell domain in a 2D context.
- A surface formulation of the quasi-periodic moduli is then derived, starting from the volumetric approach and based on the notion of shape derivative of the total potential energy stored within the unit cell, via Clapeyron's theorem allowing to link the potential energy to the internal strain energy. This approach relies on introducing a shape velocity field at the boundary of the periodic unit cell

to model the change of its design. This scheme offers comparatively to the first one a simpler way to compute the quasi-periodic moduli as it only requires the evaluation of the mechanical fields on the unit cell boundaries.

- Consideration of the strain gradient theory as to account for the design grading at the microscopic level, in context of small strains, and following the smoothness conditions. The importance of the strain gradient model appears in the considered application of inclusion-based composites as the Cauchy energy becomes insufficient to describe the impact of the variation in the internal architecture of the unit cell. This appears through the increase in the strain gradient energy contribution by a factor of 5 from the reference UC, compared to the Cauchy one.

Part II

Homogenization towards generalized continua accounting for multiphysical aspects

Chapter 4

Homogenization of piezoelectric composites and architected materials towards piezoelectric and flexoelectric effective media

Summary

In this chapter, we evaluate the effective piezoelectric properties of heterogeneous materials in the context of periodic homogenization, whereby a variational formulation is developed, articulated with the extended Hill macrohomogeneity condition. The entire set of homogenized piezoelectric moduli is obtained as the volumetric averages of the microscopic properties of the individual constituents weighted by the displacement and electric potential localization operators. To account for higher gradient effects, that may be induced by a strong contrast of properties of the composite constituents, this framework is extended to deliver a flexoelectric homogenization method investigated in the computation of the flexoelectric effective properties. A numerical algorithm is developed for the determination of the effective piezoelectric and flexoelectric moduli relying on solving the boundary value problem (BVP) by applying the macroscopic kinematic variables. The proposed homogenization is general and can be applied to composites and architected materials endowed with piezoelectric properties at the microscopic scale.

Nomenclature

$\overline{\boldsymbol{D}}$	Macroscopic electric displacement vector
$\boldsymbol{\Sigma}$	Macroscopic stress tensor
$\boldsymbol{E}$	Macroscopic strain tensor
$\boldsymbol{E_M^{elec}}$	Macroscopic electric field vector
$\in$	Medium permittivity
$\boldsymbol{\sigma}$	Microscopic stress tensor
$\boldsymbol{u}$	Microscopic displacement vector
$\boldsymbol{D}$	Microscopic electric displacement vector
$\boldsymbol{E}^{elec}$	Microscopic electric field vector
$\in_0$	Permittivity of vacuum
$\boldsymbol{P}$	Polarization vector
ϕ	Electric scalar potential
ρ_q^f	Density of free mobile charges
Ω	Volume
$\boldsymbol{f}$	Body forces vector
$\boldsymbol{t}^d$	Prescribed surface traction
$\boldsymbol{\chi}_e$	Electric susceptibility
$\boldsymbol{n}$	Normal unit vector
$\boldsymbol{\varepsilon}$	Microscopic strain tensor
$\boldsymbol{a}$	Permittivity tensor
$\boldsymbol{d}^*$	Piezoelectric tensor
$\boldsymbol{C}$	First gradient rigidity tensor
$\boldsymbol{S}$	Hyperstress tensor
$\boldsymbol{R}$	Higher order electric displacement tensor
$\boldsymbol{K}$	Strain gradient tensor
$\boldsymbol{G}_p$	Electric field gradient tensor
$\boldsymbol{I_2}, \boldsymbol{I_4}, \boldsymbol{I_6}$	Second, fourth, sixth order identity tensors
$\boldsymbol{M}^{uE}(\boldsymbol{y}), \boldsymbol{M}^{uP}(\boldsymbol{y}), \boldsymbol{M}^{uK}(\boldsymbol{y}), \boldsymbol{M}^{uG_P}(\boldsymbol{y})$	Displacement localization operators
$\boldsymbol{M}^{PE}(\boldsymbol{y}), \boldsymbol{M}^{PP}(\boldsymbol{y}), \boldsymbol{M}^{PK}(\boldsymbol{y}), \boldsymbol{M}^{PG_P}(\boldsymbol{y})$	Electric potential localization operators
$\boldsymbol{Z^{uE}}, \boldsymbol{Z^{uP}}, \boldsymbol{Z^{uK}}, \boldsymbol{Z^{uG_P}}$	Strain localization operators
$\boldsymbol{Z^{PE}}, \boldsymbol{Z^{PP}}, \boldsymbol{Z^{PK}}, \boldsymbol{Z^{PG_P}}$	Electric field localization operators

4.1 Introduction

Piezoelectricity is an electromechanical phenomenon that describes a linear coupling between the electrical polarization and mechanical strain [3, 6, 216, 217]; it was first investigated in the field of mechanics of materials by the two brothers Pierre and Jacques Curie in 1880 and it was found in various applications in engineering [218–220]. Works devoted to the computation of the effective response of piezoelectric composites rely on multiscale methods as in [102], which constitute a powerful tool for the analysis of their macroscopic behavior. Such methods can handle multifield phenomena like coupled electromechanical phenomena, providing a quantitative understanding of the impact of microscale parameters on the overall multiphysical composite response. Different homogenization methods were developed since the early seventies to determine the effective piezoelectric properties of different materials: this was achieved for laminated composites [221] and architected cellular piezoelectric metamaterials using asymptotic homogenization [222]. However, piezoelectricity possesses some limitations driving the search for richer electromechanical coupling effects.

In the recent decades (since the early sixties), a higher-order electromechanical phenomenon has received significant attention, deserving the name flexoelectricity [19, 125], which represents the linear response of electrical polarization to a mechanical strain gradient [3, 6, 216, 217] . Flexoelectricity can overcome the drawbacks of piezoelectricity. To explain it further, while piezoelectricity gives a constant electric field, flexoelectricity leads to an electric field, which is a function of position. At the molecular scale, flexoelectricity may exist in centrosymmetric materials, for example, in isotropic ones, whereas piezoelectricity requires non-centrosymmetric materials [6, 223]. In addition to that, flexoelectricity is of high importance at nanoscales where the strain gradients increase in magnitude, while piezoelectricity vanishes [224]. As the flexoelectric response is more pronounced at small scales, it was taken into account for modification of theories for nanometer-sized beams and plates, see, e.g., [225–228] and references therein. In order to improve the piezoelectric response in the literature, various flexoelectric composite materials have been proposed, see also [229, 230]. Nowadays it is already established that considering composites made of flexoelectric materials the optimized microstructure can play a crucial role for a better performance. In particular, the effective piezoelectric response could be achieved for proper microstructure, as shown by [231] and [232].

In order to improve the performance of composites and lattice materials, homogenization techniques can be applied. The availability of effective properties and their dependence on microstructure enables to optimize the microstructure to increase the required response as in [233]. Topology optimization of flexoelectric structures was discussed in [234]. As flexoelectric materials can be considered as a particular class of strain gradient materials, the homogenization schemes proposed for such material could also be useful, as in [202, 235]. Unlike piezoelectric composites, see, e.g., [102, 221, 236, 237], up to our knowledge there exist only up to now few works on the homogenization of flexoelectric composites, see [127] for the one-dimensional case. So developing a general approach for the determination of effective properties of

flexoelectric composites is of great interest.

The main objective of this chapter is to set up a homogenization method of heterogeneous piezoelectric materials towards flexoelectric effective media, which is able to deliver the entire set of piezoelectric, and flexoelectric effective properties. The proposed method relies on the variational principle (weak formulation) articulated with Hill lemma [87] extended to flexoelectricity. To the knowledge of the authors, this is the first time such a general homogenization framework is proposed.

The outline of this chapter is as follows: section 4.2 represents a first gradient homogenization towards piezoelectric medium starting from piezoelectric heterogeneous medium which is further extended to the consideration of the gradient of strain and electric fields to derive the effective flexoelectric properties in section 4.3. The algorithm for determining both piezoelectric and flexoelectric moduli is explained in section 4.4. Finally, a summary of the main thrust of the work is given in the conclusion in section 4.5.

In the context of periodic homogenization, the microstructure is identified within an irreducible representative unit cell, which by periodic translation generates the entire composite domain. In the context of composite materials Fig. 4.1, the reinforcement has higher properties in comparison to its surrounding matrix. A state of perfect adherence at the interface between both constituents is assumed in the present work, so that both the displacement and traction are continuous across the interface between reinforcement and matrix.

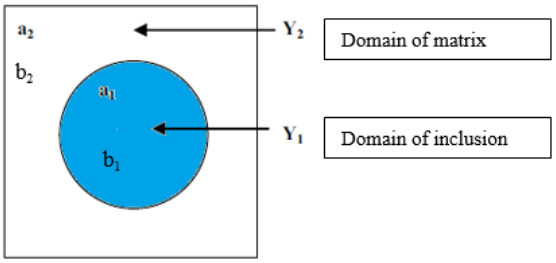

Figure 4.1 Two elastic materials with rigidity and piezoelectric coefficients a_i, b_i (the index i stands for the constituent within the unit cell)

Here and in the sequel, we distinguish the microscopic scale (at the scale of individual phases) within the unit cell, denoted by the spatial position $\boldsymbol{y}$, from the macroscopic scale of the homogenized continuum (thus replacing the initially heterogeneous composite by a homogeneous substitution media with effective piezoelectric or flexoelectric properties), for which we employ the spatial position vector $\boldsymbol{x}$.

A few words regarding notations are in order. Vectors and higher-order tensors are denoted with boldface symbols. The bracket $\langle f(\boldsymbol{y})\rangle_Y := \frac{1}{|Y|}\int\limits_Y f(\boldsymbol{y})dV_y$ denotes the volume average of any quantity, here the scalar-valued function $f(\boldsymbol{y})$ over the domain of a reference lattice unit cell Y, with infinitesimal integration volume dV_y. The partial derivative of a scalar function $f\,(x)$ is denoted alternatively $\partial_x f$or $\frac{\partial f}{\partial x}$. The gradient and divergence of a second order tensor $\boldsymbol{A}$ are successively denoted by the quantities $\boldsymbol{A}\otimes\nabla_x$ and $\boldsymbol{A}.\nabla_x$. The transpose of the second order tensor is denoted with a superscript 'T', so for instance $\boldsymbol{A}^T$.

4.2 First gradient piezoelectric homogenization

In order to set the stage, we recall the strong form of the governing equations at the microlevel of the composite constituents [238] with a few subsequent simplifications since we primarily aim to focus on the effects of electric fields – discarding magnetic phenomena in this chapter.

The primal variables are the displacement and polarization vectors $\boldsymbol{u}(\boldsymbol{x},t)$, $\boldsymbol{P}(\boldsymbol{x},t)$, which enter as arguments of the electromechanical energy density. Note that polarization or electric displacement $\boldsymbol{D}(\boldsymbol{x},t)$ can alternatively be chosen as DOF's (shortcut for degrees of freedom) since they are linearly related, viz. it holds the relation

$$\boldsymbol{D} = \in_0 \boldsymbol{E}^{elec} + \boldsymbol{P} \tag{4.1}$$

with $\in_0$ the permittivity of vacuum, and in which the electric field $\boldsymbol{E}^{elec}$ can be expressed via the electric scalar potential ϕ as follows

$$\boldsymbol{E}^{elec} = -\phi\nabla \tag{4.2}$$

The last relation automatically guarantees the satisfaction of Maxwell equation

$$\nabla \times \boldsymbol{E}^{elec} = \boldsymbol{0} \tag{4.3}$$

The electric displacement in non-deformed media relates to the electric field and polarization as

$$\boldsymbol{D} = \in_0 \boldsymbol{E}^{elec} + \boldsymbol{P} \equiv \in_0 (\boldsymbol{I_2} + \boldsymbol{\chi}_e) . \boldsymbol{E}^{elec} = \boldsymbol{\in} . \boldsymbol{E}^{elec} \tag{4.4}$$

with $\in$ the medium permittivity, $\boldsymbol{\chi}_e$ is the electric susceptibility and $\boldsymbol{I_2}$ the second order identity tensor.

The main steps in the methodology used for the first gradient homogenization can be summarized in Fig. 4.2.

Since we will focus on statics in this chapter, rate derivatives can be neglected, which entails a decoupling of the electromagnetic problem into pure electrical and pure magnetic problems. We consider only the coupling between electric fields with mechanics and ignore magnetic fields; in this case, the local set of piezoelectric balance equations resumes to

$$\begin{aligned}
&\boldsymbol{\sigma}.\nabla_y + \boldsymbol{f} = \boldsymbol{0} \\
&\boldsymbol{\varepsilon} := \boldsymbol{u} \otimes^s \nabla_y \\
&\boldsymbol{\sigma}.\boldsymbol{n} = \boldsymbol{t}^d \text{ on } S_t \\
&\boldsymbol{D}.\nabla_y = \rho_q^f \\
&\boldsymbol{E}^{elec} = -\phi\nabla_y \\
&\boldsymbol{D}.\boldsymbol{n} = D^d \text{ on } S_D
\end{aligned} \tag{4.5}$$

wherein $\boldsymbol{\sigma}$ is the Cauchy stress, and $\boldsymbol{D}$ is the electric displacement.The microscopic strain $\boldsymbol{\varepsilon}$ is defined as the symmetrical part of the gradient of micro displacement field. Note that by virtue of the mechanical-electric analogy, the electric scalar potential ϕ is the analog of the displacement in mechanics, vector $\boldsymbol{u}$

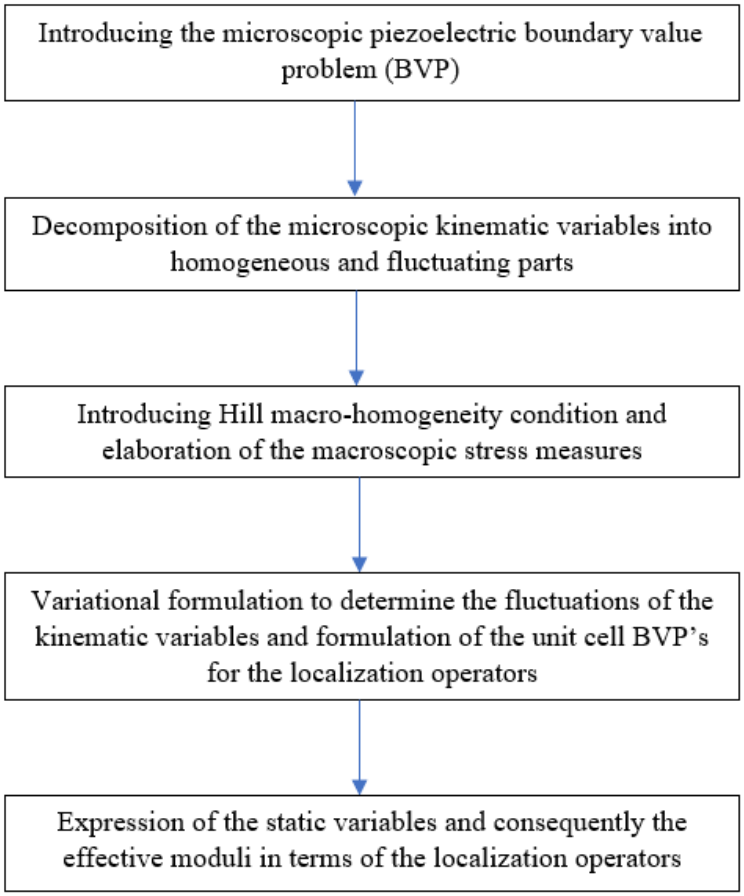

Figure 4.2 Schematic diagram of the main steps in the piezoelectric homogenization methodology

in $(Eq.\ 4.5)_2$, ensuring satisfaction of kinematic compatibility condition. The force-like variables $(\boldsymbol{\sigma}, \boldsymbol{D})$ satisfy natural boundary conditions written there above, with $\boldsymbol{n}$ the unit exterior normal to the domain, and $\left(\boldsymbol{t}^d, D^d\right)$ are input data on the parts S_t, S_D of the domain boundary respectively. The flux like variables $(\boldsymbol{u}, \phi)$ satisfy natural essential boundary conditions with prescribed values on the complementary part of the domain boundary; these values are selected to be nil here and, in the sequel, since they do not contribute to the effective piezoelectric moduli that will be computed. We have considered as a matter of simplification nil values of the traction and electric displacement in the natural boundary conditions written in Eq. 4.5. The microscopic variables, namely the displacement and electric potential, are decomposed additively into a homogeneous part and a periodic fluctuating part:

$$\begin{aligned} \boldsymbol{u}(\boldsymbol{y}) &= \boldsymbol{u}^{\boldsymbol{hom}}(\boldsymbol{y};\boldsymbol{x}) + \tilde{\boldsymbol{u}}(\boldsymbol{y}) \\ \phi(\boldsymbol{y}) &= \phi^{\boldsymbol{hom}}(\boldsymbol{y};\boldsymbol{x}) + \tilde{\phi}(\boldsymbol{y}) \end{aligned} \tag{4.6}$$

wherein the vectors $\boldsymbol{u}^{\mathrm{hom}}(\boldsymbol{y};\boldsymbol{x})$,$\phi^{\mathrm{hom}}(\boldsymbol{y};\boldsymbol{x})$ are the homogeneous parts of the microscopic displacement and electric potential, respectively, corresponding to a heterogeneous medium that would behave exactly as a homogeneous medium. Note that these fields depend on the microscopic position and on the macroscopic position appearing as a parameter (it is indicated with a semicolon in previous expressions), as their subsequent expressions will reveal. The fluctuations $\tilde{\boldsymbol{u}}(\boldsymbol{y})$, and $\tilde{\phi}(\boldsymbol{y}) \in H^1_{per}(Y)$ (the Sobolev

space of Y-periodic functions) in previous decomposition account for the deviation of the postulated effective homogeneous medium from the initially heterogeneous medium. Homogenization makes an upscaling of governing equations from the microscale to the macroscale, so that the resulting homogenized boundary value problem only involves macroscopic variables depending on the sole macroscopic position $\boldsymbol{x}$. Accordingly, the microscopic strain and electric field tensors can be decomposed into their homogeneous and fluctuating parts as:

$$\begin{aligned}
&\boldsymbol{\varepsilon}(\boldsymbol{y}) = \boldsymbol{\varepsilon}^{\hom}(\boldsymbol{x}) + \tilde{\boldsymbol{\varepsilon}}(\boldsymbol{y}),\\
&\boldsymbol{\varepsilon}^{\hom}(\boldsymbol{x}) := \boldsymbol{u}^{\hom}(\boldsymbol{y}) \otimes^{s} \nabla_y = \boldsymbol{E}\\
&\boldsymbol{E}^{\boldsymbol{elec}}(\boldsymbol{y}) = -\phi \nabla_y = \boldsymbol{E}^{\boldsymbol{elec},\hom}(\boldsymbol{x}) + \tilde{\boldsymbol{E}}^{\boldsymbol{elec}}(\boldsymbol{y}),\\
&\boldsymbol{E}^{\boldsymbol{elec},\hom}(\boldsymbol{x}) := \boldsymbol{E}_{\boldsymbol{M}}^{\boldsymbol{elec}}
\end{aligned} \tag{4.7}$$

wherein $\boldsymbol{E}$, and $\boldsymbol{E}_{\boldsymbol{M}}^{\boldsymbol{elec}}$ are the macroscopic strain, and electric field respectively. The homogenization here doesn't account for any higher order gradients so the homogeneous parts will be as shown in Eq. 4.7; for higher order homogenization, the homogeneous parts will be elaborated later in the next section. In the sequel, the letter 's' over $\otimes$, that indicates the symmetrical gradient of displacement, will be omitted for simplification.

The constitutive law for piezoelectric materials has the form:

$$\left| \begin{aligned}
&\boldsymbol{\sigma} = \boldsymbol{C} : \varepsilon - \boldsymbol{e}^{T}.\boldsymbol{E}^{elec}\\
&\boldsymbol{D} = \boldsymbol{e} : \varepsilon + \boldsymbol{a}.\boldsymbol{E}^{elec}
\end{aligned} \right. \tag{4.8}$$

wherein $\boldsymbol{a}$ is the tensor of dielectric (permittivity) coefficients, $\boldsymbol{C}$ is the tensor of rigidity coefficients, and $\boldsymbol{e}$ is the tensor of piezoelectric coefficients at the microscopic level.

Multiplication of the mechanical and electric balance laws, $(Eq.\ 4.5)_1$ and $(Eq.\ 4.5)_4$ respectively by suitable test functions, integration over the domain, integration by part with proper account of the natural boundary conditions leads to the piezoelectric enthalpy density at the micro-level written in terms of the strain tensor $\boldsymbol{\varepsilon}$ and electric field $\boldsymbol{E}^{\boldsymbol{elec}}$ defining the microscopic degrees of freedom (DOF in short):

$$w_{\mu}(\boldsymbol{\varepsilon}, \boldsymbol{E}^{\boldsymbol{elec}}) = \frac{1}{2}\left(\sigma_{ij}\varepsilon_{ij} - \mathrm{D}_k E_k^{elec}\right) \tag{4.9}$$

Hill macro-homogeneity condition for piezoelectric media states that the volumetric average of the microscopic enthalpy (or strain energy) is equal to the macroscopic enthalpy (or strain energy):

$$\left\langle w_{\mu}(\boldsymbol{\varepsilon}, \boldsymbol{E}^{\boldsymbol{elec}}) \right\rangle_{Y} = W_M\left(\boldsymbol{E}, \boldsymbol{E}_{\boldsymbol{M}}^{\boldsymbol{elec}}\right) = \frac{1}{2}\left(\boldsymbol{\Sigma} : \boldsymbol{E} - \boldsymbol{E}_{\boldsymbol{M}}^{\boldsymbol{elec}}.\overline{\boldsymbol{D}}\right) \tag{4.10}$$

wherein $\boldsymbol{\Sigma}$, and $\overline{\boldsymbol{D}}$ are the stress, and electric displacement at the macroscopic scale respectively. The bracket $\langle \bullet \rangle$ denotes the volume integration over the unit cell, normalized by the unit cell volume. The subscript in $W_M\left(\boldsymbol{E}, \boldsymbol{E}_{\boldsymbol{M}}^{\boldsymbol{elec}}\right)$ means macroscopic.

An extended minimization principle of the macroscopic energy over all periodic fluctuations holds in the absence of body forces:

$$W_M\left(\boldsymbol{E},\boldsymbol{E_M^{elec}}\right)=\underset{\tilde{\boldsymbol{u}},\tilde{\phi}\in H^1_{per}(Y)}{Min}\frac{1}{2}\int_Y\begin{Bmatrix}\boldsymbol{C}\left(\boldsymbol{y}\right):\left(\boldsymbol{E}+\tilde{\boldsymbol{u}}(\boldsymbol{y})\otimes\nabla_y\right):\left(\boldsymbol{E}+\tilde{\boldsymbol{u}}(\boldsymbol{y})\otimes\nabla_y\right)\\-\boldsymbol{e}^T(\boldsymbol{y}).\left(\boldsymbol{E_M^{elec}}-\tilde{\phi}\nabla_y\right):\left(\boldsymbol{E}+\tilde{\boldsymbol{u}}(\boldsymbol{y})\otimes\nabla_y\right)\\-\boldsymbol{e}(\boldsymbol{y}):\left(\boldsymbol{E}+\tilde{\boldsymbol{u}}(\boldsymbol{y})\otimes\nabla_y\right).\left(\boldsymbol{E_M^{elec}}-\tilde{\phi}\nabla_y\right)\\-\boldsymbol{a}(\boldsymbol{y}).\left(\boldsymbol{E_M^{elec}}-\tilde{\phi}\nabla_y\right).\left(\boldsymbol{E_M^{elec}}-\tilde{\phi}\nabla_y\right)\end{Bmatrix}dV_y \tag{4.11}$$

The stationarity condition of the previous functional delivers, as a necessary condition, the following boundary value problem (BVP in short) satisfied by the optimal fluctuation associated to the real displacement field and electric potential (in the absence of body forces for mechanical field and free charges for electric field); it describes the self-equilibrium of the unit cell:

$$\begin{vmatrix}-div_y\left\{C\left(\boldsymbol{y}\right):\left(\boldsymbol{E}+\tilde{\boldsymbol{u}}\otimes\nabla_y\right)-\boldsymbol{e}^T\left(\boldsymbol{y}\right).\left(\boldsymbol{E_M^{elec}}-\tilde{\phi}\nabla_y\right)\right\}=\boldsymbol{0}\\div_y\left\{\boldsymbol{a}\left(\boldsymbol{y}\right).\left(\boldsymbol{E_M^{elec}}-\tilde{\phi}\nabla_y\right)+\boldsymbol{e}\left(\boldsymbol{y}\right):\left(\boldsymbol{E}+\tilde{\boldsymbol{u}}\otimes\nabla_y\right)\right\}=\boldsymbol{0}\\\tilde{\boldsymbol{u}}(\boldsymbol{y}),\tilde{\phi}\text{ Y-periodic}\end{vmatrix} \tag{4.12}$$

Since the previous BVP is linear in the loading $\left(\boldsymbol{E},\boldsymbol{E_M^{elec}}\right)$ at the macroscale, the fluctuations can be written as:

$$\begin{aligned}\tilde{\boldsymbol{u}}\left(\boldsymbol{y}\right)&=\boldsymbol{M^{uE}}\left(\boldsymbol{y}\right):\boldsymbol{E}\left(\boldsymbol{x}\right)+\boldsymbol{M^{uP}}\left(\boldsymbol{y}\right).\boldsymbol{E_M^{elec}}\left(\boldsymbol{x}\right)\\\tilde{\phi}\left(\boldsymbol{y}\right)&=\boldsymbol{M^{PE}}\left(\boldsymbol{y}\right):\boldsymbol{E}\left(\boldsymbol{x}\right)+\boldsymbol{M^{PP}}\left(\boldsymbol{y}\right).\boldsymbol{E_M^{elec}}\left(\boldsymbol{x}\right)\end{aligned} \tag{4.13}$$

wherein tensors $\boldsymbol{M}^{uE}\left(\boldsymbol{y}\right),\boldsymbol{M}^{uP}\left(\boldsymbol{y}\right)$ are the displacement localization operators, and $\boldsymbol{M}^{PE}\left(\boldsymbol{y}\right),\boldsymbol{M}^{PP}\left(\boldsymbol{y}\right)$ the electric potential localization operators. The localization tensors relate the microscopic DOF's to their macroscopic counterpart. They are dependent on the microscopic position variable within the unit cell Y and are Y-periodic. Inserting these expressions into the previous BVP leads to the unit cell BVP for the first gradient piezoelectric homogenization. The previous macroscopic energy is a function of the fluctuations, written in compact form as a Lagrangian functional of the displacement and electric potential fluctuations as:

$$\begin{aligned}L\left[\tilde{\boldsymbol{u}},\tilde{\phi}\right]&:=\frac{1}{2}\int_Y\left\{\boldsymbol{C}\left(\boldsymbol{y}\right):\boldsymbol{\varepsilon}:\boldsymbol{\varepsilon}-\boldsymbol{e}^T.\boldsymbol{E^{elec}}:\boldsymbol{\varepsilon}-\boldsymbol{a}.\boldsymbol{E^{elec}}.\boldsymbol{E^{elec}}-\boldsymbol{e}:\boldsymbol{\varepsilon}.\boldsymbol{E^{elec}}\right\}dV_y\\&=\frac{1}{2}\int_Y\begin{Bmatrix}\left(\boldsymbol{E}+\tilde{\boldsymbol{u}}(\boldsymbol{y})\otimes\nabla_y\right):C\left(\boldsymbol{y}\right):\left(\boldsymbol{E}+\tilde{\boldsymbol{u}}(\boldsymbol{y})\otimes\nabla_y\right)\\-\boldsymbol{a}.\left(\boldsymbol{E_M^{elec}}-\tilde{\phi}\nabla_y\right).\left(\boldsymbol{E_M^{elec}}-\tilde{\phi}\nabla_y\right)\\-\boldsymbol{e}^T.\left(\boldsymbol{E_M^{elec}}-\tilde{\phi}\nabla_y\right):\left(\boldsymbol{E}+\tilde{\boldsymbol{u}}(\boldsymbol{y})\otimes\nabla_y\right)\\-\boldsymbol{e}:\left(\boldsymbol{E}+\tilde{\boldsymbol{u}}(\boldsymbol{y})\otimes\nabla_y\right).\left(\boldsymbol{E_M^{elec}}-\tilde{\phi}\nabla_y\right).\end{Bmatrix}dV_y\end{aligned} \tag{4.14}$$

Introducing the fluctuations as a function of the localization operators Eq. 4.13 into Eq. 4.14 leads to:

$$L\left[\tilde{\boldsymbol{u}},\tilde{\phi}\right] := \frac{1}{2}\int_Y \left\{ \begin{array}{l} \left(\boldsymbol{E}+\boldsymbol{M}^{uE}\left(\boldsymbol{y}\right)\otimes\nabla_y : \boldsymbol{E}\left(\boldsymbol{x}\right)+\boldsymbol{M}^{uP}\left(\boldsymbol{y}\right)\otimes\nabla_y.\boldsymbol{E}_{\boldsymbol{M}}^{\boldsymbol{elec}}\left(\boldsymbol{x}\right)\right) : \boldsymbol{C}\left(\boldsymbol{y}\right) \\ : \left(\boldsymbol{E}+\boldsymbol{M}^{uE}\left(\boldsymbol{y}\right)\otimes\nabla_y : \boldsymbol{E}\left(\boldsymbol{x}\right)+\boldsymbol{M}^{uP}\left(\boldsymbol{y}\right)\otimes\nabla_y.\boldsymbol{E}_{\boldsymbol{M}}^{\boldsymbol{elec}}\left(\boldsymbol{x}\right)\right) \\ -\left(\boldsymbol{E}_{\boldsymbol{M}}^{\boldsymbol{elec}}-\boldsymbol{M}^{PE}\left(\boldsymbol{y}\right)\otimes\nabla_y : \boldsymbol{E}\left(\boldsymbol{x}\right)-\boldsymbol{M}^{PP}\left(\boldsymbol{y}\right)\otimes\nabla_y.\boldsymbol{E}_{\boldsymbol{M}}^{\boldsymbol{elec}}\left(\boldsymbol{x}\right)\right).\boldsymbol{a} \\ .\left(\boldsymbol{E}_{\boldsymbol{M}}^{\boldsymbol{elec}}-\boldsymbol{M}^{PE}\left(\boldsymbol{y}\right)\otimes\nabla_y : \boldsymbol{E}\left(\boldsymbol{x}\right)-\boldsymbol{M}^{PP}\left(\boldsymbol{y}\right)\otimes\nabla_y.\boldsymbol{E}_{\boldsymbol{M}}^{\boldsymbol{elec}}\left(\boldsymbol{x}\right)\right) \\ -\boldsymbol{e}^T.\left(\boldsymbol{E}_{\boldsymbol{M}}^{\boldsymbol{elec}}-\boldsymbol{M}^{PE}\left(\boldsymbol{y}\right)\otimes\nabla_y : \boldsymbol{E}\left(\boldsymbol{x}\right)-\boldsymbol{M}^{PP}\left(\boldsymbol{y}\right)\otimes\nabla_y.\boldsymbol{E}_{\boldsymbol{M}}^{\boldsymbol{elec}}\left(\boldsymbol{x}\right)\right) \\ : \left(\boldsymbol{E}+\boldsymbol{M}^{uE}\left(\boldsymbol{y}\right)\otimes\nabla_y : \boldsymbol{E}\left(\boldsymbol{x}\right)+\boldsymbol{M}^{uP}\left(\boldsymbol{y}\right)\otimes\nabla_y.\boldsymbol{E}_{\boldsymbol{M}}^{\boldsymbol{elec}}\left(\boldsymbol{x}\right)\right) \\ -\boldsymbol{e} : \left(\boldsymbol{E}+\boldsymbol{M}^{uE}\left(\boldsymbol{y}\right)\otimes\nabla_y : \boldsymbol{E}\left(\boldsymbol{x}\right)+\boldsymbol{M}^{uP}\left(\boldsymbol{y}\right)\otimes\nabla_y.\boldsymbol{E}_{\boldsymbol{M}}^{\boldsymbol{elec}}\left(\boldsymbol{x}\right)\right) \\ .\left(\boldsymbol{E}_{\boldsymbol{M}}^{\boldsymbol{elec}}-\boldsymbol{M}^{PE}\left(\boldsymbol{y}\right)\otimes\nabla_y : \boldsymbol{E}\left(\boldsymbol{x}\right)-\boldsymbol{M}^{PP}\left(\boldsymbol{y}\right)\otimes\nabla_y.\boldsymbol{E}_{\boldsymbol{M}}^{\boldsymbol{elec}}\left(\boldsymbol{x}\right)\right) \end{array} \right\} dV_y \tag{4.15}$$

The effective piezoelectric constitutive law is then obtained by applying partial derivatives with respect to $\boldsymbol{E}$ and $\boldsymbol{E}_{\boldsymbol{M}}^{\boldsymbol{elec}}$ of the macroscopic energy, which is minimized. Since the unit cell is bounded, partial derivative and integration can be switched, thus it holds using Hill extended macro-homogeneity condition the following relations:

$$\begin{aligned} \boldsymbol{\Sigma} &= \frac{\partial W_M\left(\boldsymbol{E},\boldsymbol{E}_{\boldsymbol{M}}^{\boldsymbol{elec}}\right)}{\partial \boldsymbol{E}} \equiv \frac{\partial}{\partial \boldsymbol{E}}\left(\underset{\tilde{\boldsymbol{u}},\tilde{\phi}\in H^1_{per}(Y)}{Min} L\left[\tilde{\boldsymbol{u}},\tilde{\phi}\right]\right) \equiv \underset{\tilde{\boldsymbol{u}},\tilde{\phi}\in H^1_{per}(Y)}{Min} \frac{\partial L\left[\tilde{\boldsymbol{u}},\tilde{\phi}\right]}{\partial \boldsymbol{E}}, \\ \overline{\boldsymbol{D}} &= \frac{\partial W_M\left(\boldsymbol{E},\boldsymbol{E}_{\boldsymbol{M}}^{\boldsymbol{elec}}\right)}{\partial \boldsymbol{E}_{\boldsymbol{M}}^{\boldsymbol{elec}}} \equiv \frac{\partial}{\partial \boldsymbol{E}_M^{elec}}\left(\underset{\tilde{\boldsymbol{u}},\tilde{\phi}\in H^1_{per}(Y)}{Min} L\left[\tilde{\boldsymbol{u}},\tilde{\phi}\right]\right) \equiv \underset{\tilde{\boldsymbol{u}},\tilde{\phi}\in H^1_{per}(Y)}{Min} \frac{\partial L\left[\tilde{\boldsymbol{u}},\tilde{\phi}\right]}{\partial \boldsymbol{E}_{\boldsymbol{M}}^{\boldsymbol{elec}}} \end{aligned} \tag{4.16}$$

Inserting the fluctuations as a function of the localization operators (in Eq. 4.13) leads to the expressions of the effective driving forces for the piezoelectric effect:

$$\boldsymbol{\Sigma} = \frac{1}{2}\int_Y \left\{ \begin{array}{l} \left(\boldsymbol{E}+\boldsymbol{M}^{uE}\otimes\nabla_y : \boldsymbol{E}+\boldsymbol{M}^{uP}\otimes\nabla_y.\boldsymbol{E}_{\boldsymbol{M}}^{\boldsymbol{elec}}\right) : \boldsymbol{C} : \left(\boldsymbol{I}_4+\boldsymbol{M}^{uE}\otimes\nabla_y\right) \\ +\left(\boldsymbol{I}_4+\boldsymbol{M}^{uE}\otimes\nabla_y\right) : \boldsymbol{C} : \left(\boldsymbol{E}+\boldsymbol{M}^{uE}\otimes\nabla_y : \boldsymbol{E}+\boldsymbol{M}^{uP}\otimes\nabla_y.\boldsymbol{E}_{\boldsymbol{M}}^{\boldsymbol{elec}}\right) \\ -\left(\boldsymbol{E}_{\boldsymbol{M}}^{\boldsymbol{elec}}-\boldsymbol{M}^{PE}\left(\boldsymbol{y}\right)\otimes\nabla_y : \boldsymbol{E}-\boldsymbol{M}^{PP}\otimes\nabla_y.\boldsymbol{E}_{\boldsymbol{M}}^{\boldsymbol{elec}}\right).\boldsymbol{a}.\left(-\boldsymbol{M}^{PE}\left(\boldsymbol{y}\right)\otimes\nabla_y\right) \\ -\left(-\boldsymbol{M}^{PE}\left(\boldsymbol{y}\right)\otimes\nabla_y\right).\boldsymbol{a}.\left(\boldsymbol{E}_{\boldsymbol{M}}^{\boldsymbol{elec}}-\boldsymbol{M}^{PE}\otimes\nabla_y : \boldsymbol{E}-\boldsymbol{M}^{PP}\otimes\nabla_y.\boldsymbol{E}_{\boldsymbol{M}}^{\boldsymbol{elec}}\right) \\ -\boldsymbol{e}^T.\left(\boldsymbol{E}_{\boldsymbol{M}}^{\boldsymbol{elec}}-\boldsymbol{M}^{PE}\otimes\nabla_y : \boldsymbol{E}-\boldsymbol{M}^{PP}\otimes\nabla_y.\boldsymbol{E}_{\boldsymbol{M}}^{\boldsymbol{elec}}\right) : \left(\boldsymbol{I}_4+\boldsymbol{M}^{uE}\otimes\nabla_y\right) \\ -\boldsymbol{e}^T.\left(-\boldsymbol{M}^{PE}\otimes\nabla_y\right) : \left(\boldsymbol{E}+\boldsymbol{M}^{uE}\otimes\nabla_y : \boldsymbol{E}+\boldsymbol{M}^{uP}\otimes\nabla_y.\boldsymbol{E}_{\boldsymbol{M}}^{\boldsymbol{elec}}\right) \\ -\boldsymbol{e} : \left(\boldsymbol{E}+\boldsymbol{M}^{uE}\otimes\nabla_y : \boldsymbol{E}+\boldsymbol{M}^{uP}\otimes\nabla_y.\boldsymbol{E}_{\boldsymbol{M}}^{\boldsymbol{elec}}\right).\left(-\boldsymbol{M}^{PE}\otimes\nabla_y\right) \\ -\boldsymbol{e} : \left(\boldsymbol{I}_4+\boldsymbol{M}^{uE}\otimes\nabla_y\right).\left(\boldsymbol{E}_{\boldsymbol{M}}^{\boldsymbol{elec}}-\boldsymbol{M}^{PE}\otimes\nabla_y : \boldsymbol{E}-\boldsymbol{M}^{PP}\otimes\nabla_y.\boldsymbol{E}_{\boldsymbol{M}}^{\boldsymbol{elec}}\right) \end{array} \right\} dV_y \tag{4.17}$$

$$\overline{\boldsymbol{D}} = \frac{1}{2}\int_{Y} \left\{ \begin{array}{l} \left(\boldsymbol{M}^{uP} \otimes \nabla_y\right) : \boldsymbol{C} : \left(\boldsymbol{E} + \boldsymbol{M}^{uE} \otimes \nabla_y : \boldsymbol{E} + \boldsymbol{M}^{uP} \otimes \nabla_y . \boldsymbol{E}_{\boldsymbol{M}}^{\boldsymbol{elec}}\right) \\ + \left(\boldsymbol{E} + \boldsymbol{M}^{uE} \otimes \nabla_y : \boldsymbol{E} + \boldsymbol{M}^{uP} \otimes \nabla_y . \boldsymbol{E}_{\boldsymbol{M}}^{\boldsymbol{elec}}\right) : \boldsymbol{C} : \left(\boldsymbol{M}^{uP} \otimes \nabla_y\right) \\ - \left(\boldsymbol{I}_2 - \boldsymbol{M}^{PP} \otimes \nabla_y\right) . \boldsymbol{a} . \left(\boldsymbol{E}_{\boldsymbol{M}}^{\boldsymbol{elec}} - \boldsymbol{M}^{PE} \otimes \nabla_y : \boldsymbol{E} - \boldsymbol{M}^{PP} \otimes \nabla_y . \boldsymbol{E}_{\boldsymbol{M}}^{\boldsymbol{elec}}\right) \\ - \left(\boldsymbol{E}_{\boldsymbol{M}}^{\boldsymbol{elec}} - \boldsymbol{M}^{PE} \otimes \nabla_y : \boldsymbol{E} - \boldsymbol{M}^{PP} \otimes \nabla_y . \boldsymbol{E}_{\boldsymbol{M}}^{\boldsymbol{elec}}\right) . \boldsymbol{a} . \left(\boldsymbol{I}_2 - \boldsymbol{M}^{PP} \otimes \nabla_y\right) \\ -\boldsymbol{e}^T . \left(\boldsymbol{E}_{\boldsymbol{M}}^{\boldsymbol{elec}} - \boldsymbol{M}^{PE} \otimes \nabla_y : \boldsymbol{E} - \boldsymbol{M}^{PP} \otimes \nabla_y . \boldsymbol{E}_{\boldsymbol{M}}^{\boldsymbol{elec}}\right) : \left(\boldsymbol{M}^{uP} \otimes \nabla_y\right) \\ -\boldsymbol{e}^T . \left(\boldsymbol{I}_2 - \boldsymbol{M}^{PP} \otimes \nabla_y\right) : \left(\boldsymbol{E} + \boldsymbol{M}^{uE} \otimes \nabla_y : \boldsymbol{E} + \boldsymbol{M}^{uP} \otimes \nabla_y . \boldsymbol{E}_{\boldsymbol{M}}^{\boldsymbol{elec}}\right) \\ -\boldsymbol{e} : \left(\boldsymbol{E} + \boldsymbol{M}^{uE} \otimes \nabla_y : \boldsymbol{E} + \boldsymbol{M}^{uP} \otimes \nabla_y . \boldsymbol{E}_{\boldsymbol{M}}^{\boldsymbol{elec}}\right) . \left(\boldsymbol{I}_2 - \boldsymbol{M}^{PP} \otimes \nabla_y\right) \\ -\boldsymbol{e} : \left(\boldsymbol{M}^{uP} \otimes \nabla_y\right) . \left(\boldsymbol{E}_{\boldsymbol{M}}^{\boldsymbol{elec}} - \boldsymbol{M}^{PE} \otimes \nabla_y : \boldsymbol{E} - \boldsymbol{M}^{PP} \otimes \nabla_y . \boldsymbol{E}_{\boldsymbol{M}}^{\boldsymbol{elec}}\right) \end{array} \right\} dV_y \tag{4.18}$$

wherein $\boldsymbol{I}_4$ is the fourth order identity tensor. In the above equations Eq. 4.17 and Eq. 4.18, the factorization of the macroscopic degrees of freedom $\left(\boldsymbol{E}, \boldsymbol{E}_{\boldsymbol{M}}^{\boldsymbol{elec}}\right)$ leads to the expressions of stress and electric field versus $\left(\boldsymbol{E}, \boldsymbol{E}_{\boldsymbol{M}}^{\boldsymbol{elec}}\right)$, as shown in Eq. F.1- Eq. F.2 in Appendix F.

Previous expressions highlight the tensors of effective piezoelectric properties given by:

$$\left| \begin{array}{l} \boldsymbol{\Sigma} = \boldsymbol{C}^{\hom} : \boldsymbol{E} - \boldsymbol{e}^{T,\boldsymbol{hom}} . \boldsymbol{E}_{\boldsymbol{M}}^{\boldsymbol{elec}} \\ \overline{\boldsymbol{D}} = \boldsymbol{e}^{\boldsymbol{hom}} : \boldsymbol{E} + \boldsymbol{a}^{\hom} . \boldsymbol{E}_{\boldsymbol{M}}^{\boldsymbol{elec}} \end{array} \right. \tag{4.19}$$

wherein $\boldsymbol{C}^{\hom}$, $\boldsymbol{e}^{\hom}$, and $\boldsymbol{a}^{\hom}$ are the effective rigidity, piezoelectric and permittivity matrices for the homogenized medium given in Eq. F.3 of Appendix F .

An alternative more compact form of the effective piezoelectric constitutive law can be formulated based on the strain localization operators $\left(\boldsymbol{Z}^{\boldsymbol{uE}}, \boldsymbol{Z}^{\boldsymbol{uP}}\right)$ and electric field localization operators $\left(\boldsymbol{Z}^{\boldsymbol{PE}}, \boldsymbol{Z}^{\boldsymbol{PP}}\right)$, elaborated in Appendix F(Eq. F.4).

$$\begin{aligned} \boldsymbol{Z}^{uE}(\boldsymbol{y}) &= \boldsymbol{I}_4 + \boldsymbol{M}^{uE} \otimes \nabla_y \\ \boldsymbol{Z}^{uP}(\boldsymbol{y}) &= \boldsymbol{M}^{uP} \otimes \nabla_y \\ \boldsymbol{Z}^{\boldsymbol{PE}}(y) &= -\boldsymbol{M}^{PE}(\boldsymbol{y}) \otimes \nabla_y \\ \boldsymbol{Z}^{\boldsymbol{PP}}(\boldsymbol{y}) &= \boldsymbol{I}_2 - \boldsymbol{M}^{PP}(\boldsymbol{y}) \otimes \nabla_y \end{aligned}$$

By comparing Eq. F.6, Eq. F.7 in Appendix F and Eq. 4.19,the homogenized tensors $\boldsymbol{C}^{\hom}$, $\boldsymbol{e}^{\hom}$, and

$\boldsymbol{a}^{\hom}$ express as follows:

$$\begin{aligned}
\boldsymbol{C}^{\hom} &= \frac{1}{2}\int_Y \left\{ \begin{array}{l} \left(\boldsymbol{Z^{uE}}\right) : \boldsymbol{C} : \boldsymbol{Z^{uE}} + \left(\boldsymbol{Z^{uE}}\right)^{\boldsymbol{T}} : \boldsymbol{C} : \boldsymbol{Z^{uE}} - \left(\boldsymbol{Z^{PE}}\right) \boldsymbol{.a.} \boldsymbol{Z^{PE}} \\ -\left(\boldsymbol{Z^{PE}}\right)^T \boldsymbol{.a.} \boldsymbol{Z^{PE}} - \left(\boldsymbol{Z^{uE}}\right)^T : \boldsymbol{e}^T \boldsymbol{.} \left(\boldsymbol{Z^{PE}}\right) \\ -\boldsymbol{e}^T \boldsymbol{.} \left(\boldsymbol{Z^{PE}}\right) : \left(\boldsymbol{Z^{uE}}\right) - \left(\boldsymbol{Z^{PE}}\right)^T \boldsymbol{.e} : \left(\boldsymbol{Z^{uE}}\right) - \boldsymbol{e} : \left(\boldsymbol{Z^{uE}}\right) \boldsymbol{.} \left(\boldsymbol{Z^{PE}}\right) \end{array} \right\} dV_y \\
\boldsymbol{e}^{\hom} &= \frac{1}{2}\int_Y \left\{ \begin{array}{l} \left(\boldsymbol{Z^{uE}}\right) : \boldsymbol{C} : \boldsymbol{Z^{uE}} + \left(\boldsymbol{Z^{uE}}\right)^{\boldsymbol{T}} : \boldsymbol{C} : \boldsymbol{Z^{uE}} - \left(\boldsymbol{Z^{PE}}\right) \boldsymbol{.a.} \boldsymbol{Z^{PE}} \\ -\left(\boldsymbol{Z^{PE}}\right)^T \boldsymbol{.a.} \boldsymbol{Z^{PE}} - \left(\boldsymbol{Z^{uE}}\right)^T : \boldsymbol{e}^T \boldsymbol{.} \left(\boldsymbol{Z^{PE}}\right) \\ -\boldsymbol{e}^T \boldsymbol{.} \left(\boldsymbol{Z^{PE}}\right) : \left(\boldsymbol{Z^{uE}}\right) - \left(\boldsymbol{Z^{PE}}\right)^T \boldsymbol{.e} : \left(\boldsymbol{Z^{uE}}\right) - \boldsymbol{e} : \left(\boldsymbol{Z^{uE}}\right) \boldsymbol{.} \left(\boldsymbol{Z^{PE}}\right) \end{array} \right\} dV_y \\
\boldsymbol{a}^{\hom} &= \frac{1}{2}\int_Y \left\{ \begin{array}{l} \left(\boldsymbol{Z^{uP}}\right) : C\left(\boldsymbol{y}\right) : \left(\boldsymbol{Z}^{uP}\right) + \left(\boldsymbol{Z^{uP}}\right)^T : C\left(\boldsymbol{y}\right) : \left(\boldsymbol{Z}^{uP}\right) - \left(\boldsymbol{Z^{PP}}\right) \boldsymbol{.a.} \left(\boldsymbol{Z^{PP}}\right) \\ -\left(\boldsymbol{Z^{PP}}\right)^T \boldsymbol{.a.} \left(\boldsymbol{Z^{PP}}\right) - \left(\boldsymbol{Z^{uP}}\right)^T : \boldsymbol{e}^T \boldsymbol{.} \left(\boldsymbol{Z^{PP}}\right) \\ -\boldsymbol{e}^T \boldsymbol{.} \left(\boldsymbol{Z^{PP}}\right) : \left(\boldsymbol{Z^{uP}}\right) - \left(\boldsymbol{Z^{PP}}\right)^T \boldsymbol{.e} : \left(\boldsymbol{Z^{uP}}\right) - \boldsymbol{e} : \left(\boldsymbol{Z^{uP}}\right) \boldsymbol{.} \left(\boldsymbol{Z^{PP}}\right) \end{array} \right\} dV_y
\end{aligned} \tag{4.20}$$

In the sequel, we extend the homogenization method to the consideration of higher order effects, and compute the effective flexoelectric properties.

4.3 Homogenization towards flexoelectric substitution media

In view of the derivation of the effective flexoelectric properties of composites (or lattice materials), we express the homogeneous part of the microscopic displacement and electric potential as follows:

$$\begin{aligned}
&\boldsymbol{u}^{\hom} = \boldsymbol{E}\left(\boldsymbol{x}\right) \boldsymbol{.y} + \frac{1}{2}\boldsymbol{K}\left(\boldsymbol{x}\right) : \boldsymbol{y} \otimes \boldsymbol{y} \\
&\boldsymbol{K}\left(\boldsymbol{x}\right) := \boldsymbol{E}\left(\boldsymbol{x}\right) \otimes \nabla_x \\
&\phi^{\boldsymbol{hom}} = \boldsymbol{E_M^{elec}}\left(\boldsymbol{x}\right) \boldsymbol{.y} + \frac{1}{2}\boldsymbol{G}_p\left(\boldsymbol{x}\right) : \boldsymbol{y} \otimes \boldsymbol{y} \\
&\boldsymbol{G}_p\left(\boldsymbol{x}\right) := \boldsymbol{E_M^{elec}}\left(\boldsymbol{x}\right) \otimes \nabla_x
\end{aligned} \tag{4.21}$$

The form of the homogenized displacement vector and electric potential in Eq. 4.21 leads respectively to the expression of the homogeneous part of the microscopic strain and electric field as follows:

$$\begin{aligned}
&\boldsymbol{\varepsilon}^{\hom}\left(\boldsymbol{u}^{\hom}\right) = \boldsymbol{E}\left(\boldsymbol{x}\right) + \boldsymbol{K}\left(\boldsymbol{x}\right) \boldsymbol{.y} \\
&\boldsymbol{E}^{elec,\hom}\left(\phi^{\hom}\right) = \boldsymbol{E_M^{elec}}\left(\boldsymbol{x}\right) + \boldsymbol{G}_p\left(\boldsymbol{x}\right) \boldsymbol{.y}
\end{aligned} \tag{4.22}$$

wherein third-order tensor $\boldsymbol{K}$ is the strain gradient tensor and the second-order tensor $\boldsymbol{G}_p$ is the electric field gradient tensor.

Hill extended macro-homogeneity states that the volumetric average microscopic enthalpy density is equal to the macroscopic enthalpy density in a flexoemectric medium:

$$\left\langle w_\mu(\boldsymbol{\varepsilon}, \boldsymbol{E^{elec}}) \right\rangle_Y = W_M\left(\boldsymbol{E}, \boldsymbol{E_M^{elec}}, \boldsymbol{K}, \boldsymbol{G}_p\right) = \frac{1}{2}\left(\boldsymbol{\Sigma} : \boldsymbol{E} - \boldsymbol{E_M^{elec}} \boldsymbol{.} \overline{\boldsymbol{D}} + \boldsymbol{S} \therefore \boldsymbol{K} - \boldsymbol{R} : \boldsymbol{G}_p\right) \tag{4.23}$$

wherein $\boldsymbol{S}$ is the third-order hyperstress referring to higher gradient effects, and the second-order tensor $\boldsymbol{R}$ is related to the higher gradient electric displacement (the second gradient electric displacement).

An extended minimization principle of the macroscopic enthalpy over all periodic fluctuations holds:

$$W_M\left(\boldsymbol{E},\boldsymbol{E_M^{elec}},\boldsymbol{K},\boldsymbol{G}_p\right)=\underset{\tilde{\boldsymbol{u}},\tilde{\phi}\in H^1_{per}(Y)}{Min}\frac{1}{2}\int_Y\left\{\begin{array}{l}(\boldsymbol{E}+\boldsymbol{K}.\boldsymbol{y}+\tilde{\boldsymbol{u}}(\boldsymbol{y})\otimes\nabla_y):\boldsymbol{C}:(\boldsymbol{E}+\boldsymbol{K}.\boldsymbol{y}+\tilde{\boldsymbol{u}}(\boldsymbol{y})\otimes\nabla_y)\\-\left(\boldsymbol{E_M^{elec}}+\boldsymbol{G}_p.\boldsymbol{y}-\tilde{\phi}\nabla_y\right).\boldsymbol{a}.\left(\boldsymbol{E_M^{elec}}+\boldsymbol{G}_p.\boldsymbol{y}-\tilde{\phi}\nabla_y\right)\\-\boldsymbol{e}^T.\left(\boldsymbol{E_M^{elec}}+\boldsymbol{G}_p.\boldsymbol{y}-\tilde{\phi}\nabla_y\right):(\boldsymbol{E}+\boldsymbol{K}.\boldsymbol{y}+\tilde{\boldsymbol{u}}(\boldsymbol{y})\otimes\nabla_y)\\-\boldsymbol{e}:(\boldsymbol{E}+\boldsymbol{K}.\boldsymbol{y}+\tilde{\boldsymbol{u}}(\boldsymbol{y})\otimes\nabla_y).\left(\boldsymbol{E_M^{elec}}+\boldsymbol{G}_p.\boldsymbol{y}-\tilde{\phi}\nabla_y\right)\end{array}\right\}dV_y \tag{4.24}$$

The stationarity condition of the previous functional delivers, as a necessary condition, the second order BVP to be satisfied by the optimal fluctuations associated to the real displacement field (in the absence of body forces) and electric potential(in the absence of free electric charges) :

$$\left|\begin{array}{l}-div_y\left\{\boldsymbol{C}(\boldsymbol{y}):(\boldsymbol{E}+\boldsymbol{K}.\boldsymbol{y}+\tilde{\boldsymbol{u}}(\boldsymbol{y})\otimes\nabla_y)-\boldsymbol{e}^T.\left(\boldsymbol{E_M^{elec}}+\boldsymbol{G}_p.\boldsymbol{y}-\tilde{\phi}\nabla_y\right)\right\}=\boldsymbol{0},\\div_y\left\{\boldsymbol{a}.\left(\boldsymbol{E_M^{elec}}+\boldsymbol{G}_p.\boldsymbol{y}-\tilde{\phi}\otimes\nabla_y\right))+\boldsymbol{e}:(\boldsymbol{E}+\boldsymbol{K}.\boldsymbol{y}+\tilde{\boldsymbol{u}}(\boldsymbol{y})\otimes\nabla_y)\right\}=\boldsymbol{0},\\\tilde{\boldsymbol{u}}(\boldsymbol{y}),\tilde{\phi}\text{ Y-periodic}\end{array}\right. \tag{4.25}$$

The fluctuations $\tilde{\boldsymbol{u}}(\boldsymbol{y})$ and $\tilde{\phi}(\boldsymbol{y})$ are expressed linearly versus the effective strain and electric field tensors and their gradients $\boldsymbol{E}(\boldsymbol{x}),\boldsymbol{E_M^{elec}}(\boldsymbol{x}),\boldsymbol{K}(\boldsymbol{x}),\boldsymbol{G}_p(\boldsymbol{x})$ which constitute the loading in the BVP Eq. 4.25:

$$\begin{array}{l}\tilde{\boldsymbol{u}}(\boldsymbol{y})=\boldsymbol{M}^{uE}(\boldsymbol{y}):\boldsymbol{E}(\boldsymbol{x})+\boldsymbol{M}^{uP}(\boldsymbol{y}).\boldsymbol{E_M^{elec}}(\boldsymbol{x})+\boldsymbol{M}^{uK}(\boldsymbol{y})\therefore\boldsymbol{K}(\boldsymbol{x})+\boldsymbol{M}^{uGp}(\boldsymbol{y}):\boldsymbol{G}_p(\boldsymbol{x})\\\tilde{\phi}(\boldsymbol{y})=\boldsymbol{M}^{PE}(\boldsymbol{y}):\boldsymbol{E}(\boldsymbol{x})+\boldsymbol{M}^{PP}(\boldsymbol{y}).\boldsymbol{E_M^{elec}}(\boldsymbol{x})+\boldsymbol{M}^{PK}(\boldsymbol{y})\therefore\boldsymbol{K}(\boldsymbol{x})+\boldsymbol{M}^{PGp}(\boldsymbol{y}):\boldsymbol{G}_p(\boldsymbol{x})\end{array} \tag{4.26}$$

wherein the fourth- and third-order tensors $\boldsymbol{M}^{uK}(\boldsymbol{y})$ and $\boldsymbol{M}^{uGp}(\boldsymbol{y})$ are the localization operators that relate the fluctuating displacement to the strain gradient and electric field gradient. The third-order tensors $\boldsymbol{M}^{PK}(\boldsymbol{y})$ and the second-order tensor $\boldsymbol{M}^{PGp}(\boldsymbol{y})$ are the localization operators relating the fluctuating electric potential to the strain gradient and electric field gradient.

Introducing the microscopic strain and electric field in terms of the strain and electric field gradients $(\boldsymbol{K},\boldsymbol{G}_p)$ gives the following expressions in terms of the macroscopic degrees of freedom:

$$\begin{array}{l}\boldsymbol{u}(\boldsymbol{y})\otimes\nabla_y=\left(\boldsymbol{u}^{\hom}(\boldsymbol{y})+\tilde{\boldsymbol{u}}(\boldsymbol{y})\right)\otimes\nabla_y:=\boldsymbol{E}(\boldsymbol{x})+\boldsymbol{K}(\boldsymbol{x}).\boldsymbol{y}\\+\boldsymbol{M}^{uE}(\boldsymbol{y})\otimes\nabla_y:\boldsymbol{E}(\boldsymbol{x})+\boldsymbol{M}^{uK}(\boldsymbol{y})\otimes\nabla_y\therefore\boldsymbol{K}(\boldsymbol{x})\\+\boldsymbol{M}^{uP}(\boldsymbol{y})\otimes\nabla_y.\boldsymbol{E_M^{elec}}(\boldsymbol{x})+\boldsymbol{M}^{uGp}(\boldsymbol{y})\otimes\nabla_y:\boldsymbol{G}_p(\boldsymbol{x})\\\equiv\boldsymbol{Z}^{uE}(\boldsymbol{y}):\boldsymbol{E}(\boldsymbol{x})+\boldsymbol{Z}^{uk}(\boldsymbol{y})\therefore\boldsymbol{K}(\boldsymbol{x})+\boldsymbol{Z}^{uP}(\boldsymbol{y}).\boldsymbol{E_M^{elec}}(\boldsymbol{x})+\boldsymbol{Z}^{uG_p}(\boldsymbol{y}):\boldsymbol{G}_p(\boldsymbol{x}),\end{array} \tag{4.27}$$

$$\begin{array}{l}-\phi(\boldsymbol{y})\nabla_y=:-\left(\phi^{\boldsymbol{hom}}(\boldsymbol{y})+\tilde{\phi}(\boldsymbol{y})\right)\nabla_y=\boldsymbol{E_M^{elec}}+\boldsymbol{G}_p(\boldsymbol{x}).\boldsymbol{y}\\-\boldsymbol{M}^{PE}(\boldsymbol{y})\otimes\nabla_y:\boldsymbol{E}(\boldsymbol{x})-\boldsymbol{M}^{PK}(\boldsymbol{y})\otimes\nabla_y\therefore\boldsymbol{K}(\boldsymbol{x})\\-\boldsymbol{M}^{PP}(\boldsymbol{y})\otimes\nabla_y.\boldsymbol{E_M^{elec}}(\boldsymbol{x})-\boldsymbol{M}^{PGp}(\boldsymbol{y})\otimes\nabla_y:\boldsymbol{G}_p(\boldsymbol{x})\\\equiv\boldsymbol{Z}^{PE}(\boldsymbol{y}):\boldsymbol{E}(\boldsymbol{x})+\boldsymbol{Z}^{Pk}(\boldsymbol{y})\therefore\boldsymbol{K}(\boldsymbol{x})+\boldsymbol{Z^{PP}}.\boldsymbol{E_M^{elec}}(\boldsymbol{x})+\boldsymbol{Z}^{PG_P}(\boldsymbol{y}):\boldsymbol{G}_p(\boldsymbol{x})\end{array}$$

wherein $\boldsymbol{Z}^{uk}(\boldsymbol{y}),\boldsymbol{Z}^{uG_p}(\boldsymbol{y}),\boldsymbol{Z}^{Pk}(\boldsymbol{y}),\boldsymbol{Z}^{PG_P}(\boldsymbol{y})$ represent the localization tensors relating the microscopic

strain and electric field into the macroscopic higher order kinematic variables, viz:

$$\begin{aligned}
\boldsymbol{Z}^{uk}(\boldsymbol{y}) &= \left(\boldsymbol{I}_6.\boldsymbol{y} + \boldsymbol{M}^{uK}(\boldsymbol{y}) \otimes \nabla_y\right) \\
\boldsymbol{Z}^{uG_p}(\boldsymbol{y}) &= \boldsymbol{M}^{uGp}(\boldsymbol{y}) \otimes \nabla_y \\
\boldsymbol{Z}^{Pk}(\boldsymbol{y}) &= -\boldsymbol{M}^{PK}(\boldsymbol{y}) \otimes \nabla_y \\
\boldsymbol{Z}^{PG_P}(\boldsymbol{y}) &= \left(\boldsymbol{I}_4.\boldsymbol{y} - \boldsymbol{M}^{PGp}(\boldsymbol{y}) \otimes \nabla_y\right)
\end{aligned}$$

Using Eq. 4.27, the macroscopic energy in Eq. 4.24 is then elaborated in terms of the localization operators to get a Lagrangian functional of the displacement and electric field fluctuations extended into higher order terms (see Appendix F, Eq. F.8). The flexoelectric constitutive law is then obtained by taking the partial derivatives of the minimum macroscopic energy with respect to $\boldsymbol{E}, \boldsymbol{E}_{\boldsymbol{M}}^{\boldsymbol{elec}}, \boldsymbol{K},$ and $\boldsymbol{G}_p$ to determine the expressions of stress, electric displacement, hyperstress, and higher gradient electric displacement respectively (see Appendix F Eq. F.9- F.13). As a result of these expressions, the tensors of effective flexoelectric properties involved in the following homogenized constitutive law are obtained:

$$\left|\begin{array}{l}
\boldsymbol{\Sigma} = \boldsymbol{C}^{\mathrm{hom}} : \boldsymbol{E} - \boldsymbol{e}^{T,\boldsymbol{hom}}.\boldsymbol{E}_{\boldsymbol{M}}^{\boldsymbol{elec}} + \boldsymbol{B}^{\boldsymbol{hom}} \therefore \boldsymbol{K} - \boldsymbol{e_f}^{\boldsymbol{hom}} : \boldsymbol{G}_{\mathrm{P}} \\
\overline{\boldsymbol{D}} = \boldsymbol{e}^{\boldsymbol{hom}} : \boldsymbol{E} + \boldsymbol{a}^{\boldsymbol{hom}}.\boldsymbol{E}_{\boldsymbol{M}}^{\boldsymbol{elec}} + \boldsymbol{F}^{\boldsymbol{hom}} \therefore \boldsymbol{K} + \boldsymbol{e_D}^{\boldsymbol{hom}} : \boldsymbol{G}_P \\
\boldsymbol{S} = \boldsymbol{B}^{T,\boldsymbol{hom}} : \boldsymbol{E} - \boldsymbol{F}^{T,\boldsymbol{hom}}.\boldsymbol{E}_{\boldsymbol{M}}^{\boldsymbol{elec}} + \boldsymbol{A}^{\boldsymbol{hom}} \therefore \boldsymbol{K} + \boldsymbol{H}^{\boldsymbol{hom}} : \boldsymbol{G}_P \\
\boldsymbol{R} = \boldsymbol{e_f}^{T,\boldsymbol{hom}} : \boldsymbol{E} + \boldsymbol{e_D}^{T,\boldsymbol{hom}}.\boldsymbol{E}_{\boldsymbol{M}}^{\boldsymbol{elec}} + \boldsymbol{H}^{T,\boldsymbol{hom}} \therefore \boldsymbol{K} + \boldsymbol{N}^{\boldsymbol{hom}} : \boldsymbol{G}_P
\end{array}\right. \tag{4.28}$$

All parameters in Eq. 4.28 are defined for the homogenized medium at the macroscale. In details, $\boldsymbol{B}^{\boldsymbol{hom}}$ is the fifth-order coupling tensor between the stress and strain gradient, $\boldsymbol{e_f}^{\boldsymbol{hom}}$ the fourth-order coupling tensor between stress and electric field gradient. $\boldsymbol{F}^{\boldsymbol{hom}}$ is the fourth-order coupling tensor between electrical displacement and strain gradient. $\boldsymbol{e_D}^{\boldsymbol{hom}}$ is the third-order coupling tensor between the electric displacement and the electric field gradient. $\boldsymbol{A}^{\boldsymbol{hom}}$ is the sixth-order second gradient tensor. $\boldsymbol{H}^{\boldsymbol{hom}}$ is the fifth-order coupling tensor between hyperstress and the electric field gradient, and $\boldsymbol{N}^{\boldsymbol{hom}}$ is the fourth-order coupling tensor between higher-order electric displacement and the electric field gradient.

As done in section 4.2, a comparison between Eqs. F.10, F.11, F.12, and F.13 allows the determination of the tensors of homogenized properties $\boldsymbol{C}^{\mathrm{hom}}$, $\boldsymbol{e}^{\boldsymbol{hom}}$, $\boldsymbol{B}^{\boldsymbol{hom}}$, $\boldsymbol{e_f}^{\boldsymbol{hom}}$, $\boldsymbol{a}^{\boldsymbol{hom}}$, $\boldsymbol{F}^{\boldsymbol{hom}}$, $\boldsymbol{e_D}^{\boldsymbol{hom}}$, $\boldsymbol{A}^{\boldsymbol{hom}}$, $\boldsymbol{H}^{\boldsymbol{hom}}$, $\boldsymbol{N}^{\boldsymbol{hom}}$ as corresponding integrals of microscopic quantities over the unit cell; these tensors receive however complicated expressions that will not be explicitly written.

4.4 Algorithm for the evaluation of the homogenized piezoelectric and flexoelectric moduli

Starting from the theoretical framework mentioned in the previous section, we propose a numerical algorithm to determine the effective tensors of the homogenized constitutive law for the second gradient flexoelectric medium.

At the micro-scale, the materials are considered as linear elastic and isotropic (knowing that they should be transversely isotropic but since the direction of transverse isotropy is orthogonal to our plane of study, we have isotropy within the 2D section considered in this example). In this context, the elastic stress at a point is related to the deformation at the same point by the two Lame coefficients (λ, η), with $\lambda = \frac{E\nu}{(1+\nu)(1-2\nu)}$ the first Lamé parameter and $\eta = \frac{E}{2(1+\nu)}$ the second Lamé parameter, expressed versus Young's modulus E and Poisson's ratio ν. Taking into consideration Eq. 4.8, and Eq. 4.22, the microscopic stress and electric displacement can be written in matrix format as:

$$\begin{pmatrix} \sigma_{11} \\ \sigma_{22} \\ \sigma_{12} \\ D_1 \\ D_2 \end{pmatrix} = \begin{pmatrix} \lambda+2\eta & \lambda & 0 & -e_{11} & -e_{21} \\ \lambda & \lambda+2\eta & 0 & -e_{12} & -e_{22} \\ 0 & 0 & \eta & -e_{13} & -e_{23} \\ e_{11} & e_{12} & e_{13} & a_{11} & 0 \\ e_{21} & e_{22} & e_{23} & 0 & a_{22} \end{pmatrix} \begin{pmatrix} \tilde{\varepsilon}_{11} + E_{11} + K_{111}.y_1 + K_{112}.y_2 \\ \tilde{\varepsilon}_{22} + E_{22} + K_{221}.y_1 + K_{222}.y_2 \\ \tilde{\varepsilon}_{12} + E_{12} + K_{121}.y_1 + K_{122}.y_2 \\ \widetilde{E}_1^{elec} + {E_M^{elec}}_1 + G_{P11}.y_1 + G_{P12}.y_2 \\ \widetilde{E}_2^{elec} + {E_M^{elec}}_2 + G_{P12}.y_1 + G_{P22}.y_2 \end{pmatrix} \tag{4.29}$$

where (y_1, y_2) is the microscopic position vector in 2D situations to which we restrict the analysis here and in the sequel. The macroscopic deformation $\boldsymbol{E}$, the macroscopic gradient of deformation $\boldsymbol{K}$, the macroscopic electric field $\boldsymbol{E_M^{elec}}$, and the macroscopic gradient of electric field $\boldsymbol{G}_P$ are considered as kinematic controls applied to the unit cell Y.

The objective is to find the total displacement and electric potential of the unit cell BVP satisfying the following set of governing equations:

$$\left| \begin{array}{l} \boldsymbol{\sigma(y)}.\nabla_y = \boldsymbol{0} \quad in\ Y \\ \boldsymbol{D(y)}.\nabla_y = 0 \\ \boldsymbol{\sigma.n} = \boldsymbol{t}^d \text{ on } S_t \\ \boldsymbol{D.n} = D^d \text{ on } S_D \\ \boldsymbol{\sigma(y)} = \boldsymbol{C(y)} : \boldsymbol{\varepsilon(y)} + \boldsymbol{e}^T\boldsymbol{(y)}.\boldsymbol{E^{elec}(y)} \ \ in\ Y \\ \boldsymbol{D(y)} = \boldsymbol{e(y)} : \boldsymbol{\varepsilon(y)} + \boldsymbol{a(y)}.\boldsymbol{E^{elec}(y)} \\ \boldsymbol{\varepsilon(y)} = \boldsymbol{E} + \boldsymbol{K}.\boldsymbol{y} + \tilde{\boldsymbol{\varepsilon}}\boldsymbol{(y)} \\ \tilde{\boldsymbol{\varepsilon}}\boldsymbol{(y)} := \tilde{\boldsymbol{u}}\boldsymbol{(y)} \otimes^S \nabla_y \\ \boldsymbol{E^{elec}} = \boldsymbol{E_M^{elec}} + \boldsymbol{G_P}.\boldsymbol{y} + \tilde{\boldsymbol{E}}^{\boldsymbol{elec}} \end{array} \right. \tag{4.30}$$

A weak formulation of Eq. 4.30 is introduced to get the following formal homogenized problem, considering the decomposition of the total microscopic deformation and electrical fields,

$$\begin{aligned} &\forall \boldsymbol{v}, \psi \in H_1(Y), \\ &\int_Y \left(C(\boldsymbol{y}) : \boldsymbol{\varepsilon(u)} - \boldsymbol{e}^T\boldsymbol{(y)}.\boldsymbol{E^{elec}(y)} \right) : \boldsymbol{\varepsilon(v)} dV_y \quad - \int_Y \left(\boldsymbol{e(y)} : \boldsymbol{\varepsilon(y)} + \boldsymbol{a(y)}.\boldsymbol{E^{elec}(y)} \right) .\boldsymbol{E}^{elec}(\psi) dV_y = 0 \end{aligned} \tag{4.31}$$

$\forall \boldsymbol{v}, \psi \in H_1(Y)$,

$$\begin{aligned} &\int_Y \left(C(\boldsymbol{y}) : (\widetilde{\boldsymbol{\varepsilon}} + \boldsymbol{E} + \boldsymbol{K}.\boldsymbol{y}) - \boldsymbol{e}^T(\boldsymbol{y}).\left(\boldsymbol{E}_{\boldsymbol{M}}^{\boldsymbol{elec}} + \boldsymbol{G}_{\boldsymbol{P}}.\boldsymbol{y} + \tilde{\boldsymbol{E}}^{\boldsymbol{elec}} \right) \right) : \boldsymbol{\varepsilon}(\boldsymbol{v}) dV_y \\ &- \int_Y \left(\boldsymbol{a}(\boldsymbol{y}).\left(\boldsymbol{E}_{\boldsymbol{M}}^{\boldsymbol{elec}} + \boldsymbol{G}_{\boldsymbol{P}}.\boldsymbol{y} + \tilde{\boldsymbol{E}}^{\boldsymbol{elec}} \right) + \boldsymbol{e}(\boldsymbol{y}) : (\widetilde{\boldsymbol{\varepsilon}} + \boldsymbol{E} + \boldsymbol{K}.\boldsymbol{y}) \right) .\boldsymbol{E}^{elec}(\psi) dV_y = 0 \end{aligned} \tag{4.32}$$

where $\boldsymbol{v}$ and ψ are the test functions. By solving this variational formulation, the periodic fluctuating displacement and fluctuating electric potential satisfying Eq. 4.31 are obtained. This problem is solved using FreeFem++ open source finite element software as well as for the subsequent determination of the first gradient, second gradient, the piezoelectric and the flexoelectric moduli in Eq. 4.28.

4.4.1 Determination of the homogenized first and second gradient moduli

The goal in this section is to determine the first gradient moduli $\boldsymbol{C}^{\text{hom}}$ (rigidity matrix), the second gradient moduli $\boldsymbol{A}^{\text{hom}}$ and the coupling moduli $\boldsymbol{B}^{\text{hom}}$ between first and second gradient terms. The coupling moduli between the electrical displacement and strain gradient tensor $\boldsymbol{F}^{\text{hom}}$ will be determined as well. Applying the macroscopic strain $\boldsymbol{E}$ as the sole kinematic boundary condition over the unit cell leads to $\boldsymbol{C}^{\text{hom}}$ while applying $\boldsymbol{K}$ alone as a kinematic boundary condition over the unit cell entails the evaluation of $\boldsymbol{B}^{\text{hom}}$, $\boldsymbol{F}^{\text{hom}}$ and $\boldsymbol{A}^{\text{hom}}$. This procedure is condensed in algorithmic format in Fig. 4.3.

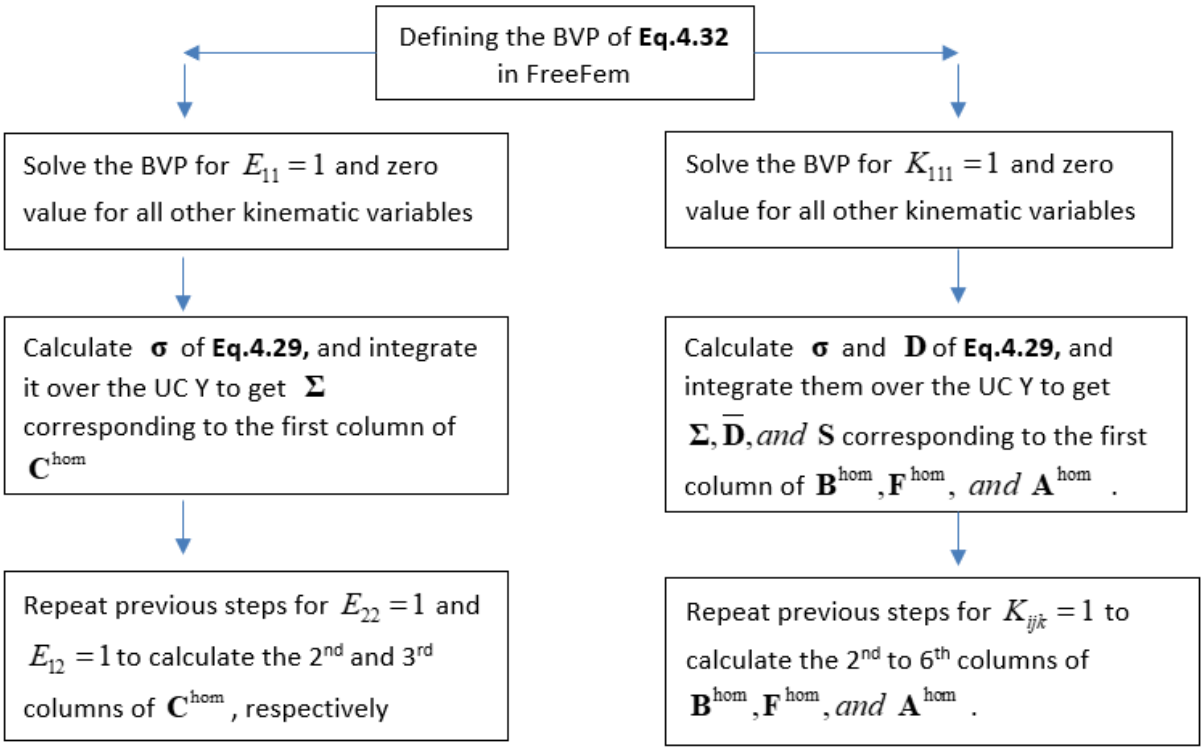

Figure 4.3 Schematic diagram for the computation of the effective moduli $\boldsymbol{C}^{\text{hom}}, \boldsymbol{B}^{\text{hom}}, \boldsymbol{F}^{\text{hom}}, and\ \boldsymbol{A}^{\text{hom}}$

The moduli $\boldsymbol{C}^{\text{hom}}$, $\boldsymbol{B}^{\text{hom}}$, and $\boldsymbol{F}^{\text{hom}}$ are written in the form:

$$\boldsymbol{C}^{\text{hom}} : \boldsymbol{E} = \frac{1}{|Y|} \int_Y \boldsymbol{C}(\boldsymbol{y}) : \boldsymbol{\varepsilon}(\boldsymbol{u}) dV_y \tag{4.33}$$

$$\boldsymbol{B}^{\text{hom}} \therefore \boldsymbol{K} = \frac{1}{|Y|} \int_Y \boldsymbol{C}(\boldsymbol{y}) : \boldsymbol{\varepsilon}(\boldsymbol{u}) dV_y \tag{4.34}$$

$$\boldsymbol{F}^{\text{hom}} \therefore \boldsymbol{K} = \frac{1}{|\mathrm{Y}|} \int_Y \boldsymbol{D}\, dV_y \tag{4.35}$$

wherein $|Y|$ is the volume (the area in 2D) of the unit cell.

The average macroscopic hyperstress is written according to the Hill Lemma, as follows:

$$S_{ijk} = \frac{\partial W_M}{\partial K_{ijk}} = \frac{\partial}{\partial K_{ijk}} \langle w_\mu(\boldsymbol{\varepsilon}) \rangle_Y = \left\langle \frac{\partial w_\mu(\boldsymbol{\varepsilon})}{\partial K_{ijk}} \right\rangle_Y = \left\langle \frac{\partial w_\mu(\boldsymbol{\varepsilon})}{\partial \varepsilon_{ij}} \frac{\partial \varepsilon_{ij}}{\partial K_{ijk}} \right\rangle_Y = \left\langle \sigma_{ij} \frac{\partial \varepsilon_{ij}}{\partial K_{ijk}} \right\rangle_Y \tag{4.36}$$

The microscopic strain field evaluated from the perturbation displacement (determined from the boundary value problem in Eq. 4.32) and used in Eq. 4.36 is:

$$\begin{cases} \varepsilon_{11} = \tilde{\varepsilon}_{11} + E_{11} + K_{111} y_1 + K_{112} y_2 \equiv \dfrac{\partial u_1(y_1, y_2)}{\partial y_1}, \\ \varepsilon_{22} = \tilde{\varepsilon}_{22} + E_{22} + K_{221} y_1 + K_{222} y_2 \equiv \dfrac{\partial u_2(y_1, y_2)}{\partial y_2}, \\ \varepsilon_{12} = \tilde{\varepsilon}_{12} + E_{21} + \dfrac{1}{2}(K_{121} + K_{211}) y_1 + \dfrac{1}{2}(K_{122} + K_{212}) y_2 \equiv \dfrac{1}{2}\left(\dfrac{\partial u_1(y_1, y_2)}{\partial y_2} + \dfrac{\partial u_2(y_1, y_2)}{\partial y_1} \right) \end{cases} \tag{4.37}$$

Then, the tensor $\boldsymbol{A}^{\text{hom}}$ can be related to the hyperstress as follows:

$$\boldsymbol{A}^{\text{hom}} \therefore \boldsymbol{K} = \frac{1}{|Y|} \int_Y \left(\sigma_{ij} \frac{\partial \varepsilon_{ij}}{\partial K_{ijk}} \right) dV_y \tag{4.38}$$

4.4.2 Determination of the homogenized piezoelectric and flexoelectric moduli

In this section, the tensors of effective moduli related to piezoelectricity $\boldsymbol{e}^{\text{hom}}$, $\boldsymbol{a}^{\text{hom}}$, and flexoelectricity $\boldsymbol{H}^{\boldsymbol{hom}}$, $\boldsymbol{e_D}^{\boldsymbol{hom}}$, $\boldsymbol{e_f}^{\boldsymbol{hom}}$, and $\boldsymbol{N}^{\boldsymbol{hom}}$ are determined. By selecting $\boldsymbol{E} = \boldsymbol{1}$ and applying only vector $\boldsymbol{E}_{\boldsymbol{M}}^{\boldsymbol{elec}}$ as a kinematic boundary condition over the RVE, the piezoelectric matrix $\boldsymbol{e}^{\text{hom}}$ and permittivity matrix $\boldsymbol{a}^{\text{hom}}$ are obtained, while, by selecting $\boldsymbol{K} = \boldsymbol{1}$ and applying, only, $\boldsymbol{G_P}$ as a kinematic boundary condition over the RVE, the matrices $\boldsymbol{e_f}^{\boldsymbol{hom}}, \boldsymbol{e_D}^{\text{hom}}, \boldsymbol{H}^{\text{hom}}$ and $\boldsymbol{N}^{\boldsymbol{hom}}$ are determined. This procedure is written in algorithmic format in Fig. 4.4.

The tensors $\boldsymbol{e}^{\text{hom}}, \boldsymbol{a}^{\text{hom}}, \boldsymbol{e}^{\text{hom}}, \boldsymbol{e}_D^{\text{hom}}$ are obtained from the relations:

$$\boldsymbol{e}^{\text{hom}} . \boldsymbol{E}_{\boldsymbol{M}}^{\boldsymbol{elec}} = \frac{1}{|Y|} \int_Y \boldsymbol{C}(\boldsymbol{y}) : \boldsymbol{\varepsilon}(\boldsymbol{u}) dV_y - \boldsymbol{C}^{\text{hom}} : \boldsymbol{E} \tag{4.39}$$

$$\boldsymbol{a}^{\text{hom}} . \boldsymbol{E}_{\boldsymbol{M}}^{\boldsymbol{elec}} = \frac{1}{|\mathrm{Y}|} \int_Y \boldsymbol{D}\, dV_y - \boldsymbol{e}^{\text{hom}} : \boldsymbol{E} \tag{4.40}$$

$$\boldsymbol{e_f}^{\text{hom}} : \boldsymbol{G_P} = \frac{1}{|Y|} \int_Y \boldsymbol{C}(\boldsymbol{y}) : \boldsymbol{\varepsilon}(\boldsymbol{u}) dV_y - \boldsymbol{B}^{\text{hom}} \therefore \boldsymbol{K} \tag{4.41}$$

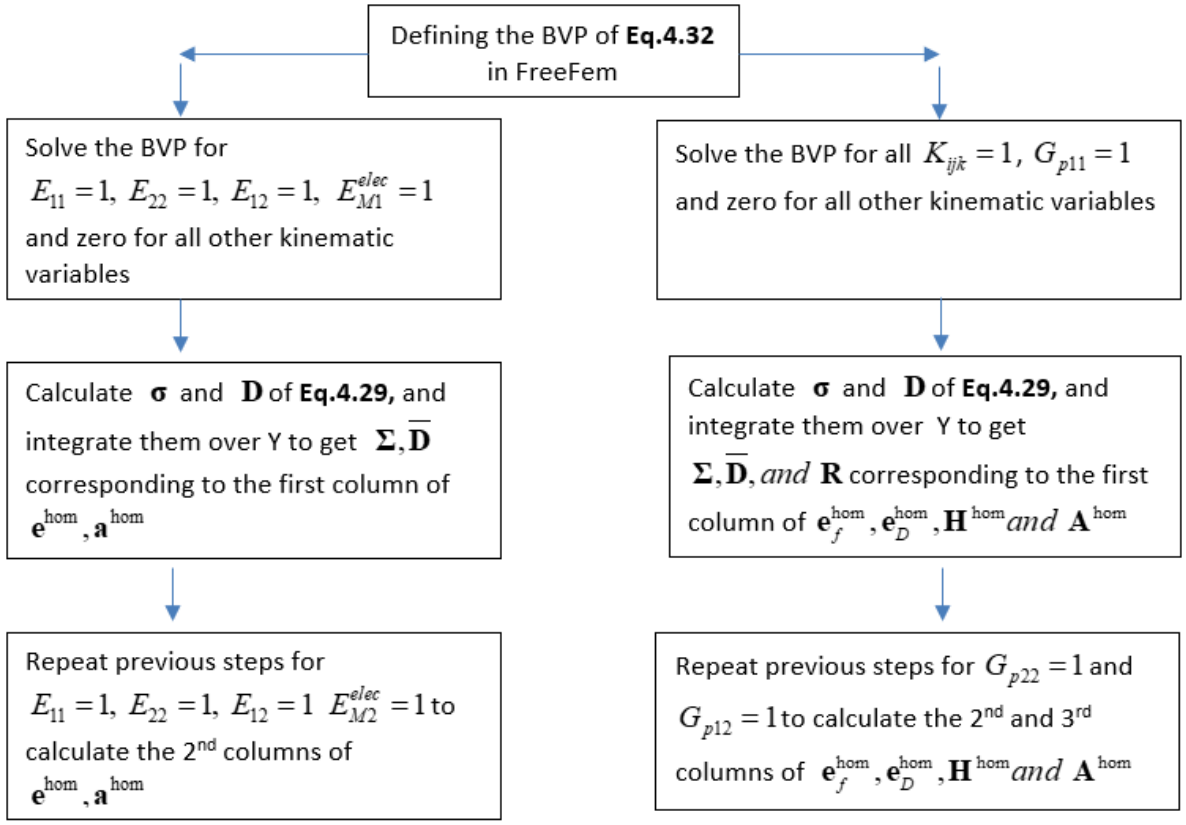

Figure 4.4 Schematic diagram for computing the effective moduli $\boldsymbol{e}^{\hom},\boldsymbol{a}^{\hom},\boldsymbol{e_f}^{\boldsymbol{hom}},\boldsymbol{e}_D^{\hom},\boldsymbol{H}^{\hom}and\ \boldsymbol{A}^{\hom}$

$$\boldsymbol{e_D}^{\hom} : \boldsymbol{G_P} = \frac{1}{|\mathrm{Y}|}\int_Y \boldsymbol{D}\ dV_y - \boldsymbol{F}^{\hom} \therefore \boldsymbol{K} \tag{4.42}$$

The macroscopic tensor $\boldsymbol{R}$ can be written according to Hill Lemma as follows:

$$R_{ij} = \left\langle D_k \frac{\partial E_k^{elec}}{\partial G_{ij}} \right\rangle_Y \tag{4.43}$$

wherein the microscopic electric field is determined from the perturbation electric potential (determined from solving the B.V.P Eq. 4.32), and can be written according to $Eq.\ 4.30_7$ as:

$$\begin{cases} E_1^{elec} = \tilde{E}_1^{\mathrm{elec}} + \mathrm{E}_{\mathrm{M1}}^{\mathrm{elec}} + G_{P11}y_1 + G_{P12}y_2 \\ E_2^{elec} = \tilde{E}_2^{elec} + E_{M2}^{elec} + G_{P12}y_1 + G_{P22}y_2 \end{cases} \tag{4.44}$$

The tensors $\mathbf{H}^{\mathbf{hom}}$ and $\mathbf{N}^{\mathbf{hom}}$ are then determined from the relations:

$$\mathbf{H}^{\mathbf{hom}} : \mathbf{G_P} = \frac{1}{|Y|}\int_Y \left(\sigma_{ij}\frac{\partial \varepsilon_{ij}}{\partial K_{ijk}}\right) dV_y - \mathbf{A}^{\mathbf{hom}} \therefore \mathbf{K} \tag{4.45}$$

$$\mathbf{N}^{\mathbf{hom}} : \mathbf{G_P} = \frac{1}{|Y|}\int_Y \left(D_i\frac{\partial E_i^{elec}}{\partial G_{ij}}\right) dV_y - \mathbf{H}^{\mathbf{hom}} \therefore \mathbf{K} \tag{4.46}$$

4.5 Conclusion

In this chapter, the effective linear piezoelectric properties of heterogeneous materials have been evaluated in the context of periodic homogenization, employing a variational formulation in combination with the extended Hill macro-homogeneity condition. The microscopic variables – the displacement vector and electric potential – have been expressed as the sum of a homogeneous part and a fluctuation obeying a minimum principle of the energy functional. The entire set of homogenized moduli has been obtained, expressing as volumetric averages of the microscopic properties of the individual constituents weighted by the displacement and electric potential localization operators.

This framework has then been extended to the computation of the effective flexoelectric properties, thereby accounting for higher gradient effects that may be induced by a strong contrast of properties of the constituents within the composite. A numerical algorithm relying on solving the weak formulation of the BVP when applying different macroscopic kinematic boundary conditions is adopted and can be applied to both composite and architected materials.

The proposed homogenization method has given rise to a finite element implementation for the efficient computation of the effective flexoelectric properties of composites in a broad sense. This numerical platform is convenient to investigate in the next chapter the flexoelectric properties of architected materials and composite materials.

Chapter 5

Applications of piezoelectric and flexoelectric homogenization

Summary

In this chapter, we compute the effective piezoelectric and flexoelectric properties of heterogeneous piezoelectric materials in the context of the previously developed periodic homogenization, that is based on a variational formulation and articulated with the extended Hill macro-homogeneity condition. The obtained homogenized properties are employed for the determination of the wave propagation attributes of piezoelectric composites. The dynamic equilibrium equations, accounting for higher gradient effects, are formulated to deal with wave propagation in flexoelectric media, considering the Classical Flexoelectric Theory (CFE) and the Non-Local Flexoelectric Theory (NLFE). The obtained dispersion relations show that flexoelectric medium is a dispersive medium and anisotropic when increasing the wavenumber unlike the piezoelectric medium.

An analysis is performed to study the sensitivity of the effective flexoelectric moduli to the geometrical variables of the considered unit cells of periodic lattice materials. More specifically, hexagonal, re-entrant auxetic, and rectangular unit cells are investigated in terms of their relative piezoelectric and flexoelectric response. Regular hexagonal, re-entrant hexagonal and rectangular lattice unit cells are mutually compared in terms of their flexoelectric properties. The coupling between mechanical and electrical fields is attested by the non-uniform distribution of the electric potential within the three studied architected materials subjected to a uniform strain.

5.1 Introduction

The capability of certain materials to convert electrical fields into mechanical deformation and vice versa is essential in numerous engineering applications such as sensors [239], actuators [240], and energy harvestors [1, 241], thanks to the piezoelectric effect. Nowadays there exist various natural and artificial piezoelectric materials, such as quartz, zirconate titanate (PZT), barium titanate and many others. However, due to the advantageous properties of flexoelectricity over piezoelectricity, it was highly studied and demonstrated in a wide range of materials such as liquid crystals [19], crystalline dielectrics [3], and polymers [242]. This phenomenon can offer a path for designing alternative materials and devices for electromechanical transduction that exploit gradients, either alone, such as in the micro (MEMS) and nano-electromechanical systems (NEMS) [243–246], or in combination with piezoelectricity as a way to enhance the apparent piezoelectricity [247].

Recent works focused on flexoelectricity for lattice materials; this class of materials is defined as porous materials with reticulated structures, typically constructed with a periodic microstructure allowing the identification of a repeated unit cell (UC). Among the architected materials that deserved extensive studies, the hexagonal honeycomb configuration was selected due to its simplicity and easy manufacturability. Different variants of the hexagonal honeycomb (HC) exist as a result of the orientation of the ligaments, leading to the realization of an auxetic effect with negative Poisson's ratio [248]. Many works were devoted to studying the mechanical behavior of these variants constructed from elastically isotropic materials showing both conventional and auxetic responses [248–250]. Considering piezoelectricity in such metamaterials allows the analysis of their electromechanical properties [251].

Wave propagation in composite piezoelectric materials has raised a lot of research attention in the last four decades, starting with Tiersten [252] who derived the analytical solution of wave propagation in an infinite piezoelectric plate relying on classical piezoelectric theory. [253] obtained the exact solution of wave equations within an infinite plate including the electromechanical coupling. More recently, the quasi-electrostatic wave propagation analysis within stratified composites was performed in the framework of the nonlocal piezoelectric theory in [221, 254] with special focus on two-layer stratified composites made of $LiNbO_3$ and PVDF layers.

It is worth mentioning in the context of wave propagation the prevalence of two main theories for piezoelectric phenomena, namely classical piezoelectricity (CPE) and nonlocal piezoelectricity (NLPE). The effective properties obtained by mathematical homogenization have been used to compute the wave propagation features accounting for the influence of an internal length parameter of the so-called NLPE (nonlocal piezoelectric theory) developed by Eringen [255]. It is well-known that piezoelectricity has the ability to modify structure of wave propagation characteristics in composites, by modifying the locality –and thus intensity- of the applied field, [256]. The coupling of the electric and mechanical fields leads indeed to considerably modified dispersion attributes, a behavior typically observed for highly anisotropic microstructural designs [257, 258]. Moreover, while CPE theory is local in space (the stress

at one material point depends on the strain and electric field at the same point), it faces limitations for size-dependent continua, which incorporate internal length in their very formulation. For such media with a microstructure giving rise to size-effects, one has to resort to the NLPE continuum theory, which states that the stress and electric displacement are affected by the strains and electric fields at all points within an influence region. The size of this region is fixed by a nonlocal scalar parameter, as exposed in [255, 259].

In this chapter we apply the flexoelectric homogenization approach to calculate the effective electromechanical moduli for different structures including composite materials and lattice structures. As well, we extend the wave propagation analysis done so far in the literature for piezoelectric waves in periodic composites by including higher gradients of the strain and electric fields as a novel aspect. The wave propagation analysis is performed based on the computed effective flexoelectric properties in situations where gradients are of importance, like in composite materials showing a strong contrast of mechanical and electrical properties of their constituents. Moreover, we employ the nonlocal flexoelectric theory by combining the flexoelectric static properties computed by homogenization with the nonlocality inherent to the NLPE theory.

The outline of this chapter is as follows: The piezoelectric and flexoelectic homogenization theory is exemplified by numerical computations of the homogenized flexoelectric properties of inclusion-based composites in section 5.2 followed by a wave propagation analysis performed in section 5.3, adopting successively the classical flexoelectric theory and the nonlocal flexoelectric theory. Studying of the electromechanical coupling for architected materials is performed in section 5.4 . A summary of the main thrust of the work is given in the conclusion in section 5.5.

5.2 Effective flexoelectric strain gradient properties of composites

We subsequently employ the methodology elaborated in chapter 4 and the algorithm described in section 4.4 to compute the effective homogenized properties of a piezoelectric composite consisting of two piezoelectric materials, namely $LiNbO_3$ employed for the inclusion and Polyfluorure of Vinylidene (PVDF in short) used as the matrix phase. The representative unit cell(UC) is shown in Fig. 5.1 and the properties of both constituents are listed in Table 5.1 [260] and Table 5.2 [261] . The volumetric percentage of $LiNbO_3$ within the unit cell is characterized by the parameter ν_f (here $\nu_f = 0.3$).

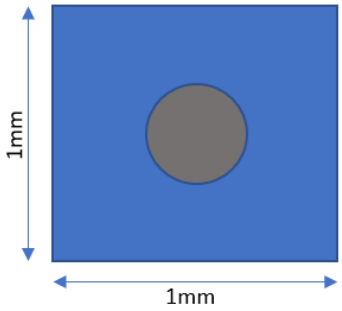

Figure 5.1 Representative unit cell with circular inclusion and square matrix. The unit cell has a linear unit length. The volume fraction of inclusion is 0.3.

Table 5.1 Mechanical and electrical properties of $LiNbO_3$ inclusion [260].

	$LiNbO_3$
Mechanical properties	$E_1 = 170000MPa$
	$\nu_1 = 0.25$
Piezoelectric properties (C/m^2)	$(e_{15})_1 = 3.69$
	$(e_{22})_1 = 2.42$
	$(e_{31})_1 = 0.3$
	$(e_{33})_1 = 1.77$
Dielectric properties $(10^{-10}F/m)$	$(a_{11})_1 = 4.04$
	$(a_{33})_1 = 2.32$

Table 5.2 Mechanical and electrical properties of PVDF matrix [261].

	PVDF
Mechanical properties	$E_2 = 2450MPa$
	$\nu_2 = 0.34$
Piezoelectric properties (C/m^2)	$(e_{15})_2 = 0$
	$(e_{31})_2 = 0.024$
	$(e_{33})_2 = -0.027$
Dielectric properties $(10^{-10}F/m)$	$(a_{11})_2 = 0.655$
	$(a_{33})_2 = 0.673$

The general effective flexoelectric constitutive law for the homogenized medium can be expressed in matrix format as follows (the effective homogenized moduli hold the superscript 'hom' but it is omitted here in the matrix format for simplicity):

$$\begin{pmatrix} \Sigma_{11} \\ \Sigma_{22} \\ \Sigma_{12} \\ \overline{D}_1 \\ \overline{D}_2 \\ S_{111} \\ S_{112} \\ S_{222} \\ S_{221} \\ S_{121} \\ S_{122} \\ R_{11} \\ R_{22} \\ R_{12} \end{pmatrix} = \begin{pmatrix} C_{11} & C_{12} & C_{13} & -e_{11} & -e_{12} & B_{11} & B_{12} & B_{13} & B_{14} & B_{15} & B_{16} & -e_{f11} & -e_{f12} & e_{f13} \\ C_{12} & C_{22} & C_{23} & -e_{21} & -e_{22} & B_{21} & B_{22} & B_{23} & B_{24} & B_{25} & B_{26} & -e_{f21} & -e_{f22} & e_{f23} \\ C_{13} & C_{23} & C_{33} & -e_{31} & -e_{32} & B_{31} & B_{32} & B_{33} & B_{34} & B_{35} & B_{36} & -e_{f31} & -e_{f32} & e_{f33} \\ e_{11} & e_{21} & e_{31} & a_{11} & 0 & F_{11} & F_{12} & F_{13} & F_{14} & F_{15} & F_{16} & e_{D11} & e_{D12} & e_{D13} \\ e_{12} & e_{22} & e_{32} & 0 & a_{22} & F_{21} & F_{22} & F_{23} & F_{24} & F_{25} & F_{26} & e_{D21} & e_{D22} & e_{D23} \\ B_{11} & B_{21} & B_{31} & -F_{11} & -F_{21} & A_{11} & A_{12} & A_{13} & A_{14} & A_{15} & A_{16} & H_{11} & H_{12} & H_{13} \\ B_{12} & B_{22} & B_{32} & -F_{12} & -F_{22} & A_{21} & A_{22} & A_{23} & A_{24} & A_{25} & A_{26} & H_{21} & H_{22} & H_{23} \\ B_{13} & B_{23} & B_{33} & -F_{13} & -F_{23} & A_{31} & A_{32} & A_{33} & A_{34} & A_{35} & A_{36} & H_{31} & H_{32} & H_{33} \\ B_{14} & B_{24} & B_{34} & -F_{14} & -F_{24} & A_{41} & A_{42} & A_{43} & A_{44} & A_{45} & A_{46} & H_{41} & H_{42} & H_{43} \\ B_{15} & B_{25} & B_{35} & -F_{15} & -F_{25} & A_{51} & A_{52} & A_{53} & A_{54} & A_{55} & A_{56} & H_{51} & H_{52} & H_{53} \\ B_{16} & B_{26} & B_{36} & -F_{16} & -F_{26} & A_{61} & A_{62} & A_{63} & A_{64} & A_{65} & A_{66} & H_{61} & H_{62} & H_{63} \\ e_{f11} & e_{f21} & e_{f31} & e_{D11} & e_{D21} & H_{11} & H_{21} & H_{31} & H_{41} & H_{51} & H_{61} & N_{11} & N_{12} & N_{13} \\ e_{f12} & e_{f22} & e_{f32} & e_{D12} & e_{D22} & H_{12} & H_{22} & H_{32} & H_{42} & H_{52} & H_{62} & N_{21} & N_{22} & N_{23} \\ e_{f13} & e_{f32} & e_{f33} & e_{D13} & e_{D23} & H_{13} & H_{23} & H_{33} & H_{43} & H_{53} & H_{63} & N_{31} & N_{32} & N_{33} \end{pmatrix} \begin{pmatrix} E_{11} \\ E_{22} \\ E_{12} \\ E^{elec}_{M\ 1} \\ E^{elec}_{M\ 2} \\ K_{111} \\ K_{112} \\ K_{221} \\ K_{222} \\ K_{121} \\ K_{122} \\ G_{P11} \\ G_{P22} \\ G_{P12} \end{pmatrix} \tag{5.1}$$

The main homogenized flexoelectric properties determined by the proposed flexoelectric homogenization are listed in Table 5.3, with the following physical units: C_{ij}^{hom} is in (MPa), a_{ij}^{hom} is in (10^{-10}F/m), e_{fij}^{hom} is in (10^{-10}C/m), $A_{ij}^{\text{hom}}$is in ($MPa.mm^2$), F_{ij}^{hom} is in (10^{-10} C/m), and N_{ij}^{hom} in ($N.mm^2/V^2$).

Table 5.3 Homogenized mechanical and electrical properties of composite structures modeled as flexoelectric media.

C_{11}^{hom}	C_{12}^{hom}	C_{22}^{hom}	C_{33}^{hom}	a_{11}^{hom}	a_{22}^{hom}	e_{f11}^{hom}	e_{f22}^{hom}	e_{f33}^{hom}	e_{f12}^{hom}
5956.46	2617.33	5956.24	1347.76	0.991	0.92	0.176	0.18	0.0076	-0.21
A_{11}^{hom}	A_{12}^{hom}	A_{22}^{hom}	A_{33}^{hom}	A_{66}^{hom}	A_{55}^{hom}	F_{11}^{hom}	F_{21}^{hom}	N_{11}^{hom}	N_{22}^{hom}
1374.78	485.087	1494.28	473.541	473.448	1493.01	1.8	0.69	1.43	1.4

A comparison with the results obtained in [262] shows a good agreement for the piezoelectric and dielectric coefficients with maximum relative error for the piezoelectric coefficient 3% and for the dielectric coefficient (permittivity) around 1% (see Appendix G).

5.2.1 Impact of the inclusion volume fraction and contrast of properties

The first parameter of interest, influencing the homogenized properties, is the volume fraction of inclusion which is studied by changing the inclusion diameter D (the inclusion domain is the circle, the matrix domain is the square in Fig. 5.1 and L is the unit cell linear length). The second parameter is the ratio of inclusion to matrix tensile moduli, E_f/E_m. Fig. 5.2 through Fig. 5.4 show the variation of the homogenized moduli with the inclusion diameter.

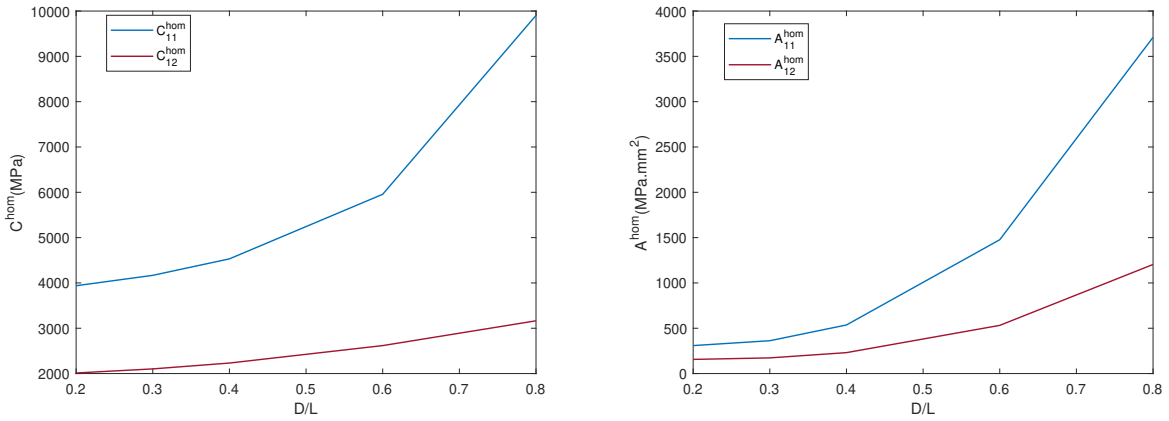

(a) **(b)**

Figure 5.2 Homogenized (a) First gradient rigidity coefficients, (b) Strain gradient rigidity coefficients as function of D/L.

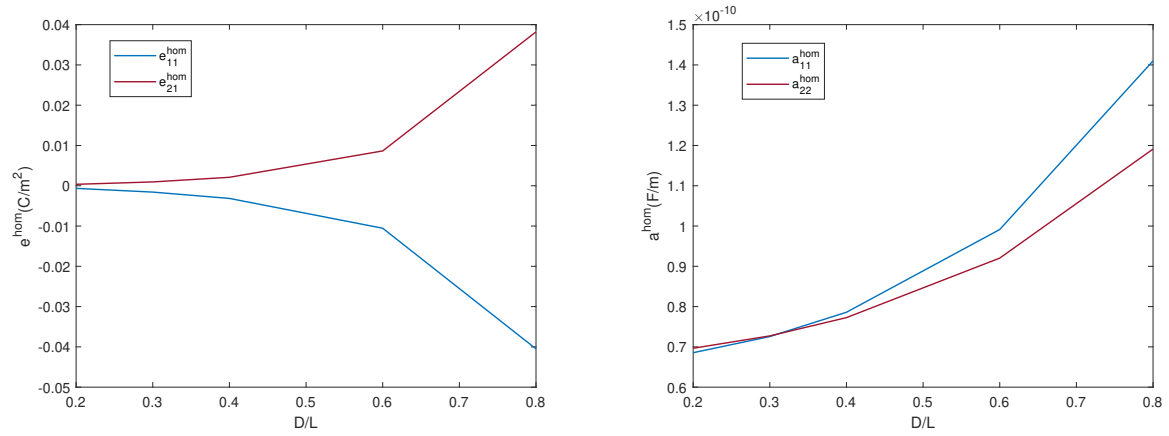

(a) **(b)**

Figure 5.3 Homogenized (a) piezoelectric coefficients $\boldsymbol{e}^{\text{hom}}$, (b) permittivity coefficients $\boldsymbol{a}^{\text{hom}}$ as function of D/L.

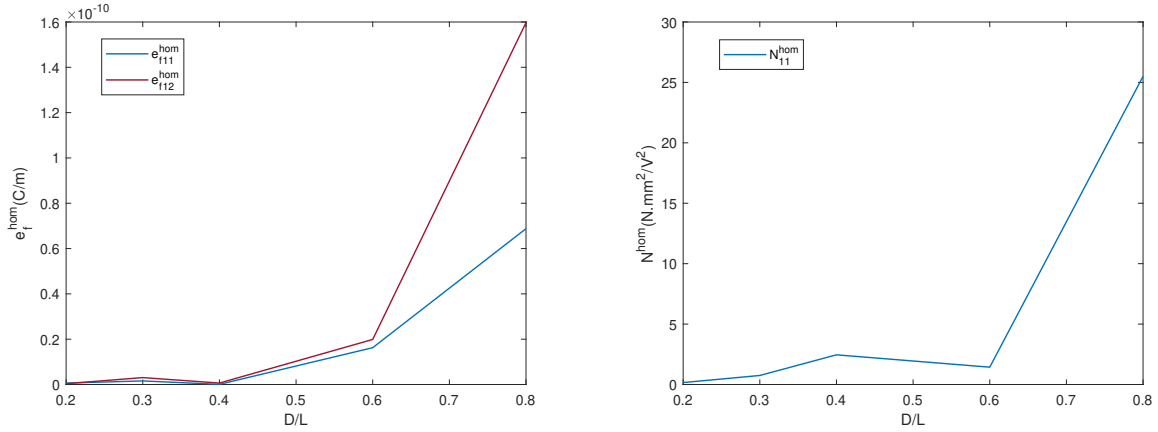

(a) **(b)**

Figure 5.4 Homogenized (a) flexoelectric coefficients $\boldsymbol{e_f}^{\text{hom}}$, (b) coupling coefficient $\boldsymbol{N}^{\text{hom}}$ as function of D/L.

The homogenized coefficients of the first gradient rigidity matrix $\left(C_{11}^{\text{hom}}, C_{12}^{\text{hom}}\right)$ and the strain gradient rigidity matrix $\left(A_{11}^{\text{hom}}, A_{31}^{\text{hom}}\right)$ shown in Fig. 5.2 increase with the inclusion diameter; the increase is due to the corresponding increase in the relative amount of the more rigid phase (inclusion). In the graphs of Fig. 5.3, the absolute value of the coefficient e_{11}^{hom}, and the coefficient e_{21}^{hom} increase with the inclusion's diameter, as well, the permittivity coefficients a_{11}^{hom} and a_{22}^{hom} increase with the diameter of the inclusion. This increase is due to the increasing percentage of the inclusion phase ($LiNbO_3$) having the higher values of permittivity (a_{11}, a_{22}). The flexoelectric coefficients e_{f11}^{hom}, e_{f12}^{hom} in Fig. 5.4(a) are also increasing with the diameter of the inclusion. As well,the coupling coefficient N_{11}^{hom} increase as diameter of the inclusion (ratio D/L) increases in Fig. 5.4(b).

Next, the analysis focuses on how the effective properties of the homogeneous unit cell are impacted by the contrast in Young's modulus between the inclusion and the matrix. To this end, the unit cell in Fig. 5.1 is considered with a radius $R = 0.3\,mm$. The mechanical properties of the PVDF matrix are chosen as in Table 5.2, while those of the inclusion are varied. Fig. 5.5(a) illustrates that when the unit cell is homogeneous (with $E_f/E_m = 1$), the first gradient moduli matches the mechanical properties of PVDF, and experiences a sharp increase as the ratio of inclusion to matrix Young's modulus increases until it reaches a plateau. Fig. 5.5(b) shows that the strain gradient rigidity coefficients start from a non-zero value for the homogeneous unit cell and increase rapidly for a ratio close to 10, beyond which they remain constant. The permittivity coefficient in Fig. 5.6(a) starts from a value that matches the permittivity of PVDF for the homogenized unit cell and then starts decreasing with the ratio of Young's modulus. However, Fig. 5.6(b) shows that the coefficient related to flexoelectricity increases rapidly then converges to a constant value with the ratio of Young's modulus.

The internal lengths are defined in full generality as the ratio between second gradient to first gradient coefficients for the different deformation modes; they quantify the strengths of strain gradient phenomena relative to first gradient ones. For mechanics, the internal lengths express in terms of the rigidity

coefficients as (the superscript s refers to the static case).

$$l^s_{xx} = \sqrt{\frac{A^{\text{hom}}_{11}}{C^{\text{hom}}_{11}}},\ l^s_{xy} = \sqrt{\frac{A^{\text{hom}}_{12}}{C^{\text{hom}}_{12}}} \tag{5.2}$$

These lengths in extension and shear remain nearly constant over the considered range of moduli ratio, with a value about one-half that of the unit cell size. This indicates that the first and second gradient effects equally contribute to the internal length in terms of their sensitivity to the mechanical properties of the individual composite constituents.

The internal lengths for electrical phenomena (described by superscript E) express as the ratio of flexoelectric and permittivity coefficients as

$$l^E_{xx} = \sqrt{\frac{N^{\text{hom}}_{11}}{a^{\text{hom}}_{11}}} \tag{5.3}$$

l^E_{xx} is found to be constant with a value around one-half. This shows that the internal lengths associated to electrical phenomena are approximately the same as those of mechanical phenomena quantified by the internal lengths l^s_{xx}, l^s_{xy}.

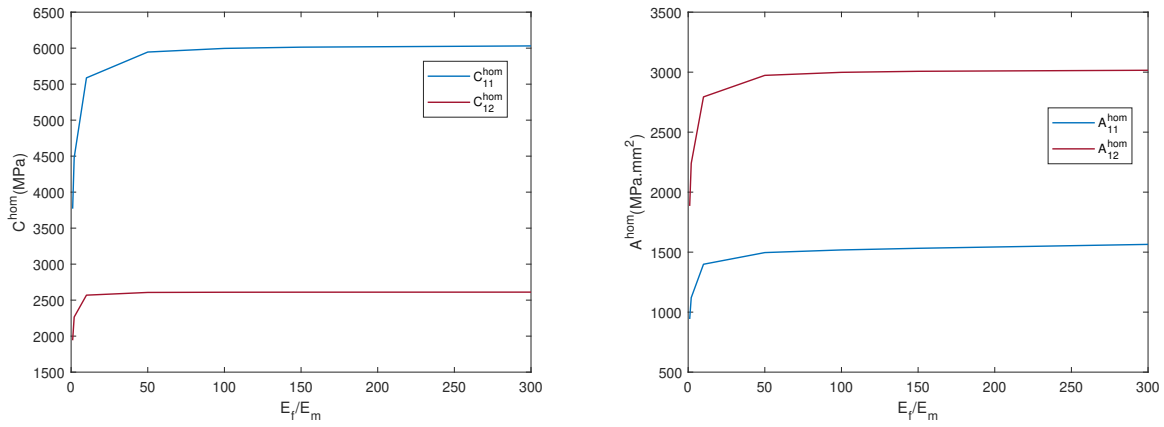

(a) **(b)**

Figure 5.5 Variation of (a) the first gradient rigidity coefficients, and (b) strain gradient rigidity coefficients versus the ratio of inclusion to matrix Young's moduli.

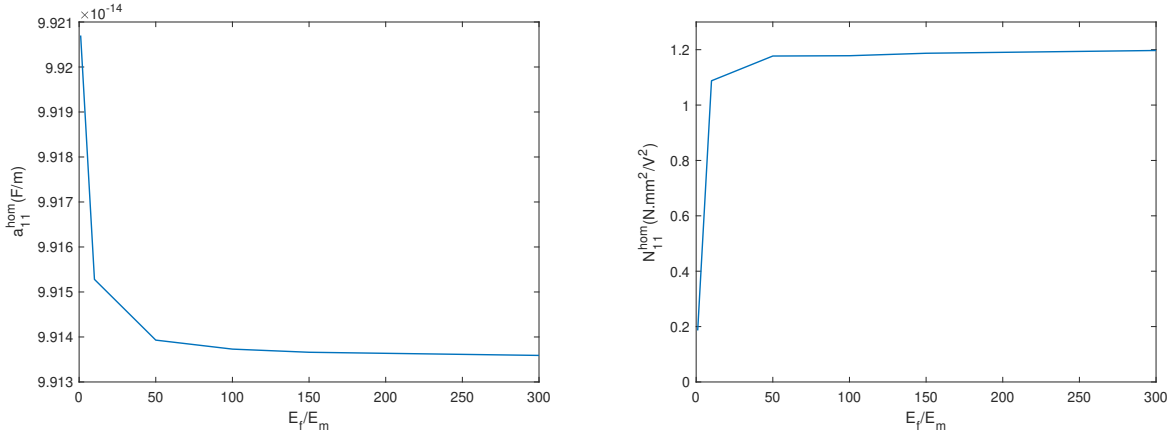

(a) **(b)**

Figure 5.6 Variation of (a) the permittivity coefficient , and (b) the flexoelectric coefficient versus the ratio of inclusion to matrix Young's moduli.

The distribution of the fluctuating displacement along a vertical line passing through the center of the inclusions is represented for one- and four-unit cells (Fig. 5.7) when applying the macroscopic strain $\boldsymbol{E}$ and strain gradient $\boldsymbol{K}$ as kinematic loading over the unit cell. The fluctuating vertical displacement $\tilde{u}_{y2}$ is plotted along the vertical line with the microscopic position y_2 varying from 0 to 1. To this end, Fig. 5.8 shows the computed values of $\tilde{u}_{y2}$ when the unit cell is subjected to the kinematic loading $E_{11} = 1$, and $K_{111} = 1$ respectively for the flexoelectric medium. Across the interface of the inclusion and matrix, the displacement remains continuous. For four unit cells, the fluctuating displacement $\tilde{u}_{y2}$ is repeating the pattern obtained for a single unit cell, and it appears to be nearly constant far away from the interface (in the inclusion). Strong displacement variations are indicators of the existence of the interface between inclusion and matrix.

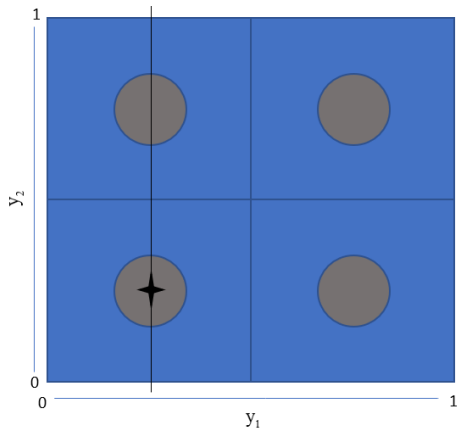

Figure 5.7 Four unit cells with a vertical line passing through the center of inclusions.

In Fig. 5.9 the values of $\tilde{u}_{y2}$ for a single unit cell determined when applying the strain component E_{11} are approximately twice the values for four unit cells; they will become identical when a normalization by the number of unit cells is applied (number of vertical cells as shown in Fig. 5.7,N=2 here), repeating the

pattern obtained for a single unit cell over the neighboring (internal) unit cells. Consequently, the Cauchy homogenized elastic coefficients remain unchanged for computations done with one or a multiple number of periods (since the spatial distribution of the fluctuating displacement does not depend on the unit cell after normalization). Meanwhile, the values of $\tilde{u}_{y2}$ for a single unit cell, determined when applying the strain gradient component K_{111}, are approximately four times the values of for four unit cells.

The constant values of $\tilde{u}_{y2}$ in Fig. 5.9 are related to the position of the inclusion; one can thus predict the diameter of the inclusion from the figures where there is a constant line (for example, from Fig. 5.9, for 1-unit cell: the diameter value is 0.8-0.2=0.6). As observed in Fig. 5.8, the fluctuating displacement values in a flexoelectric medium are less than those in pure elastic medium. This can be related to the piezoelectric nature of materials that can lead to an electric field besides the mechanical deformation.

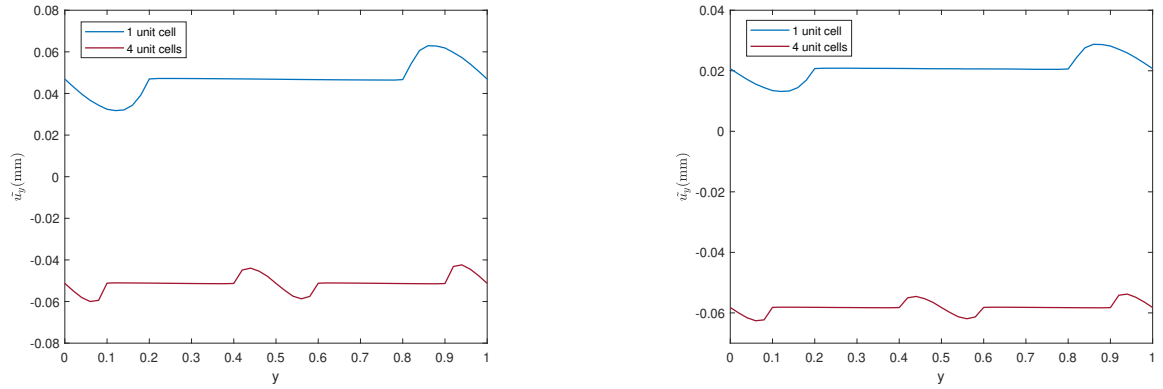

(a) **(b)**

Figure 5.8 Distribution of the vertical fluctuating displacement (in mm) on the vertical axis, due to a) $E_{11} = 1$, and b) $K_{111} = 1$ along a vertical line through the centers of the inclusions for flexoelectric medium.

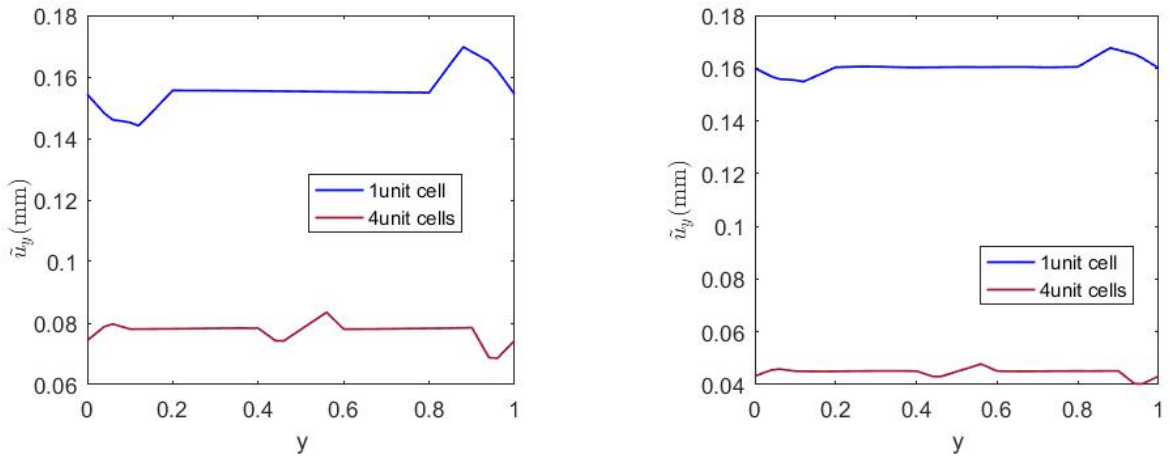

(a) **(b)**

Figure 5.9 Distribution of the vertical fluctuating displacement (in mm) on the vertical axis, due to a) $E_{11} = 1$, and b) $K_{111} = 1$ along a vertical line through the centers of the inclusions for the pure elastic medium with no electric effects.

5.2.2 Contribution of the fluctuation enthalpy for flexoelectric composite materials

In order to investigate the accuracy of modeling the composite by a flexoelectric second gradient continuum, the relative contribution of the fluctuation enthalpy over the total microscopic enthalpy density for the successive components of the Cauchy strain, electric field, strain gradient, and electric field gradient kinematic measures are evaluated. Table 5.4 shows the macroscopic, microscopic, and fluctuation enthalpies for a unit cell with a volume fraction of the $LiNbO_3$ (inclusion) $\nu_f = 0.3$; these energetic contributions are successively defined as follows:

$$\begin{aligned} W_{Macro} &= \frac{1}{2}\left(\boldsymbol{\Sigma} : \boldsymbol{E}-\boldsymbol{E}_{\boldsymbol{M}}^{\boldsymbol{elec}}.\overline{\boldsymbol{D}} + \boldsymbol{S} \therefore \boldsymbol{K}-\boldsymbol{R} : \boldsymbol{G}_p\right) \\ W_{micro} &= \frac{1}{2}\left(\boldsymbol{\sigma} : \boldsymbol{\varepsilon}-\boldsymbol{E}^{elec}.\boldsymbol{D}\right) \\ W_{fluctuation} &= \frac{1}{2}(\boldsymbol{\sigma} : \widetilde{\boldsymbol{\varepsilon}}-\tilde{\boldsymbol{E}}^{elec}.\boldsymbol{D}) \end{aligned} \tag{5.4}$$

As shown in Table 5.4, the values of the microscopic enthalpies, macroscopic and fluctuation enthalpies satisfy the additive decomposition

$$W_{micro} = W_{Macro} + W_{fluctuation} \tag{5.5}$$

Noting that this relation follows from the corresponding decomposition of the microscopic strain and microscopic electric fields into their macroscopic and fluctuating parts.

Over all, the fluctuation enthalpy represents a small amount (about 3%) of the total enthalpy, which shows that the effective flexoelectric medium represents a quite good approximation of the initially heterogeneous piezoelectric composite.

On the other hand, increasing the number of unit cells into four shows that the contribution of fluctuating enthalpy is decreasing, which reveals a convergence of the strain gradient properties as the number of unit cells increases, as shown in Table 5.5.

Table 5.4 Comparison between macroscopic and microscopic enthalpies, and contribution of the fluctuation enthalpy to the total enthalpy (N/mm^2).

Applied component	Macroscopic Enthalpy	Total microscopic Enthalpy	Fluctuation Enthalpy	Contribution of the fluctuation (%)
E_{11}	2978.31	2921.99	-56.3213	1.93
E_{22}	2978.23	2921.88	-56.3507	1.93
$E^{elec}_{M\ 1}$	2620	2540	-76.8	3
$E^{elec}_{M\ 2}$	2616.26	2539.84	-77.328	3
K_{111}	745.243	730.984	-14.2582	1.95
K_{112}	884.494	865.708	-18.7859	2.17
K_{221}	884.491	865.448	-19.043	2.2
K_{222}	745.353	731.083	-14.27	1.95
G_{p11}	5600	5460	-134	2.5
G_{p22}	5597.179	5462.7	-134.4	2.5
G_{p12}	5597.179	5462.78	-134.4	2.5

Table 5.5 Comparison between macroscopic and microscopic enthalpies, and contribution of the fluctuation enthalpy to the total enthalpy (N/mm^2).

Applied component	Contribution of Fluctuating enthalpy for 1 Unit cell	Contribution of Fluctuating enthalpy for 4 Unit cells
E_{11}	1.93	1.89
E_{22}	1.93	1.89
$E^{elec}_{M\ 1}$	3	2.9
$E^{elec}_{M\ 2}$	3	2.9
K_{111}	1.95	1.9
K_{112}	2.17	2
K_{221}	2.2	2
K_{222}	1.95	1.9
G_{p11}	2.5	2.4
G_{p22}	2.5	2.4
G_{p12}	2.5	2.4

The subsequent section of the chapter is devoted to planar wave propagation analysis within flexoelectric media, based on the effective medium description and properties that have been computed.

5.3 Wave propagation analysis in a flexoelectric medium

In this section, the wave propagation analysis within flexoelectric media will be investigated. In such media, the second gradient parameters are incorporated to be more precise in describing the dynamic behavior of the heterogeneous medium based on its effective properties. Using the effective homogenized properties towards piezoelectric and flexoelectric continua in Table 5.3 of the unit cell in Fig. 5.1, the wave propagation attributes of the piezoelectric and flexoelectric composites are determined.

5.3.1 Planar wave formulation for nonlocal flexoelectric media

There are two theories describing the piezoelectric phenomenon: the classical piezoelectricity theory (CPE), and the non-local piezoelectricity theory (NLPE). In the classical piezoelectricity theory (CPE), the stress and electrical displacement at one point depend solely on the local strain and electric field at the same point. Whereas in the NLPE, the stress and electric displacement at one point depend on the strain and electric field of the whole body or within an influence region around each material point [255]. We

extend in this section the CPE and NLPE theories to consider the strain gradient aspects of the medium; (CFE): classical flexoelectric theory and the non-local flexoelectric theory (NLFE in short). Referring to [259], the governing partial differential equations, obtained after a mathematical transformation from the local stress to the non-local stress can be approximated as follows:

$$\begin{aligned}(1-n^2\nabla^2)\boldsymbol{\tau_{ij}} &= \boldsymbol{\Sigma_{ij}}\\ (1-n^2\nabla^2)\boldsymbol{d_k} &= \boldsymbol{D_k}\end{aligned} \tag{5.6}$$

wherein τ_{ij} and d_k are the non-local stress and electric displacement components respectively; Σ_{ij} and D_k are the local stress and electric displacement components, respectively and n is the internal length, which represents the size of the influence region of the stress (it has the dimension of length scale).∇^2 is the 2-D Laplace operator given in Cartesian coordinates by: $\nabla^2 = \frac{\partial^2}{\partial {x_1}^2} + \frac{\partial^2}{\partial {x_2}^2}$.
Under the quasi-electrostatic assumption, and according to [263], the partial differential equations of mechanical wave motion for in-plane wave modes are given by:

$$\begin{aligned}\boldsymbol{\tau_{ij,j}} &= \boldsymbol{\rho \ddot{u}_i}\\ \boldsymbol{d_{k,k}} &= 0\end{aligned} \tag{5.7}$$

where ρ is the effective density of the homogenized medium. The substitution of Eq. 5.6 into Eq. 5.7 leads to the following general equations of motion based on the NLPE theory:

$$\begin{aligned}\boldsymbol{\Sigma_{ij,j}} &= (1-n^2\nabla^2)\boldsymbol{\rho \ddot{u}_i}\\ \boldsymbol{D_{k,k}} &= 0\end{aligned} \tag{5.8}$$

In the context of the non-local theory, the dynamic equilibrium equations describing the wave motion in the homogenized flexoelectric medium write more specifically from Eq. 5.8, and using notation in Eq. 5.1 as:

$$\begin{aligned}&\frac{\partial \Sigma_{11}}{\partial x_1} + \frac{\partial \Sigma_{12}}{\partial x_2} - \frac{\partial^2 S_{111}}{\partial x_1^2} - \frac{\partial^2 S_{122}}{\partial x_2^2} - \frac{\partial^2 S_{121}}{\partial x_1 \partial x_2} = (1-n^2\nabla^2)\rho(\frac{\partial^2 U_1}{\partial t^2})\\ &\frac{\partial \Sigma_{12}}{\partial x_1} + \frac{\partial \Sigma_{22}}{\partial x_2} - \frac{\partial^2 S_{211}}{\partial {x_1}^2} - \frac{\partial^2 S_{222}}{\partial x_2^2} - \frac{\partial^2 S_{221}}{\partial x_1 \partial x_2} = (1-n^2\nabla^2)\rho(\frac{\partial^2 U_2}{\partial t^2})\\ &\frac{\partial \overline{D}_1}{\partial x_1} + \frac{\partial \overline{D}_2}{\partial x_2} - \frac{\partial^2 R_{11}}{\partial x_1^2} - \frac{\partial^2 R_{22}}{\partial x_2^2} - \frac{\partial^2 R_{12}}{\partial x_1 \partial x_2} = 0\end{aligned} \tag{5.9}$$

We consider the propagation of harmonic planar waves for the mechanical and electrical fields of the form:

$$\begin{aligned}U_1(x_1,x_2,t) &= U \exp\ i(\omega t - k_1 x_1 - k_2 x_2)\\ U_2(x_1,x_2,t) &= V \exp\ i(\omega t - k_1 x_1 - k_2 x_2)\\ \Phi(x_1,x_2,t) &= \Phi_0 \exp\ i(\omega t - k_1 x_1 - k_2 x_2)\end{aligned} \tag{5.10}$$

wherein (U_1, U_2) are the components of the displacement field, Φ is the electric potential, all quantities being expressed in a Cartesian basis. The scalar quantities (U, V, Φ_0) are the wave amplitudes, (k_1, k_2) is the wave vector, and ω is the frequency of propagating waves.

By substituting the constitutive law in Eq. 5.1 and the harmonic wave solutions Eq. 5.10 in Eq. 5.9, the wave motion equation is derived in the synthetic form:

$$\Pi(k_1, k_2, \omega, t, \rho, n) \begin{pmatrix} U \\ V \\ \Phi \end{pmatrix} = 0 \tag{5.11}$$

with the matrix Π therein having its components expressed in the Appendix H. The necessary condition of a vanishing determinant of matrix Π is needed for Eq. 5.11 to have an infinite number of solutions. For planar waves without attenuation in the Cartesian coordinate system in 2-D, the propagation constants along the x_1 and x_2 directions are respectively $k_1 = |k|\cos(\Theta)$ and $k_2 = |k|\sin(\Theta)$, where k is the wavenumber and Θ is the angle of incidence of the propagating wave. Any triad (k_1, k_2, ω) obtained by solving the eigenvalue problem in Eq. 5.11 represents the dispersive plane wave propagation at the frequency ω.

5.3.2 Dispersion relations in flexoelectric media in the framework of the classical flexoelectric theory

In this section, the analysis of wave propagation is done on the homogenized composite of Fig. 5.1, using the classical flexoelectric theory ($n = 0$).

Fig. 5.10 shows the dependence of the frequency on the propagating direction for the two given wavenumbers $|k|$=1 and $|k|$=2 in the effective flexoelectric medium. It is observed that as the wavenumber increases, the frequency increases for both shear and longitudinal waves. The non-linear increase in wave frequency as a function of wavenumber (Fig. 5.11) indicates that the flexoelectric medium is a dispersive medium. That is, for each wavenumber, and at a certain incident angle, the wave propagating in the medium will depend on the frequency of incident waves. The irregular shapes of the shear and longitudinal wave diagrams (for $|kL|$=1 and $|kL|$=2) indicate the non-isotropic behavior of the homogenized medium. This is justified by the dependency of the wave frequency on the incident angle of wave propagation. As the wavenumber increases, the irregularity in the shape of the band-diagrams increases for both modes, causing the behavior of the medium to become more anisotropic.

Fig. 5.12 shows the dependency of the propagating frequency on the incident angle of propagation for the wave numbers $|kL|$=1 and $|kL|$=2 within a piezoelectric medium considering no higher gradient effects thus taking only the effective properties related to a pure piezoelectric effective behavior. Inspection of Fig. 5.12 shows that when increasing the wavenumber, an increase in the propagating frequency of the shear and longitudinal waves occur. Unlike the flexoelectric medium (Fig. 5.10), the irregularity in the shape of the wave diagrams (Fig. 5.12) remains the same when increasing the wavenumber. This means that the anisotropic behavior of the piezoelectric medium is similar for increasing wavenumbers.

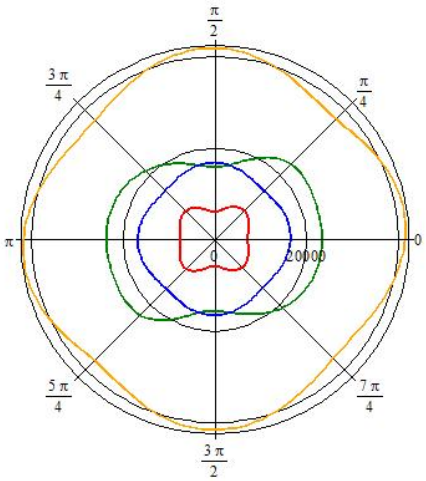

Figure 5.10 Wave frequency in the effective flexoelectric medium for a wavenumber $|kL|$=1 (red: shear waves, blue: longitudinal waves), $|kL|$=2 (green: shear waves, orange: longitudinal waves) as function of the incident angle.

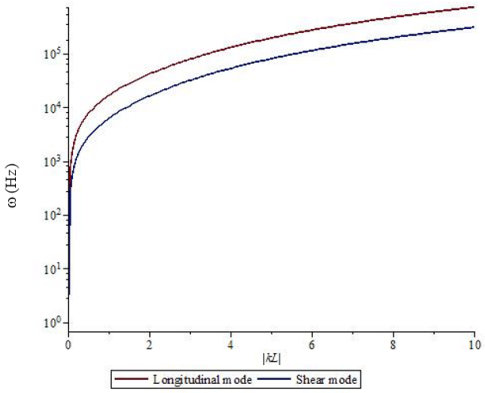

Figure 5.11 Wave frequency as a function of wavenumber in the effective flexoelectric medium.

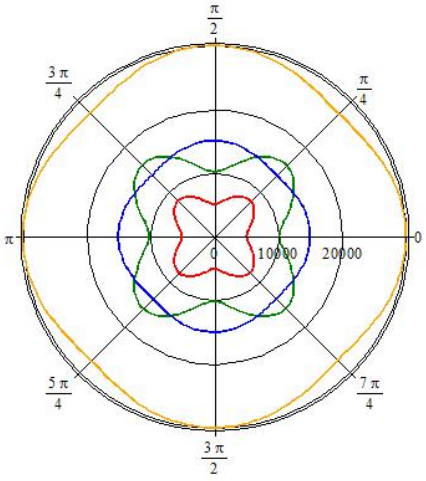

Figure 5.12 Wave frequency in the piezoelectric medium for a wavenumber $|kL|$=1 (red: shear waves, blue: longitudinal waves), $|kL|$=2 (green: shear waves, orange: longitudinal waves) as function of the incident angle.

5.3.3 Effect of the non-locality of the electric field on wave propagation analysis

In this section, the influence of the characteristic internal length n in Eq. 5.9 is analyzed: this parameter affects the non-locality of the electric field.

In Fig. 5.13, we analyze the dependence of the frequency on the wave propagation direction for several values of the normalized non-local parameter n^*, where $n^* := \frac{n}{L}$ and L is the unit cell linear length so that $n^* \in [0,\ 0.01,\ 0.025,\ 0.1,\ 0.4]$. It shows that the frequencies of both propagating modes are impacted by the non-locality parameter n^* of the piezoelectric field. Upon increasing n^*, the cut-off frequencies of the band-diagram decrease for both modes. This entails that the maximum frequency value beyond which no elastic waves can propagate in the composite decreases with the field non-locality to function as a high frequency isolator [263].

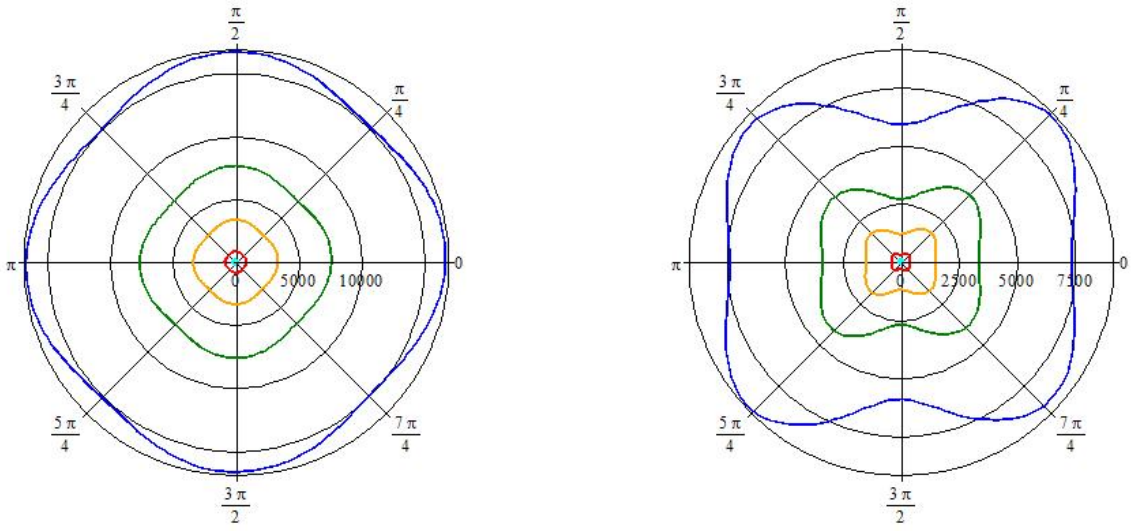

(a) **(b)**

Figure 5.13 Wave frequency in the flexoelectric medium for a) longitudinal waves, b) shear waves, as a function of the incident angle, for $|kL|$=1. Blue: n*=0, green: n*=0.01, orange: n*=0.025, red: n*=0.1, light blue: n*=0.4.

Fig. 5.14 compares the wave frequencies between a piezoelectric medium and a pure elastic medium for the parameter value $n^* = 0.01$ and $|kL|$=1. As shown in Fig. 5.14, the frequencies for a piezoelectric medium are less than those for a pure elastic medium. In the case of a pure piezoelectric medium, the total incident energy is distributed into a mechanical energy that is significant for wave propagation, and an electric energy due to the piezoelectric characteristic of the material. Thus, the consideration of the electric field on a wider region (taking the non-locality effect into consideration) causes the propagating wave frequency to be lower compared to a material with pure mechanical energy.

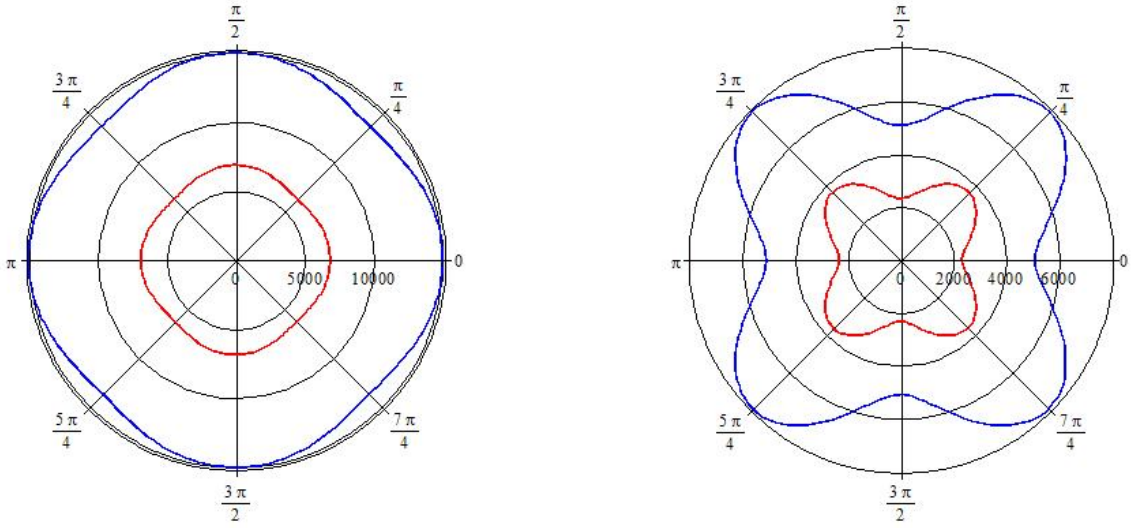

(a) **(b)**

Figure 5.14 Piezoelectric (red) and elastic (blue) frequencies for $|kL|$=1 and $n^* = 0.01$ as a function of the incident angle for a) longitudinal waves and b) shear waves.

In the next section, the previously described homogenization method towards flexoelectric media is applied to different architected materials in order to study the mechanical to electrical coupling.

5.4 Coupling between electric and mechanical effects within lattice structures

The main interest in this section is to study the piezoelectric and flexoelectric response of three different lattice materials, namely the regular hexagon, the re-entrant auxetic hexagon, and the rectangle shown in Fig. 5.15. The regular hexagonal and re-entrant unit cells are defined with length parameters L and h, but with a positive (respectively negative) angular variable θ. For the rectangular unit cell, the defining geometrical parameters are the two lengths L and h (θ=0)(see Fig. 5.15). The methodology mentioned in the previous chapter is applied for different unit cells corresponding to the different lattice structures of Fig. 5.15.

The based materials considered are Lithium Niobate $LiNbO_3$ and Polyvinylidene Fluoride PVDF with their properties mentioned in Table 5.1 and Table 5.2

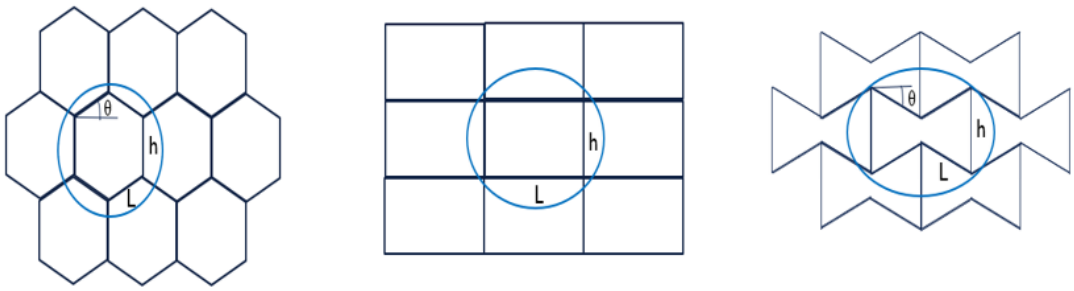

Figure 5.15 Schematic representation of periodic regular hexagonal (θ>0), rectangular (θ=0) and Re-entrant (θ<0) lattices; the UC is indicated with a circle for each microarchitecture.

5.4.1 Distribution of electric potential under a mechanical loading

In this section, the three lattice geometries mentioned above are investigated to show the distribution of the electric field potential ϕ when applying the uniaxial strain component E_{11} over the unit cell boundary. A ratio value $t/L = 0.2$ and an angular variable $\theta = 30^{\circ}$ are adopted for the regular hexagon, while a negative angular variable $\theta = -15^{\circ}$ is selected for the re-entrant hexagonal lattice. Fig. 5.16 highlights the coupling between the electrical and mechanical fields that is visible from the distribution of the electric potential in the beams building the UC.

5.4.2 Sensitivity analysis of piezoelectric and flexoelectric properties to the geometrical UC parameters

A sensitivity analysis of the piezoelectric and flexoelectric coefficients to the geometrical UC parameters is done for the three lattices; the adopted design variables are the dimensionless ratio t/L and the angular variable θ. In Fig. 5.17, and Fig. 5.18, the considered ratio belongs to the interval $t/L \in [0.04, 0.184]$. In Fig. 5.17 the constituent material of the considered regular hexagon, the rectangle, and the re-entrant UCs is $LiNbO_3$. The flexoelectric coupling coefficients for these three UCs are obtained in Fig. 5.18.

As shown in Fig. 5.17, for the three considered UCs, the piezoelectric coefficient increases with the slenderness ratio t/L. The values of e_{22}^{hom} shows that the lattice structure may have a different overall crystal symmetry than that of the constituent material.

However, the flexoelectric coefficient for the hexagonal lattice in Fig. 5.18(a) seems to be decreasing with the ratio t/L, whereas the flexoelectric coefficient increases for the rectangular and re-entrant lattice structures as shown in Fig. 5.18(b)(c). Note that adding a polymer (bi-material structure) makes the structure less rigid under bending thus leading to have higher values of e_{f11}^{hom}. The feature of a two components UC increases the heterogeneity at the microlevel, which entails an increase of the higher order coefficients (flexoelectric coefficient) at the macrolevel.

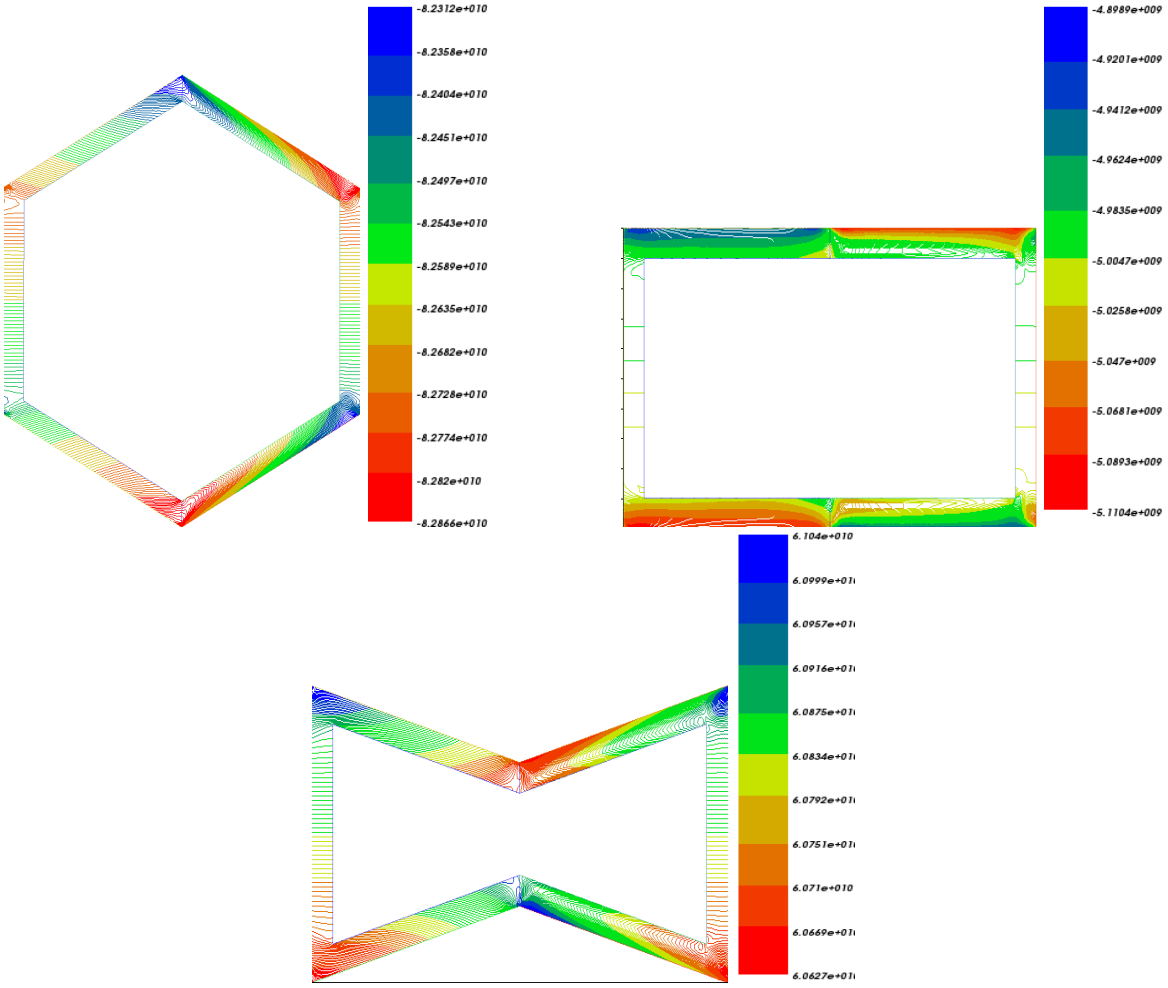

Figure 5.16 Distribution of the electric potential ϕ resulting from the application of the strain component E_{11} for the regular hexagon (first figure), rectangular (second figure) and re-entrant (third figure) UC.

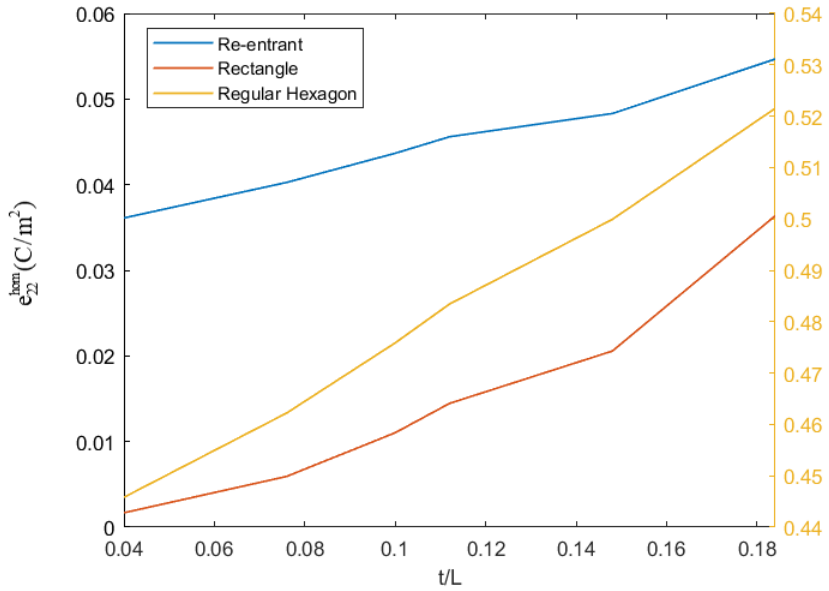

Figure 5.17 Effective piezoelectric coupling coefficient e_{22}^{hom} as a function of the ratio t/L for the three UCs using $LiNbO_3$.

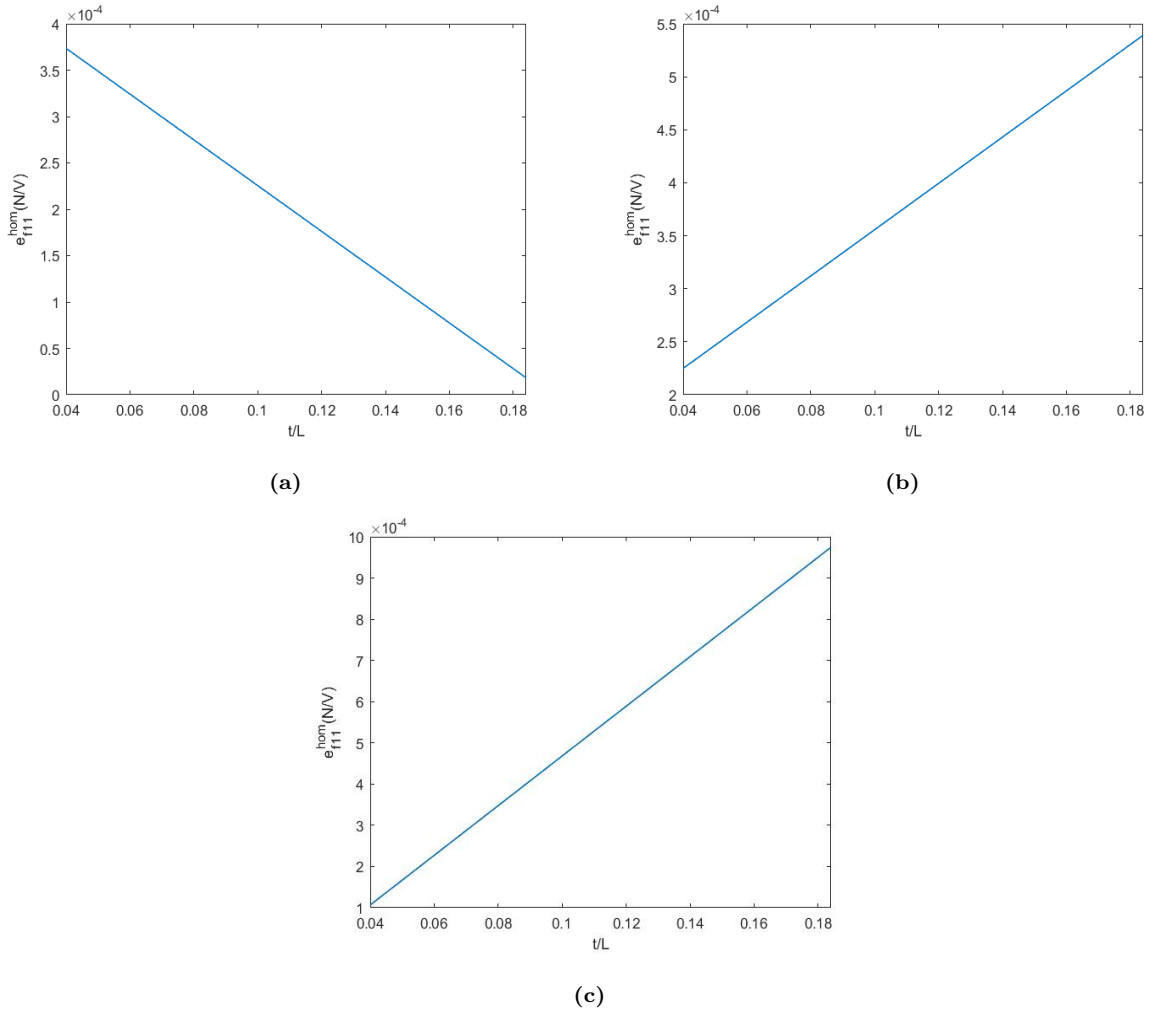

Figure 5.18 Effective flexoelectric coupling coefficient e_{f11}^{hom} as a function of the ratio t/L for a) regular hexagon UC, b) rectangular UC, and c) re-entrant UC considering $LiNbO_3$.

The effective piezoelectric and flexoelectric coefficients are next evaluated as a function of the angular variable for two values of t/L . This angular variable is able to control the topology and auxeticity of the lattice material's UC. Fig. 5.19 shows that the piezoelectric coefficient e_{22}^{hom} reaches the highest value for the regular hexagon, in comparison to the other UCs, for both slenderness ratio values $t/L = 0.04$ and $t/L = 0.1$. In contrast to this behavior, for the flexoelectric coefficient e_{f11}^{hom}, Fig. 5.19 shows that, for both values of t/L, the highest values are obtained for the rectangular lattice (the maximum being reached for $\theta = 0°$). The flexoelectric coefficient decreases further for the regular hexagonal UC($\theta > 0°$).

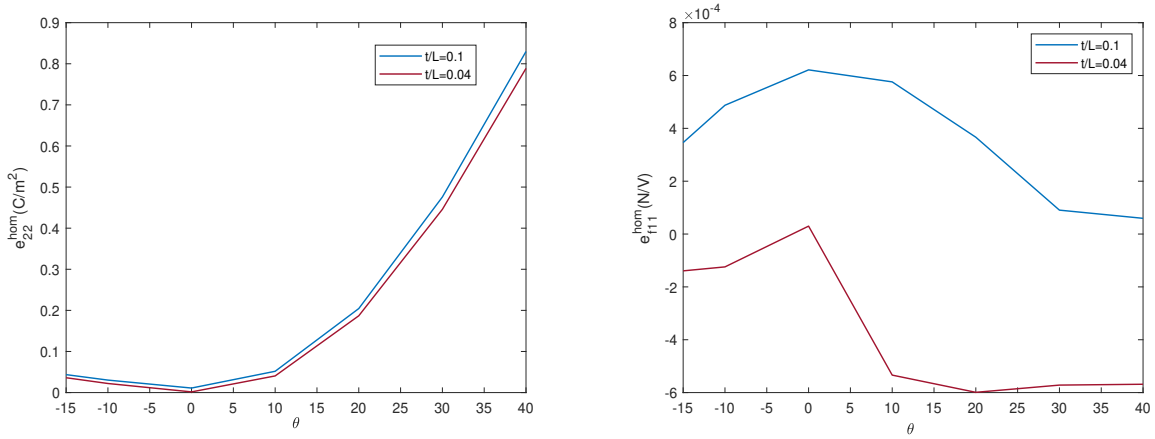

(a) **(b)**

Figure 5.19 Effective piezoelectric coupling coefficient e_{22}^{hom}(a) and flexoelectric coupling coefficient e_{f11}^{hom} (b) as a function of the angular variable of the UC.

5.5 Conclusion

In this chapter, the effective piezoelectric and flexoelectric properties of heterogeneous inclusion-based composites and architected materials have been evaluated numerically as an application of the proposed general homogenization framework that is based on a variational formulation and extended multiphysical Hill macro-homogeneity condition. The effect of the volume fraction and relative tensile modulus of the inclusion versus the one of the matrix phase has been assessed. Energy Computations show that the effective flexoelectric medium represents a quite good approximation of the initially heterogeneous piezoelectric composite. Based on the effective flexoelectric properties, wave propagation has been studied successively in the frameworks of Classical Flexoelectric Theory (CFE) and Non-Local Flexoelectric Theory (NLFE). The results of wave propagation analysis show that flexoelectric medium is a dispersive medium. However, the flexoelectric medium shows a higher anisotropic behavior for increasing the wavenumber, in comparison to the piezoelectric medium. In addition to that, the frequency of wave propagation is found to decrease with the non-local parameter. The frequencies of wave propagation are found to be lower in a piezoelectric medium compared with the pure elastic medium.

A sensitivity analysis to the lattice topology has been carried out, focusing on three types of architected materials having different unit cells: the regular hexagonal UC, the rectangular UC, and the re-entrant UC. This analysis allows studying the variation of the effective piezoelectric and flexoelectric moduli induced by a modification of the topology of the considered UCs. Comparing the three geometries shows that the highest piezoelectric modulus are obtained for the regular hexagonal UC, whereas the flexoelectric modulus is found to be maximum for the rectangular UC. The coupling between mechanical and electrical fields can also be observed through the non-uniform distribution of the electric potential when applying a mechanical strain over the three architected materials.

Chapter 6

Homogenization of magnetoelastic heterogeneous solid bodies based on micropolar magnetoelasticity

Summary

A variational based homogenization method for magnetoelastic composite materials is established in a small strains framework. The existence of a non-symmetrical stress tensor motivates the elaboration of a homogenized Cosserat (micropolar) type magnetoelastic effective medium at the macroscale. Generic expressions of the effective magnetic and elastic properties are derived, showing the existence of couplings between the elastic and magnetic behaviors at the macrolevel. Application of the developed homogenization methodology is done for periodic heterogeneous media where the influence of the magnetic field on the mechanical behaviour of the considered magnetoelastic structure is assessed. The static boundary condition that is applied causes a strong magnetic field to form inside the structure, while the magnetic field leads to a very low strain at the macro level because no such coupling exists at the micro level. The proposed formulation opens new possibilities for an efficient design of multifunctional metamaterials via computational modelling.

6.1 Introduction

The design of metamaterials presents promising avenues for the development of fast actuator systems. The principal bottleneck for their use in applications such as soft biomedical devices, is the need of a mechanical trigger to activate the structural transition. To overcome such a limitation and allow for a remote activation of the metamaterial, the use of stimuli-responsive polymers as bulk material for the metastructure can be considered. In this regard, the emergence of smart materials that respond to external stimuli has been observed. These responsive materials have revolutionized the design and conceptualization of the structures that, now, not only provide mechanical support but also specific functionalities. Some examples of these materials are thermally activated shape memory polymers [264], photo-activated polymers [265], electro-active polymers [266], and magneto-active polymers (MAPs) [267–269]. Currently, responsive polymers can be found in soft robotics [270, 271], vibration controllers or dampers [272] and, especially, in bioengineering applications [273–275].

Specifically, magnetorheological elastomers (MRE) outstand as the preferred solution to activate such transition response, as they allow for a remote activation with several possibilities. The concept of MRE represents magneto-sensitive materials that can adapt their shape, elasticity and motion by external magnetic stimuli [276], undergoing large mechanical deformations. The magneto-mechanical behavior of MREs is determined by the interaction between magnetic forces and the internal stresses within the polymeric matrix. These stimuli-responsive materials have been used for the development of metamaterials with controllable structural changes by application of an external stimulus. In this regard, Schaeffer and Ruzzene [277] proposed a first approach to responsive metamaterials by embedding macroscopic permanent magnets into an elastomeric lattice. Thus, they determined that mechanical instabilities caused by magnetic interactions can be used to trigger changes in the topology and stiffness of the lattice. These mechanical changes can be used to control mechanical wave propagation characteristics within the two-dimensional metastructure. A more advanced system for magneto-active metastructures is due to [278], presenting a new magneto-mechanical metamaterial that allows great tunability through a novel concept of deformation mode branching. Very recently, reconfigurable mechanical behavior of auxetic metamaterial structures has been reported by [279], by proposing a high-throughput magnetic programming strategy based on heating magnetic soft materials above the Curie temperature of the embedded ferromagnetic particles. Then, magnetic domains are reoriented by applying magnetic fields during cooling. A reconfigurable mechanical behavior of an auxetic metamaterial structure was demonstrated using the reprogrammable magnetization capability. Thus, MREs have caught the attention of both industry and scientists, resulting into timely new applications such as soft robotics, vibration absorbers, actuators, soft and flexible electronics, or drug delivery systems [270, 274, 280–283].

To perform the constitutive modelling of these magnetically-hard soft materials, a great amount of articles has been published in recent years, approaching the problem from different points of view. [268, 284] use continuum theories for the elastic deformation of these materials, while [285] and [286, 287] take

into account their viscoelastic effects. On the other hand, micromechanical and lattice models have also been investigated by [288–290]. More recent approaches for modelling these materials propose unified formulations for soft and hard-magnetic particles [287, 291]. A still open question in the modelling of hard-magnetic MREs is whether the presence of body couples arising from Zeeman effects due to the residual magnetization of the particles must be modelled following couple stress continuum theories or, in turn, may be described by micropolar continuum theories.

In this chapter, we explore the latter possibility and the potential of homogenization frameworks to provide efficient computational models for the future design of multifunctional metamaterials. To this end, we first develop a unified formulation of the minimum principle of potential energy in linear magnetoelasticity combined with an extension of Hill-Mandel macrohomogeneity condition for the determination of the effective moduli of magnetoelastic substitution media in the framework of a micropolar (Cosserat) magnetoelastic formulation. The existence of a magnetic torque at the microlevel triggers to go further in the homogenization into Cosserat effective medium where general expressions of the entire set of magnetoelastic Cosserat moduli are provided from localization operators solution of unit cell boundary value problems. Finally, an application of the proposed magnetoelastic homogenization framework is done for a given microstructure showing strain and bending induced by the application of a magnetic field.

Regarding notations, vectors and tensors are denoted by boldface symbols. The transpose of a tensor is written with a superscript notation, for instance $\boldsymbol{B}^T$. The gradient of a tensor field $\boldsymbol{A}(\boldsymbol{y})$ is denoted with the nabla operator $\boldsymbol{A}(\boldsymbol{y}) \otimes \nabla_y$, (with $\otimes$ the tensor product) and its divergence is obtained as the trace of the gradient, denoted $\boldsymbol{A}(\boldsymbol{y}).\nabla_y$, with $\nabla_y$the gradient operator acting on the microscopic position $\boldsymbol{y}$. The symmetrized dyadic product is denoted with $\otimes^s$. The dot product therein represents the internal product in the space of Cartesian tensors. The vector product of two vectors $\boldsymbol{U}, \boldsymbol{V}$ is denoted $(\boldsymbol{U} \times \boldsymbol{V})$, with components $(\boldsymbol{U} \times \boldsymbol{V})_i := \varepsilon_{ijk} U_j V_k$. The vector product of a second order tensor and a vector is the second order tensor defined as $(A \times v)_{ij} := \varepsilon_{jmk} A_{im} v_k$.

6.2 General methodology for the homogenization of magnetoelastic heterogeneous solid bodies

Two distinct scales for composites with periodic microstructures can be identified: the scale of the microstructure and the macroscopic structural scale; an intermediate scale called mesoscopic is sometimes introduced, representing the homogenized microstructure with effective properties that have been computed from an upscaling of the microscopic behavior of the individual constituents of the initially heterogeneous pattern of the composite. Here and in the sequel, vectors $\boldsymbol{y}$ and $\boldsymbol{x}$ denote the microscopic and macroscopic spatial positions of material points with respect to a fixed Cartesian basis, respectively. In the present context of periodic homogenization, the microstructure is identified within a representative

unit cell (Fig. 6.1), which by periodic translation generates the entire composite domain. The unit cell domain consists of at least two phases or constituents with specific mechanical properties.

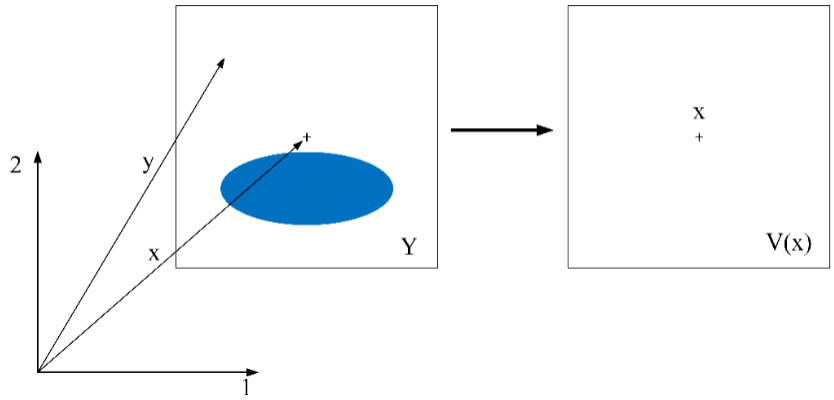

Figure 6.1 Composite periodic unit cell Y made of two elastic materials (left) and the homogeneous substitution medium (right) with domain $V(\boldsymbol{x})$ centered around point $\boldsymbol{x}$.

The center of area of the unit cell, point $\boldsymbol{x}$ on Fig. 6.1, is defined implicitly by the integral relation adopting a fixed Cartesian basis:

$$\frac{1}{|Y|}\int_{Y}(\boldsymbol{y}-\boldsymbol{x})dV_y=\boldsymbol{0} \tag{6.1}$$

In Eq. 6.1, the integration is performed over all micro-points labeled with the position vector within the representative volume element (RVE)(which is the unit cell in this case); relation 6.1 has the significance that the relative position $(\boldsymbol{y}-\boldsymbol{x})$ of the micro-points has zero average over the unit cell. Note that the definition given in Eq. 6.1 is simplified when the origin of coordinates is selected at the center of area of the RVE and it further guarantees the objectivity of the virtual power of internal forces [292]. This will be our choice here and in the sequel so that the relative position vector simply coincides with the microscopic position. The volume average can be defined therein as $\langle(\bullet)\rangle_Y=\frac{1}{|Y|}\int_Y(\bullet)\ \mathrm{dY}$.

6.2.1 Microscopic magnetoelastic boundary value problem

In this subsection, we write the governing equations of magnetoelasticity in small strains framework and in a static situation, so that dynamic terms can be ignored. The set of local governing equations include the stress and magnetic field equilibrium; the constitutive laws are those of an incompressible elastic medium. The small strain tensor which is the symmetrical part of the gradient of the micro-displacement field:

$$\boldsymbol{\varepsilon}:=\boldsymbol{u}\otimes^{s}\nabla \tag{6.2}$$

where $\boldsymbol{u}$ is the displacement field vector.

The magnetic problem includes three main variables, i.e., the magnetic field $\boldsymbol{H}$, the magnetic induction (also called magnetic flux density vector) $\boldsymbol{B}$, and the magnetization vector $\boldsymbol{M}$. These variables can be related by the constitutive equation:

$$\boldsymbol{B} = \mu_0 \left(\boldsymbol{H} + \boldsymbol{M}\right) \rightarrow \boldsymbol{B} = \boldsymbol{B}^r + \mu_0 \boldsymbol{H} \tag{6.3}$$

where μ_0 is the magnetic permeability of vacuum. Note that the work of this chapter considers a magneto-active material composed of a polymeric matrix filled with hard-magnetic particles. These particles, i.e., NdFeB, present high coercivity and a relative magnetic permeability close to one. Therefore, if they are exposed to a strong magnetic field so that the saturation magnetization is reached, a significant residual magnetic flux $\boldsymbol{B}^r$ is present. This residual magnetization remains constant under external magnetic fields below coercivity. Hereafter, we follow these hypotheses to simplify the magnetic problem as proposed by [268], and assume no magnetic dissipation in the hard-magnetic particles under the actuation of low external magnetic fields. For further reading on the effects of considering magnetic dissipation and full magneto-elastic coupling, the reader is referred to the recent works by Danas and co-authors [286,293]. In addition, the recent review by [283] can be consulted for current modelling approaches in hard-magnetic soft materials.

The magneto-elastic problem can be then conceptualized from an energetic formulation based on the definition of a total energy $\Omega\left(\boldsymbol{\varepsilon}, \boldsymbol{H}\right)$ as:

$$\begin{aligned} \Omega\left(\boldsymbol{\varepsilon}, \boldsymbol{H}\right) &= \Psi\left(\boldsymbol{\varepsilon}, \boldsymbol{H}\right) + M_0^*\left(\boldsymbol{H}\right) \\ \Psi\left(\boldsymbol{\varepsilon}, \boldsymbol{H}\right) &= \Psi^{ela}\left(\boldsymbol{\varepsilon}\right) + \Psi^{mag}\left(\boldsymbol{\varepsilon}, \boldsymbol{H}\right) \end{aligned} \tag{6.4}$$

where $M_0^*\left(\boldsymbol{H}\right) = -\frac{1}{2}\mu_0 \boldsymbol{H}.\boldsymbol{H}$ is the free space contribution due to vacuum magnetic permeability, and $\Psi\left(\boldsymbol{\varepsilon}, \boldsymbol{H}\right)$ is the free energy of the material. The latter is additively decomposed into elastic and magnetic contributions. From the definition of this energy, making use of the second law of thermodynamics and with the help of Coleman-Noll argumentation, the following constitutive equations can be obtained:

$$\boldsymbol{\sigma} := \frac{\partial \Omega}{\partial \boldsymbol{\varepsilon}}, \ \boldsymbol{B} = -\frac{\partial \Omega}{\partial \boldsymbol{H}} \tag{6.5}$$

For more details on this derivation and fundamental equations of magneto-mechanics, readers are referred to recent publications [289, 294, 295] and some classical textbooks such as [296, 297].

In the following we define the mechanical potential using linear elasticity theory and the magnetic contribution for hard-magnetic materials as proposed in [268]. The set of balance laws splits into mechanical and magnetic balance equations; the balance of linear momentum writes in terms of Cauchy stress as:

$$
\begin{aligned}
&\boldsymbol{\sigma}.\nabla_y + \boldsymbol{f} = 0 \\
&\boldsymbol{\sigma} = \boldsymbol{\sigma}^{ela} + \boldsymbol{\sigma}^{mag} + \boldsymbol{\sigma}^{Max} \\
&\boldsymbol{\sigma}^{ela} = \lambda Tr\left(\varepsilon\right)\boldsymbol{I} + 2\mu\varepsilon \\
&\boldsymbol{\sigma}^{mag} = \frac{1}{\mu_0}\boldsymbol{B}^r \otimes \boldsymbol{B} = \boldsymbol{\sigma}^{mag,sym} + \boldsymbol{\sigma}^{mag,skew} \\
&\boldsymbol{\sigma}^{mag,sym} = \frac{1}{\mu_0}\left(\boldsymbol{B}^r \otimes \boldsymbol{B} + \boldsymbol{B} \otimes \boldsymbol{B}^r\right), \boldsymbol{\sigma}^{mag,skew} = -\boldsymbol{\tau} \\
&\boldsymbol{\sigma}^{Max} = \frac{1}{\mu_0}\boldsymbol{B} \otimes \boldsymbol{B} - \frac{1}{2\mu_0}\left[\boldsymbol{B}.\boldsymbol{B}\right]\boldsymbol{I}
\end{aligned}
\tag{6.6}
$$

The Cauchy microscopic stress, according to the energetic definition of the problem, has been decomposed additively into elastic, magnetic and Maxwell contributions, tensor $\boldsymbol{\sigma}^{ela}, \boldsymbol{\sigma}^{mag} and\, \boldsymbol{\sigma}^{Max}$, respectively, thereby showing the influence of the magnetic field on the mechanical response; λ and ε are the Lamé coefficients while the vectors $\boldsymbol{f}$ and $\boldsymbol{\tau}$ denote the body forces and magnetic torque respectively. Hereafter the Maxwell term associated to vacuum permeability of free space is not considered as it has negligible effects in the current problem [267]. The magnetic part of the Cauchy stress will be elaborated later on.

The balance of angular momentum shows the non-symmetric nature of Cauchy stress, due to the existence of a magnetic torque $\boldsymbol{\tau}$:

$$
\begin{aligned}
&\epsilon : \left(\frac{\boldsymbol{\sigma} - \boldsymbol{\sigma}^T}{2}\right) + \boldsymbol{\tau} = \boldsymbol{0} \Leftrightarrow \boldsymbol{\sigma}^{skew} + \boldsymbol{\tau} = \boldsymbol{0} \text{ in } Y \\
&\boldsymbol{\tau} = \frac{1}{\mu_0}\boldsymbol{B}^r \times \boldsymbol{B} \text{ in } Y \\
&\boldsymbol{n}.\left[\boldsymbol{\sigma}\right] = \boldsymbol{0} \text{ on } \partial Y
\end{aligned}
\tag{6.7}
$$

with ϵ the third order permutation symbol (Levi-Civita symbol), and $\boldsymbol{\sigma}^{skew}$ the skew symmetric part of the microscopic Cauchy stress, here represented as a pseudo-vector.

The magnetostatic Maxwell's equations are taken for the magnetic balance laws as:

$$
\begin{aligned}
&\boldsymbol{H}(\boldsymbol{y}) = -\varphi(\boldsymbol{y})\nabla_y \Rightarrow Curl\boldsymbol{H} = 0 \text{ in } Y \\
&\boldsymbol{B}.\nabla_y = 0 \text{ in } Y \\
&\boldsymbol{n}.\left[\boldsymbol{B}\right] = 0 \text{ on } \partial Y \\
&\boldsymbol{n} \times \left[\boldsymbol{H}\right] = \boldsymbol{0} \text{ on } \partial Y
\end{aligned}
\tag{6.8}
$$

The magnetic field $\boldsymbol{H}$ is defined from a scalar valued potential φ so that the first balance equation is automatically satisfied. Note that the magnetic potential plays the same role as the displacement, both determining the magnetic field and strain respectively. Within small strains there is non-reciprocity of magnetic and mechanical effects, since the magnetic field generates a stress tensor, whereas mechanics does not influence magnetic phenomena at the microscale (The non-reciprocity is considered as an assumption in this contribution). We note that further extensions of the proposed formulation to finite deformation theory would introduce such a reciprocity due to the spatial gradient in the magnetic balance equation and the transformation of the magnetic fields from reference to current configurations.

The magnetic balance equation writes accordingly, considering here magnetization as an input datum of the BVP

$$\left(\mu_0 . \left(-\varphi(\boldsymbol{y})\nabla_y\right) + \boldsymbol{B^r}\right) . \nabla_y = 0 \tag{6.9}$$

Note that the magnetic field influences the elastic behavior, but the converse does not hold at the microlevel; however, as it will appear later on in this chapter, the cross-coupling (mutual) effects of magnetic and elastic field will be reciprocal after homogenization.

6.2.2 Decomposition of the microscopic kinematic variables into homogeneous and fluctuating contributions

In order to set the stage, the displacement vector is decomposed additively into a homogeneous part $\boldsymbol{u}^{\mathrm{hom}}(\boldsymbol{y})$ affine in the macrostrain kinematic variables of the Cosserat continuum and a periodic fluctuation denoted $\tilde{\boldsymbol{u}}(\boldsymbol{y}) \in H^1_{per}(Y)$, the Sobolev space of Y-periodic displacements, viz it holds

$$\begin{aligned} &\boldsymbol{u}(\boldsymbol{y}) = \boldsymbol{u}^{\mathrm{hom}}(\boldsymbol{y};\boldsymbol{x}) + \tilde{\boldsymbol{u}}(\boldsymbol{y}) \\ &\tilde{\boldsymbol{u}}(\boldsymbol{y}) \;\; Y\text{-periodic} \end{aligned} \tag{6.10}$$

The same decomposition holds for the magnetic field,

$$\begin{aligned} &\boldsymbol{H}(\boldsymbol{y}) = \boldsymbol{H}_M(\boldsymbol{x}) + \tilde{\boldsymbol{H}}(\boldsymbol{y}) \\ &\tilde{\boldsymbol{H}}(\boldsymbol{y}) \;\; Y\text{-periodic} \end{aligned} \tag{6.11}$$

with $\boldsymbol{H}_M(\boldsymbol{x})$ the macroscopic magnetic h-field. Since the magnetization is represented as the gradient of a scalar valued function $\varphi(\boldsymbol{y})$, it holds the following relations:

$$\begin{aligned} &\varphi(\boldsymbol{y}) = \varphi^{\mathrm{hom}}(\boldsymbol{y};\boldsymbol{x}) + \tilde{\varphi}(\boldsymbol{y}) \\ &\tilde{\varphi}(\boldsymbol{y}) \text{ Y-periodic} \\ &\varphi^{\mathrm{hom}}(\boldsymbol{y};\boldsymbol{x}) = -\boldsymbol{H}_M(\boldsymbol{x}).\boldsymbol{y} \\ &\Rightarrow \boldsymbol{H}^{\mathrm{hom}}(\boldsymbol{x}) := -\varphi^{\mathrm{hom}}(\boldsymbol{y};\boldsymbol{x})\nabla_x = \boldsymbol{H}_M(\boldsymbol{x}) \\ &\tilde{\boldsymbol{H}}(\boldsymbol{y}) = -\tilde{\varphi}(\boldsymbol{y})\nabla_y \end{aligned} \tag{6.12}$$

The introduced homogeneous solution $\left\{\boldsymbol{u}^{\mathrm{hom}}(\boldsymbol{y};\boldsymbol{x}), \varphi^{\mathrm{hom}}(\boldsymbol{y};\boldsymbol{x})\right\}$ is a function of both the microscopic and macroscopic variables. The macroscopic position will intervene due to the presence of the macroscopic variables that will enter the homogeneous fields as will appear later. Such a solution describes the response of a (fictive) effective continuum that would behave exactly as the selected homogeneous substitution medium. Thus, the added fluctuation $\{\tilde{\varphi}(\boldsymbol{y}), \tilde{\boldsymbol{u}}(\boldsymbol{y})\}$ in Eq. 6.12 corrects the deviation of the microscopic displacement of the initially heterogeneous medium from that of the postulated homogeneous Cosserat substitution medium. The homogeneous displacement is comparatively more involved and will be evaluated later on.

The determination of the homogeneous displacement, representative of both classical and Cosserat effects, is the first step of the proposed higher-order homogenization method. We will proceed in a two steps method as follows: i) evaluation of the microscopic homogeneous displacement - $\boldsymbol{u}^{\text{hom}}(\boldsymbol{y})$ in Eq. 6.10, and subsequently ii) computation of the fluctuating displacement, vector $\tilde{\boldsymbol{u}}(\boldsymbol{y})$ in the same Eq. 6.10, relying on a variational formulation, before evaluating the effective classical and micropolar moduli.

6.2.3 Elaboration of the balance laws of the effective Cosserat magnetoelastic continuum

The integration of the balance of linear momentum for the stress tensor, Eq. 6.6 over the unit cell domain Y (using the bracket notation) and using Gauss divergence theorem as well as considering the Whitaker averaging theorem for continuous interfaces, namely the relation $<\boldsymbol{\sigma}\otimes\nabla_y>_y =<\boldsymbol{\sigma}>_y\otimes\nabla_x$ [298, 299] leads to the macroscopic equilibrium equation as follows:

$$\langle\boldsymbol{\sigma}\rangle_Y\cdot\nabla_x+\langle\boldsymbol{f}\rangle_Y=0 \tag{6.13}$$

The second microbalance relation is a result of taking the vector product of Cauchy stress equilibrium in the balance Eq. 6.6 by the microscopic position vector '$\boldsymbol{y}$', giving the relation:

$$\epsilon_{ijk}y_j\sigma_{kl,l}+\epsilon_{ijk}y_jf_k=0 \tag{6.14}$$

The couple stress tensor is defined as the second-order tensor $\mu_{ij}:=\epsilon_{ilk}y_l\sigma_{kj}$ and the internal body couple forces as $c_i:=\epsilon_{ijk}y_jf_k$. Recoursing to the divergence theorem, Eq. 6.14 is integrated over the unit cell domain leading to an integral format of the balance law as follows:

$$\int_Y\left(\frac{\partial\mu_{ij}}{\partial y_j}+c_i\right)dV=0 \tag{6.15}$$

Applying the Gauss divergence theorem and averaging Eq. 6.15 over the Y domain, we obtain the second macroscopic equilibrium equation. The equation is adjusted with Whitaker's averaging theorem in cases of coherent and continuous interfaces (where the displacement and traction vectors are uninterrupted across the boundary between different materials), namely $<\boldsymbol{\mu}\otimes\nabla_y>_y =<\boldsymbol{\mu}>_y\otimes\nabla_x$ [298, 299]:

$$\langle\boldsymbol{\mu}\rangle_Y\cdot\nabla_x+\langle\boldsymbol{c}\rangle_Y=0 \tag{6.16}$$

From a physical perspective, the previous equation implies that the average microscopic couple stress tensor within a unit cell, created from Cauchy stress, is balanced to the body couple produced by the body couple density. $\boldsymbol{c}:=\boldsymbol{y}\times\boldsymbol{f}$.

The balance law for the scalar magnetic potential writes similarly based on Eq. 6.9 and on the repeated application of Whitaker theorem in integral format as:

$$\begin{aligned}
&\langle\left(-\mu_0\varphi\left(\boldsymbol{y}\right)\nabla_y+\boldsymbol{B}^{\boldsymbol{r}}\left(\boldsymbol{y}\right)\right).\nabla_y\rangle_Y=0\Rightarrow\langle-\mu_0\varphi\left(\boldsymbol{y}\right)\nabla_y+\boldsymbol{B}^{\boldsymbol{r}}\left(\boldsymbol{y}\right)\rangle_Y.\nabla_x=0\\
&\Rightarrow\mu_0\langle\varphi\left(\boldsymbol{y}\right)\nabla_y\rangle_Y.\nabla_x=\langle\boldsymbol{B}^{\boldsymbol{r}}\left(\boldsymbol{y}\right)\rangle_Y.\nabla_x\Rightarrow\mu_0\Delta_x\langle\varphi\left(\boldsymbol{y}\right)\rangle_Y=\langle\boldsymbol{B}^{\boldsymbol{r}}\left(\boldsymbol{y}\right)\rangle_Y.\nabla_x\\
&\langle\left(\mu_0\boldsymbol{H}+\boldsymbol{B}^{\boldsymbol{r}}\right).\nabla_y\rangle_Y=0\Rightarrow\langle\mu_0\boldsymbol{H}+\boldsymbol{B}^{\boldsymbol{r}}\rangle_Y.\nabla_x=0\Rightarrow\boldsymbol{B}_M:=\langle\mu_0\boldsymbol{H}+\boldsymbol{B}^{\boldsymbol{r}}\rangle_Y
\end{aligned} \tag{6.17}$$

in which Δ_x denotes the macroscopic Laplacian. The last set of relations in Eq. 6.17 is an alternative writing of the same micro and macro magnetic balance equations resulting in the definition of the macro magnetic b-field as the volume average $\boldsymbol{B}_M := \langle \mu_0 \boldsymbol{H} + \boldsymbol{B}^{\boldsymbol{r}} \rangle_Y$. Eqs. 6.13, 6.16, 6.17, are multiplied respectively by the fields $(\boldsymbol{v}, \phi, \psi)$ that represent virtual variations of the micro deformation field, micro rotational field and micro scalar magnetic potential successively. Then, these equations are integrated over the macroscopic homogeneous volume $V(x)$ depicted in Fig. 6.1, leading to the total virtual power of internal forces. After some straightforward steps, the following three balance equations are derived :

$$-\int_{V(x)} \langle \boldsymbol{\sigma} \rangle_Y : \boldsymbol{v} \otimes \nabla_x \; dV + \int_{V(x)} \langle \boldsymbol{f} \rangle_Y \cdot \boldsymbol{v} \; dV + \int_{\partial V(x)} \langle \boldsymbol{\sigma} \rangle_Y \cdot \boldsymbol{v} \; dS = 0 \tag{6.18}$$

$$-\int_{V(x)} \langle \boldsymbol{\mu} \rangle_Y : \phi \nabla_x \; dV + \int_{V(x)} \langle \boldsymbol{c} \rangle_Y \cdot \phi \; dV + \int_{\partial V(x)} \langle \boldsymbol{\mu} \rangle_Y \cdot \phi \; dS = 0 \tag{6.19}$$

$$\int_{V(x)} -\mu_0 \langle \varphi(\boldsymbol{y}) \rangle_y \nabla_x . \; \psi(\boldsymbol{x}) \nabla_x \; dV + \mu_0 \int_{\partial V(x)} \langle \varphi(\boldsymbol{y}) \rangle_y \nabla_x \psi \; dS - \int_{V(x)} \langle \boldsymbol{B}^r(\boldsymbol{y}) \rangle_y . \nabla_x \; \psi(\boldsymbol{x}) \; dV = 0 \tag{6.20}$$

The additive decomposition of the microscopic stress into an elastic and magnetic contribution entails a similar decomposition of the macroscopic stress and bending moment ($\overline{\boldsymbol{M}}$):

$$\begin{aligned}
&\boldsymbol{\Sigma}_M := \langle \boldsymbol{\sigma} \rangle_Y = \langle \boldsymbol{\sigma}^{sym} \rangle_Y + \langle \boldsymbol{\sigma}^{skew} \rangle_Y = \boldsymbol{\Sigma}_M^{ela} + \boldsymbol{\Sigma}_M^{mag} \\
&\boldsymbol{\Sigma}_M^{ela} := \langle \boldsymbol{\sigma}^{ela} \rangle_Y, \; \boldsymbol{\Sigma}_M^{mag} := \langle \boldsymbol{\sigma}^{skew} \rangle_Y = -\langle \boldsymbol{\tau} \rangle_Y \\
&\overline{\boldsymbol{M}} := \langle \boldsymbol{\mu} \rangle_Y = \overline{\boldsymbol{M}}^{ela} + \overline{\boldsymbol{M}}^{mag} \\
&\overline{\boldsymbol{M}}^{ela} := \langle \boldsymbol{\mu}^{ela} \rangle_Y, \; \overline{\boldsymbol{M}}^{mag} := \langle \boldsymbol{\mu}^{mag} \rangle_Y
\end{aligned} \tag{6.21}$$

The superscripts 'sym' and 'skew' respectively denote the symmetrical and skew-symmetrical parts of a second order tensor, with the decomposition of the macro fields into symmetrical and skew-symmetrical parts following the corresponding split done at the microlevel in Eq. 6.6. The subscript 'M' is used here and in the sequel to denote quantities evaluated at the macrolevel, to distinguish them from their microscopic counterpart.

Eqs. 6.18, 6.19, 6.20 can then lead to six contributions, P_c^e,P_{mag}^e,P_m^e, P_c^i,P_{mag}^i,P_m^i,with the indices e, i, c, m, mag representing respectively the external, internal, Cauchy, magnetic and micropolar powers (the mechanical powers themselves decomposing into elastic and magnetic contributions):

$$\begin{aligned}
P_c^i &= -\int_{V(x)} \langle \boldsymbol{\sigma} \rangle_Y : \boldsymbol{v} \otimes \nabla_x dV = -\int_{V(x)} \langle \boldsymbol{\sigma}^{sym} \rangle_Y : \boldsymbol{v} \otimes \nabla_x dV - \int_{V(x)} \langle \boldsymbol{\sigma}^{skew} \rangle_Y : (\boldsymbol{v} \otimes \nabla_x)^{skew} dV = P_{c,ela}^i + P_{c,mag}^i \\
P_m^i &= -\int_{V(x)} \langle \boldsymbol{\mu} \rangle_Y : \phi \otimes \nabla_x dV = P_{m,mag}^i \\
P_{mag}^i &= -\mu_0 \int_{V(x)} \langle \varphi(\boldsymbol{y}) \rangle_Y \nabla_x . \; \psi \nabla_x dV + \int_{V(x)} \langle \boldsymbol{B}^r(\boldsymbol{y}) \rangle_Y . \; \psi \nabla_x dV
\end{aligned} \tag{6.22}$$

$$
\begin{aligned}
P_c^e &= \int\limits_{V(x)} \langle \boldsymbol{f} \rangle_Y \cdot \boldsymbol{v} dV + \int\limits_{\partial V(x)} \langle \boldsymbol{\sigma} \rangle_Y \cdot \boldsymbol{v} ds = P_{c,ela}^e + P_{c,mag}^e \\
P_m^e &= \int\limits_{V(x)} \langle \boldsymbol{c} \rangle_Y \cdot \phi dV + \int\limits_{\partial V(x)} \langle \boldsymbol{\mu} \rangle_Y \cdot \phi ds = P_{m,ela}^e + P_{m,mag}^e \\
P_{mag}^e &= \mu_0 \int\limits_{\partial V(x)} \langle \varphi(\boldsymbol{y}) \rangle_Y \nabla_x . \psi dS - \int\limits_{\partial V(x)} \left(\boldsymbol{B}^r(\boldsymbol{x}) \right) . \psi dV
\end{aligned}
\tag{6.23}
$$

In Eq. 6.22, we have introduced the additive decomposition of the stress into a symmetrical part reflecting mechanical effects and a skew-symmetrical one associated to the magnetic torque, see Eq. 6.7. The conjugated kinematic variables are respectively the small strain tensor and the skew-symmetrical part of the micro displacement gradient, represented by its axial vector (when similarly, the magnetic stress is represented as a pseudo-vector). Relations 6.22 for the inner virtual powers completed by the definition introduced in Eq. 6.21 include part of the effective macro variables, the full elaboration of which articulated in Hill macrohomogeneity condition will deserve the developments of next section.

6.3 Hill-Mandel macrohomogeneity condition and magnetoelastic homogenization

The postulated Hill macrohomogeneity condition for the magnetoelastic formulation states that the average of the microscopic virtual power is identical to the macroscopic virtual power of the effective Cosserat magnetic continuum. It holds the following identity in a situation of scale separation, i.e. when the microstructure typical size is much smaller than the macroscopic characteristic length:

$$
\Omega_M(\boldsymbol{E}_M, \boldsymbol{K}_M, \boldsymbol{H}_M) = \frac{1}{2}\left(\boldsymbol{\Sigma}_M : \boldsymbol{E}_M + \overline{\boldsymbol{M}} : \boldsymbol{K}_M - \boldsymbol{B}_M . \boldsymbol{H}_M \right) = \frac{1}{2} \langle \boldsymbol{\sigma} : \boldsymbol{\varepsilon} - \boldsymbol{B} . \boldsymbol{H} \rangle_Y \tag{6.24}
$$

Previous relation entails the following macroscopic constitutive law given from the macroscopic potential $\Omega_M(\boldsymbol{E}_M, \boldsymbol{K}_M, \boldsymbol{H}_M)$:

$$
\boldsymbol{\Sigma}_M = \frac{\partial \Omega_M(\boldsymbol{E}_M, \boldsymbol{K}_M, \boldsymbol{H}_M)}{\partial \boldsymbol{E}_M}, \ \overline{\boldsymbol{M}} = \frac{\partial \Omega_M(\boldsymbol{E}_M, \boldsymbol{K}_M, \boldsymbol{H}_M)}{\partial \boldsymbol{K}_M}, \ \boldsymbol{B}_M = -\frac{\partial \Omega_M(\boldsymbol{E}_M, \boldsymbol{K}_M, \boldsymbol{H}_M)}{\partial \boldsymbol{H}_M} \tag{6.25}
$$

The strain energy contribution can further be decomposed into a symmetrical and skew-symmetrical part reflecting the fact that the stress is not symmetrical due to the existence of a magnetic torque responsible for a non-symmetric microscopic stress tensor:

$$
\begin{aligned}
&\frac{1}{2}(\boldsymbol{\Sigma}_M : \boldsymbol{E}_M + \overline{\boldsymbol{M}} : \boldsymbol{K}_M - \boldsymbol{B}_M . \boldsymbol{H}_M) = \frac{1}{2}(\boldsymbol{\Sigma}_M^{sym} : \boldsymbol{E}_M^{sym} + \boldsymbol{\Sigma}_M^{skew} . \boldsymbol{E}_M^{skew} + \overline{\boldsymbol{M}} : \boldsymbol{K}_M - \boldsymbol{B}_M . \boldsymbol{H}_M) = \\
&= \frac{1}{2} \langle \boldsymbol{\sigma} : \boldsymbol{\varepsilon} - \boldsymbol{B} . \boldsymbol{H} \rangle_Y
\end{aligned}
\tag{6.26}
$$

wherein the last relation traduces the same Hill macrohomogeneity condition written in Eq. 6.24, but here explicitly distinguishing the symmetrical and skew-symmetrical contributions.

The virtual power of the effective continuum at the macroscopic level can be expressed as the sum of the Cauchy internal power, the power of magnetic fields, and the internal power of micropolar medium,

using Hill-Mandel macrohomogeneity condition for the last relation:

$$\begin{aligned}\delta W_M = -(P^i_{ela} + P^i_m + P^i_{mag}) &= \frac{1}{|V(x)|}\left\{\int_{V(x)} \langle\boldsymbol{\sigma}\rangle_Y : \boldsymbol{v}\otimes\nabla_x dV + \int_{V(x)} \langle\boldsymbol{\mu}\rangle_Y : \phi\nabla_x dV - \int_{V(x)} \langle\boldsymbol{B}\rangle_Y .\psi\nabla_x dV\right\} \\ &\equiv \delta\left(\frac{1}{|Y|}\int_Y \frac{1}{2}\left(\boldsymbol{\sigma}:\boldsymbol{\varepsilon} - \boldsymbol{B}.\boldsymbol{H}\right) dV_y\right) = \boldsymbol{\Sigma}_M : \delta\boldsymbol{E}_M + \overline{\boldsymbol{M}} : \delta\boldsymbol{K}_M - \boldsymbol{B}_M.\delta\boldsymbol{H}_M\end{aligned} \tag{6.27}$$

The last relation in Eq. 6.27 is the extended Hill macrohomogeneity condition representing the equivalence between the macroscopic energy and the volume-averaged microscopic energy density, expressed here in the form of virtual power.

The macroscopic kinematic variables, $\boldsymbol{E}_M(\boldsymbol{x})$, $\boldsymbol{K}_M(\boldsymbol{x})$, $\boldsymbol{H}_M$ are then defined, representing the second-order micropolar strain tensor, the macroscopic curvature tensor and the macro magnetic field, respectively:

$$\boldsymbol{E}_M(\boldsymbol{x}) := \boldsymbol{U}\otimes\nabla_x - \epsilon\cdot\boldsymbol{\Phi}(\boldsymbol{x}) \tag{6.28}$$

$$\boldsymbol{K}_M(\boldsymbol{x}) := \boldsymbol{\Phi}(\boldsymbol{x})\otimes\nabla_x \tag{6.29}$$

$$\boldsymbol{H}_M(\boldsymbol{x}) :=\text{-}\langle\varphi(\boldsymbol{y})\rangle_Y\nabla_x \tag{6.30}$$

wherein $\boldsymbol{U}$ is the macro displacement and $\boldsymbol{\Phi}(\boldsymbol{x})$ is the macro rotation tensor. The definition of the averaged kinematic tensors is presented by the set of following relations:

$$\begin{aligned}&\boldsymbol{U}(\boldsymbol{x}) := \frac{1}{|Y|}\int_Y \boldsymbol{u}(\boldsymbol{y})dV_y \\ &\boldsymbol{E}^{sym}_M(\boldsymbol{x}) := \frac{1}{2}\left(\boldsymbol{E}_M(\boldsymbol{x}) + \boldsymbol{E}_M{}^T(\boldsymbol{x})\right) = \frac{1}{|Y|}\int_Y \boldsymbol{\varepsilon}(\boldsymbol{y})dV_y = \left(\frac{1}{|Y|}\int_Y \boldsymbol{u}(\boldsymbol{y})\otimes\nabla_y dV_y\right)^{sym} \\ &\boldsymbol{\Phi}(\boldsymbol{x}) := \frac{1}{|Y|}\int_Y \phi(\boldsymbol{y})dV_y \rightarrow \epsilon_{ijk}\Phi_k(\boldsymbol{x}) := \frac{6}{l^2\,|Y|}\int_Y \boldsymbol{u}(\boldsymbol{y})\times(\boldsymbol{y}-\boldsymbol{x})\,dV_y \\ &\boldsymbol{E}^{Tskew}_M(\boldsymbol{x}) = skew(\boldsymbol{U}\otimes\nabla_x)^{skew} - \epsilon\cdot\boldsymbol{\Phi}(\boldsymbol{x}) = \frac{1}{|Y|}\int_Y\left((\boldsymbol{u}(\boldsymbol{y})\otimes\nabla_y)^{skew} + \frac{6}{l^2}\boldsymbol{u}(\boldsymbol{y})\times(\boldsymbol{y}-\boldsymbol{x})\right)dV_y \\ &\rightarrow \boldsymbol{E}_M = \boldsymbol{E}^{sym}_M + \boldsymbol{E}^{Tskew}_M \\ &\boldsymbol{K}_M(\boldsymbol{x}) := \boldsymbol{\Phi}(\boldsymbol{x})\otimes\nabla_x\end{aligned} \tag{6.31}$$

with $\boldsymbol{E}^{Tskew}_M$ the second-order skew-symmetric strain tensor, and the scalar l the side length of the unit cell. The skew-symmetric part of the macroscopic strain can be elaborated as:

$$\begin{aligned}&\boldsymbol{\omega} = \frac{1}{2}\left((\boldsymbol{U}\otimes\nabla_x) - (\boldsymbol{U}\otimes\nabla_x)^T\right) \\ &\varpi = \epsilon:\boldsymbol{\omega} \\ &\boldsymbol{E}^{skew}_M = \varpi - 2\boldsymbol{\Phi}\end{aligned} \tag{6.32}$$

with $\boldsymbol{E}^{skew}_M$ being the pseudo-vector dual to the antisymmetric tensor $\boldsymbol{E}^{Tskew}_M$ (likewise, the vector ϖ is dual to the skew-symmetric tensor $\boldsymbol{\omega}$). As mentioned in [300], the macroscopic kinematic tensors can be derived by minimizing the quadratic difference between the microscopic displacement field and its

quadratic homogeneous approximation. The subsequent computations use the vector form of $\boldsymbol{E}_M^{skew}$. The consideration of the expressions Eq. 6.28 through Eq. 6.31 leads to the macroscopic micropolar energy density, function $\Omega_M\left(\boldsymbol{E}_M^{sym},\boldsymbol{E}_M^{skew},\boldsymbol{K}_M,\boldsymbol{H}_M\right)$ in a variational form as:

$$\begin{aligned}\delta W_M &= \boldsymbol{\Sigma}_M : (\delta \boldsymbol{E}_M + \epsilon \cdot \delta \boldsymbol{\Phi}) + \overline{\boldsymbol{M}} : \delta \boldsymbol{K}_M - \boldsymbol{B}_M.\delta \boldsymbol{H}_M \\ \rightarrow \delta W_M &= \boldsymbol{\Sigma}_M^{sym} : \delta \boldsymbol{E}_M^{sym} + \boldsymbol{\Sigma}_M^{skew} \cdot \delta \boldsymbol{E}_M^{skew} + \overline{\boldsymbol{M}} : \delta \boldsymbol{K}_M - \boldsymbol{B}_M.\delta \boldsymbol{H}_M\end{aligned} \tag{6.33}$$

with the macroscopic stress and the couple stress tensors expressed as follows:

$$\begin{aligned}&\frac{1}{2}\left(\boldsymbol{\Sigma}_M(\boldsymbol{x}) + \boldsymbol{\Sigma}_M^T(\boldsymbol{x})\right) = \boldsymbol{\Sigma}_M^{sym}(\boldsymbol{x}) := \frac{1}{|Y|}\int\limits_Y \boldsymbol{\sigma}^{sym}(\boldsymbol{y})dV_y \\ &\boldsymbol{\Sigma}_M^{skew}(\boldsymbol{x}).\boldsymbol{N}(\boldsymbol{x}) := \int\limits_{\partial Y} \boldsymbol{n}\cdot(\boldsymbol{y}\times\boldsymbol{\sigma}(\boldsymbol{y}))\,ds = \int\limits_{\partial Y} \boldsymbol{n}\cdot\epsilon\cdot\boldsymbol{y}\otimes\boldsymbol{\sigma}(\boldsymbol{y})ds = \\ &\int\limits_Y (\boldsymbol{y}\times\boldsymbol{\sigma}(\boldsymbol{y}))\,.\nabla_y dv \equiv \langle \boldsymbol{y}\times\boldsymbol{\sigma}(\boldsymbol{y})\rangle\,.\nabla_x \Rightarrow \boldsymbol{\Sigma}_M^{skew} := \int\limits_Y (\epsilon\cdot\boldsymbol{y}\otimes\boldsymbol{\sigma}(\boldsymbol{y}))\,.\nabla_y\, dv \equiv \int\limits_Y \boldsymbol{\sigma}^{skew}(\boldsymbol{y})dv \\ &\boldsymbol{\Sigma}_M^{Tskew} = -\epsilon\cdot\boldsymbol{\Sigma}_M^{skew} \\ \rightarrow &\boldsymbol{\Sigma}_M = \boldsymbol{\Sigma}_M^{sym} + \boldsymbol{\Sigma}_M^{Tskew} \\ &\boldsymbol{\mu}(\boldsymbol{y}) := \boldsymbol{y}\times\boldsymbol{\sigma}(\boldsymbol{y}) \Leftrightarrow \mu_{ij} := \varepsilon_{imk}\sigma_{jm}y_k \rightarrow \overline{\boldsymbol{M}}(\boldsymbol{x}) := \frac{1}{|Y|}\int\limits_Y \boldsymbol{\mu}(\boldsymbol{y})dV_y\end{aligned} \tag{6.34}$$

Here, $\boldsymbol{\Sigma}_M^{skew}$ represents the pseudo-vector, dual to the second-order skew-symmetric stress tensor $\boldsymbol{\Sigma}_M^{Tskew}$; we have considered as a matter of simplification the case of nil body forces. The stress measures further decompose into elastic and magnetic contributions, based on Eq. 6.25:

$$\begin{aligned}\boldsymbol{\Sigma}_M^{sym} &= \frac{\partial \Omega_M}{\partial \boldsymbol{E}_M^{sym}} = \boldsymbol{\Sigma}_M^{sym,ela} + \boldsymbol{\Sigma}_M^{sym,mag}, \\ \boldsymbol{\Sigma}_M^{skew} &= \frac{\partial \Omega_M}{\partial \boldsymbol{E}_M^{skew}} = \boldsymbol{\Sigma}_M^{skew,ela} + \boldsymbol{\Sigma}_M^{skew,mag}, \\ \overline{\boldsymbol{M}} &= \frac{\partial \Omega_M}{\partial \boldsymbol{K}} = \overline{\boldsymbol{M}}^{ela} + \overline{\boldsymbol{M}}^{mag}\end{aligned} \tag{6.35}$$

The reader is referred to [301] for more details of the homogenization method for pure Cosserat homogenization (without magnetic effects).

6.4 Determination of the homogenized micropolar magnetoelastic properties

To find the effective moduli of the Cosserat magnetoelastic substitution medium, a two-step process is followed. The first step involves determining the homogeneous part of the microscopic displacement and magnetic potential, as shown in Eq. 6.10 and Eq. 6.12. The second step involves using a variational principle to obtain the fluctuating part, which corrects for any deviation in the response of the heterogeneous medium from the homogenized substitution medium. The successive situations of magnetoelastic homogenization in the Cauchy and micropolar contexts are successively handled. The first situation corresponds to a nil or negligible magnetic torque, which entails a symmetrical

microscopic Cauchy stress. In order to set the stage in the homogenization methodology, the homogeneous contribution to the microscopic displacement is evaluated versus the macroscopic flux type variables.

6.4.1 Elaboration of the microscopic homogeneous part of the displacement

By examining the static variables defined in Eq. 6.34, we can relate the homogeneous component of the displacement defined in Eq. 6.10 to the macroscopic kinematic variables, grouped together in a set $\left\{\boldsymbol{E}_M^{sym}(\boldsymbol{x}), \boldsymbol{E}_M^{skew}(\boldsymbol{x}), \boldsymbol{K}(\boldsymbol{x})\right\}$, and can be determined by adding up the following contributions. The first contribution comes from *Eq.* 6.34_1, which relates the stress and strain energy densities at the micro level, $\sigma_{ij} = \frac{\partial w_\mu(\varepsilon_{ij})}{\partial \varepsilon_{ij}}$, and provides a set of relations that are valid for any stress component:

$$\Sigma_{M}{}_{ij}^{sym} = \left\langle \sigma_{ij}^{sym} \right\rangle_Y = \left\langle \sigma_{kl}^{sym} \frac{\partial \varepsilon_{kl}}{\partial E_{M}{}_{ij}^{sym}} \right\rangle_Y \rightarrow \int_Y \sigma_{kl}^{sym} \left(\frac{\partial \varepsilon_{kl}}{\partial E_{M}{}_{ij}^{sym}} - I_{ijkl} \right) dV_y = 0, \quad \forall \sigma_{kl}^{sym} \tag{6.36}$$

where I_{ijkl} is defined as the fourth-order identity tensor. Note that the magnetic torque arising in Eq. 6.7 does only influence the skew-symmetrical part of the stress. Considering the arbitrary stress tensor in Eq. 6.36 leads to the expression of the microscopic strain versus the macroscopic strain

$$\frac{\partial \varepsilon_{kl}}{\partial E_{M}{}_{ij}^{sym}} - I_{ijkl} = 0 \rightarrow \varepsilon_{kl} = I_{ijkl} E_{M}{}_{ij}^{sym} \rightarrow \varepsilon_{kl} = E_{M}{}_{kl}^{sym} = \varepsilon_{lk} \tag{6.37}$$

The definition of Cauchy strain versus displacement is substituted in Eq. 6.37 resulting in the first part of the micro displacement field up to a macroscopic rigid body translation, that is not written here:

$$\frac{\partial u_k^{\text{hom}}}{\partial y_l} = E_{M}{}_{kl}^{sym} \rightarrow u_k^{\text{hom}}(\boldsymbol{y}) = y_l E_{M}{}_{kl}^{sym} \tag{6.38}$$

To calculate the second part of the micropolar displacement field, a boundary value problem is formulated using Eq. 6.34. The relation between the microscopic displacement and the antisymmetric strain vector $\boldsymbol{E}_M^{skew}(\boldsymbol{x})$ is obtained starting from:

$$\Sigma_{M}{}_{i}^{skew} = \left\langle \epsilon_{ikj} \sigma_{jk}^{skew,mag} \right\rangle_Y + \left\langle \epsilon_{ijk} y_j \sigma_{kl,l} \right\rangle_Y = \left\langle \sigma_{kl} \frac{\partial \varepsilon_{kl}}{\partial E_{M}{}_{i}^{skew}} \right\rangle_Y \tag{6.39}$$

In Eq. 6.34, the magnetic skew-symmetrical stress, the pseudo vector with components $\sigma_i^{skew} := \epsilon_{ijk}\sigma_{kj}^{skew,mag} = -\tau_i$ has been introduced, arising from the balance of angular momentum, Eq. 6.7, with the magnetic torque on the right hand side of the last relation.

Eq. 6.39 is reformulated as

$$\int_Y \left(-\epsilon_{ijk} y_j \sigma_{kl,l} - \epsilon_{ijk} \sigma_{kj}^{skew} + \sigma_{kl} \frac{\partial \varepsilon_{kl}}{\partial E_{M}{}_{i}^{skew}} \right) = 0 \tag{6.40}$$

The integration by parts of Eq. 6.40 leads to:

$$\int_Y \left(\epsilon_{ijk} y_j \sigma_{kl,l} + \sigma_{kl,l} \frac{\partial u_k}{\partial E_{M}{}_{i}^{skew}} + \epsilon_{ijk} \sigma_{kj}^{skew} \right) dV_y - \int_{\partial Y} n_l \sigma_{kl} \frac{\partial u_k}{\partial E_{M}{}_{i}^{skew}} ds_y = 0 \tag{6.41}$$

The volume integral in the boundary value problem of Eq. 6.41 is isolated, which results in the condition (up to boundary terms denoted 'B.T.' that do however not interfere with the derivations therein):

$$\int_Y \left(\epsilon_{ijk}\delta_{jl}\sigma_{kl} - \sigma_{kl}\frac{\partial}{\partial y_l}\left(\frac{\partial u_k}{\partial E_{M_i}^{skew}}\right) + \epsilon_{ijk}\sigma_{kj}^{skew}\right)dV_y + B.T. = 0 \Rightarrow 2\epsilon_{ilk}\sigma_{kl} - \sigma_{kl}\frac{\partial}{\partial y_l}\left(\frac{\partial u_k}{\partial E_{M_i}^{skew}}\right) = 0,\ \forall\sigma_{kl}$$
$$\Rightarrow 2\sigma_3^{skew} - \sigma_{12}\frac{\partial}{\partial y_2}\left(\frac{\partial u_1}{\partial E_{M3}^{skew}}\right) - \sigma_{21}\frac{\partial}{\partial y_1}\left(\frac{\partial u_2}{\partial E_{M3}^{skew}}\right) = 0,\ \sigma_3^{skew} = -\tau_3$$

Taking the skew part of previous relation delivers:

$$\sigma_{12}^{skew} = -\sigma_{21}^{skew},\ \varepsilon_{321}\sigma_{12}^{skew} + \varepsilon_{312}\sigma_{12}^{skew} =: \sigma_3^{skew} \rightarrow 2\sigma_{12}^{skew} = \sigma_3^{skew} = -\tau_3$$
$$\Rightarrow -\frac{\partial}{\partial y_2}\left(\frac{\partial u_1}{\partial E_{M3}^{skew}}\right) + \frac{\partial}{\partial y_1}\left(\frac{\partial u_2}{\partial E_{M3}^{skew}}\right) = 2$$
$$\Rightarrow \frac{\partial u_1}{\partial E_{M3}^{skew}} = -y_2,\ \frac{\partial u_2}{\partial E_{M3}^{skew}} = y_1 \Rightarrow u_1(\boldsymbol{y}) = E_{M3}^{skew}y_1,\ u_2(\boldsymbol{y}) = -E_{M3}^{skew}y_2 \Rightarrow \boldsymbol{u}^{hom}(\boldsymbol{y}) = -\epsilon : \boldsymbol{E}_M^{skew}.\boldsymbol{y} \tag{6.42}$$

We have used in Eq. 6.42 the fact that the skew-symmetrical stress field in 2D only has one independent component. Using the definition of the internal bending moment and applying the same steps as described earlier, the third contribution of the displacement field is computed:

$$\overline{M}_{ij} = \langle\epsilon_{inm}y_n\sigma_{mj}\rangle_Y = \left\langle\sigma_{kl}\frac{\partial\varepsilon_{kl}}{\partial K_{Mij}}\right\rangle_Y \rightarrow \int_Y \sigma_{kl}\left(\frac{\partial\varepsilon_{kl}}{\partial K_{Mij}} - \epsilon_{inm}y_nI_{mjkl}\right)dV_y = 0, \quad \forall\sigma_{kl} \tag{6.43}$$

this results in a relationship between the microscopic deformation and the micropolar gradient as:

$$\frac{\partial\varepsilon_{kl}}{\partial K_{Mij}} - \epsilon_{inm}y_nI_{mjkl} = 0 \rightarrow \varepsilon_{kl} = \epsilon_{inm}y_nI_{mjkl}K_{Mij} \rightarrow \varepsilon_{kl} = \epsilon_{ink}y_nK_{Mil} \tag{6.44}$$

The definition of Cauchy strain is substituted in Eq. 6.44, which results in:

$$\frac{\partial u_k^{\hom}}{\partial y_l} = \epsilon_{ink}y_nK_{Mil} \tag{6.45}$$

Summing up the three previous contributions Eq. 6.38, Eq. 6.42, and Eq. 6.45, one can conclude that the homogeneous part of the displacement can be expressed as a quadratic function of the microscopic position as follows:

$$\boldsymbol{u}_i^{\hom}(\boldsymbol{y},\boldsymbol{x}) = \boldsymbol{U}^0(\boldsymbol{x}) + \boldsymbol{E}_M^{sym}(\boldsymbol{x})\cdot\boldsymbol{y} - \epsilon\cdot\boldsymbol{E}_M^{skew}(\boldsymbol{x})\cdot\boldsymbol{y} + \epsilon\cdot\boldsymbol{K}_M : (\boldsymbol{y}\otimes\boldsymbol{y}) \tag{6.46}$$

wherein $\boldsymbol{U}^0(\boldsymbol{x})$ is a rigid body motion. If non-homogeneous body forces are present in the (RVE), the microscopic displacement will exhibit further associations with both the skew-symmetrical macroscopic strain components and the body force components.

6.4.2 Variational based homogenization and evaluation of the Cosserat magnetic moduli

The determination of the effective moduli of the micropolar magnetoelastic continuum is based on the quadratic displacement and the homogeneous part of the magnetic h-field described in Eq. 6.46 and Eq. 6.12, respectively. By applying the Hill extended macrohomogeneity condition and the principle of

minimum potential energy in the absence of body forces, one can express the generalized minimization principle applied to all periodic fluctuations of the displacement and magnetic h-field:

$$\Omega_M\left(\boldsymbol{E}_M^{sym},\boldsymbol{E}_M^{skew},\boldsymbol{K}_M,\boldsymbol{H}_M\right)= \underset{\underline{\tilde{\boldsymbol{u}}},\tilde{\boldsymbol{H}}\in H^1_{per}(Y)}{Min}\left\{\begin{array}{l}\displaystyle\int_Y \frac{1}{2}\left(\boldsymbol{u}^{\hom}\otimes\nabla_y+\tilde{\boldsymbol{u}}(\boldsymbol{y})\otimes\nabla_y\right):\boldsymbol{C}(\boldsymbol{y}):\left(\boldsymbol{u}^{\hom}\otimes\nabla_y+\tilde{\boldsymbol{u}}(\boldsymbol{y})\otimes\nabla_y\right)+\\ \left(\mu_0\left(\boldsymbol{H}^{\hom}(\boldsymbol{x})-\widetilde{\varphi}(\boldsymbol{y})\nabla_y\right)+\boldsymbol{B}^{\boldsymbol{r}}\right).\left(\boldsymbol{H}^{\hom}(\boldsymbol{x})-\widetilde{\varphi}(\boldsymbol{y})\nabla_y\right)dV_y\end{array}\right\} \tag{6.47}$$

where $\boldsymbol{C}(\boldsymbol{y})$ is the microscopic rigidity matrix.

The stationarity condition of the functional on the right-hand side of Eq. 6.47 provides as a necessary condition, a BVP to be satisfied by the optimal fluctuation associated to the real displacement field (in the absence of body forces) and magnetic field:

$$\left|\begin{array}{l}-\left\{\boldsymbol{C}(\boldsymbol{y}):\left(\boldsymbol{E}_M^{sym}(\boldsymbol{x})-\epsilon\cdot\boldsymbol{E}_M^{skew}(x)+\epsilon\cdot\boldsymbol{y}\cdot\boldsymbol{K}_M(x)+\tilde{\boldsymbol{u}}(\boldsymbol{y})\otimes\nabla_y\right)\right\}.\nabla_y=0\\ \left[\mu_0\left(\boldsymbol{H}_M(\boldsymbol{x})-\widetilde{\varphi}(\boldsymbol{y})\nabla_y\right)+\boldsymbol{B}^{\boldsymbol{r}}(y)\right].\nabla_y=0\\ \tilde{\boldsymbol{u}}(y),\widetilde{\varphi}(y)\ \text{ Y-periodic}\end{array}\right. \tag{6.48}$$

The linearity of the solution of BVP of Eq.(48) versus the prescribed kinematic macroscopic loading, tensors $\boldsymbol{E}_M^{sym}(\boldsymbol{x})$, $\boldsymbol{E}_M^{skew}(\boldsymbol{x})$, $\boldsymbol{K}_M(\boldsymbol{x})$, and $\boldsymbol{H}_M(\boldsymbol{x})$, guarantees the existence of localizators for the strain, rotation, curvature and magnetic h-field loadings, successively the tensors $\boldsymbol{L}^{uE^{sym}}(\boldsymbol{y}),\boldsymbol{L}^{uE^{skew}}(\boldsymbol{y}),\boldsymbol{L}^{uK}(\boldsymbol{y}),\boldsymbol{L}^{uH_M}(\boldsymbol{y}),\boldsymbol{L}^{\varphi E^{sym}}(\boldsymbol{y}),\boldsymbol{L}^{\varphi E^{skew}}(\boldsymbol{y}),\boldsymbol{L}^{\varphi K}(\boldsymbol{y}),\boldsymbol{L}^{\varphi H_M}(\boldsymbol{y})$, so that the displacement and magnetic potential fluctuations are written as:

$$\begin{array}{l}\tilde{\boldsymbol{u}}(\boldsymbol{y})=\boldsymbol{L}^{uE^{sym}}(\boldsymbol{y}):\boldsymbol{E}_M^{sym}(\boldsymbol{x})+\boldsymbol{L}^{uE^{skew}}(\boldsymbol{y})\cdot\boldsymbol{E}_M^{skew}(\boldsymbol{x})+\boldsymbol{L}^{uK}(\boldsymbol{y}):\boldsymbol{K}_M(\boldsymbol{x})+\boldsymbol{L}^{uH_M}(\boldsymbol{y})\cdot\boldsymbol{H}_M(x)\\ \widetilde{\varphi}(\boldsymbol{y})=\boldsymbol{L}^{\varphi E^{sym}}(\boldsymbol{y}):\boldsymbol{E}_M^{sym}(\boldsymbol{x})+\boldsymbol{L}^{\varphi E^{skew}}(\boldsymbol{y})\cdot\boldsymbol{E}_M^{skew}(\boldsymbol{x})+\boldsymbol{L}^{\varphi K}(\boldsymbol{y}):\boldsymbol{K}_M(\boldsymbol{x})+\boldsymbol{L}^{\varphi H_M}(\boldsymbol{y})\cdot\boldsymbol{H}_M(x)\end{array} \tag{6.49}$$

The order of the localization operators (tensors) is indicated in Table 6.1.

The expression of the fluctuation, Eq. 6.49, results in the full microscopic displacement and scalar magnetic h-field given by

$$\begin{array}{l}\boldsymbol{u}(\boldsymbol{y},\boldsymbol{x})=\left((\boldsymbol{I}_4\cdot\boldsymbol{y})+\boldsymbol{L}^{uE^{sym}}(\boldsymbol{y})\right):\boldsymbol{E}_M^{sym}(\boldsymbol{x})+\left(-\epsilon\cdot\boldsymbol{y}+\boldsymbol{L}^{uE^{skew}}(\boldsymbol{y})\right)\cdot\boldsymbol{E}_M^{skew}(\boldsymbol{x})\\ +\left(\frac{1}{2}(\epsilon\cdot(\boldsymbol{y}\otimes\boldsymbol{y}))+\boldsymbol{L}^{uK}(\boldsymbol{y})\right):\boldsymbol{K}_M(\boldsymbol{x})+\boldsymbol{L}^{uH_M}(\boldsymbol{y}).\boldsymbol{H}_M(x),\\ \varphi(\boldsymbol{y})=\boldsymbol{L}^{\varphi E^{sym}}(\boldsymbol{y}):\boldsymbol{E}_M^{sym}(\boldsymbol{x})+\boldsymbol{L}^{\varphi E^{skew}}(\boldsymbol{y})\cdot\boldsymbol{E}_M^{skew}(\boldsymbol{x})+\boldsymbol{L}^{\varphi K}(\boldsymbol{y}):\boldsymbol{K}_M(\boldsymbol{x})\ -\boldsymbol{y}.\boldsymbol{H}_M(x)+\boldsymbol{L}^{\varphi H_M}(\boldsymbol{y}).\boldsymbol{H}_M(x)\end{array} \tag{6.50}$$

We further conveniently define the microstrain and micro h-field, as the symmetrical part of the micro displacement gradient and magnetic potential gradient respectively, resulting in the localization relations

$$\begin{array}{l}\boldsymbol{u}\otimes\nabla_y\equiv\boldsymbol{A}^{uE^{sym}}(\boldsymbol{y}):\boldsymbol{E}_M^{sym}(\boldsymbol{x})+\boldsymbol{A}^{uE^{skew}}(\boldsymbol{y}).\boldsymbol{E}_M^{skew}(\boldsymbol{x})+\boldsymbol{A}^{uK}(\boldsymbol{y}):\boldsymbol{K}_M(\boldsymbol{x})+\boldsymbol{A}^{uH_M}(\boldsymbol{y}).\boldsymbol{H}_M(x)\\ \boldsymbol{H}(\boldsymbol{y})=-\varphi(\boldsymbol{y})\otimes\nabla_y=\boldsymbol{A}^{\varphi E^{sym}}(\boldsymbol{y}):\boldsymbol{E}_M^{sym}(\boldsymbol{x})+\boldsymbol{A}^{\varphi E^{skew}}(\boldsymbol{y}).\boldsymbol{E}_M^{skew}(\boldsymbol{x})+\boldsymbol{A}^{\varphi K}(\boldsymbol{y}):\boldsymbol{K}_M(\boldsymbol{x})+\boldsymbol{A}^{\varphi H_M}(\boldsymbol{y}).\boldsymbol{H}_M(x)\end{array} \tag{6.51}$$

with $\boldsymbol{A}^{uE^{sym}}(\boldsymbol{y}),\boldsymbol{A}^{uE^{skew}}(\boldsymbol{y}),\boldsymbol{A}^{uK}(\boldsymbol{y}),\boldsymbol{A}^{uH_M}(\boldsymbol{y}),\boldsymbol{A}^{\varphi E^{sym}}(\boldsymbol{y}),\boldsymbol{A}^{\varphi E^{skew}}(\boldsymbol{y}),\boldsymbol{A}^{\varphi K}(\boldsymbol{y}),\boldsymbol{A}^{\varphi H_M}(\boldsymbol{y})$ representing the localization tensors relating the microstrain tensor and microscopic magnetic h-field vector to their

Table 6.1 Order of the localization operators (tensors) for the displacement (a 1-tensor) and scalar magnetic potential (a zero-tensor)

Localization operators	Order of the tensor
$\boldsymbol{L}^{uE^{sym}}(\boldsymbol{y})$	3
$\boldsymbol{L}^{uE^{skew}}(\boldsymbol{y})$	2
$\boldsymbol{L}^{uK}(\boldsymbol{y})$	3
$\boldsymbol{L}^{uH_M}(\boldsymbol{y})$	2
$\boldsymbol{L}^{\varphi E^{sym}}(\boldsymbol{y})$	2
$\boldsymbol{L}^{\varphi E^{skew}}(\boldsymbol{y})$	1
$\boldsymbol{L}^{\varphi K}(\boldsymbol{y})$	2
$\boldsymbol{L}^{\varphi H_M}(\boldsymbol{y})$	1

macroscopic kinematic variables, with their expression given by

$$\begin{aligned}
&\boldsymbol{A}^{uE^{sym}}(\boldsymbol{y}) = \boldsymbol{I}_4 + \boldsymbol{L}^{uE^{sym}}(\boldsymbol{y}) \otimes \nabla_y,\ \boldsymbol{A}^{uE^{skew}}(\boldsymbol{y}) = -\epsilon.\boldsymbol{y} + \boldsymbol{L}^{uE^{skew}}(\boldsymbol{y}) \otimes \nabla_y,\ \boldsymbol{A}^{uK}(\boldsymbol{y}) = \epsilon \cdot \boldsymbol{y} \otimes \boldsymbol{I}_2 + \boldsymbol{L}^{uK}(\boldsymbol{y}) \otimes \nabla_y \\
&\boldsymbol{A}^{uH_M}(\boldsymbol{y}) = \boldsymbol{L}^{uH_M}(\boldsymbol{y}) \otimes \nabla_y \\
&\boldsymbol{A}^{\varphi E^{sym}}(\boldsymbol{y}) = -\boldsymbol{L}^{\varphi E^{sym}}(\boldsymbol{y}) \otimes \nabla_y,\ \boldsymbol{A}^{\varphi E^{skew}}(\boldsymbol{y}) = -\boldsymbol{L}^{\varphi E^{skew}}(\boldsymbol{y}) \otimes \nabla_y,\ \boldsymbol{A}^{\varphi K}(\boldsymbol{y}) = \boldsymbol{L}^{\varphi K}(\boldsymbol{y}) \otimes \nabla_y \\
&\boldsymbol{A}^{\varphi H_M}(\boldsymbol{y}) = -\boldsymbol{I}_2 - \boldsymbol{L}^{\varphi H_M}(\boldsymbol{y}) \otimes \nabla_y
\end{aligned} \tag{6.52}$$

The tensor order of the localization operators is indicated in the following Table 6.2.

Table 6.2 Order of the localization operators (tensors) for the displacement gradient and magnetic h-field.

Localization operators	Order of the tensor
$\boldsymbol{A}^{uE^{sym}}(\boldsymbol{y})$	4
$\boldsymbol{A}^{uE^{skew}}(\boldsymbol{y})$	3
$\boldsymbol{A}^{uK}(\boldsymbol{y})$	4
$\boldsymbol{A}^{uH_M}(\boldsymbol{y})$	3
$\boldsymbol{A}^{\varphi E^{sym}}(\boldsymbol{y})$	3
$\boldsymbol{A}^{\varphi E^{skew}}(\boldsymbol{y})$	2
$\boldsymbol{A}^{\varphi K}(\boldsymbol{y})$	3
$\boldsymbol{A}^{\varphi H_M}(\boldsymbol{y})$	2

Eq. 6.52 is then inserted into the BVP of Eq. 6.48 which leads to a new BVP for the localization operator

tensors, which will be solved in a sequential manner:

$$\left|\begin{array}{l} -\left\{\boldsymbol{C}\left(\boldsymbol{y}\right):\left[\boldsymbol{A}^{uE^{sym}}\left(y\right):\boldsymbol{E}_M^{sym}\left(\boldsymbol{x}\right)+\boldsymbol{A}^{uE^{skew}}\left(\boldsymbol{y}\right).\boldsymbol{E}_M^{skew}\left(\boldsymbol{x}\right)+\boldsymbol{A}^{uK}\left(\boldsymbol{y}\right):\boldsymbol{K}_M\left(\boldsymbol{x}\right)+\boldsymbol{A}^{uH_M}\left(\boldsymbol{y}\right).\boldsymbol{H}_M\left(\boldsymbol{x}\right)\right]\right\}.\nabla_y=0 \\ \left[\mu_0\left(\boldsymbol{A}^{\varphi E^{sym}}\left(\boldsymbol{y}\right):E_M^{sym}\left(\boldsymbol{x}\right)+\boldsymbol{A}^{\varphi E^{skew}}\left(\boldsymbol{y}\right).E_M^{skew}\left(\boldsymbol{x}\right)+\boldsymbol{A}^{\varphi K}\left(\boldsymbol{y}\right):\boldsymbol{K}_M\left(\boldsymbol{x}\right)+\boldsymbol{A}^{\varphi H_M}\left(\boldsymbol{y}\right).\boldsymbol{H}_M\left(\boldsymbol{x}\right)\right)+\boldsymbol{B}^{\boldsymbol{r}}\left(\boldsymbol{y}\right)\right].\nabla_y=0 \end{array}\right. \tag{6.53}$$

6.4.3 General form of the homogenized constitutive properties

Anticipating the evaluation of the homogenized tensors, the macroscopic homogenized constitutive law writes formally as follows:

$$\begin{aligned} \boldsymbol{\Sigma}_M^{sym} &:= \left\langle\boldsymbol{\sigma}^{sym}\right\rangle_Y = \boldsymbol{C}^{\hom}:\boldsymbol{E}_M^{sym}+\boldsymbol{B}^{\hom}.\boldsymbol{E}_M^{skew}+\boldsymbol{D}^{\hom}:\boldsymbol{K}_M+\boldsymbol{d}^{\hom\cdot}.\boldsymbol{H}_M \\ \boldsymbol{\Sigma}_M^{skew} &:= \left\langle\boldsymbol{\sigma}^{skew}\right\rangle_Y = \boldsymbol{B}^{\hom,T}.\boldsymbol{E}_M^{sym}+\boldsymbol{R}^{\hom}:\boldsymbol{E}_M^{skew}+\boldsymbol{F}^{\hom}:\boldsymbol{K}_M+\boldsymbol{g}^{\hom}.\boldsymbol{H}_M \\ \overline{\boldsymbol{M}} &:= \left\langle\boldsymbol{\mu}\right\rangle_Y = \boldsymbol{e}^{\hom}:\boldsymbol{E}_M^{sym}+\boldsymbol{F}^{\hom,T}.\boldsymbol{E}_M^{skew}+\boldsymbol{G}^{\hom}:\boldsymbol{K}_M+\boldsymbol{N}^{\hom\cdot}.\boldsymbol{H}_M \\ \boldsymbol{B}_M &:= \left\langle\boldsymbol{B}\right\rangle_Y = \overline{\boldsymbol{d}}^{\hom}:\boldsymbol{E}_M^{sym}+\boldsymbol{g}^{\hom,T}.\boldsymbol{E}_M^{skew}+\overline{\boldsymbol{N}}^{\hom}:\boldsymbol{K}_M+\boldsymbol{a}^{\hom}.\boldsymbol{H}_M \end{aligned} \tag{6.54}$$

wherein $\boldsymbol{C}^{\hom}$ is the first gradient modulus (rigidity matrix), $\boldsymbol{G}^{\hom}$ is Cosserat modulus and $\boldsymbol{D}^{\hom}$ is the coupling tensor between first and gradient terms. $\boldsymbol{B}^{\hom}$, and $\boldsymbol{F}^{\hom}$ are coupling tensors and $\boldsymbol{d}^{\hom}$ is the coupling magneto-elastic tensor. $\boldsymbol{a}^{\hom}$ represents the magnetic permittivity tensor, $\boldsymbol{g}^{\hom}$, $\boldsymbol{N}^{\hom}$, and $\overline{\boldsymbol{N}}$ represent coupling tensors with the magnetic field.

The set of constitutive relations Eq. 6.54 entail that the elastic and magnetic contributions of the macroscopic stress, moment and magnetic field formally express as

$$\begin{aligned} \boldsymbol{\Sigma}_M^{sym,ela} &:= \boldsymbol{C}^{\hom}:\boldsymbol{E}_M^{sym}+\boldsymbol{B}^{\hom}.\boldsymbol{E}_M^{skew}+\boldsymbol{D}^{\hom}:\boldsymbol{K}_M,\ \boldsymbol{\Sigma}_M^{sym,mag} := \boldsymbol{d}^{\hom\cdot}.\boldsymbol{H}_M \\ \boldsymbol{\Sigma}_M^{skew,ela} &= \boldsymbol{B}^{\hom,T}:\boldsymbol{E}_M^{sym}+\boldsymbol{R}^{\hom}.\boldsymbol{E}_M^{skew}+\boldsymbol{F}^{\hom}:\boldsymbol{K}_M,\ \boldsymbol{\Sigma}_M^{skew,mag}=\boldsymbol{g}^{\hom}.\boldsymbol{H}_M \\ \overline{\boldsymbol{M}}^{ela} &:= \boldsymbol{e}^{\hom}:\boldsymbol{E}_M^{sym}+\boldsymbol{F}^{\hom,T}.\boldsymbol{E}_M^{skew}+\boldsymbol{G}^{\hom}:\boldsymbol{K}_M,\ \overline{\boldsymbol{M}}^{mag} := \boldsymbol{N}^{\hom\cdot}.\boldsymbol{H}_M \\ \boldsymbol{B}_M^{ela} &:= \overline{\boldsymbol{d}}^{\hom}:\boldsymbol{E}_M^{sym}+\boldsymbol{g}^{\hom,T}.\boldsymbol{E}_M^{skew}+\overline{\boldsymbol{N}}^{\hom}:\boldsymbol{K}_M,\ \boldsymbol{B}_M^{mag} := \boldsymbol{a}^{\hom\cdot}.\boldsymbol{H}_M \end{aligned} \tag{6.55}$$

An extended minimization principle of the macroscopic magnetoelastic energy over all periodic fluctuations holds, so that inserting relations Eq. 6.51 into the functional in Eq. 6.47 delivers:

$$\begin{aligned} &\Omega_M\left(\boldsymbol{E}_M^{sym},\boldsymbol{E}_M^{skew},\boldsymbol{K}_M,\boldsymbol{H}_M\right)= \\ &\left\{\begin{array}{l} \int\limits_Y \frac{1}{2}\left(\boldsymbol{A}^{uE^{sym}}(\boldsymbol{y}):\boldsymbol{E}_M^{sym}(\boldsymbol{x})+\boldsymbol{A}^{uE^{skew}}(\boldsymbol{y}).\boldsymbol{E}_M^{skew}(\boldsymbol{x})+\boldsymbol{A}^{uK}(\boldsymbol{y}):\boldsymbol{K}_M(\boldsymbol{x})+\boldsymbol{A}^{uH_M}(\boldsymbol{y}).\boldsymbol{H}_M(\boldsymbol{x})\right):\boldsymbol{C}\left(\boldsymbol{y}\right): \\ \left(\boldsymbol{A}^{uE^{sym}}(\boldsymbol{y}):\boldsymbol{E}_M^{sym}(\boldsymbol{x})+\boldsymbol{A}^{uE^{skew}}(\boldsymbol{y}).\boldsymbol{E}_M^{skew}(\boldsymbol{x})+\boldsymbol{A}^{uK}(\boldsymbol{y}):\boldsymbol{K}_M(\boldsymbol{x})+\boldsymbol{A}^{uH_M}(\boldsymbol{y}).\boldsymbol{H}_M(x)\right)+ \\ \left(\mu_0\left(\boldsymbol{A}^{\varphi E^{sym}}(\boldsymbol{y}):\boldsymbol{E}_M^{sym}(\boldsymbol{x})+\boldsymbol{A}^{\varphi E^{skew}}(\boldsymbol{y}).\boldsymbol{E}_M^{skew}(\boldsymbol{x})+\boldsymbol{A}^{\varphi K}(\boldsymbol{y}):\boldsymbol{K}_M(\boldsymbol{x})+\boldsymbol{A}^{\varphi H_M}(\boldsymbol{y}).\boldsymbol{H}_M(\boldsymbol{x})\right)+\boldsymbol{B}^{\boldsymbol{r}}\left(\boldsymbol{y}\right)\right). \\ \left(\boldsymbol{A}^{\varphi E^{sym}}(\boldsymbol{y}):\boldsymbol{E}_M^{sym}(\boldsymbol{x})+\boldsymbol{A}^{\varphi E^{skew}}(\boldsymbol{y}).\boldsymbol{E}_M^{skew}(\boldsymbol{x})+\boldsymbol{A}^{\varphi K}(\boldsymbol{y}):\boldsymbol{K}_M(\boldsymbol{x})+\boldsymbol{A}^{\varphi H_M}(\boldsymbol{y}).\boldsymbol{H}_M(\boldsymbol{x})\right)dV_y \end{array}\right\} \end{aligned} \tag{6.56}$$

Since $\Omega_M\left(\boldsymbol{E}_M^{sym},\boldsymbol{E}_M^{skew},\boldsymbol{K}_M,\boldsymbol{H}_M\right)$ defines a macroscopic potential, the homogenized constitutive law follows considering Eq. 6.35 and the fact that partial derivative with respect to the macro parameters $\left(\boldsymbol{E}_M^{sym},\boldsymbol{E}_M^{skew},\boldsymbol{K}_M,\boldsymbol{H}_M\right)$ and integration over the unit cell can be switched:

$$\begin{aligned}
\boldsymbol{\Sigma}_M^{sym} &= \frac{\partial\Omega_M}{\partial\boldsymbol{E}_M^{sym}} = \int\limits_Y \left(\boldsymbol{A}^{uE^{sym}} : \boldsymbol{E}_M^{sym} + \boldsymbol{A}^{uE^{skew}}.\boldsymbol{E}_M^{skew} + \boldsymbol{A}^{uK} : \boldsymbol{K}_M + \boldsymbol{A}^{uH_M}.\boldsymbol{H}_M\right) : \boldsymbol{C} : \boldsymbol{A}^{uE^{sym}} + \\
&\left(\mu_0\left(\boldsymbol{A}^{\varphi E^{sym}} : \boldsymbol{E}_M^{sym} + \boldsymbol{A}^{\varphi E^{skew}}.\boldsymbol{E}_M^{skew} + \boldsymbol{A}^{\varphi K} : \boldsymbol{K}_M + \boldsymbol{A}^{\varphi H_M}.\boldsymbol{H}_M\right) + \boldsymbol{B}^{\boldsymbol{r}}(\boldsymbol{y})\right).\boldsymbol{A}^{\varphi E^{sym}} dV_y = \\
&\left\{\int\limits_Y \left(\boldsymbol{A}^{uE^{sym}}\right)^T : \boldsymbol{C} : \boldsymbol{A}^{uE^{sym}} dV_y\right\} : \boldsymbol{E}_M^{sym} + \left\{\int\limits_Y \left(\boldsymbol{A}^{uE^{skew}}\right)^T : \boldsymbol{C} : \boldsymbol{A}^{uE^{sym}} dV_y\right\}.\boldsymbol{E}_M^{skew} + \\
&\left\{\int\limits_Y \left(\boldsymbol{A}^{uK}\right)^T : \boldsymbol{C} : \boldsymbol{A}^{uE^{sym}} dV_y\right\} : \boldsymbol{K}_M + \left\{\int\limits_Y \left(\boldsymbol{A}^{uH_M}\right)^T : \boldsymbol{C} : \boldsymbol{A}^{uE^{sym}} dV_y\right\}.\boldsymbol{H}_M + \\
&\left\{\int\limits_Y \mu_0\left(\boldsymbol{A}^{\varphi E^{sym}}\right)^T.\boldsymbol{A}^{\varphi E^{sym}} dV_y\right\} : \boldsymbol{E}_M^{sym} + \left\{\int\limits_Y \mu_0\left(\boldsymbol{A}^{\varphi E^{skew}}\right)^T.\boldsymbol{A}^{\varphi E^{sym}} dV_y\right\}.\boldsymbol{E}_M^{skew} + \\
&\left\{\int\limits_Y \mu_0\left(\boldsymbol{A}^{\varphi K}\right)^T.\boldsymbol{A}^{\varphi E^{sym}} dV_y\right\} : \boldsymbol{K}_M + \left\{\int\limits_Y \mu_0\left(\boldsymbol{A}^{\varphi H_M}\right)^T.\boldsymbol{A}^{\varphi E^{sym}} dV_y\right\}.\boldsymbol{H}_M + \left\{\int\limits_Y \boldsymbol{B}^{\boldsymbol{r}}(\boldsymbol{y}).\boldsymbol{A}^{\varphi E^{sym}} dV_y\right\}
\end{aligned} \tag{6.57}$$

$$\begin{aligned}
\boldsymbol{\Sigma}_M^{skew} &= \frac{\partial\Omega_M}{\partial\boldsymbol{E}_M^{skew}} = \int\limits_Y \left(\boldsymbol{A}^{uE^{sym}} : \boldsymbol{E}_M^{sym} + \boldsymbol{A}^{uE^{skew}}.\boldsymbol{E}_M^{skew} + \boldsymbol{A}^{uK} : \boldsymbol{K}_M + \boldsymbol{A}^{uH_M}.\boldsymbol{H}_M\right) : \boldsymbol{C} : \boldsymbol{A}^{uE^{skew}} + \\
&\left(\mu_0\left(\boldsymbol{A}^{\varphi E^{sym}} : \boldsymbol{E}_M^{sym} + \boldsymbol{A}^{\varphi E^{skew}}.\boldsymbol{E}_M^{skew} + \boldsymbol{A}^{\varphi K} : \boldsymbol{K}_M + \boldsymbol{A}^{\varphi H_M}.\boldsymbol{H}_M\right) + \boldsymbol{B}^{\boldsymbol{r}}(\boldsymbol{y})\right).\boldsymbol{A}^{\varphi E^{skew}} dV_y = \\
&\left\{\int\limits_Y \left(\boldsymbol{A}^{uE^{sym}}\right)^T : \boldsymbol{C} : \boldsymbol{A}^{uE^{skew}} dV_y\right\} : \boldsymbol{E}_M^{sym} + \left\{\int\limits_Y \left(\boldsymbol{A}^{uE^{skew}}\right)^T : \boldsymbol{C} : \boldsymbol{A}^{uE^{skew}} dV_y\right\}.\boldsymbol{E}_M^{skew} + \\
&\left\{\int\limits_Y \left(\boldsymbol{A}^{uK}\right)^T : \boldsymbol{C} : \boldsymbol{A}^{uE^{skew}} dV_y\right\} : \boldsymbol{K}_M + \left\{\int\limits_Y \left(\boldsymbol{A}^{uH_M}\right)^T : \boldsymbol{C} : \boldsymbol{A}^{uE^{skew}} dV_y\right\}.\boldsymbol{H}_M + \\
&\left\{\int\limits_Y \mu_0\left(\boldsymbol{A}^{\varphi E^{sym}}\right)^T.\boldsymbol{A}^{\varphi E^{skew}} dV_y\right\} : \boldsymbol{E}_M^{sym} + \left\{\int\limits_Y \mu_0\left(\boldsymbol{A}^{\varphi E^{skew}}\right)^T.\boldsymbol{A}^{\varphi E^{skew}} dV_y\right\}.\boldsymbol{E}_M^{skew} + \\
&\left\{\int\limits_Y \mu_0\left(\boldsymbol{A}^{\varphi K}\right)^T.\boldsymbol{A}^{\varphi E^{skew}} dV_y\right\} : \boldsymbol{K}_M + \left\{\int\limits_Y \mu_0\left(\boldsymbol{A}^{\varphi H_M}\right)^T.\boldsymbol{A}^{\varphi E^{skew}} dV_y\right\}.\boldsymbol{H}_M + \left\{\int\limits_Y \boldsymbol{B}^{\boldsymbol{r}}(\boldsymbol{y}).\boldsymbol{A}^{\varphi E^{skew}} dV_y\right\}
\end{aligned} \tag{6.58}$$

$$\begin{aligned}
\overline{\boldsymbol{M}} &= \frac{\partial\Omega_M}{\partial\boldsymbol{K}_M} = \left\{\int\limits_Y \left(\boldsymbol{A}^{uE^{sym}}\right)^T : \boldsymbol{C}(\boldsymbol{y}) : \boldsymbol{A}^{uK} dV_y\right\} : \boldsymbol{E}_M^{sym} + \left\{\int\limits_Y \left(\boldsymbol{A}^{uE^{skew}}\right)^T : \boldsymbol{C}(\boldsymbol{y}) : \boldsymbol{A}^{uK} dV_y\right\}.\boldsymbol{E}_M^{skew} + \\
&\left\{\int\limits_Y \left(\boldsymbol{A}^{uK}\right)^T : \boldsymbol{C}(\boldsymbol{y}) : \boldsymbol{A}^{uK} dV_y\right\} : \boldsymbol{K}_M + \left\{\int\limits_Y \left(\boldsymbol{A}^{uH_M}\right)^T : \boldsymbol{C}(\boldsymbol{y}) : \boldsymbol{A}^{uK} dV_y\right\}.\boldsymbol{H}_M + \\
&\int\limits_Y \mu_0\left\{\left(\boldsymbol{A}^{\varphi E^{sym}}\right)^T.\boldsymbol{A}^{\varphi K} dV_y\right\} : \boldsymbol{E}_M^{sym} + \left\{\int\limits_Y \mu_0\left(\boldsymbol{A}^{\varphi E^{skew}}\right)^T.\boldsymbol{A}^{\varphi K} dV_y\right\}.\boldsymbol{E}_M^{skew} + \\
&\left\{\int\limits_Y \mu_0\left(\boldsymbol{A}^{\varphi K}\right).\boldsymbol{A}^{\varphi K} dV_y\right\} : \boldsymbol{K}_M + \left\{\int\limits_Y \mu_0\left(\boldsymbol{A}^{\phi H_M}\right)^T.\boldsymbol{A}^{\varphi K} dV_y\right\}.\boldsymbol{H}_M + \left\{\int\limits_Y \boldsymbol{B}^{\boldsymbol{r}}(\boldsymbol{y}).\boldsymbol{A}^{\varphi K} dV_y\right\}
\end{aligned} \tag{6.59}$$

$$\boldsymbol{B}_M = \frac{\partial \Omega_M}{\partial \boldsymbol{H}_M} = \left\{ \int_Y \left(\boldsymbol{A}^{uE^{sym}} \right)^T : \boldsymbol{C}\left(\boldsymbol{y}\right) : \boldsymbol{A}^{uH_M} dV_y \right\} : \boldsymbol{E}_M^{sym} + \left\{ \int_Y \left(\boldsymbol{A}^{uE^{skew}} \right)^T : \boldsymbol{C}\left(\boldsymbol{y}\right) : \boldsymbol{A}^{uH_M} dV_y \right\} .\boldsymbol{E}_M^{skew} +$$
$$\left\{ \int_Y \left(\boldsymbol{A}^{uK} \right)^T : \boldsymbol{C}\left(\boldsymbol{y}\right) : \boldsymbol{A}^{uH_M} dV_y \right\} : \boldsymbol{K}_M + \left\{ \int_Y \left(\boldsymbol{A}^{uH_M} \right)^T : \boldsymbol{C}\left(\boldsymbol{y}\right) : \boldsymbol{A}^{uH_M} dV^y \right\} .\boldsymbol{H}_M +$$
$$\left\{ \int_Y \mu_0 \left(\boldsymbol{A}^{\varphi E^{sym}} \right)^T .\boldsymbol{A}^{\varphi H_M} dV_y \right\} : \boldsymbol{E}_M^{sym} + \left\{ \int_Y \mu_0 \left(\boldsymbol{A}^{\varphi E^{skew}} \right)^T .\boldsymbol{A}^{\varphi H_M} dV_y \right\} .\boldsymbol{E}_M^{skew} +$$
$$\left\{ \int_Y \mu_0 \left(\boldsymbol{A}^{\varphi K} \right)^T .\boldsymbol{A}^{\varphi H_M} dV_y \right\} : \boldsymbol{K}_M + \left\{ \int_Y \mu_0 \left(\boldsymbol{A}^{\varphi H_M} \right)^T .\boldsymbol{A}^{\varphi H_M} dV_y \right\} .\boldsymbol{H}_M + \left\{ \int_Y \boldsymbol{B^r}\left(\boldsymbol{y}\right) .\boldsymbol{A}^{\varphi H_M} dV_y \right\} \tag{6.60}$$

Previous expressions lead by comparison with the general form of the macroscopic constitutive law in Eq. 6.54 to the expression of the homogenized moduli, with the localization operators therein defined in Eqs. 6.52:

$$
\begin{aligned}
\boldsymbol{C}^{\text{hom}} &= \left\{ \int\limits_Y \left(\boldsymbol{A}^{uE^{sym}}\right)^T : \boldsymbol{C} : \boldsymbol{A}^{uE^{sym}} dV_y + \int\limits_Y \mu_0 \left(\boldsymbol{A}^{\varphi E^{sym}}\right)^T . \boldsymbol{A}^{\varphi E^{sym}} dV_y \right\} \\
\boldsymbol{B}^{\text{hom}} &= \left\{ \int\limits_Y \left(\boldsymbol{A}^{uE^{skew}}\right)^T : \boldsymbol{C} : \boldsymbol{A}^{uE^{sym}} dV_y + \int\limits_Y \mu_0 \left(\boldsymbol{A}^{\varphi E^{skew}}\right)^T . \boldsymbol{A}^{\varphi E^{sym}} dV_y \right\} \\
\boldsymbol{D}^{\text{hom}} &= \left\{ \int\limits_Y \left(\boldsymbol{A}^{uK}\right)^T : \boldsymbol{C} : \boldsymbol{A}^{uE^{sym}} dV_y + \int\limits_Y \mu_0 \left(\boldsymbol{A}^{\varphi K}\right)^T . \boldsymbol{A}^{\varphi E^{sym}} dV_y \right\} \\
\boldsymbol{d}^{\text{hom}\,.} &= \left\{ \int\limits_Y \left(\boldsymbol{A}^{uH_M}\right)^T : \boldsymbol{C} : \boldsymbol{A}^{uE^{sym}} dV_y + \int\limits_Y \mu_0 \left(\boldsymbol{A}^{\varphi H_M}\right)^T . \boldsymbol{A}^{\varphi E^{sym}} dV_y \right\} \\
\boldsymbol{R}^{\text{hom}} &= \left\{ \int\limits_Y \left(\boldsymbol{A}^{uE^{skew}}\right)^T : \boldsymbol{C} : \boldsymbol{A}^{uE^{skew}} dV_y + \int\limits_Y \mu_0 \left(\boldsymbol{A}^{\varphi E^{skew}}\right)^T . \boldsymbol{A}^{\varphi E^{skew}} dV_y \right\} \\
\boldsymbol{F}^{\text{hom}} &= \left\{ \int\limits_Y \left(\boldsymbol{A}^{uK}\right)^T : \boldsymbol{C} : \boldsymbol{A}^{uE^{skew}} dV_y + \int\limits_Y \mu_0 \left(\boldsymbol{A}^{\phi K}\right)^T . \boldsymbol{A}^{\varphi E^{skew}} dV_y \right\} \\
\boldsymbol{g}^{\text{hom}} &= \left\{ \int\limits_Y \left(\boldsymbol{A}^{uH_M}\right)^T : \boldsymbol{C} : \boldsymbol{A}^{uE^{skew}} dV_y + \int\limits_Y \mu_0 \left(\boldsymbol{A}^{\varphi H_M}\right)^T . \boldsymbol{A}^{\varphi E^{skew}} dV_y \right\} \\
\boldsymbol{G}^{\text{hom}} &= \left\{ \int\limits_Y \left(\boldsymbol{A}^{uK}\right)^T : \boldsymbol{C}\left(\boldsymbol{y}\right) : \boldsymbol{A}^{uK} dV_y + \int\limits_Y \mu_0 \left(\boldsymbol{A}^{\varphi K}\right) . \boldsymbol{A}^{\varphi K} dV_y \right\} \\
\boldsymbol{N}^{\text{hom}} &= \left\{ \int\limits_Y \left(\boldsymbol{A}^{uH_M}\right)^T : \boldsymbol{C}\left(\boldsymbol{y}\right) : \boldsymbol{A}^{uK} dV_y + \int\limits_Y \mu_0 \left(\boldsymbol{A}^{\varphi H_M}\right)^T . \boldsymbol{A}^{\varphi K} dV_y \right\} \\
\boldsymbol{a}^{\text{hom}} &= \left\{ \int\limits_Y \left(\boldsymbol{A}^{uH_M}\right)^T : \boldsymbol{C}\left(\boldsymbol{y}\right) : \boldsymbol{A}^{uH_M} dV_y + \int\limits_Y \mu_0 \left(\boldsymbol{A}^{\varphi H_M}\right)^T . \boldsymbol{A}^{\varphi H_M} dV_y \right\} \\
\overline{\boldsymbol{d}}^{\text{hom}} &= \left\{ \int\limits_Y \left(\boldsymbol{A}^{uE^{sym}}\right)^T : \boldsymbol{C}\left(\boldsymbol{y}\right) : \boldsymbol{A}^{uH_M} dV_y + \int\limits_Y \mu_0 \left(\boldsymbol{A}^{\varphi E^{sym}}\right)^T . \boldsymbol{A}^{\varphi H_M} dV_y \right\} \\
\overline{\boldsymbol{N}}^{\text{hom}} &= \left\{ \int\limits_Y \left(\boldsymbol{A}^{uK}\right)^T : \boldsymbol{C}\left(\boldsymbol{y}\right) : \boldsymbol{A}^{uH_M} dV_y + \int\limits_Y \mu_0 \left(\boldsymbol{A}^{\varphi K}\right)^T . \boldsymbol{A}^{\varphi H_M} dV_y \right\} \\
\boldsymbol{e}^{\text{hom}} &= \left\{ \int\limits_Y \left(\boldsymbol{A}^{uE^{sym}}\right)^T : \boldsymbol{C}\left(\boldsymbol{y}\right) : \boldsymbol{A}^{uK} dV_y + \int\limits_Y \mu_0 \left\{ \left(\boldsymbol{A}^{\varphi E^{sym}}\right)^T . \boldsymbol{A}^{\varphi K} dV_y \right\}_y \right\}
\end{aligned}
\tag{6.61}
$$

In the next section, the homogenized magnetoelastic micropolar moduli will be computed for composites in a planar situation and coupling effects between the elastic and magnetic fields will be investigated.

6.5 Algorithm for the evaluation of the homogenized magnetoelastic medium and numerical results

Based on the theoretical framework discussed earlier, we suggest a computational method for calculating the effective tensors of the homogenized constitutive law for the magneto-elastic effective medium. It is

based on solving the weak formulation of the BVP for the total displacement and magnetic potential. Starting from the constitutive equations at the microscopic level for the stress and magnetic induction:

$$\begin{aligned} \boldsymbol{\sigma}(\boldsymbol{y}) &= \boldsymbol{C}(\boldsymbol{y}) : \boldsymbol{\varepsilon}(\boldsymbol{y}) + \boldsymbol{d}(\boldsymbol{y}) \left(-\varphi(\boldsymbol{y}) \nabla_y\right) \\ \boldsymbol{B}(\boldsymbol{y}) &= \mu_0 . \left(-\varphi(\boldsymbol{y}) \nabla_y\right) + \boldsymbol{B}^{\boldsymbol{r}}(\boldsymbol{y}) \end{aligned} \tag{6.62}$$

wherein $\boldsymbol{d}(\boldsymbol{y})$ is the microscopic coupling matrix between the elastic and magnetic fields, and $\boldsymbol{\varepsilon}(\boldsymbol{y})$ is the microscopic deformation, the variational formulation to be solved is expressed as :

$$\begin{aligned} &\forall \boldsymbol{v} \in H_1(Y), \\ &\int_Y \left(\boldsymbol{C}(\boldsymbol{y}) : \varepsilon(\boldsymbol{u}) + \boldsymbol{d}(\boldsymbol{y}) \left(-\varphi(\boldsymbol{y}) \nabla_y\right)\right) : \varepsilon_a(\boldsymbol{v}) \, dV_y - \int_Y \left[\mu_0 . \left(-\varphi(\boldsymbol{y}) \nabla_y\right) + \boldsymbol{B}^{\boldsymbol{r}}(\boldsymbol{y})\right] . \boldsymbol{E}_a^{mag}(\psi) \, dV_y = 0 \end{aligned} \tag{6.63}$$

This problem is solved using FreeFem++ open source finite element software as well as for the subsequent determination of the first gradient, Cosserat, and the magnetic moduli in Eq. 6.54. An example of the procedure followed for the determination of the homogenized moduli is condensed in algorithmic format in Fig. 6.2.

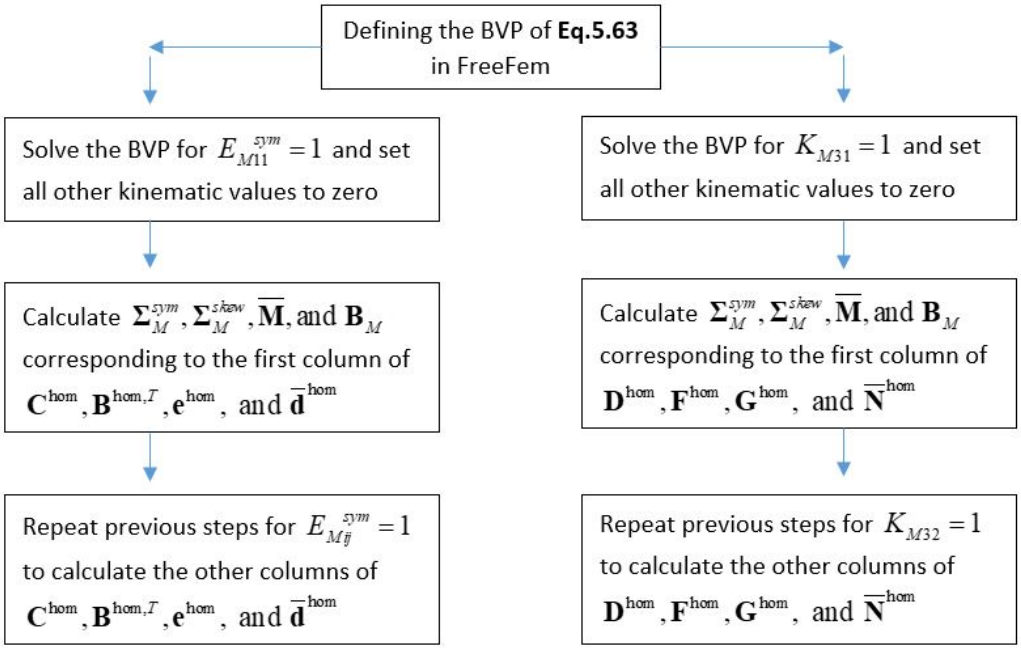

Figure 6.2 Schematic algorithm for the computation of some effective moduli.

The next subsection deals with a numerical example for the determination of the effective moduli of a magneto elastic structure.

6.5.1 Couplings between magnetic effects and mechanics at the macrolevel

The methodology mentioned in section 6.5 is applied for the unit cell geometry pictured in Fig. 6.3. Different colors are used to identify regions sharing the same mechanical properties (all regions have

the same E and mu in Table 6.3) but endowed with different magnetic properties. The blue regions correspond to the non-magnetic material, and black and red regions correspond to magnetic materials of opposite directions of the residual magnetization ($M^{\mathrm{r}} = \mu_0 \mathrm{B}^{\mathrm{r}}$) vector direction. Table 6.3 includes the mechanical and magnetic properties used in this example.

Table 6.3 Mechanical and magnetic properties.

E (kPa)	ν	$\mu_0\left(NA^{-2}\right)$	$\mathrm{M}^{\mathrm{r}}\,(kA/m)$
500	0.4	$4\pi\ 10^{-7}$	500

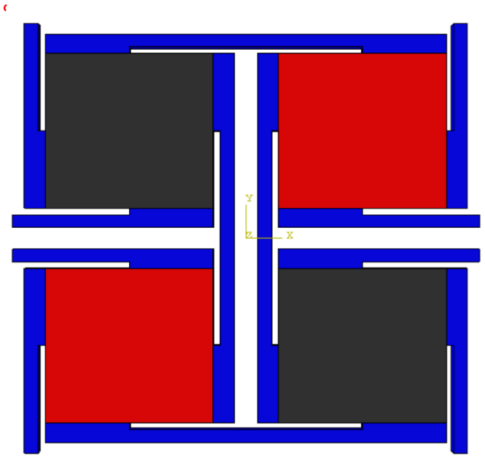

Figure 6.3 Unit cell with regions having different magnetic properties.

The effective macroscopic tensors are computed (with their physical units indicated under brackets) from the previous homogenization method over the unit cell of Fig. 6.3 with periodic boundary conditions:

$$C^{\mathrm{hom}} = \begin{bmatrix} 16963.8 & -16229.6 & 330.348 & 330.348 \\ -16406.9 & 16752 & 124.324 & 124.324 \\ 19411.2 & 19411.2 & 376554 & 19411.2 \\ 19686.8 & 19686.8 & 19686.8 & 376830 \end{bmatrix} [Pa]$$

$$D^{\mathrm{hom}} = \begin{bmatrix} 260.037 & 216.472 \\ 312.66 & -87.3952 \\ -1614.5 & -1519.81 \\ -1338.88 & -1244.19 \end{bmatrix} [Pa.m]$$

$$d^{\mathrm{hom}} = \begin{bmatrix} 320.705 & 320.705 \\ 401.249 & 401.24 \\ -1567.3 & -1567.34 \\ -1291.69 & -1291.69 \end{bmatrix} [T]$$

$$e^{\text{hom}} = \begin{bmatrix} -67.899 & -371.47 & 125.318 & 125.318 \\ 945.664 & -453.649 & 243.569 & 243.569 \end{bmatrix} [Pa.m]$$

$$G^{\text{hom}} = \begin{bmatrix} 170001 & 3863.86 \\ 6532.02 & 180030 \end{bmatrix} [Pa.m^2]$$

$$N^{\text{hom}} = \begin{bmatrix} 170.564 & 170.56 \\ -365.729 & -365.73 \end{bmatrix} [NA^{-1}]$$

$$\overline{d}^{\text{hom}} = \begin{bmatrix} -0.0257 & -0.0257 & -0.025 & -0.0257 \\ 0.0266 & 0.0266 & 0.0265 & 0.0266 \end{bmatrix} [T]$$

$$\overline{N}^{\text{hom}} = \begin{bmatrix} -0.0257 & -0.0257 \\ 0.02661 & 0.0266 \end{bmatrix} [NA^{-1}]$$

$$a^{\text{hom}} = \begin{bmatrix} 0.02571 & 0 \\ 0 & 0.0266 \end{bmatrix} [NA^{-2}]$$

From the values of the effective properties within these matrices, one can underline the following main results:

1. The microstructure has an auxetic and chiral behavior, especially a high coupling effect between the shear stress and the normal deformation (evidenced by the mechanical effective properties in C^{hom}), and further evidenced in the plot of Fig. 6.4(b).
2. A non-centrosymmetric behavior emerges for the magneto-mechanical coupling, due to the lack of coupling between the magnetic field and the micro-deformation at microscopic level, thus the absence of reciprocity at the microlevel is transferred to the macrolevel. This effect appears from the comparison of the coefficients within the submatrices d^{hom} and $\overline{d}^{\text{hom}}$.
3. There is a lower coupling effect of couple stress with deformation compared to the Cauchy first gradient response, as one can see from the comparison between D^{hom} and e^{hom}.
4. The resulting homogenized medium is a shear-stiff material, since the ratio between the normal to shear coefficient is lower than 1, and since within matrix C^{hom}, the homogenized shear modulus is higher than the homogenized Young's modulus.
5. The bending effect induced by the application of a magnetic field is important, accounted for by the corresponding coupling tensor $\overline{N}^{\text{hom}}$ in Eq. 6.54.
6. The magnetic field induced by an applied shear stress is higher in d^{hom} than the one induced from a normal stress (-1291,69 T compared to 320,705 T).
7. As mentioned in the theory above, the imposed static boundary condition induces high magnetic field within the structure, while the magnetic field leads to a very low strain at the macro level because no such coupling exists at the micro level. This lack of reciprocity appears in the computed macroscopic submatrices a^{hom}, $\overline{N}^{\text{hom}}$ and $\overline{d}^{\text{hom}}$.

Figures (Fig. 6.4(a)-(e)) show the deformed modes of the unit cell caused by the application over its boundary of the independent components of strain, the gradient of rotation, and magnetic field. The visually apparent small interpenetration between different parts of the domain is an artefact due to the magnification of the deformed shape.

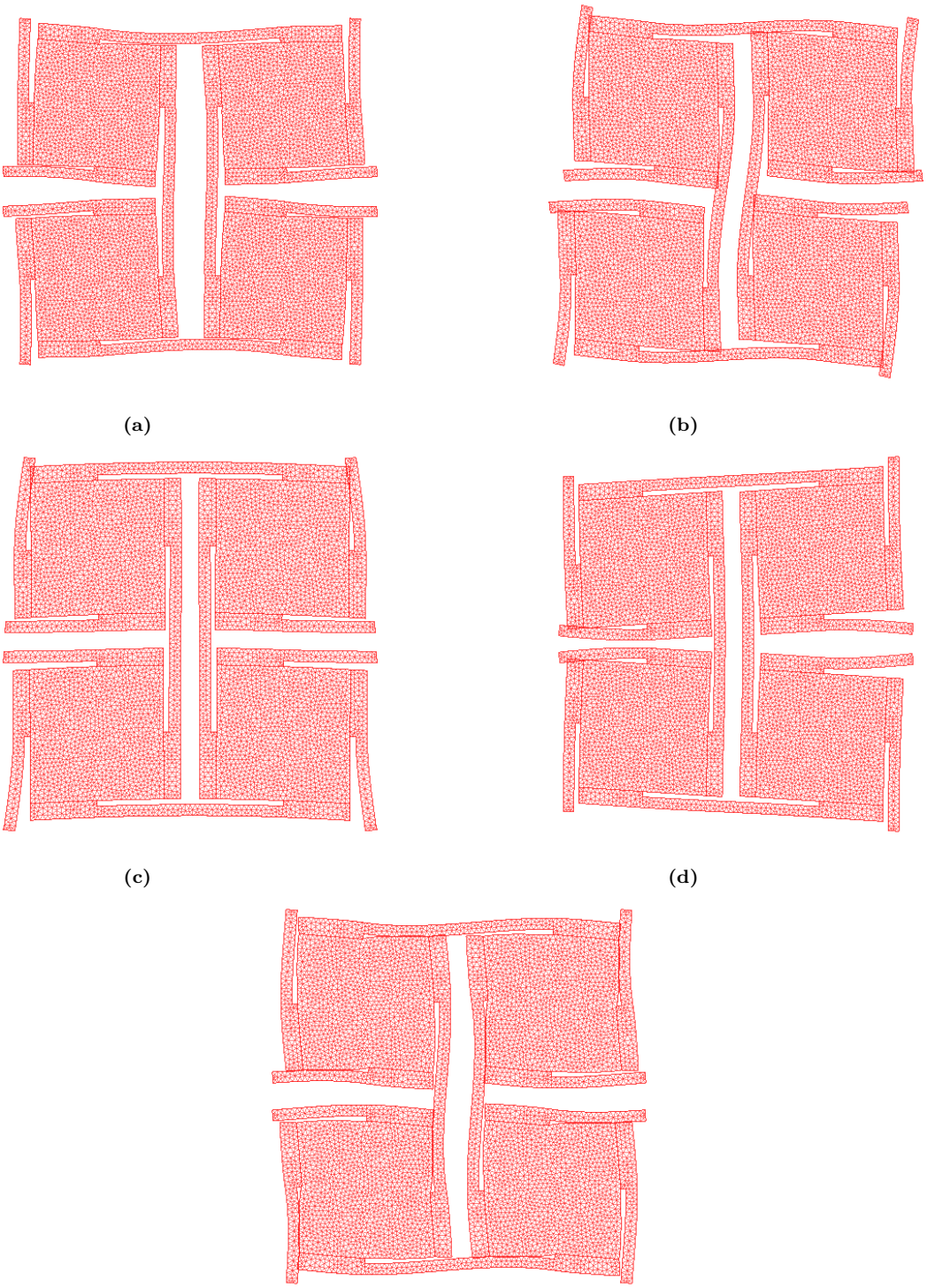

Figure 6.4 Deformation modes of the unit cell induced by (a) E_{M11},(b) E_{M12}, (c) K_{M31}, (d) K_{M32}, (e) H_{M1}

The unit cell structure undergoes the deformation modes shown in Fig. 6.4(a) and Fig. 6.4(b) due to application of the mechanical strains and respectively. The deformed modes in Fig. 6.4(c) and Fig. 6.4(d) are due to the gradients of rotation and respectively. Fig. 6.4(e) shows the deformation of the unit cell under a magnetic field applied as a boundary condition; the structure undergoes bending due to the applied magnetic field, revealing the coupling between the mechanical and magnetic fields. This coupling can also be seen from the distribution of the magnetic potential when the mechanical strain component is applied over the unit cell boundary Fig. 6.5.

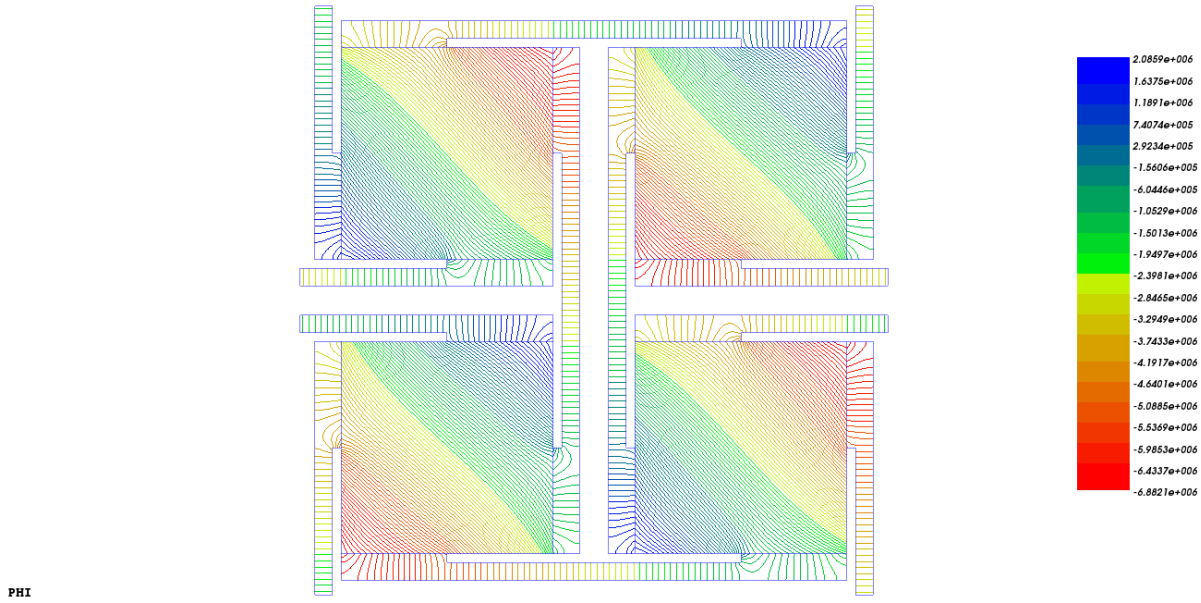

Figure 6.5 Distribution of the magnetic potential φ resulting from the application of the strain component E_{M11}

6.6 Conclusion

In this chapter we established a variational-based homogenization method for magnetoelastic composite materials in a small strains framework. The existence of a non-symmetrical stress tensor prompts the development of a homogenized magnetoelastic Cosserat effective medium at the macroscale. Generic expressions of the effective magnetic and elastic properties are derived, showing the existence of couplings between the elastic and magnetic behaviors at the macrolevel, despite that the behavior is non-reciprocal at the microscale. The considered microstructure has an auxetic and chiral behavior, especially a high coupling effect between the shear stress and the normal deformation. A non-centrosymmetric behavior emerges for the magneto-mechanical coupling, due to the lack of coupling between the magnetic field and the micro-deformation at microscopic level, thus the absence of reciprocity at the microlevel is transferred to the macrolevel. It entails the existence of a coupling between tension and bending. Furthermore, the application of a magnetic field also leads to bending. The imposed static boundary condition induces high magnetic field within the structure, while the magnetic field leads to a very low strain at the macro

level because no such coupling exists at the micro level. The bending effect induced by the application of a magnetic field is important. In comparison to the classical Cauchy response, the importance of couple stress effects are weaker.

The proposed magnetoelastic homogenization framework defines a base of simulation tools for the computation of the effective magnetoelastic properties of a wide variety of architected materials.

General conclusion and perspectives

Multiphysical couplings, such as *piezoelectricity*, *flexoelectricity*, and *magnetoelasticity*, are exhibited by *composites* and *architected materials* in many engineering applications (such as sensors, actuators..) because of their capability to offer high mechanical performance (such as strength, energy absorption capacity, acoustic and thermal insulation properties) while maintaining a low weight. While piezoelectricity shows a coupling between the electric polarization and the mechanical strain, flexoelectricity is a higher-order phenomenon that involves the coupling between electric polarization and strain gradient. Furthermore, magnetoelasticity refers to the interaction between the magnetic and elastic fields.

To fully realize the potential of these materials, it is crucial to understand and predict their mechanical behavior at the unit cell level, incorporating the microstructural information available. In this context, developing predictive micromechanical schemes that account for the impact of the existing microstructure on the mechanical response at both mesoscopic and macroscopic levels is necessary for bridging the scales and relating equivalent properties to the structural geometry and mechanical parameters.

To predict the overall mechanical response of microstructured materials such as architected and composite materials, it is not feasible to conduct direct numerical simulations that fully resolve all microstructural details using a fine mesh resolution. Such simulations are usually computationally expensive, making them impractical for typical engineering problems. Additionally, determining the mechanical properties of these structures experimentally is challenging since the overall anisotropy needs to be considered. Furthermore, there may not be a clear scale separation, which may necessitate using enriched continuum theories that involve more constitutive parameters than Cauchy elasticity theory. Therefore, it is relevant to perform homogenization to derive effective models, which can be used to conduct macrostructural level computations conveniently in a subsequent step.

Outcome of the research

The thesis aims to bring some new developments in the field of homogenization of heterogeneous materials prone to multiphysical phenomena, focusing on piezoelectricity and magnetoelasticity in the context of generalized continua. All developments are limited to linearized elasticity. As well, this thesis revisits higher gradient homogenization schemes towards higher-gradient continuum of periodic and quasi-

periodic microstructures. Besides the continuous homogenization schemes for periodic media, a discrete homogenization method is proposed in this thesis, which can be adopted for architected materials that are made up of slender structural elements such as beam elements. **Part I** exposes the homogenization of periodic and quasi-periodic media towards a strain gradient effective continuum, whereas **Part II** accounts for multiphysical aspects in the homogenization approaches towards generalized continua.

In the spirit of micromechanics, we construct a strain gradient model of periodic architected media employing a discrete homogenization method towards a strain gradient effective substitution medium and using Hill extended macrohomogeneity condition. This approach involves using a reduced number of degrees of freedom at the level of the unit cell, combined with a continuous set of kinematic variables representative of a strain gradient continuum at the macro level. The resulting classical and strain gradient moduli can be expressed as closed-form analytical expressions of the microstructural parameters of the square and hexagonal lattices. Although Cauchy moduli cannot describe surface properties, the theoretical and numerical analysis demonstrate that the strain gradient moduli scale with the edge contribution of the surface material, indicating a quadratic relationship with the absolute edge length. A similar scaling law is derived through a shape sensitivity analysis of the internal macroscopic energy where kinematic strain gradient tensors are employed as kinematic edge conditions on self-similar unit cells with varying edge lengths, while Cauchy moduli remain constant. Moreover, the energetic formulation of a second strain gradient continuum allows to revisit the notion of anisotropic surface energy, thereby providing a generalization of Mindlin's model of surface energy.

Secondly, the theoretical background beyond quasi-periodic homogenization for quasi-periodic media is presented in **chapter 3**. The main idea behind this homogenization is to map any unit cell of the quasi-periodic domain to the parent periodic (fixed) unit cell. In this context, the first scheme developed relies on the average of the microscopic energy and obeys the established smoothness conditions of the mapping. This allows determining the effective quasi-periodic moduli tensors versus those of the periodic domain and the associated perturbation terms which are expressed in a volumetric format over the reference unit cell domain in a 2D context. Following this approach, a surface formulation of the quasi-periodic moduli is then derived, based on the notion of shape derivative of the total potential energy stored within the unit cell, and via Clapeyron's theorem which allows to link the potential energy to the internal strain energy. This scheme offers comparative to the first one a simpler way to compute the quasi-periodic moduli as it only requires the evaluation of the mechanical fields on the unit cell boundaries. The strain gradient theory is then considered to account for the design grading at the microscopic level. From the considered numerical application of inclusion-based composites, the importance of the strain gradient model arises where the contribution of strain gradient energy dominates and Cauchy energy becomes insufficient to describe the effect of the design variation of the unit cell.

In **Part II** of the thesis, some multiphysical aspects are incorporated in the periodic homogenization methods adopted. The basic concept behind these suggested homogenization approaches involves dividing the microscopic displacement and the electric (magnetic) potential into two parts: a homogeneous

part that reflects the kinematics of the effective continuum, and a fluctuating part that is determined through a variational principle and is defined by the unit cell boundary value problem. Within this framework, and using Hill macro-homogeneity condition, the evaluation of effective linear piezoelectric properties of heterogeneous materials is addressed in **chapter 4**. The entire set of homogenized moduli has been obtained, expressing as volumetric averages of the microscopic properties of the individual constituents weighted by the displacement and electric potential localization operators. This framework is then extended to the computation of the effective flexoelectric properties, thereby accounting for higher gradient effects. To exemplify these theories, numerical applications are done for composites and architected materials. The computational scheme involves solving the boundary value problem expressed in its weak formulation when applying different macroscopic kinematic boundary conditions to determine the effective piezoelectric and flexoelectric properties (**chapter 5**). Energy computations show that the effective flexoelectric medium represents a quite good approximation of the initially heterogeneous piezoelectric composite.

Based on the effective flexoelectric properties, a wave propagation analysis has been addressed successively in the frameworks of Classical Flexoelectric Theory (CFE) and Non-Local Flexoelectric Theory (NLFE) (**chapter 5**). The results show that flexoelectric medium is a dispersive medium and of higher anisotropic behaviour when increasing the wavenumber, compared to the piezoelectric medium.

Numerical application are subsequently done to architected materials, selecting the following three different unit cells;the regular hexagonal UC, the rectangular UC, and the re-entrant hexagonal UC. The non-uniform distribution of the electric potential resulting from the application of mechanical strain over the three architected materials serves as an evidence of the coupling between the mechanical and the electric fields. The sensitivity analysis to geometrical parameters of these architected materials shows that the regular hexagonal UC yields the highest piezoelectric modulus, while the re-entrant UC exhibits the highest flexoelectric modulus.

In **chapter 6**, a homogenization towards Cosserat (micropolar) effective continuum is addressed for magnetoelastic heterogeneous solids, in a small strains framework. The existence of a non-symmetrical stress tensor prompts the development of a homogenized magnetoelastic Cosserat effective medium at the macroscale. A numerical application made for a unit cell microstructure with magnetoelastic properties shows a coupling between the elastic and magnetic behaviors at the macrolevel.

Perspectives

Based on the developed theoretical and numerical contributions we are entitled to propose some **perspectives** regarding different aspects as exposed in the sequel.

- The choice of the most appropriate generalized continuum for a given class of architected materials remains a significant matter that requires attention in future advancements.
- Although the concept of modifying the topology of architected materials to improve their

electromechanical properties is important, it is relevant to develop a systematic approach for identifying architectures that result in the emergence of enhanced behaviors; topology optimization methods regarding piezoelectricity and flexoelectricity can offer such a strategy.

- In the generalization of Mindlin's model of surface energy, there are more terms representative of surface energies that have not been investigated; yet these terms can be analyzed in future contributions.
- In order to validate the homogenization schemes and constitutive models formulated for periodic magnetoelastic media and quasi-periodic media, numerical simulations have be to incorporated with experimental investigations. It would be interesting to link these homogenization schemes with atomistic simulations.
- Since the developed finite element models are limited to 2D, an extension of these models into 3D is planned to determine the homogenized mechanical, piezoelectric, flexoelectric, and magnetic properties of architected materials.
- It would be interesting to incorporate multiphysics with dynamics by developing dynamic homogenization schemes for high frequencies.
- Amongst the perspectives of this thesis, investigating the response of lattice materials to large strains within the framework of generalized continua is of high interest (architected materials are made of slender elements and they are porous materials that can develop large strains for soft base materials. One example of applications can be artificial skin).
- Finally, it's worth mentioning interesting scientific prospects and applications of the proposed flexoelectric homogenization method in the field of bone bio-mechanics, specifically in bone remodeling despite the added complexity of incorporating microstructure changes during remodeling. Furthermore, the quasi-periodic homogenization scheme can be further applied to conformal architected materials undergoing a conformal transformation of their design.

Résumé de la thèse en français

Introduction

Les aspects multiphysiques font référence à l'interaction de plusieurs phénomènes physiques qui se produisent simultanément dans un système ou un matériau. Ces phénomènes peuvent inclure des processus mécaniques, thermiques, électriques, magnétiques, chimiques et biologiques. Parmi les différents phénomènes multiphysiques, les couplages électromécaniques et magnéto-mécaniques, qui relient respectivement les champs électriques et magnétiques aux champs mécaniques, ont attiré beaucoup d'attention. La piézoélectricité est une forme de couplage électromécanique largement reconnue et fréquemment utilisée, où la polarisation électrique et les contraintes mécaniques sont linéairement couplées(Fig. R.1 [2]). L'un de ces couplages électromécaniques qui a reçu moins d'attention et qui est le sujet principal de cette thèse est la flexoélectricité [3]. La flexoélectricité implique le couplage entre les gradients de déformation et la polarisation électrique (ou entre un gradient de polarisation et la déformation) [4,5]. L'effet flexoélectrique directe se réfère à la polarisation d'un matériau résultant d'une déformation non uniforme telle que la flexion ou la torsion [6]. Outre les études réalisées sur les différents

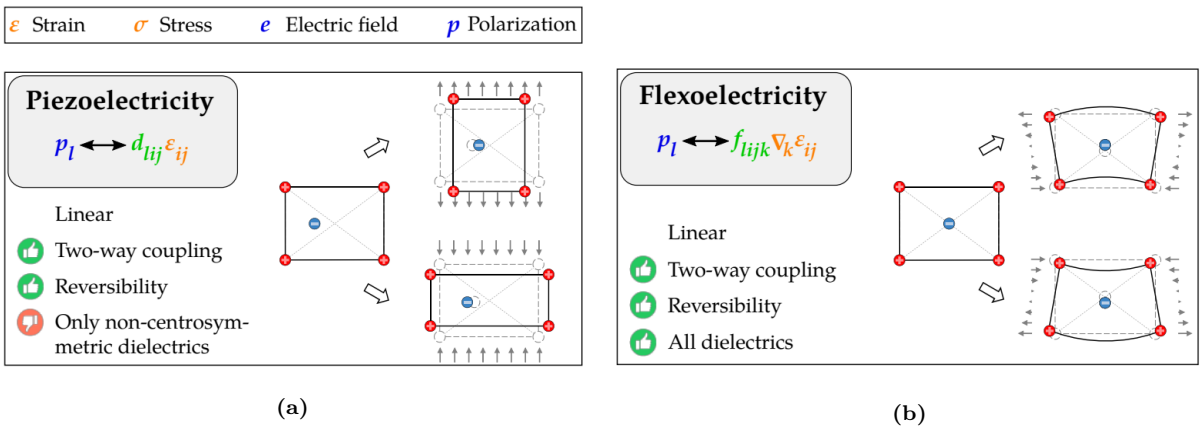

Figure R.1 Présentation schématique de la piézoélectricité (a) et de la flexoélectricité (b) dans les cristaux diélectriques.

effets de couplage électromécanique, beaucoup se sont concentrées sur le couplage magnéto-élastique qui fait référence à l'interconnexion entre les champs magnétiques et élastiques.

Les couplages multiphysiques, tels que la piézoélectricité, la flexoélectricité, et la magnétoélasticité, sont présentés par composites et matériaux architecturés (Fig. R.2 [43]) dans de nombreuses applications d'ingénierie (telles que les capteurs, les actionneurs...) en raison de leur capacité à offrir des performances mécaniques élevées (telles que la résistance, la capacité d'absorption d'énergie, les propriétés d'isolation acoustique et thermique) tout en conservant un faible poids.

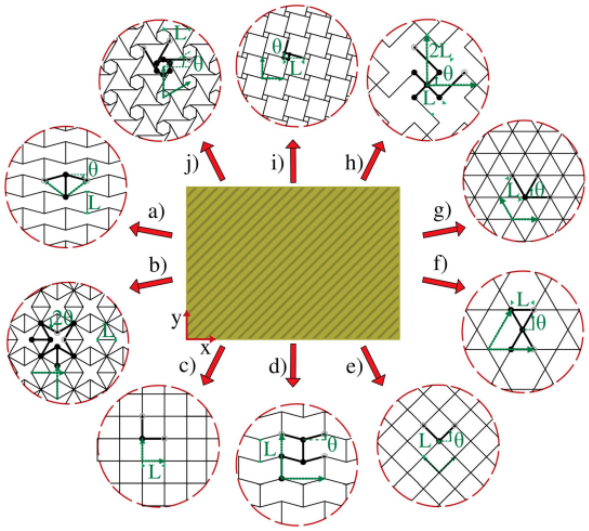

Figure R.2 Matériaux architecturés en 2D : (a)Hexagone, (b) étoile rentrante, (c) rectangulaire,(d) semi-entrant, (e, f, g) diamant, kagome, forme triangulaire, réseaux chiraux : (h) diamant chiral, (i) tétrachiral, (j)hexachiral.

Pour exploiter pleinement le potentiel de ces matériaux, il est essentiel de comprendre et de prédire leur comportement mécanique au niveau de la cellule unitaire, en incorporant les informations microstructurelles disponibles. Dans ce contexte, le développement de schémas micromécaniques prédictifs qui tiennent compte de l'impact de la microstructure existante sur la réponse mécanique aux niveaux mésoscopique et macroscopique est nécessaire pour faire le lien entre les échelles et relier les propriétés équivalentes à la géométrie structurelle et aux paramètres mécaniques.

Pour prédire la réponse mécanique globale des matériaux microstructurés tels que les matériaux architecturés et composites, il n'est pas possible d'effectuer des simulations numériques directes qui résolvent entièrement tous les détails microstructuraux à l'aide d'une résolution de maillage fine. Ces simulations sont généralement coûteuses en termes de calcul, ce qui les rend peu pratiques pour les problèmes d'ingénierie typiques. En outre, la détermination expérimentale des propriétés mécaniques de ces structures est un défi car l'anisotropie globale doit être prise en compte. En outre, il se peut qu'il n'y ait pas de séparation d'échelle claire, ce qui peut nécessiter l'utilisation de théories du continuum enrichies qui impliquent plus de paramètres constitutifs que la théorie de l'élasticité de Cauchy. Il est donc utile de procéder à une homogénéisation pour dériver des modèles efficaces, qui peuvent être utilisés pour effectuer des calculs au niveau macrostructurel de manière pratique dans une étape ultérieure.

L'homogénéisation vers des continuums généralisés (au-delà de Cauchy) vise à répondre aux limites d'une séparation d'échelle stricte et à élargir le domaine de validité de l'approche du continuum au-delà de l'hypothèse restreinte de la séparation d'échelle [53, 54]. La définition d'un continuum généralisé peut être étendue grâce à deux approches principales, basées sur la classification en deux catégories principales, à savoir les continuums d'ordre supérieur et les continuums à gradient supérieur, comme le montre l'illustration de la Fig. R.3 [55].

L'existence d'un couple par unité de volume dans les matériaux électromagnétiques a souvent été suggérée comme une raison de prendre en compte des tenseurs de contrainte non symétriques [46]; cette idée a été la motivation première pour l'introduction de la généralisation de la mécanique du continuum et de la nécessité de théories du continuum enrichies [77, 78].

Outre le besoin de théories du continuum enrichies lorsqu'il s'agit de multiphysique, ces milieux sont nécessaires dans des situations pour capturer l'influence des fluctuations spatialement rapides aux niveaux mésoscopique et macroscopique.

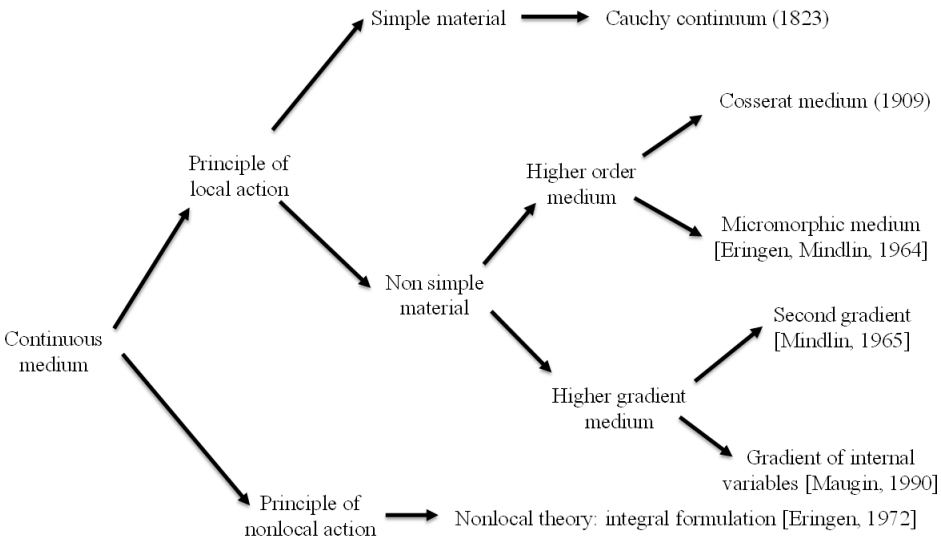

Figure R.3 Illustration montrant la classification des continuums généralisés en milieux d'ordre supérieur et de qualité supérieure.

Depuis le début des années soixante, la plupart des modèles de continuum généralisés étaient purement formels et ne reposaient pas sur des microstructures réelles. Par conséquent, les lois constitutives ont été développées de manière phénoménologique, sans qu'il soit nécessaire de recourir à des méthodes micromécaniques. Cependant, la situation a changé de manière significative au début des années 90 avec le développement de nouvelles classes de matériaux telles que les composites, les solides cellulaires (mousses) et les matériaux architecturés, ainsi qu'avec les progrès de la puissance de calcul et des techniques de fabrication telles que la fabrication additive. Cela a suscité un intérêt croissant dans les communautés mécaniques et mathématiques pour comprendre la relation entre les comportements émergents enrichis au niveau d'un continuum effectif et les modes de déformation microscopiques.

Travail de thèse

La thèse a pour objectif d'aborder de façon théorique et numérique l'homogénéisation de milieux architecturés et composites périodiques présentant un comportement multiphysique, dans le contexte des milieux continus généralisés. Le manuscrit est donc décomposé en deux parties qui couvrent explicitement ces questions.

La première partie du manuscrit traite l'homogénéisation des milieux périodiques et quasi-périodiques vers un continuum effectif à gradient de déformation. Une méthode d'homogénéisation discrète est appliquée pour les matériaux périodiques architecturés, conduisant à l'élaboration des propriétés effectives d'ordre supérieur sous forme d'expressions analytiques dépendant de la longueur du bord de la cellule unité. Dans un autre chapitre, une homogénéisation quasi-périodique est développée à partir d'une expression volumétrique de l'énergie et en s'appuyant sur la notion de dérivée de forme pour déterminer les propriétés effectives quasi-périodiques basées sur le domaine périodique transformé.

La deuxième partie du manuscrit intègre des aspects multiphysiques dans les approches d'homogénéisation vers les continuums généralisés. La théorie de l'homogénéisation piézoélectrique et flexoélectrique est élaborée et suivie d'applications numériques pour l'homogénéisation des composites piézoélectriques et des matériaux architecturés ainsi que pour l'analyse de la propagation des ondes. En outre, l'homogénéisation vers le continuum effectif de Cosserat (micropolaire) est abordée pour les solides hétérogènes magnétoélastiques.

L'objectif général de la thèse est de développer de nouvelles méthodes d'homogénéisation pour les milieux hétérogènes vers des milieux continus à gradient d'ordre supérieur, en prenant en compte différents aspects multiphysiques tels que la piézoélectricité, la flexoélectricité et la magnétoélasticité.

Dans cette thèse, nous exposons une méthode d'homogénéisation discrète pour les matériaux architecturés périodiques vers une formulation de milieux continus à gradient de déformation, fournissant le module classique effectif et le module de gradient de déformation selon des expressions analytiques des paramètres microstructuraux du réseau. Le recours à une formulation à gradient de déformation permet de quantifier les effets de surface (les effets de bord en 2D) de matériaux architecturés. Alors que les modules de Cauchy ne capturent pas les propriétés de surface, un examen théorique et numérique a donné la loi d'échelle des modules de gradient de déformation avec la contribution du bord du matériau de surface, montrant une variation quadratique avec la longueur absolue du bord (Fig. R.4). Pour atteindre cet objectif, la condition de macrohomogénéité de Hill étendue pour les milieux à gradient de déformation a été formulée à partir de champs mécaniques purement surfaciques, ayant pour support le bord (interne ou externe) de la cellule unitaire.

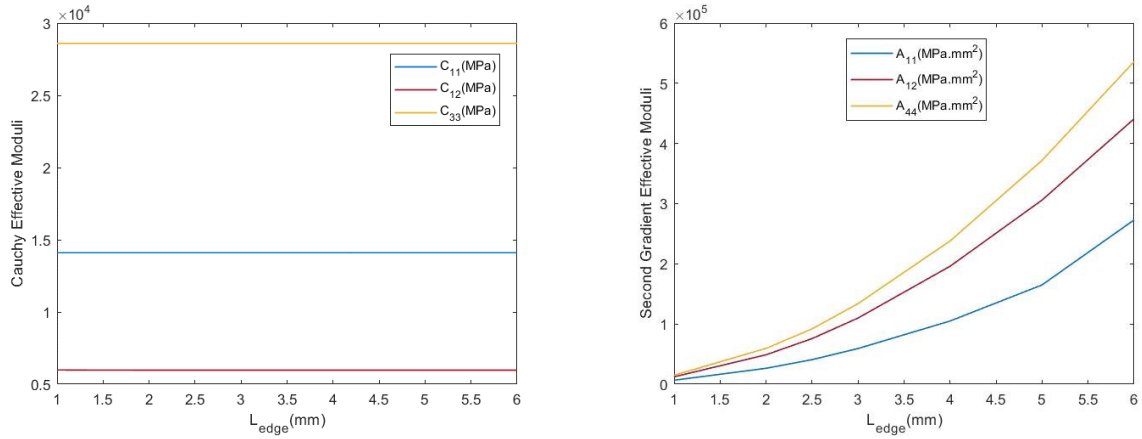

(a) **(b)**

Figure R.4 Modules de Cauchy (a) et de gradient de déformation (b) en fonction de la longueur du bord de la cellule unitaire pour la cellule unitaire hexagonale régulière.

La même loi d'échelle a été obtenue à partir d'une analyse de sensibilité à la forme de l'énergie macroscopique interne, dans laquelle des tenseurs cinématiques de gradient de déformation ont été appliqués comme conditions de bord cinématiques sur des cellules unitaires autosimilaires avec des longueurs de bord variables (les modules de Cauchy sont inchangés). En outre, sur la base d'un modèle de continuum effectif à gradient de déformation, nous formulons la notion d'énergie de surface de manière anisotrope, en nous appuyant sur l'identification de deux contributions intégrales de surface impliquant des invariants cinématiques des tenseurs macroscopiques des premier et second gradients de déformation (Eq. 6.64, Eq. 6.65). Ceci fournit une généralisation du modèle de Mindlin [129] de l'énergie de surface.

$$\frac{1}{4}\int_{\partial V_x} \boldsymbol{N}\cdot\boldsymbol{A}^{\mathrm{hom}}_{\{(2,3),(4,5)\}}\cdot(\boldsymbol{U}\cdot\nabla_x)^{2}\otimes\nabla_x \mathrm{dS} \tag{6.64}$$

$$\frac{1}{2}\int_{\partial V_x} \boldsymbol{N}\cdot\overline{\boldsymbol{A}}^{\mathrm{hom}}_{\{(2,3,4),(5,6,7)\}}\cdot(\boldsymbol{K}\therefore\boldsymbol{K})\otimes\nabla_x \mathrm{dS} \tag{6.65}$$

En outre, nous présentons des schémas d'homogénéisation quasi-périodique pour les milieux quasi-périodiques, qui ne présentent pas de périodicité mais qui peuvent être transformés en un milieu périodique parent (Fig. R.5).

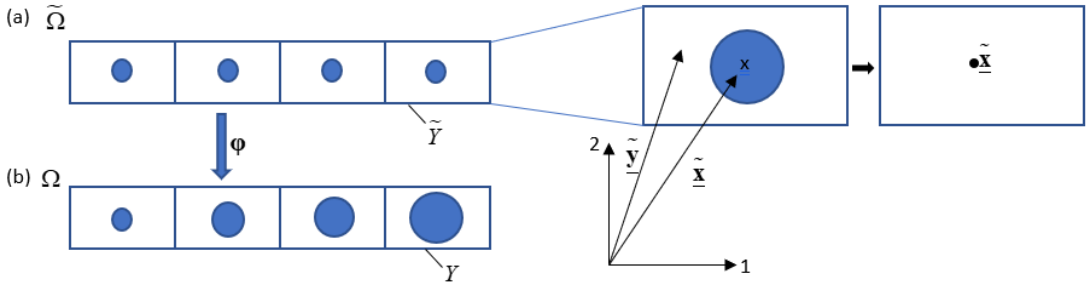

Figure R.5 Illustration de la transformation introduite qui est définie par une correspondance $\boldsymbol{\varphi}$ entre (a) le domaine périodique $\widetilde{\Omega}$ et (b) le domaine quasi-périodique Ω. La cellule unitaire périodique à droite montre les vecteurs de position microscopiques $\underline{\widetilde{\boldsymbol{y}}}$ et macroscopiques $\underline{\tilde{\boldsymbol{x}}}$.

Dans ce contexte, nous développons d'abord une approche théorique de l'homogénéisation quasi-périodique, pour de petites perturbations de l'architecture de la cellule unitaire selon la macroéchelle, en partant de la moyenne de l'énergie microscopique et en suivant les conditions de lissage établies de la cartographie (ce qui signifie une petite variation de la conception de la CU). Cela permet de relier les tenseurs de modules effectifs quasi-périodiques à ceux du domaine périodique et aux termes de perturbation associés qui sont exprimés dans un format volumétrique sur le domaine de la cellule unitaire de référence dans un contexte 2D.

Suivant cette approche, une formulation de surface des modules quasi-périodiques est ensuite dérivée, basée sur la notion de dérivée de forme de l'énergie potentielle totale stockée dans la cellule unitaire, via le théorème de Clapeyron permettant de relier l'énergie potentielle à l'energie de déformation. Cette approche repose sur l'introduction d'un champ de vitesse de forme à la frontière de la cellule unitaire périodique pour modéliser le changement de sa conception. Ce schéma offre, par rapport au premier, un moyen plus simple de calculer les modules quasi-périodiques, car il ne nécessite que l'évaluation des champs mécaniques aux frontières de la cellule unitaire.

La théorie du gradient de déformation est ensuite envisagée pour rendre compte de la gradation de topologie au niveau microscopique. les milieux à gradient de propriétés sont très utilisés dans diverses applications en ingénierie ainsi que pour la réalisation de biosubstituts en biomécanique. L'importance du modèle à gradient de déformation apparaît dans l'application considérée des composites à base d'inclusion car l'énergie de Cauchy devient insuffisante pour décrire l'impact de la variation de l'architecture interne de la cellule unitaire. Cela se traduit par une augmentation de la contribution de l'énergie du gradient de déformation d'un facteur 5 à partir de la CU de référence, par rapport à l'énergie de Cauchy (Fig. R.6).

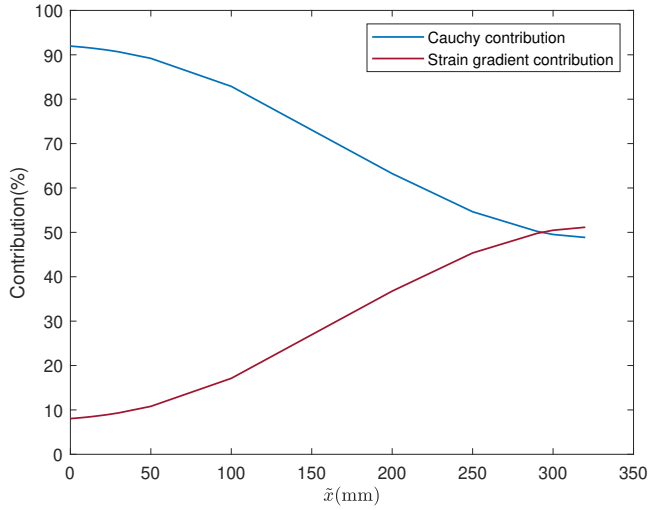

Figure R.6 Contributions énergétiques en fonction de la position macroscopique.

D'autre part, nous abordons dans cette thèse le calcul des propriétés piézoélectriques linéaires effectives de matériaux hétérogènes dans le contexte de l'homogénéisation périodique, en employant une formulation variationnelle en combinaison avec la condition de macro-homogénéité de Hill étendue. Les variables microscopiques - le vecteur de déplacement et le potentiel électrique - ont été exprimées comme la somme d'une partie homogène et d'une fluctuation obéissant à un principe de minimum de la fonctionnelle d'énergie. L'ensemble des modules homogénéisés a été obtenu, en exprimant les moyennes volumétriques des propriétés microscopiques des constituants individuels pondérées par les opérateurs de localisation du déplacement et du potentiel électrique.

Nous étendons ensuite ce cadre au calcul des propriétés flexoélectriques effectives, prenant ainsi en compte les effets de gradient plus élevés qui peuvent être induits par un fort contraste de propriétés des constituants au sein du composite. Nous adoptons un algorithme numérique reposant sur la résolution de la formulation faible du problème aux limites lors de l'application de différentes conditions limites cinématiques macroscopiques. Cette approche peut être appliquée aux matériaux composites et architecturés.

En application du cadre général d'homogénéisation proposé, nous évaluons numériquement les propriétés piézoélectriques et flexoélectriques effectives de composites à base d'inclusions hétérogènes et des matériaux architecturés. Sur la base de ces propriétés homogénéisées, nous évaluons l'effet de la fraction volumique et du module de traction relatif de l'inclusion par rapport à celui de la phase de la matrice. Les calculs énergétiques montrent que le milieu flexoélectrique effectif représente une assez bonne approximation du composite piézoélectrique initialement hétérogène.

Sur la base des propriétés flexoélectriques effectives, la propagation des ondes a été étudiée successivement dans le cadre de la théorie flexoélectrique classique (CFE) et de la théorie flexoélectrique non locale (NLFE). Les résultats montrent que le milieu flexoélectrique est dispersif (Fig. R.7).

Cependant, le milieu flexoélectrique présente un comportement anisotrope plus important lorsque le nombre d'onde augmente, par rapport au milieu piézoélectrique. En outre, la fréquence de propagation des ondes diminue avec le paramètre non local. Les fréquences de propagation des ondes sont plus basses dans un milieu piézoélectrique que dans un milieu élastique pur.

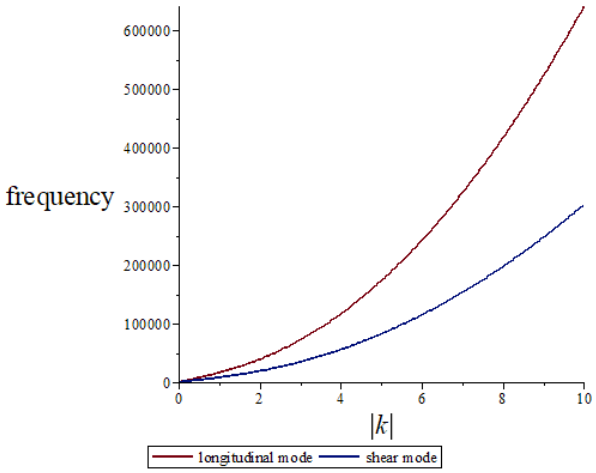

Figure R.7 Fréquence d'onde en fonction du nombre d'ondes dans le milieu flexoélectrique effectif.

En outre, nous effectuons une analyse de sensibilité à la topologie du réseau, en nous concentrant sur trois types de matériaux architecturés de cellules unitaires différentes : la CU hexagonale régulière, la CU rectangulaire et la CU ré-entrante. Cette analyse permet d'étudier la variation des modules piézoélectriques et flexoélectriques effectifs induite par une modification de la topologie des CU considérées. La comparaison des trois géométries montre que les modules piézoélectriques les plus élevés sont obtenus pour la CU hexagonal régulier, tandis que le module flexoélectrique est maximal pour la CU ré-entrante. Le couplage entre les champs mécaniques et électriques peut également être observé à travers la distribution non uniforme du potentiel électrique lors de l'application d'une contrainte mécanique sur les trois matériaux architecturés.

Les tendances obtenues s'avéreront utiles pour concevoir des matériaux composites et des matériaux architecturés présentant des propriétés piézoélectriques et flexoélectriques obéissant à un cahier des charges donné par le concepteur.

Un autre aspect intéressant abordé dans la thèse est la magnétoélasticité qui relie le champ magnétique et le champ élastique. Dans ce contexte, nous établissons une méthode d'homogénéisation variationnelle pour les matériaux composites magnétoélastiques dans un cadre de petites déformations. L'existence d'un tenseur de contrainte non symétrique incite à développer un milieu effectif de Cosserat magnétoélastique homogénéisé à l'échelle macroscopique. Nous dérivons des expressions génériques des propriétés magnétiques et élastiques effectives, montrant l'existence de couplages entre les comportements élastiques et magnétiques à l'échelle macroscopique, bien que le comportement soit non réciproque à l'échelle microscopique.

La microstructure considérée a un comportement auxétique et chiral, en particulier un effet de couplage élevé entre la contrainte de cisaillement et la déformation normale. Un comportement non centrosymétrique émerge pour le couplage magnéto-mécanique, en raison de l'absence de couplage entre le champ magnétique et la micro-déformation au niveau microscopique, de sorte que l'absence de réciprocité au niveau micro est transférée au niveau macroscopique. Cela implique l'existence d'un couplage entre la tension et la flexion.

En outre, l'application d'un champ magnétique entraîne également une flexion. La condition limite statique imposée induit un champ magnétique élevé à l'intérieur de la structure, alors que le champ magnétique entraîne une très faible déformation au niveau macroscopique car il n'y a pas de couplage de ce type au niveau microscopique. L'effet de flexion induit par l'application d'un champ magnétique est important. Par rapport à la réponse classique de Cauchy, l'importance des effets de contrainte de couple est plus faible.

Le cadre d'homogénéisation magnétoélastique proposé définit un socle d'outils de simulations pour la calcul des propriétés magnétoélastiques effectives d'une grande variété de matériaux architecturés.

Perspectives de la thèse

Sur la base des contributions théoriques et numériques développées, nous sommes en droit de proposer quelques **perspectives** concernant les différents aspects exposés dans la suite.

- Le choix du continuum généralisé le plus approprié pour une classe donnée de matériaux architecturés reste une question importante qui nécessite une attention particulière dans les progrès futurs.
- Bien que le concept de modification de la topologie des matériaux architecturés pour améliorer leurs propriétés électromécaniques soit important, il est pertinent de développer une approche systématique pour identifier les architectures qui aboutissent à l'émergence de comportements améliorés ; les méthodes d'optimisation de la topologie concernant la piézoélectricité et la flexoélectricité peuvent offrir une telle stratégie.
- Dans la généralisation du modèle d'énergie de surface de Mindlin, il existe d'autres termes représentatifs des énergies de surface qui n'ont pas été étudiés ; cependant, ces termes peuvent être analysés dans de futures contributions.
- Afin de valider les schémas d'homogénéisation et les modèles constitutifs formulés pour les milieux magnétoélastiques périodiques et quasi-périodiques, des simulations numériques doivent être incorporées aux études expérimentales.
- Les modèles d'éléments finis développés étant limités à la 2D, une extension de ces modèles à la 3D est prévue pour déterminer les propriétés mécaniques, piézoélectriques, flexoélectriques et magnétiques homogénéisées des matériaux architecturés.

- Il serait intéressant d'intégrer la multiphysique à la dynamique en développant des schémas d'homogénéisation dynamique pour les hautes fréquences.
- Parmi les perspectives de cette thèse, l'étude de la réponse des matériaux en treillis aux grandes déformations dans le cadre des continuums généralisés est d'un grand intérêt (les matériaux architecturés sont constitués d'éléments minces et ce sont des matériaux poreux qui peuvent développer de grandes déformations pour des matériaux de base souples. Un exemple d'application peut être la peau artificielle).
- Enfin, il convient de mentionner les perspectives scientifiques et les applications intéressantes de la méthode d'homogénéisation flexoélectrique proposée dans le domaine de la biomécanique osseuse, en particulier dans le remodelage osseux, malgré la complexité supplémentaire de l'incorporation des changements de microstructure au cours du remodelage. En outre, le schéma d'homogénéisation quasi-périodique peut être appliqué aux matériaux à architecture conforme subissant une transformation conforme de leur conception.

References

[1] Canan Dagdeviren, Pauline Joe, Ozlem L. Tuzman, Kwi-Il Park, Keon Jae Lee, Yan Shi, Yonggang Huang, and John A. Rogers. Recent progress in flexible and stretchable piezoelectric devices for mechanical energy harvesting, sensing and actuation. *Extreme Mechanics Letters*, 9:269–281, 2016.

[2] David Codony. *Mathematical and computational modeling of flexoelectricity at mesoscopic and atomistic scales*. PhD thesis, Universitat Politècnica de Catalunya, 2021.

[3] Peter V. Yudin and Alexander K. Tagantsev. Fundamentals of flexoelectricity in solids. *Nanotechnology*, 24, 2013.

[4] Raymond David Mindlin. Polarization gradient in elastic dielectrics. *International Journal of Solids and Structures*, 4(6):637–642, 1968.

[5] Koffi Enakoutsa, Alessandro Della Corte, and Ivan Giorgio. A model for elastic flexoelectric materials including strain gradient effects. *Mathematics and Mechanics of Solids*, 21(2):242–254, 2016.

[6] Pavlo Zubko, Gustau Catalan, and Alexander K. Tagantsev. Flexoelectric effect in solids. *Annual Review of Materials Research*, 43(1):387–421, 2013.

[7] VS Mashkevich and KB Tolpygo. Electrical, optical and elastic properties of diamond type crystals. *Sov. Phys. JETP*, 5(3):435–439, 1957.

[8] EV Bursian and ZAIKOVSK. OI. Changes in curvature of a ferroelectric film due to polarization. *Soviet Physics Solid State, USSR*, 10(5):1121–+, 1968.

[9] Sergei V. Kalinin, Stephen Jesse, Weili Liu, and Alexander A. Balandin. Evidence for possible flexoelectricity in tobacco mosaic viruses used as nanotemplates. *Applied Physics Letters*, 88(15):153902, 2006.

[10] Fatemeh Ahmadpoor and Pradeep Sharma. Flexoelectricity in two-dimensional crystalline and biological membranes. *Nanoscale*, 7:16555–16570, 2015.

[11] Alexander G. Petrov. Flexoelectricity of model and living membranes. *Biochimica et Biophysica Acta (BBA) - Biomembranes*, 1561(1):1–25, 2002.

[12] Sivapalan Baskaran, Xiangtong He, Qin Chen, and John Y. Fu. Experimental studies on the direct flexoelectric effect in α-phase polyvinylidene fluoride films. *Applied Physics Letters*, 98(24):242901, 2011.

[13] Sivapalan Baskaran, Narayanan Ramachandran, Xiangtong He, Sankar Thiruvannamalai, Ho Joon Lee, Hyun Heo, Qin Chen, and John Y. Fu. Giant flexoelectricity in polyvinylidene fluoride films. *Physics Letters A*, 375(20):2082–2084, 2011.

[14] Sivapalan Baskaran, Xiangtong He, Yu Wang, and John Y. Fu. Strain gradient induced electric polarization in α-phase polyvinylidene fluoride films under bending conditions. *Journal of Applied Physics*, 111(1):014109, 2012.

[15] Qian Deng, Mejdi Kammoun, Alper Erturk, and Pradeep Sharma. Nanoscale flexoelectric energy harvesting. *International Journal of Solids and Structures*, 51(18):3218–3225, 2014.

[16] Shuwen Zhang, Minglong Xu, Guoliang Ma, Xu Liang, and Shengping Shen. Experimental method research on transverse flexoelectric response of poly(vinylidene fluoride). *Japanese Journal of Applied Physics*, 55(7):071601, jun 2016.

[17] Yang Zhou, Jie Liu, Xinping Hu, Baojin Chu, Shutao Chen, and David Salem. Flexoelectric effect in pvdf-based polymers. *IEEE Transactions on Dielectrics and Electrical Insulation*, 24(2):727–731, 2017.

[18] John Harden, Badel Mbanga, Nandor Éber, Katalin Fodor-Csorba, Samuel Sprunt, James T. Gleeson, and Antal Jákli. Giant flexoelectricity of bent-core nematic liquid crystals. *Phys. Rev. Lett.*, 97:157802, Oct 2006.

[19] Robert B Meyer. Piezoelectric effects in liquid crystals. *Physical Review Letters*, 22(18):918, 1969.

[20] Traian Dumitrică, Chad M. Landis, and Boris I. Yakobson. Curvature-induced polarization in carbon nanoshells. *Chemical Physics Letters*, 360(1):182–188, 2002.

[21] Sergei V. Kalinin and Vincent Meunier. Electronic flexoelectricity in low-dimensional systems. *Phys. Rev. B*, 77:033403, Jan 2008.

[22] Sana Krichen and Pradeep Sharma. Flexoelectricity: A Perspective on an Unusual Electromechanical Coupling. *Journal of Applied Mechanics*, 83(3), 01 2016. 030801.

[23] John S. Oghalai, Hong-Bo Zhao, J. Walter Kutz, and William E. Brownell. Voltage- and tension-dependent lipid mobility in the outer hair cell plasma membrane. *Science*, 287(5453):658–661, 2000.

[24] Anthony W Peng, Felipe T Salles, Bifeng Pan, and Anthony J Ricci. Integrating the biophysical and molecular mechanisms of auditory hair cell mechanotransduction. *Nature communications*, 2(1):523, 2011.

[25] Fabian Vasquez-Sancho, Amir Abdollahi, Dragan Damjanovic, and Gustau Catalan. Flexoelectricity in bones. *Advanced Materials*, 30(9):1705316, 2018.

[26] Mané Harutyunyan. *Mathematical Modeling and Numerical Simulation of Magnetoelastic Coupling.* doctoralthesis, Technische Universität Kaiserslautern, 2019.

[27] Jagdish Rathod and Bhumi Bhatt. A comparative study of electronic article surveillance (eas) system. *Proceedings of Second International Conference on Signals, Systems & Automation (ICSSA-11)*, 01 2011.

[28] Ee Lim Tan, Brandon D. Pereles, Ranyuan Shao, Justin Ong, and Keat Ghee Ong. A wireless, passive strain sensor based on the harmonic response of magnetically soft materials. *Smart Material Structures*, 17(2):025015, April 2008.

[29] Yisong Tan, Jiale Hu, Limin Ren, Jianhua Zhu, Jiaqi Yang, and Di Liu. A passive and wireless sensor for bone plate strain monitoring. *Sensors*, 17(11), 2017.

[30] Limin Ren, Kun Yu, and Yisong Tan. Applications and advances of magnetoelastic sensors in biomedical engineering: A review. *Materials*, 12(7):1135, 2019.

[31] Limin Ren, Kun Yu, and Yisong Tan. Wireless and passive magnetoelastic-based sensor for force monitoring of artificial bone. *IEEE Sensors Journal*, 19:2096–2104, 2019.

[32] Robert Y. Ting. Evaluation of new piezoelectric composite materials for hydrophone applications. *Ferroelectrics*, 67(1):143–157, 1986.

[33] Gururaja T.R., Walter A. Schulze, Leslie E. Cross, Robert E. Newnham, Bertram A. Auld, and Yuzhong J. Wang. Piezoelectric composite materials for ultrasonic transducer applications. part i: Resonant modes of vibration of pzt rod-polymer composites. *IEEE Transactions on Sonics and Ultrasonics*, 32(4):481–498, 1985.

[34] E Koray Akdogan, Mehdi Allahverdi, and Ahmad Safari. Piezoelectric composites for sensor and actuator applications. *IEEE transactions on ultrasonics, ferroelectrics, and frequency control*, 52(5):746–775, 2005.

[35] Xiu juan LIN, Ke chao ZHOU, Xiao yong ZHANG, and Dou ZHANG. Development, modeling and application of piezoelectric fiber composites. *Transactions of Nonferrous Metals Society of China*, 23(1):98–107, 2013.

[36] Jun Zhu, Zhi Wang, Xingyi Zhu, Bo Yang, and Chuanqing Fu. Theoretical and experimental study on the effective piezoelectric properties of 1-3 type cement-based piezoelectric composites. *Materials*, 11(9), 2018.

[37] Xue-Qian Fang, Ming-Juan Huang, Jin-Xi Liu, and Wen-Jie Feng. Dynamic effective property of piezoelectric composites with coated piezoelectric nano-fibers. *Composites Science and Technology*, 98:79–85, 2014.

[38] Mike F Ashby and Yves JM Bréchet. Designing hybrid materials. *Acta materialia*, 51(19):5801–5821, 2003.

[39] Benoit B Mandelbrot. The fractal geometry of nature. *New York*, page 468, 1983.

[40] Tobias Fey, Franziska Eichhorn, Guifang Han, Kathrin Ebert, Moritz Wegener, Andreas Roosen, Ken-ichi Kakimoto, and Peter Greil. Mechanical and electrical strain response of a piezoelectric auxetic pzt lattice structure. *Smart Materials and Structures*, 25(1):015017, 2015.

[41] Kamran A Khan and Muhammad Ali Khan. 3-3 piezoelectric metamaterial with negative and zero poisson's ratio for hydrophones applications. *Materials Research Bulletin*, 112:194–204, 2019.

[42] Alice Mocci, Jordi Barceló-Mercader, David Codony, and Irene Arias. Geometrically polarized architected dielectrics with apparent piezoelectricity. *Journal of the Mechanics and Physics of*

Solids, 157:104643, 2021.

[43] Nikolaos Karathanasopoulos, Francisco Dos Reis, Hilal Reda, and J-F Ganghoffer. Computing the effective bulk and normal to shear properties of common two-dimensional architectured materials. *Computational Materials Science*, 154:284–294, 2018.

[44] Clifford Truesdell and Richard Toupin. The classical field theories. In *Principles of classical mechanics and field theory/Prinzipien der Klassischen Mechanik und Feldtheorie*. Springer, 1960.

[45] Walter Noll and Clifford Ambrose Truesdell. *The non-linear field theories of mechanics*. Springer-Verlag Berlin, 1992.

[46] Holm Altenbach and Victor A Eremeyev. *Generalized continua-from the theory to engineering applications*, volume 541. Springer, 2012.

[47] Roman Poya, Antonio J. Gil, Rogelio Ortigosa, and Roberto Palma. On a family of numerical models for couple stress based flexoelectricity for continua and beams. *Journal of the Mechanics and Physics of Solids*, 125:613–652, 2019.

[48] Ali R. Hadjesfandiari. Size-dependent piezoelectricity. *International Journal of Solids and Structures*, 50(18):2781–2791, 2013.

[49] Li Anqing, Zhou Shenjie, Qi Lu, and Chen Xi. A flexoelectric theory with rotation gradient effects for elastic dielectrics. *Modelling and Simulation in Materials Science and Engineering*, 24(1):015009, dec 2015.

[50] Anqing Li, Shenjie Zhou, Lu Qi, and Xi Chen. A reformulated flexoelectric theory for isotropic dielectrics. *Journal of Physics D: Applied Physics*, 48(46):465502, oct 2015.

[51] Ekram Sahin and S. Dost. A strain-gradients theory of elastic dielectrics with spatial dispersion. *International journal of engineering science*, 26(12):1231–1245, 1988.

[52] McBride A.T., Denis Davydov, and Paul Steinmann. Modelling the flexoelectric effect in solids: A micromorphic approach. *Computer Methods in Applied Mechanics and Engineering*, 371:113320, 2020.

[53] Raymond David Mindlin. Microstructure in linear elasticity. Technical report, Columbia Univ New York Dept of Civil Engineering and Engineering Mechanics, 1963.

[54] A. Cemal Eringen and E.S. Suhubi. Nonlinear theory of simple micro-elastic solids—i. *International Journal of Engineering Science*, 2(2):189–203, 1964. Publisher: Elsevier.

[55] Samuel Forest. Mechanics of generalized continua: construction by homogenizaton. *Le Journal de Physique IV*, 8:Pr4–39, 1998.

[56] Eugene Cosserat and François Cosserat. *Theorie des corps dédormables*. A. Hermann et fils, 1909.

[57] Paul Germain. La méthode des puissances virtuelles en mécanique des milieux continus, premiere partie: théorie du second gradient. *J. Mécanique*, 12(2):235–274, 1973.

[58] A. Cemal Eringen. Theory of micropolar fluids. *Journal of Mathematics and Mechanics*, pages 1–18, 1966.

[59] Chas.B. Kafadar and A.Cemal Eringen. Micropolar media—i the classical theory. *International*

Journal of Engineering Science, 9(3):271–305, 1971.

[60] Samuel Forest and Duy Khanh Trinh. Generalized continua and non-homogeneous boundary conditions in homogenisation methods. *ZAMM-Journal of Applied Mathematics and Mechanics/Zeitschrift für Angewandte Mathematik und Mechanik*, 91(2):90–109, 2011. Publisher: Wiley Online Library.

[61] Barbara Gambin and E Kröner. Higher-order terms in the homogenized stress-strain relation of periodic elastic media. *physica status solidi (b)*, 151(2):513–519, 1989.

[62] Claude Boutin. Microstructural effects in elastic composites. *International Journal of Solids and Structures*, 33(7):1023–1051, 1996.

[63] Valery P. Smyshlyaev and Kirill D. Cherednichenko. On rigorous derivation of strain gradient effects in the overall behaviour of periodic heterogeneous media. *Journal of the Mechanics and Physics of Solids*, 48(6-7):1325–1357, 2000.

[64] Salma Barboura and Jia Li. Establishment of strain gradient constitutive relations by using asymptotic analysis and the finite element method for complex periodic microstructures. *International Journal of Solids and Structures*, 136:60–76, 2018.

[65] Vincent Monchiet, Nicolas Auffray, and Julien Yvonnet. Strain-gradient homogenization: A bridge between the asymptotic expansion and quadratic boundary condition methods. *Mechanics of Materials*, 143, 2020.

[66] Duy Khanh Trinh, Ralf Janicke, Nicolas Auffray, Stefan Diebels, and Samuel Forest. Evaluation of generalized continuum substitution models for heterogeneous materials. *International Journal for Multiscale Computational Engineering*, 10(6), 2012.

[67] Raymond David Mindlin and N. N. Eshel. On first strain-gradient theories in linear elasticity. *International Journal of Solids and Structures*, 4(1):109–124, 1968.

[68] Julien Yvonnet, Nicolas Auffray, and Vincent Monchiet. Computational second-order homogenization of materials with effective anisotropic strain-gradient behavior. *International Journal of Solids and Structures*, 191:434–448, 2020.

[69] Nicolas Auffray, Francesco dell'Isola, Victor A. Eremeyev, Angela Madeo, and Giuseppe Rosi. Analytical continuum mechanics a la hamilton-piola least action principle for second gradient continua and capillary fluids. *Mathematics and Mechancs of Solids*, 20(4):375–417, 2015.

[70] Andrea Bacigalupo. Second-order homogenization of periodic materials based on asymptotic approximation of the strain energy: formulation and validity limits. *Meccanica*, 49(6):1407–1425, 2014.

[71] Thu-Huong Tran, Vincent Monchiet, and Guy Bonnet. A micromechanics-based approach for the derivation of constitutive elastic coefficients of strain-gradient media. *International Journal of Solids and Structures*, 49(5):783–792, 2012.

[72] Andrea Bacigalupo and Luigi Gambarotta. Second-order computational homogenization of heterogeneous materials with periodic microstructure. *ZAMM - Journal of Applied Mathematics*

and Mechanics / Zeitschrift für Angewandte Mathematik und Mechanik, 90(10):796–811, 2010.

[73] Mohammad Ayad, Nikolaos Karathanasopoulos, Hilal Reda, Jean-François Ganghoffer, and Hassan Lakiss. On the role of second gradient constitutive parameters in the static and dynamic analysis of heterogeneous media with micro-inertia effects. *International Journal of Solids and Structures*, 190:58–75, 2020.

[74] Andrea Bacigalupo and Luigi Gambarotta. Homogenization of periodic hexa- and tetrachiral cellular solids. *Composite Structures*, 116:461–476, 2014.

[75] Ibrahim Goda and Jean-François Ganghoffer. Construction of first and second order grade anisotropic continuum media for 3d porous and textile composite structures. *Composite Structures*, 141:292–327, 2016. Publisher: Elsevier.

[76] Kamel Berkache, S Deogekar, Ibrahim Goda, Catalin Picu, and Jean-François Ganghoffer. Construction of second gradient continuum models for random fibrous networks and analysis of size effects. *Composite Structures*, 181:347–357, 2017.

[77] Gérard A. Maugin and Andrei V. Metrikine. *Mechanics of generalized continua*. Springer, 2010.

[78] Holm Altenbach, Gérard A. Maugin, and Vladimir Erofeev. *Mechanics of generalized continua*, volume 7. Springer, 2011.

[79] Gérard A. Maugin. *Continuum mechanics of electromagnetic solids*. Elsevier, 1988.

[80] Gérard A. Maugin. *Micromagnetism and polar media*. Princeton University, 1971.

[81] Matthew Mosby and Karel Matouš. Computational homogenization at extreme scales. *Extreme Mechanics Letters*, 6:68–74, 2016.

[82] Scott J Hollister and Noboru Kikuchi. A comparison of homogenization and standard mechanics analyses for periodic porous composites. *Computational mechanics*, 10(2):73–95, 1992.

[83] Enrique Sánchez-Palencia. Non-homogeneous media and vibration theory. *Lecture notes in physics*, 127, 1980. Publisher: Springer-Verlag.

[84] A Bensoussan, J Lions, and G Papanicolau. *Homogenization: Averaging Processes in Periodic Media*. Amsterdam: North Holland, 1978.

[85] Luc Tartar. Cours peccot, collège de france,(1977), partially written in: F. *Murat, H-Convergence, Séminaire d'analyse fonctionnelle et numérique de l'Université d'Alger*, 1978.

[86] Rodney Hill. Generalized constitutive relations for incremental deformation of metal crystals by multislip. *Journal of the Mechanics and Physics of Solids*, 14(2):95–102, 1966.

[87] Rodney Hill. The essential structure of constitutive laws for metal composites and polycrystals. *Journal of the Mechanics and Physics of Solids*, 15(2):79–95, 1967.

[88] Jean Mandel. Contribution théorique à l'étude de l'écrouissage et des lois de l'écoulement plastique. In *Applied Mechanics*, pages 502–509. Springer, 1966.

[89] Grigorii Petrovich Panasenko. *Multi-scale modelling for structures and composites*, volume 615. Springer, 2005.

[90] Sergei M. Kozlov. Averaging differential operators with almost periodic, rapidly oscillating

coefficients. *Mathematics of the USSR-Sbornik*, 35(4):481, 1979. Publisher: IOP Publishing.

[91] Vasilii Vasil'evich Zhikov, Sergei M Kozlov, Olga Arsen'evna Oleinik, and Kha T'en Ngoan. Averaging and g-convergence of differential operators. *Russian Mathematical Surveys*, 34(5):69, 1979.

[92] Edward W Larsen and Joseph B Keller. Asymptotic solution of neutron transport problems for small mean free paths. *Journal of Mathematical Physics*, 15(1):75–81, 1974.

[93] Edward W Larsen. Neutron transport and diffusion in inhomogeneous media. i. *Journal of Mathematical Physics*, 16(7):1421–1427, 1975.

[94] Edward W Larsen. Neutron transport and diffusion in inhomogeneous media. ii. *Nuclear science and engineering*, 60(4):357–368, 1976.

[95] Sergio Spagnolo. Sul limite delle soluzioni di problemi di cauchy relativi all'equazione del calore. *Annali della Scuola Normale Superiore di Pisa-Classe di Scienze*, 21(4):657–699, 1967.

[96] Luc Tartar. Cours peccot au collège de france. *Manuscript,(unpublished)*, 1977.

[97] François Murat and Luc Tartar. H-convergence. In Andrej V. Cherkaev and Robert Kohn, editors, *Topics in the Mathematical Modelling of Composite Materials*, Modern Birkhäuser Classics, pages 21–43. Springer International Publishing, 2018.

[98] Ennio De Giorgi. G-operators and γ-convergence. In *Proceedings of the International Congress of Mathematicians*, volume 1, pages 1175–1191, 1984. Issue: 2.

[99] Gabriel Nguetseng. A general convergence result for a functional related to the theory of homogenization. *SIAM Journal on Mathematical Analysis*, 20(3):608–623, 1989. Publisher: SIAM.

[100] BE Pobedrya. Principles of computational mechanics of composites. *Mechanics of composite materials*, 32(6):504–515, 1996.

[101] Graeme W. Milton. The theory of composites (cambridge monographs on applied and computational mathematics) cambridge university press. *Cambridge, UK*, 2002.

[102] A. A. Grekov, S. O. Kramarov, and A. A. Kuprienko. Anomalous behavior of the two-phase lamellar piezoelectric texture. *Ferroelectrics*, 76(1):43–48, 1987.

[103] Y Benveniste and GJ Dvorak. Uniform fields and universal relations in piezoelectric composites. *Journal of the Mechanics and Physics of Solids*, 40(6):1295–1312, 1992.

[104] Julián Bravo Castillero, Josè A. Otero, Reinaldo Rodríguez Ramos, and Alain Bourgeat. Asymptotic homogenization of laminated piezocomposite materials. *International Journal of Solids and Structures*, 35(5-6):527–541, 1998.

[105] A. Galka, Józef Joachim Telega, and Ryszard Wojnar. Some computational aspects of homogenization of thermopiezoelectric composites. *Computer Assisted Mechanics and Engineering Sciences*, 3:133–154, 01 1996.

[106] Hilal Reda, Nikos Karathanasopoulos, Gérard Maurice, Jean François Ganghoffer, and Hassan Lakiss. Computation of effective piezoelectric properties of stratified composites and application to wave propagation analysis. *ZAMM Zeitschrift fur Angewandte Mathematik und Mechanik*, 100(2),

February 2020.

[107] Francisco Dos Reis and Jean-François Ganghoffer. Equivalent mechanical properties of auxetic lattices from discrete homogenization. *Computational Materials Science*, 51:314–321, 2012.

[108] Nikolaos Karathanasopoulos, Francisco Dos Reis, Hilal Reda, and Jean-François Ganghoffer. Computing the effective bulk and normal to shear properties of common two-dimensional architectured materials. *Computational Materials Science*, 154:284–294, 2018.

[109] Z. P Baant and M. Christensen. Analogy between micropolar continuum and grid frames under initial stress. *International Journal of Solids and Structures*, 8:327–346, 1972.

[110] Andrea Bacigalupo and Luigi Gambarotta. Identification of non-local continua for lattice-like materials. *International Journal of Engineering Science*, 159:103430, 2021.

[111] Harm Askes and Andrei V. Metrikine. Higher-order continua derived from discrete media: continualisation aspects and boundary conditions. *International Journal of Solids and Structures*, 42(1):187–202, 2005.

[112] Rajesh S. Kumar and David L. McDowell. Generalized continuum modeling of 2-d periodic cellular solids. *International Journal of Solids and Structures*, 41(26):7399–7422, 2004.

[113] Andrei V. Metrikine and Harm Askes. One-dimensional dynamically consistent gradient elasticity models derived from a discrete microstructure: Part 1: Generic formulation. *European Journal of Mechanics - A/Solids*, 21(4):555–572, 2002.

[114] P. R. Onck, E. W. Andrews, and L. J. Gibson. Size effects in ductile cellular solids. part i: modeling. *International Journal of Mechanical Sciences*, 43(3):681–699, 2001.

[115] David CC Lam, Fan Yang, ACM Chong, Jianxun Wang, and Pin Tong. Experiments and theory in strain gradient elasticity. *Journal of the Mechanics and Physics of Solids*, 51(8):1477–1508, 2003.

[116] C. Tekoglu, Lorna J. Gibson, and Patrick Onck. Size-effects of metal foams. *Tessellations in the Sciences: Virtues, Techniques and Applications of Geometric Tilings*, 2011.

[117] Harm Askes and Elias C. Aifantis. Gradient elasticity in statics and dynamics: An overview of formulations, length scale identification procedures, finite element implementations and new results. *International Journal of Solids and Structures*, 48(13):1962–1990, 2011.

[118] Jia Li and Xiao-Bing Zhang. A numerical approach for the establishment of strain gradient constitutive relations in periodic heterogeneous materials. *European Journal of Mechanics - A/Solids*, 41:70–85, 2013.

[119] Hua Yang and Wolfgang H. Müller. Size effects of mechanical metamaterials: a computational study based on a second-order asymptotic homogenization method. *Arch Appl Mech*, 91(3):1037–1053, 2021.

[120] Shutian Liu and Wenzheng Su. Effective couple-stress continuum model of cellular solids and size effects analysis. *International Journal of Solids and Structures*, 46(14):2787–2799, 2009.

[121] Armelle Anthoine. Second-order homogenisation of functionally graded materials. *International Journal of Solids and Structures*, 47(11):1477–1489, 2010.

[122] Sreena Suresh. Graded materials for resistance to contact deformation and damage. *Science*, 292(5526):2447–2451, 2001.

[123] Thomas Reiter, George J Dvorak, and Viggo Tvergaard. Micromechanical models for graded composite materials. *Journal of the Mechanics and Physics of Solids*, 45(8):1281–1302, 1997. Publisher: Elsevier.

[124] Kumar Vemaganti and Pushkaraj Deshmukh. An adaptive global–local approach to modeling functionally graded materials. *Computer methods in applied mechanics and engineering*, 195(33-36):4230–4243, 2006.

[125] Sh M Kogan. Piezoelectric effect during inhomogeneous deformation and acoustic scattering of carriers in crystals. *Soviet Physics-Solid State*, 5(10):2069–2070, 1964.

[126] Ravi Maranganti, Nikhil D. Sharma, and Pradeep Sharma. Electromechanical coupling in nonpiezoelectric materials due to nanoscale nonlocal size effects: Green's function solutions and embedded inclusions. *Phys. Rev. B*, 74:014110, Jul 2006.

[127] David Guinovart-Sanjuán, Jose Merodio, Juan Carlos López-Realpozo, Kuppalapalle Vajravelu, Reinaldo Rodríguez-Ramos, Raúl Guinovart-Díaz, Julián Bravo-Castillero, and Federico J. Sabina. Asymptotic homogenization applied to flexoelectric rods. *Materials*, 12(2), 2019.

[128] Maryam Nasimsobhan, Jean-François Ganghoffer, and Mahnaz Shamshirsaz. Construction of piezoelectric and flexoelectric models of composites by asymptotic homogenization and application to laminates. *Mathematics and Mechanics of Solids*, 27(4):602–637, 2022.

[129] Raymond David Mindlin. Second gradient of strain and surface-tension in linear elasticity. *International Journal of Solids and Structures*, 1:417–438, 1965.

[130] Harm Askes and Elias C. Aifantis. Gradient elasticity in statics and dynamics: An overview of formulations, length scale identification procedures, finite element implementations and new results. *International Journal of Solids and Structures*, 48:1962–1990, 2011.

[131] Duy Khanh Trinh, Ralf Janicke, Nicolas Auffray, Stefan Diebels, and Samuel Forest. Evaluation of generalized continuum substitution models for heterogeneous materials. *International Journal for Multiscale Computational Engineering*, 10:527–549, 2012.

[132] Eugène Cosserat and François Cosserat. Sur la théorie de l'élasticité. premier mémoire. *Annales de la faculté des sciences de Toulouse Mathématiques*, 10:1–116, 1896.

[133] A. Cemal Eringen and E.S. Suhubi. Nonlinear theory of simple micro-elastic solids—i. *International Journal of Engineering Science*, 2(2):189–203, 1964.

[134] R. A. Toupin. Elastic materials with couple-stresses. *Archive for Rational Mechanics and Analysis*, 11:385–414, 1962.

[135] Raymond David Mindlin and N.N. Eshel. On first strain-gradient theories in linear elasticity. *International Journal of Solids and Structures*, 4:109–124, 1968.

[136] Youping Chen, James D. Lee, and Azim Eskandarian. Atomistic viewpoint of the applicability of microcontinuum theories. *International Journal of Solids and Structures*, 41:2085–2097, 2004.

[137] Dominic G. B. Edelen. Protoelastic bodies with large deformation. *Archive for Rational Mechanics and Analysis*, 34:283–300, 1969.

[138] A. Cemal Eringen. *Microcontinuum Field Theories*. Springer New York, 1999.

[139] A.Cemal Eringen. A unified theory of thermomechanical materials. *International Journal of Engineering Science*, 4:179–202, 1966.

[140] Ali R. Hadjesfandiari and Gary F. Dargush. Couple stress theory for solids. *International Journal of Solids and Structures*, 48:2496–2510, 2011.

[141] David CC Lam, Fan Yang, ACM Chong, Jianxun Wang, and Pin Tong. Experiments and theory in strain gradient elasticity. *Journal of the Mechanics and Physics of Solids*, 51(8):1477–1508, 2003.

[142] Raymond David Mindlin and Harry F. Tiersten. Effects of couple-stresses in linear elasticity. *Archive for Rational Mechanics and Analysis*, 11:415–448, 1962.

[143] Demosthenes Polyzos and Dimitrios I.Fotiadis. Derivation of mindlin's first and second strain gradient elastic theory via simple lattice and continuum models. *International Journal of Solids and Structures*, 49:470–480, 2012.

[144] FACM Yang, ACM Chong, David Chuen Chun Lam, and Pin Tong. Couple stress based strain gradient theory for elasticity. *International journal of solids and structures*, 39(10):2731–2743, 2002.

[145] Samuel Forest. Mechanics of generalized continua: construction by homogenizaton. *Le Journal de Physique IV*, 08:Pr4–39–Pr4–48, 1998.

[146] Samuel Forest. Homogenization methods and mechanics of generalized continua - part 2. *Theoretical and Applied Mechanics*, pages 113–144, 2002.

[147] Varvara Kouznetsova, Marc GD Geers, and WA Marcel Brekelmans. Multi-scale constitutive modelling of heterogeneous materials with a gradient-enhanced computational homogenization scheme. *International Journal for Numerical Methods in Engineering*, 54:1235–1260, 2002.

[148] Raymond David Mindlin. Micro-structure in linear elasticity. *Archive for Rational Mechanics and Analysis*, 16:51–78, 1964.

[149] Nicolas Auffray, Francesco dell'Isola, Victor A Eremeyev, Angela Madeo, and Giuseppe Rosi. Analytical continuum mechanics à la hamilton–piola least action principle for second gradient continua and capillary fluids. *Mathematics and Mechanics of Solids*, 20(4):375–417, 2015.

[150] Francesco Dell'Isola, Ivan Giorgio, and Ugo Andreaus. Elastic pantographic 2d lattices: a numerical analysis on the static response and wave propagation. *Proceedings of the Estonian Academy of Sciences*, 64(3):219, 2015.

[151] Cosserat Eugène and Cosserat François. Théorie des corps déformables. *Herman et Fils, Paris*, 1909.

[152] Paul Germain. The method of virtual power in continuum mechanics. part 2: Microstructure. *SIAM Journal on Applied Mathematics*, 25:556–575, 1973.

[153] Leonid Ivanovich Sedov. Mathematical methods for constructing new models of continuous media. *Russian Mathematical Surveys*, 20(5):123, 1965.

[154] Hilal Reda, Yosra Rahali, Jean-François Ganghoffer, and Hassan Lakiss. Analysis of dispersive waves in repetitive lattices based on homogenized second-gradient continuum models. *Composite Structures*, 152:712–728, 2016.

[155] Hilal Reda, Ibrahim Goda, Jean-François Ganghoffer, Gildas L'Hostis, and Hassan Lakiss. Dynamical analysis of homogenized second gradient anisotropic media for textile composite structures and analysis of size effects. *Composite Structures*, 161:540–551, 2017.

[156] Julien Yvonnet, Nicolas Auffray, and Vincent Monchiet. Computational second-order homogenization of materials with effective anisotropic strain-gradient behavior. *International Journal of Solids and Structures*, 191-192:434–448, 2020.

[157] Raja Biswas, Leong Hien Poh, and Amit Subhash Shedbale. A micromorphic computational homogenization framework for auxetic tetra-chiral structures. *Journal of the Mechanics and Physics of Solids*, 135:103801, 2020.

[158] Hilal Reda, Seyed Ehsan Alavi, Maryam Nasimsobhan, and Jean-François Ganghoffer. Homogenization towards chiral cosserat continua and applications to enhanced timoshenko beam theories. *Mechanics of Materials*, 155:103728, 2021.

[159] Seyed Ehsan Alavi, Jean-François Ganghoffer, Hilal Reda, and Mojtaba Sadighi. Construction of micromorphic continua by homogenization based on variational principles. *Journal of the Mechanics and Physics of Solids*, 153:104278, 2021.

[160] Stéphane Cuenot, Christian Frétigny, Sophie Demoustier-Champagne, and Bernard Nysten. Surface tension effect on the mechanical properties of nanomaterials measured by atomic force microscopy. *Physical Review B*, 69:165410, 2004.

[161] G. Y. Jing, H. L. Duan, X. M. Sun, Z. S. Zhang, J. Xu, Y. D. Li, J. X. Wang, and D. P. Yu. Surface effects on elastic properties of silver nanowires: Contact atomic-force microscopy. *Physical Review B*, 73:235409, 2006.

[162] C. Q. Chen, Y. Shi, Y. S. Zhang, J. Zhu, and Y. J. Yan. Size dependence of young's modulus in zno nanowires. *Physical Review Letters*, 96:075505, 2006.

[163] Jin He and Carmen M. Lilley. Surface effect on the elastic behavior of static bending nanowires. *Nano Letters*, 8:1798–1802, 2008.

[164] Xiaohua Liu, Jun Luo, and Jing Zhu. Size effect on the crystal structure of silver nanowires. *Nano Letters*, 6:408–412, 2006.

[165] Pierre Simon Laplace. *Sur l'action capillaire. supplément à la théorie de l'action capillaire, In: Traité de mécanique céleste*, volume 4. 1805.

[166] Pierre Simon Laplace. *À la théorie de l'action capillaire. supplément à la théorie de l'action capillaire, In: Traité de mécanique céleste*, volume 4. 1806.

[167] Thomas Young. III. an essay on the cohesion of fluids. *Philosophical Transactions of the Royal Society of London*, 95:65–87, 1805.

[168] S.D Poisson. *Nouvelle théorie de l'action capillaire*. 1831.

[169] Josiah Willard Gibbs. *The collected works of J. Willard Gibbs*. PhD thesis, 1928.

[170] Pierre-Gilles de Gennes, Françoise Brochard-Wyart, and David Quéré. *Capillarity and Wetting Phenomena*. Springer New York, 2004.

[171] John Shipley Rowlinson and Benjamin Widom. *Molecular theory of capillarity*. Courier Corporation, 2013.

[172] Morton E. Gurtin and A. Ian Murdoch. A continuum theory of elastic material surfaces. *Archive for Rational Mechanics and Analysis*, 57:291–323, 1975.

[173] Morton E. Gurtin and A. Ian Murdoch. Addenda to our paper a continuum theory of elastic material surfaces. *Archive for Rational Mechanics and Analysis*, 59:389–390, 1975.

[174] J Wang, H.L. Duan, Z.P Huang, and Bhushan Lal Karihaloo. A scaling law for properties of nano-structured materials. *Proceedings of the Royal Society A: Mathematical, Physical and Engineering Sciences*, 462:1355–1363, 2006.

[175] David J. Steigmann and R. W. Ogden. Plane deformations of elastic solids with intrinsic boundary elasticity. *Proceedings of the Royal Society of London. Series A: Mathematical, Physical and Engineering Sciences*, 453:853–877, 1997.

[176] David J. Steigmann and R. W. Ogden. Elastic surface—substrate interactions. *Proceedings of the Royal Society of London. Series A: Mathematical, Physical and Engineering Sciences*, 455:437–474, 1999.

[177] Ali Javili, Andrew McBride, and Paul Steinmann. Thermomechanics of solids with lower-dimensional energetics: On the importance of surface, interface, and curve structures at the nanoscale. a unifying review. *Applied Mechanics Reviews*, 65, 2013.

[178] Ali Javili, Francesco dell'Isola, and Paul Steinmann. Geometrically nonlinear higher-gradient elasticity with energetic boundaries. *Journal of the Mechanics and Physics of Solids*, 61:2381–2401, 2013.

[179] Paolo Podio-Guidugli and Giorgio Vergara Caffarelli. *Surface Interaction Potentials in Elasticity*. Springer Berlin Heidelberg, 1991.

[180] Yuriy Povstenko. Mathematical modeling of phenomena caused by surface stresses in solids. *Surface Effects in Solid Mechanics: Models, Simulations and Applications*, pages 135–153, 2013.

[181] Miroslav Šilhavý. A direct approach to nonlinear shells with application to surface-substrate interactions. *Mathematics and Mechanics of Complex Systems*, 1:211–232, 2013.

[182] Sergey Lurie and Petr Belov. Gradient effects in fracture mechanics for nano-structured materials. *Engineering Fracture Mechanics*, 130:3–11, 2014.

[183] Sergey Lurie, D. Volkov-Bogorodsky, Vladimir Zubov, and Natalia Tuchkova. Advanced theoretical and numerical multiscale modeling of cohesion/adhesion interactions in continuum mechanics and its applications for filled nanocomposites. *Computational Materials Science*, 45:709–714, 2009.

[184] Sergey Lurie and Petr Belov. Cohesion field: Barenblatt's hypothesis as formal corollary of theory of continuous media with conserved dislocations. *International Journal of Fracture*, 150:181–194,

2008.

[185] Sergey A. Lurie and Alexander L. Kalamkarov. General theory of continuous media with conserved dislocations. *International Journal of Solids and Structures*, 44:7468–7485, 2007.

[186] M.B. Rubin and Y. Benveniste. A cosserat shell model for interphases in elastic media. *Journal of the Mechanics and Physics of Solids*, 52:1023–1052, 2004.

[187] H.L. Duan and Bhushan Lal Karihaloo. Thermo-elastic properties of heterogeneous materials with imperfect interfaces: Generalized levin's formula and hill's connections. *Journal of the Mechanics and Physics of Solids*, 55:1036–1052, 2007.

[188] H.L. Duan, J. Wang, Bhushan Lal Karihaloo, and Z.P. Huang. Nanoporous materials can be made stiffer than non-porous counterparts by surface modification. *Acta Materialia*, 54:2983–2990, 2006.

[189] H.L. Duan, J. Wang, Z.P. Huang, and Bhushan Lal Karihaloo. Size-dependent effective elastic constants of solids containing nano-inhomogeneities with interface stress. *Journal of the Mechanics and Physics of Solids*, 53:1574–1596, 2005.

[190] H.L. Duan, Jianxiang Wang, and Bhushan Lal Karihaloo. Theory of elasticity at the nanoscale. *Advances in applied mechanics*, 42:1–68, 2009.

[191] V.I. Kushch, Volodymyr Chernobai, and Gennady Mishuris. Longitudinal shear of a composite with elliptic nanofibers: Local stresses and effective stiffness. *International Journal of Engineering Science*, 84:79–94, 2014.

[192] V.I. Kushch, Igor Sevostianov, and Volodymyr Chernobai. Effective conductivity of composite with imperfect contact between elliptic fibers and matrix: Maxwell's homogenization scheme. *International Journal of Engineering Science*, 83:146–161, 2014.

[193] Jianxiang Wang, Zhuping Huang, Huiling Duan, Shouwen Yu, Xiqiao Feng, Gangfeng Wang, Weixu Zhang, and Tiejun Wang. Surface stress effect in mechanics of nanostructured materials. *Acta Mechanica Solida Sinica*, 24:52–82, 2011.

[194] Nikolaos Karathanasopoulos, Francisco Dos Reis, M. Diamantopoulou, and Jean-François Ganghoffer. Mechanics of beams made from chiral metamaterials: Tuning deflections through normal-shear strain couplings. *Materials & Design*, 189:108520, 2020.

[195] Matthew Mosby and Karel Matouš. Computational homogenization at extreme scales. *Extreme Mechanics Letters*, 6:68–74, 2016.

[196] Łukasz Kaczmarczyk, Chris J. Pearce, and Nenad Bićanić. Studies of microstructural size effect and higher-order deformation in second-order computational homogenization. *Computers & Structures*, 88:1383–1390, 2010.

[197] Mostafa El Sayed. *Multiscale mechanics and structural design of periodic cellular materials*. PhD thesis, 2011.

[198] Jean-François Ganghoffer and Hilal Reda. A variational approach of homogenization of heterogeneous materials towards second gradient continua. *Mechanics of Materials*, 158:103743, 2021.

[199] Stefano Gonella and Massimo Ruzzene. Multicell homogenization of one-dimensional periodic structures. *Journal of Vibration and Acoustics*, 132, 2010.

[200] Stefano Gonella and Massimo Ruzzene. Homogenization and equivalent in-plane properties of two-dimensional periodic lattices. *International Journal of Solids and Structures*, 45:2897–2915, 2008.

[201] Mariateresa Lombardo and Harm Askes. Higher-order gradient continuum modelling of periodic lattice materials. *Computational Materials Science*, 52:204–208, 2012.

[202] Yosra Rahali, Francisco Dos Reis, and Jean-François Ganghoffer. Multiscale homogenization schemes for the construction of second-order grade anisotropic continuum media of architectured materials. *International Journal for Multiscale Computational Engineering*, 15:35–78, 2017.

[203] Antonio André Novotny, Raul Antonino Feijóo, Edgardo O. Taroco, and Claudio Padra. Topological sensitivity analysis for three-dimensional linear elasticity problem. *Computer Methods in Applied Mechanics and Engineering*, 196:4354–4364, 2007.

[204] Antonio André Novotny and Jan Sokołowski. *Topological Derivatives in Shape Optimization*. Springer Berlin Heidelberg, 2013.

[205] Yosra Rahali, Ivan Giorgio, Jean-François Ganghoffer, and Francesco dell'Isola. Homogenization à la piola produces second gradient continuum models for linear pantographic lattices. *International Journal of Engineering Science*, 97:148–172, 2015.

[206] Cristian Barbarosie and Anca-Maria Toader. Shape and topology optimization for periodic problems. *Structural and Multidisciplinary Optimization*, 40:381–391, 2010.

[207] Igor V Andrianov, Jan Awrejcewicz, and Alexander A Diskovsky. Homogenization of quasi-periodic structures. *Journal of Vibration and Acoustics*, 128(4):532, 2006. Publisher: American Society of Mechanical Engineers.

[208] SU F., XU Z., CUI J. Z., and DONG Q. L. Multi-scale method for the quasi-periodic structures of composite materials. *Applied mathematics and computation*, 2011.

[209] Laurent Guillot, Yann Capdeville, and Jean-Jacques Marigo. 2-D non-periodic homogenization of the elastic wave equation: SH case. *Geophysical Journal International*, 182(3):1438–1454, 2010. Publisher: Blackwell Publishing Ltd Oxford, UK.

[210] Yann Capdeville, Laurent Guillot, and Jean-Jacques Marigo. 2-D non-periodic homogenization to upscale elastic media for p–sv waves. *Geophysical Journal International*, 182(2):903–922, 2010.

[211] Duc Trung Le and Jean-Jacques Marigo. Second order homogenization of quasi-periodic structures. *Vietnam Journal of Mechanics*, 40(4):325–348, 2018.

[212] Seyed Ehsan Alavi. *Homogenization of periodic and quasi-periodic architectural media towards generalized continua*. PhD thesis, Université de Lorraine, 12 2021.

[213] Denis Caillerie. Homogénéisation des matériaux à structure périodique. 2012.

[214] David Lovelock and Hanno Rund. *Tensors, differential forms, and variational principles*. Courier Corporation, 1989.

[215] Nagham Mawassy, Jean-Francois Ganghoffer, Hilal Reda, Seyed Ehsan Alavi, and Hassan Lakiss.

Analysis of surface effects based on first and second strain gradient mechanics. *Mechanics of Materials*, 175:104462, 2022.

[216] Thanh D. Nguyen, Sheng Mao, Yao-Wen Yeh, Prashant K. Purohit, and Michael C. McAlpine. Nanoscale flexoelectricity. *Advanced Materials*, 25(7):946–974, 2013.

[217] Bo Wang, Yijia Gu, Shujun Zhang, and Long-Qing Chen. Flexoelectricity in solids: Progress, challenges, and perspectives. *Progress in Materials Science*, 106:100570, 2019.

[218] Gérard A. Maugin. *Continuum mechanics of electromagnetic solids*. Elsevier,Oxford, 1988.

[219] A. Cemal Eringen and Gérard A. Maugin. *Electrodynamics of Continua*. Springer,New York, 1990.

[220] Jiashi Yang. *Analysis of piezoelectric devices*. World Scientific, 2006.

[221] Hilal Reda, Nikos Karathanasopoulos, Gérard Maurice, Jean François Ganghoffer, and Hassan Lakiss. Computation of effective piezoelectric properties of stratified composites and application to wave propagation analysis. *ZAMM - Journal of Applied Mathematics and Mechanics / Zeitschrift für Angewandte Mathematik und Mechanik*, 100(2):e201900251, 2020.

[222] Jiahao Shi and A.H. Akbarzadeh. Architected cellular piezoelectric metamaterials: Thermo-electro-mechanical properties. *Acta Materialia*, 163:91–121, 2019.

[223] H. Le Quang and Q.-C. He. The number and types of all possible rotational symmetries for flexoelectric tensors. *Proceedings of the Royal Society A: Mathematical, Physical and Engineering Sciences*, 467(2132):2369–2386, 2011.

[224] Jiawang Hong. Journal club for november 2018: Beyond piezoelectricity: Flexoelectricity in solids. 2018.

[225] Yanmei Yue, K.Y. Xu, and T. Chen. A micro scale Timoshenko beam model for piezoelectricity with flexoelectricity and surface effects. *Composite Structures*, 136:278–286, 2016.

[226] Mohammad Reza Barati. On non-linear vibrations of flexoelectric nanobeams. *International Journal of Engineering Science*, 121:143–153, 2017.

[227] Lu Qi, Shujin Huang, Guangyang Fu, Shenjie Zhou, and Xiaoning Jiang. On the mechanics of curved flexoelectric microbeams. *International Journal of Engineering Science*, 124:1–15, 2018.

[228] Mohammad Malikan and Victor A. Eremeyev. On the geometrically nonlinear vibration of a piezo-flexomagnetic nanotube. *Mathematical Methods in the Applied Sciences*, 2020.

[229] Xu Liang, Runzhi Zhang, Shuling Hu, and Shengping Shen. Flexoelectric energy harvesters based on Timoshenko laminated beam theory. *Journal of Intelligent Material Systems and Structures*, 28(15):2064–2073, 2017.

[230] Kishor Shingare and S.I. Kundalwal. Static and dynamic response of graphene nanocomposite plates with flexoelectric effect. *Mechanics of Materials*, 134:69–84, 2019.

[231] Nikhil D. Sharma, Ravi Maranganti, and Pradeep Sharma. On the possibility of piezoelectric nanocomposites without using piezoelectric materials. *Journal of the Mechanics and Physics of Solids*, 55(11):2328–2350, 2007.

[232] Victor A. Eremeyev, Jean-François Ganghoffer, Violetta Konopińska-Zmysłowska, and Nikolay S.

Uglov. Flexoelectricity and apparent piezoelectricity of a pantographic micro-bar. *International Journal of Engineering Science*, 149:103213, 2020.

[233] Arnaldo Casalotti, Francesco D'Annibale, and Giuseppe Rosi. Multi-scale design of an architected composite structure with optimized graded properties. *Composite Structures*, 252:112608, 2020.

[234] Nanthakumar Subbiah, Xiaoying Zhuang, Harold S. Park, and Timon Rabczuk. Topology optimization of flexoelectric structures. *Journal of the Mechanics and Physics of Solids*, 105:217–234, August 2017.

[235] Houssam Abdoul-Anziz and Pierre Seppecher. Strain gradient and generalized continua obtained by homogenizing frame lattices. *Mathematics and Mechanics of Complex Systems*, 6:213–250, 07 2018.

[236] Igor Sevostianov, Valery Levin, and M. Kachanov. On the modeling and design of piezocomposites with prescribed properties. *Archive of Applied Mechanics (Ingenieur Archiv)*, 71:733–747, 01 2001.

[237] Bertrand Chambion, Laurent Goujon, Laurent Badie, Yannick Mugnier, Christine Barthod, Christine Galez, Sandrine Wiebel, and Cécile Venet. Optimization of the piezoelectric response of 0–3 composites: a modeling approach. *Smart materials and Structures*, 20(11):115006, 2011.

[238] Pablo Moreno-Navarro, Adnan Ibrahimbegovic, and Jose Perez-Aparicio. Linear elastic mechanical system interacting with coupled thermo-electro-magnetic fields. *Coupled Systems Mechanics*, 7:5–25, 02 2018.

[239] Gustav Gautschi and Gustav Gautschi. *Piezoelectric sensors*. Springer, 2002.

[240] Nipun Sinha, Graham E. Wabiszewski, Rashed Mahameed, Valery V. Felmetsger, Shawn M. Tanner, Robert W. Carpick, and Gianluca Piazza. Piezoelectric aluminum nitride nanoelectromechanical actuators. *Applied Physics Letters*, 95(5):053106, 2009.

[241] Mohsen Safaei, Henry A Sodano, and Steven R Anton. A review of energy harvesting using piezoelectric materials: state-of-the-art a decade later (2008–2018). *Smart Materials and Structures*, 28(11):113001, oct 2019.

[242] Qian Deng, Liping Liu, and Pradeep Sharma. Flexoelectricity in soft materials and biological membranes. *Journal of the Mechanics and Physics of Solids*, 62:209–227, 2014. Sixtieth anniversary issue in honor of Professor Rodney Hill.

[243] M. S. Majdoub, Pradeep Sharma, and Tcagin Cagin. Enhanced size-dependent piezoelectricity and elasticity in nanostructures due to the flexoelectric effect. *Physical Review B*, 77:125424, 3 2008.

[244] Qian Deng, Mejdi Kammoun, Alper Erturk, and Pradeep Sharma. Nanoscale flexoelectric energy harvesting. *International Journal of Solids and Structures*, 51:3218–3225, 9 2014.

[245] Shuwen Zhang, Minglong Xu, Kaiyuan Liu, and Shengping Shen. A flexoelectricity effect-based sensor for direct torque measurement. *Journal of Physics D: Applied Physics*, 48:485502, 12 2015.

[246] Chang Liu, Huaping Wu, and Jie Wang. Giant piezoelectric response in piezoelectric/dielectric superlattices due to flexoelectric effect. *Applied Physics Letters*, 109:192901, 11 2016.

[247] Nikhil D. Sharma, Ravi Maranganti, and Pradeep Sharma. On the possibility of piezoelectric

nanocomposites without using piezoelectric materials. *Journal of the Mechanics and Physics of Solids*, 55:2328–2350, 11 2007.

[248] Joseph N Grima, Ludovica Oliveri, Daphne Attard, Brian Ellul, Ruben Gatt, Gianluca Cicala, and Giuseppe Recca. Hexagonal honeycombs with zero poisson's ratios and enhanced stiffness. *Advanced Engineering Materials*, 12(9):855–862, 2010.

[249] David Codony, Onofre Marco, Sonia Fernández-Méndez, and Irene Arias. An immersed boundary hierarchical b-spline method for flexoelectricity. *Computer Methods in Applied Mechanics and Engineering*, 354:750–782, 2019.

[250] H.X. Zhu, J.F. Knott, and N.J. Mills. Analysis of the elastic properties of open-cell foams with tetrakaidecahedral cells. *Journal of the Mechanics and Physics of Solids*, 45:319–343, 3 1997.

[251] Tobias Fey, Franziska Eichhorn, Guifang Han, Kathrin Ebert, Moritz Wegener, Andreas Roosen, Ken ichi Kakimoto, and Peter Greil. Mechanical and electrical strain response of a piezoelectric auxetic pzt lattice structure. *Smart Materials and Structures*, 25:015017, 1 2016.

[252] Harry F. Tiersten. Wave propagation in an infinite piezoelectric plate. *The Journal of the Acoustical Society of America*, 35(2):234–239, 1963.

[253] Jeffrey L. Bleustein. Some simple modes of wave propagation in an infinite piezoelectric plate. *The Journal of the Acoustical Society of America*, 45(3):614–620, 1969.

[254] Alexander K. Tagantsev. Piezoelectricity and flexoelectricity in crystalline dielectrics. *Phys. Rev. B*, 34:5883–5889, Oct 1986.

[255] A. Cemal Eringen. Nonlocal continuum mechanics based on distributions. *International Journal of Engineering Science*, 44(3):141–147, 2006.

[256] Dong-Jia Yan, A-Li Chen, Yue-Sheng Wang, Chuanzeng Zhang, and Mikhail Golub. Propagation of guided elastic waves in nanoscale layered periodic piezoelectric composites. *European Journal of Mechanics - A/Solids*, 66:158–167, 2017.

[257] Nikolaos Karathanasopoulos, Hilal Reda, and Jean francois Ganghoffer. Designing two-dimensional metamaterials of controlled static and dynamic properties. *Computational Materials Science*, 138:323–332, 2017.

[258] Hilal Reda, Nikolaos Karathanasopoulos, Khaled Elnady, Jean-François Ganghoffer, and Hassan Lakiss. The role of anisotropy on the static and wave propagation characteristics of two-dimensional architectured materials under finite strains. *Materials & Design*, 147:134–145, 2018.

[259] A. Cemal Eringen. On differential equations of nonlocal elasticity and solutions of screw dislocation and surface waves. *Journal of Applied Physics*, 54(9):4703–4710, 1983.

[260] G. Kovacs, M. Anhorn, H.E. Engan, G. Visintini, and C.C.W. Ruppel. Improved material constants for linbo/sub 3/ and litao/sub 3/. pages 435–438 vol.1, 1990.

[261] Feng-Ming Li, Yi-Ze Wang, Bo Fang, and Yue-Sheng Wang. Propagation and localization of two-dimensional in-plane elastic waves in randomly disordered layered piezoelectric phononic crystals. *International Journal of Solids and Structures*, 44(22):7444–7456, 2007.

[262] Igor Sevostianov and Federico J. Sabina. Cross-property connections for fiber reinforced piezoelectric materials with anisotropic constituents. *International Journal of Engineering Science*, 45(9):719–735, 2007.

[263] A-Li Chen, Dong-Jia Yan, Yue-Sheng Wang, and Chuanzeng Zhang. Anti-plane transverse waves propagation in nanoscale periodic layered piezoelectric structures. *Ultrasonics*, 65:154–164, 2016.

[264] Mohadeseh Zare, Molamma P. Prabhakaran, Nader Parvin, and Seeram Ramakrishna. Thermally-induced two-way shape memory polymers: Mechanisms, structures, and applications. *Chemical Engineering Journal*, 374, 2019.

[265] Kunhao Yu, An Xin, and Qiming Wang. Mechanics of light-activated self-healing polymer networks. *Journal of the Mechanics and Physics of Solids*, 124, 2019.

[266] Zisheng Liao, Mokarram Hossain, Xiaohu Yao, Markus Mehnert, and Paul Steinmann. On thermo-viscoelastic experimental characterization and numerical modelling of vhb polymer. *International Journal of Non-Linear Mechanics*, 118, 2020.

[267] Markus Mehnert, Mokarram Hossain, and Paul Steinmann. Towards a thermo-magneto-mechanical coupling framework for magneto-rheological elastomers. *International Journal of Solids and Structures*, 128, 2017.

[268] Ruike Zhao, Yoonho Kim, Shawn A. Chester, Pradeep Sharma, and Xuanhe Zhao. Mechanics of hard-magnetic soft materials. *Journal of the Mechanics and Physics of Solids*, 124, 2019.

[269] Miguel Angel Moreno-Mateos, Jorge Gonzalez-Rico, María Luisa Lopez-Donaire, Angel Arias, and Daniel Garcia-Gonzalez. New experimental insights into magneto-mechanical rate dependences of magnetorheological elastomers. *Composites Part B: Engineering*, 224, 2021.

[270] Wenqi Hu, Guo Zhan Lum, Massimo Mastrangeli, and Metin Sitti. Small-scale soft-bodied robot with multimodal locomotion. *Nature*, 554, 2018.

[271] Jessica A.C. Liu, Jonathan H. Gillen, Sumeet R. Mishra, Benjamin A. Evans, and Joseph B. Tracy. Photothermally and magnetically controlled reconfiguration of polymer composites for soft robotics. *Science Advances*, 5, 2019.

[272] Timur A. Nadzharyan, S. A. Kostrov, Gennady V. Stepanov, and Elena Yu Kramarenko. Fractional rheological models of dynamic mechanical behavior of magnetoactive elastomers in magnetic fields. *Polymer*, 142, 2018.

[273] Yoonho Kim, German A. Parada, Shengduo Liu, and Xuanhe Zhao. Ferromagnetic soft continuum robots. *Science Robotics*, 4, 2019.

[274] Xuanhe Zhao, Jaeyun Kim, Christine A. Cezar, Nathaniel Huebsch, Kangwon Lee, Kamal Bouhadir, and David J. Mooney. Active scaffolds for on-demand drug and cell delivery. *Proceedings of the National Academy of Sciences of the United States of America*, 108, 2011.

[275] Miguel Angel Moreno-Mateos, Jorge Gonzalez-Rico, Emanuel Nunez-Sardinha, Clara Gomez-Cruz, Maria Luisa Lopez-Donaire, Sergio Lucarini, Angel Arias, Arrate Muñoz-Barrutia, Diego Velasco, and Daniel Garcia-Gonzalez. Magneto-mechanical system to reproduce and quantify complex strain

patterns in biological materials. *Applied Materials Today*, 27, 6 2022.

[276] Stefan Odenbach. Microstructure and rheology of magnetic hybrid materials. *Archive of Applied Mechanics*, 86, 2016.

[277] Marshall Schaeffer and Massimo Ruzzene. Wave propagation in reconfigurable magneto-elastic kagome lattice structures. *Journal of Applied Physics*, 117, 2015.

[278] S. Macrae Montgomery, Shuai Wu, Xiao Kuang, Connor D. Armstrong, Cole Zemelka, Qiji Ze, Rundong Zhang, Ruike Zhao, and H. Jerry Qi. Magneto-mechanical metamaterials with widely tunable mechanical properties and acoustic bandgaps. *Advanced Functional Materials*, 31(3):2005319, 2021.

[279] Yunus Alapan, Alp C. Karacakol, Seyda N. Guzelhan, Irem Isik, and Metin Sitti. Reprogrammable shape morphing of magnetic soft machines. *Science Advances*, 6, 2020.

[280] Marissa M. Schmauch, Sumeet R. Mishra, Benjamin A. Evans, Orlin D. Velev, and Joseph B. Tracy. Chained iron microparticles for directionally controlled actuation of soft robots. *ACS Applied Materials and Interfaces*, 9, 2017.

[281] Shuai Wu, Wenqi Hu, Qiji Ze, Metin Sitti, and Ruike Zhao. Multifunctional magnetic soft composites: A review. *Multifunctional Materials*, 3, 2020.

[282] Anil K. Bastola and Mokarram Hossain. The shape – morphing performance of magnetoactive soft materials performance. *Materials and Design*, 211, 2021.

[283] Sergio Lucarini, Mokarram Hossain, and Daniel Garcia-Gonzalez. Recent advances in hard-magnetic soft composites: Synthesis, characterisation, computational modelling, and applications. *Composite Structures*, 279, 2022.

[284] Karl Alexander Kalina, Jörg Brummund, Philipp Metsch, Markus Kästner, D Yu Borin, JM Linke, and S Odenbach. Modeling of magnetic hystereses in soft mres filled with ndfeb particles. *Smart Materials and Structures*, 26(10):105019, 2017.

[285] Daniel Garcia-Gonzalez. Magneto-visco-hyperelasticity for hard-magnetic soft materials: Theory and numerical applications. *Smart Materials and Structures*, 28, 2019.

[286] Dipayan Mukherjee, Matthias Rambausek, and Kostas Danas. An explicit dissipative model for isotropic hard magnetorheological elastomers. *Journal of the Mechanics and Physics of Solids*, 151, 2021.

[287] Dipayan Mukherjee and Kostas Danas. A unified dual modeling framework for soft and hard magnetorheological elastomers. *International Journal of Solids and Structures*, page 111513, 2 2022.

[288] Rundong Zhang, Shuai Wu, Qiji Ze, and Ruike Zhao. Micromechanics study on actuation efficiency of hard-magnetic soft active materials. *Journal of Applied Mechanics, Transactions ASME*, 87, 2020.

[289] Daniel Garcia-Gonzalez and Mokarram Hossain. A microstructural-based approach to model magneto-viscoelastic materials at finite strains. *International Journal of Solids and Structures*,

208-209, 2021.

[290] Daniel Garcia-Gonzalez and Mokarram Hossain. Microstructural modelling of hard-magnetic soft materials: Dipole–dipole interactions versus zeeman effect. *Extreme Mechanics Letters*, 48, 2021.

[291] Chennakesava Kadapa and Mokarram Hossain. A unified numerical approach for soft to hard magneto-viscoelastically coupled polymers. *Mechanics of Materials*, 166:104207, 3 2022.

[292] Mihai Gologanu, J-B. Leblond, Gilles Perrin, and J. Devaux. *Recent extensions of Gurson's model for porous ductile metals*. Springer, 1997.

[293] Matthias Rambausek, Dipayan Mukherjee, and Kostas Danas. A computational framework for magnetically hard and soft viscoelastic magnetorheological elastomers. *Computer Methods in Applied Mechanics and Engineering*, 391:114500, 3 2022.

[294] Mokarram Hossain, Prashant Saxena, and Paul Steinmann. Modelling the mechanical aspects of the curing process of magneto-sensitive elastomeric materials. *International Journal of Solids and Structures*, 58, 2015.

[295] Kostas Danas. Effective response of classical, auxetic and chiral magnetoelastic materials by use of a new variational principle. *Journal of the Mechanics and Physics of Solids*, 105, 2017.

[296] David J. Griffiths and Colin Inglefield. Introduction to electrodynamics. *American Journal of Physics*, 73, 2005.

[297] William Fuller Brown. *Magnetoelastic Interactions*, volume 9. Springer Berlin Heidelberg, 1966.

[298] Frederick A. Howes and Stephen Whitaker. The spatial averaging theorem revisited. *Chemical Engineering Science*, 40, 1985.

[299] Brian D. Wood. Technical note: Revisiting the geometric theorems for volume averaging. *Advances in Water Resources*, 62, 2013.

[300] Duy-Khanh Trinh, Ralf Jänicke, Nicolas Auffray, Stefan Diebels, and Samuel Forest. Evaluation of generalized continuum substitution models for heterogeneous materials. *International Journal for Multiscale Computational Engineering*, 10:527–549, 01 2012.

[301] Hilal Reda, Seyed Ehsan Alavi, Maryam Nasimsobhan, and Jean-François Ganghoffer. Homogenization towards chiral cosserat continua and applications to enhanced timoshenko beam theories. *Mechanics of Materials*, 155:103728, 2021.

[302] Yosra Rahali, Hilal Reda, Benoit Vieille, Hassan Lakiss, and Jean-François Ganghoffer. Influence of first to second gradient coupling tensors terms with surface effects on the wave propagation of 2d network materials. *Nonlinear Wave Dynamics of Materials and Structures*, pages 335–352, 2020.

[303] Behrooz Hassani and Ernest Hinton. *Homogenization and structural topology optimization: theory, practice and software*. Springer Science & Business Media, 2012.

Appendix A

Derivation of Hill-Mandel lemma in surface integral format

The surface integral formulation for the kinematic and static variables entering Hill-Mandel macrohomogeneity condition for the effective strain gradient formulation is derived. These stress and hyperstress tensors will be expressed as surface integrals over part of the boundary of the unit cell where the macroscopic kinematic loading is applied (wherever material is present) as follows:

$$\begin{aligned}
&\boldsymbol{\Sigma} = \langle \boldsymbol{\sigma} \rangle_Y := \frac{1}{|Y|} \int_Y \boldsymbol{\sigma} dV_y = \frac{1}{|Y|} \int_{\partial Y} \boldsymbol{y} \otimes \boldsymbol{\sigma}.\boldsymbol{n} dS_y = \frac{1}{|Y|} \int_{\partial Y} \boldsymbol{y} \otimes \boldsymbol{t} dS_y \equiv \langle \boldsymbol{y} \otimes \boldsymbol{t} \rangle_{\partial Y}, \\
&\boldsymbol{S} = \langle \boldsymbol{y} \otimes \boldsymbol{\sigma} \rangle_Y := \frac{1}{|Y|} \int_Y \boldsymbol{y} \otimes \boldsymbol{\sigma} dV_y = \frac{1}{2\,|Y|} \int_{\partial Y} \boldsymbol{y} \otimes \boldsymbol{y} \otimes \boldsymbol{\sigma}.\boldsymbol{n} dS_y = \frac{1}{2\,|Y|} \int_{\partial Y} \boldsymbol{y} \otimes \boldsymbol{y} \otimes \boldsymbol{t} dS_y \equiv \frac{1}{2} \langle \boldsymbol{y} \otimes \boldsymbol{y} \otimes \boldsymbol{t} \rangle_{\partial Y}
\end{aligned} \tag{A.1}$$

The last equality in Eq. A.1 results from the choice of the strain gradient as the higher order kinematic variable and the fact that the hyperstress has the same index symmetry as the conjugated stress variable. Similar surface integral expressions hold for the strain measures and use of Whitaker theorem, stating that the average of the microscopic gradient is equal to the macroscopic gradient of the average for continuous interfaces:

$$\begin{aligned}
&\boldsymbol{E} := \langle \boldsymbol{\varepsilon} \rangle = \frac{1}{|Y|} \int_Y \boldsymbol{\varepsilon}\ dV_y = \frac{1}{|Y|} \int_{\partial Y} (\boldsymbol{u} \otimes \boldsymbol{n})^S dS_y = \left\langle (\boldsymbol{u} \otimes \boldsymbol{n})^S \right\rangle_{\partial Y} \\
&\boldsymbol{K} := \langle \boldsymbol{\varepsilon}(\boldsymbol{y}) \rangle_Y \otimes \nabla_x \underset{Whita\,\ker}{=} \langle \boldsymbol{\varepsilon}(\boldsymbol{y}) \otimes \nabla_y \rangle_Y \underset{Whita\,\ker}{=} \langle \boldsymbol{\varepsilon}(\boldsymbol{y}) \rangle_Y \otimes \nabla_x = \langle \boldsymbol{\varepsilon}(\boldsymbol{y}) \otimes \boldsymbol{n} \rangle_{\partial Y} \\
&\quad = \left\{ \frac{1}{|Y|} \int_{\partial Y} (\boldsymbol{u} \otimes \boldsymbol{n})^S dS \right\} \otimes \nabla_x \equiv \left\langle (\boldsymbol{u} \otimes \boldsymbol{n})^S \right\rangle_{\partial Y} \otimes \nabla_x = \frac{1}{|V_x|} \int_{V_x} \left(\left\langle (\boldsymbol{u} \otimes \boldsymbol{n})^S \right\rangle_{\partial Y} \otimes \nabla_x \right) dV_x \\
&\quad = \frac{1}{|V_x|} \int_{\partial V_x} \boldsymbol{E}(\boldsymbol{x}) \otimes \boldsymbol{N}(\boldsymbol{x}) dS_x = \frac{1}{|V_x|} \left[\left[\langle \boldsymbol{E}(\boldsymbol{x}) \rangle_{\partial V_x} \right] \right]
\end{aligned} \tag{A.2}$$

in which the bracket $[[(.)]]$ denotes the relative variation of the enclosed quantity between the two opposite faces or edges of the unit cell. The last equality in the third line results from the homogeneity of the macroscopic quantities. The last relation results from the periodicity of the unit cell (the homogeneous

domain called V_x), with the macroscopic normal vector therein $\boldsymbol{N}(\boldsymbol{x})$ taking opposite values on opposite faces (in 3D) or edges (in 2D).

Thus, the strain gradient tensor can be elaborated from the macroscopic normalized variation of the macrostrain over the macroscale. The macroscopic energy (up to a factor 2) of the effective strain gradient continuum can be purely expressed with surface fields; it holds indeed the following relations in the absence of body forces:

$$\begin{aligned} W_M(\boldsymbol{E},\boldsymbol{K}) &= \boldsymbol{\Sigma}:\boldsymbol{E}+\boldsymbol{S}\therefore\boldsymbol{K}=\boldsymbol{E}:\boldsymbol{C}^{\text{hom}}:\boldsymbol{E}+\boldsymbol{K}\therefore\boldsymbol{A}^{\text{hom}}:\boldsymbol{K}+2\boldsymbol{E}:\left(\boldsymbol{B}^{\text{hom}}+\boldsymbol{B}^{\text{hom},T}\right):\boldsymbol{K} \\ &= \langle\boldsymbol{y}\otimes\boldsymbol{t}\rangle_{\partial Y}:\left\langle(\boldsymbol{u}\otimes\boldsymbol{n})^S\right\rangle_{\partial Y}+\frac{1}{2}\langle\boldsymbol{y}\otimes\boldsymbol{y}\otimes\boldsymbol{t}\rangle_{\partial Y}\therefore\left\langle(\boldsymbol{u}\otimes\boldsymbol{n})^S\right\rangle_{\partial Y}\otimes\nabla_x \\ &\rightarrow \boldsymbol{\Sigma}:=\langle\boldsymbol{y}\otimes\boldsymbol{t}\rangle_{\partial Y}\text{ average Cauchy stress over the unit cell} \\ &\rightarrow \boldsymbol{S}:=\frac{1}{2}\langle\boldsymbol{y}\otimes\boldsymbol{y}\otimes\boldsymbol{t}\rangle_{\partial Y}\text{ average hyperstress over the unit cell} \end{aligned} \tag{A.3}$$

wherein $\boldsymbol{C}^{\text{hom}}$,$\boldsymbol{A}^{\text{hom}}$, $\boldsymbol{B}^{\text{hom}}$ are the effective homogenized first gradient moduli (Cauchy effective moduli), second gradient effective moduli and coupling moduli, respectively.

Thereby, the mesoscopic work of internal forces has been fully expressed from the surface displacements and tractions. The last two relations in Eq. A.3 highlight the surface elaboration of the stress and hyperstress tensors over the unit cell area or edges in the adopted 2D geometrical context.

This parallels the fact that the hyperstress involves a higher order dyadic product of the surface microscopic position, viz. $\boldsymbol{S}:=\frac{1}{2}\langle\boldsymbol{y}\otimes\boldsymbol{y}\otimes\boldsymbol{t}\rangle_{\partial Y}$, in comparison to Cauchy stress tensor formulated as a surface integral and involving a single dyadic product, viz. $\boldsymbol{\Sigma}:=\langle\boldsymbol{y}\otimes\boldsymbol{t}\rangle_{\partial Y}$, as evidenced in Eq. A.3.

The comparison of Eqs. A.3 with the surface formulation of Hill-Mandel macro-homogeneity condition of Eq. A.4:

$$\begin{aligned} \int_Y\boldsymbol{\sigma}:(\boldsymbol{\omega}\otimes\nabla_y)dV &= \frac{1}{|Y|}\sum_{i=1,2}\left(\left(\boldsymbol{E}(\boldsymbol{x})\cdot\boldsymbol{Y}^i\right)\otimes\boldsymbol{N}^i\right):\sum_{j=1,2}\left(\int_{\partial Y}(\boldsymbol{\sigma}\cdot\boldsymbol{n})\,ds\otimes\boldsymbol{Y}^j\right) \\ &+\sum_{i=1,2}\left(\left(\boldsymbol{K}(\boldsymbol{x})\cdot\boldsymbol{Y}^i\right)\otimes\boldsymbol{N}^i\right)\therefore\sum_{j=1,2}\left(\frac{1}{2\,|Y|}\int_{\partial Y}(\boldsymbol{\sigma}\cdot\boldsymbol{n})\,ds\right)\otimes\boldsymbol{Y}^j\otimes\boldsymbol{Y}^j \\ &=\langle\boldsymbol{\sigma}\rangle_Y:\boldsymbol{E}+\langle\boldsymbol{\xi}\otimes\boldsymbol{\sigma}\rangle_Y\therefore\boldsymbol{K}=\boldsymbol{\Sigma}:\boldsymbol{E}+\boldsymbol{S}\therefore\boldsymbol{K} \end{aligned} \tag{A.4}$$

leads to the following alternative formulation of the stress and hyperstress tensors:

$$\begin{aligned} \boldsymbol{\Sigma}&:=\langle\boldsymbol{y}\otimes\boldsymbol{t}\rangle_{\partial Y}=\frac{1}{|Y|}\sum_{j=1,2}\left(\int_{\Gamma_j}\boldsymbol{t}ds_y\otimes\underset{-}{\boldsymbol{Y}}^j\right) \\ \boldsymbol{S}&:=\frac{1}{2}\langle\boldsymbol{y}\otimes\boldsymbol{y}\otimes\boldsymbol{t}\rangle_{\partial Y}=\frac{1}{|Y|}\sum_{j=1,2}\frac{1}{2}\left(\int_{\Gamma_j}\boldsymbol{t}ds_y\otimes\underset{-}{\boldsymbol{Y}}^j\otimes\underset{-}{\boldsymbol{Y}}^j\right) \end{aligned} \tag{A.5}$$

Recall that the last two expressions of the stress and hyperstress in Eq. A.3 result from the fact that the traction vector is antiperiodic. The presence of the microscopic position on the boundary where material is present reflects the importance of surface effects.

The surface expression of the strain and strain gradient tensors in Eq. A.2 is dual to that of the stress and hyperstress tensors respectively. It includes the density of strain as a flux reflected by the presence of the normal vector therein, that 'compensates' for the surface effects accounted for by the microscopic position $\boldsymbol{y}$ present in the stress tensors, so that the product of stress with strain still has the (as for the first strain gradient effective continuum) unit of an energy per unit volume. This fact is clear since the strain gradient tensor has the unit of the inverse of a length.

We observe from previous relations that both the average stress and average strain are expressed as surface integrals with a linear integrand in the microscopic position, which entails that the tensor of homogenized Cauchy moduli relating them mutually does not depend on surface (or edge in 2D) properties. In contrast to Cauchy effective medium, due to the scaling of the hyperstress and strain gradient tensors, the strain gradient moduli includes a dependency upon the square of a length parameter.

Appendix B

Discrete homogenization method for repetitive periodic lattices

The discrete homogenization method aims to replace the vector of discrete microscopic displacements $\boldsymbol{u_i} = \left(u_{i_x}, u_{i_y}\right)$ by a vector of continuous macroscopic components $\boldsymbol{u} = (u_x(x,y), u_y(x,y))$: this continualization process is achieved by expanding the discrete displacement as a Taylor series expansion [201].

$$\boldsymbol{u}_i = \boldsymbol{u}(x_i, y_i) = \sum_{m=0}^{N} \sum_{n=0}^{N} \frac{(x_i)^m}{m!} \frac{(y_i)^n}{n!} \frac{\partial^{m+n} \boldsymbol{u}\,(x_0, y_0)}{\partial x^m \partial y^n} \tag{B.1}$$

wherein $\boldsymbol{u}\,(x_0, y_0) = (u_x\,(x_0, y_0)\,,\, u_y\,(x_0, y_0))$ is the vector of macroscopic continuous generalized displacements. Also, x_i and y_i are the coordinates of the node number i.

For instance, the truncation of the Taylor series expansion in Eq. B.1 leads to the construction of the macroscopic continuum as follows:

$$u_{x_i} = u_{x_0} + x_i \frac{\partial u_{x_0}}{\partial x} + y_i \frac{\partial u_{x_0}}{\partial y} + \frac{x_i^2}{2} \frac{\partial^2 u_{x_0}}{\partial x^2} + \frac{y_i^2}{2} \frac{\partial^2 u_{x_0}}{\partial y^2} + x_i y_i \frac{\partial^2 u_{x_0}}{\partial x \partial y} \tag{B.2}$$

$$u_{y_i} = u_{y_0} + x_i \frac{\partial u_{y_0}}{\partial x} + y_i \frac{\partial u_{y_0}}{\partial y} + \frac{x_i^2}{2} \frac{\partial^2 u_{y_0}}{\partial x^2} + \frac{y_i^2}{2} \frac{\partial^2 u_{y_0}}{\partial y^2} + x_i y_i \frac{\partial^2 u_{y_0}}{\partial x \partial y} \tag{B.3}$$

Periodic boundary conditions must be applied to a periodic structure before the calculation of the effective mechanical properties. For this purpose, a set of definitions are required, and they are presented in the following subsections.

B.1 Direct Translational Bases

$\vec{a}_k$ denotes the translational symmetric primitive bases of the lattice and it refers to as the direct translational bases. The UC, that fills the space under translational symmetry, is tessellated using these translational bases. The direct translational bases are feature of the UC envelope, that reveals the axes along which the UC is tessellated to fill the space.

B.1.1 Direct Translational Vector

The reference UC is translated to any other cell in the lattice space using a direct translational vector, which is represented as a linear combination of the direct translational bases. This appears as a basic (primitive) lattice vector that covers a set of cells in lattice space and is expressed as:

$$\vec{R} = \sum_{k}^{n} m_k \vec{a}_k \tag{B.4}$$

wherein n is the dimensional space of the lattice (n = 2 in 2D and n =3 in 3D) and m_k is any set of integers.

B.1.2 Position Vector

The position vector of nodes throughout the entire lattice can be described as a function of the node bases, defined with respect to the UC envelope along with the direct translational vector as:

$$p_l = j_l + \vec{R} = j_l + \sum_{k}^{n} m_k \vec{a}_k \qquad \forall l \in \{1, ..., J\} \tag{B.5}$$

where p_l is defined as the node position vector, and J is the number of independent nodes within the reference UC.

B.1.3 Direct Lattice

The direct lattice is the collection of independent node bases, across the reference UC envelope, spanned over the infinite periodic lattice by their position vectors. To determine this independent set of node vectors over the reference UC, we check whether a vector j_{l-1} relies on a vector j_l across one UC period through the relation:

$$j_{l-1} = j_l + \sum_{k}^{n} \hat{x}_k \vec{a}_k \tag{B.6}$$

This dependency information is employed later on to adjust the strain energy over the reference UC to obtain the periodic strain energy throughout the entire lattice material.

B.1.4 Periodic Transformation matrices

Periodic displacement boundary conditions are applied over the generic UC of Fig. B.1 which results in the following conditions:

$$q_R = q_L; \;\; q_T = q_B; \;\; q_{RB} = q_{LB}; \;\; q_{LT} = q_{LB}; \;\; q_{RT} = q_{LB}; \tag{B.7}$$

wherein R, L, B, and T are respectively the right, left, bottom, and top edges, and q is a generic nodal

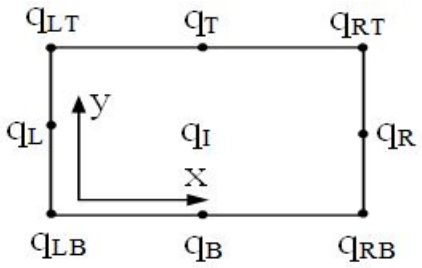

Figure B.1 The periodic displacement boundary conditions of a generic unit cell

or element function, such as deformation and force. Eq. B.7 is rewritten in matrix format as:

$$\begin{bmatrix} q_I \\ q_B \\ q_T \\ q_L \\ q_R \\ q_{LB} \\ q_{RB} \\ q_{LT} \\ q_{RT} \end{bmatrix} = \begin{bmatrix} 1 & 0 & 0 & 0 \\ 0 & 1 & 0 & 0 \\ 0 & 1 & 0 & 0 \\ 0 & 0 & 1 & 0 \\ 0 & 0 & 1 & 0 \\ 0 & 0 & 0 & 1 \\ 0 & 0 & 0 & 1 \\ 0 & 0 & 0 & 1 \\ 0 & 0 & 0 & 1 \end{bmatrix} \begin{bmatrix} q_I \\ q_B \\ q_L \\ q_{LB} \end{bmatrix}, \quad or\ q = \boldsymbol{T}\tilde{q} \tag{B.8}$$

where T denotes the transformation matrix from the degrees of freedom of the primitive cell , 'q' to degrees of freedom of the reduced cell , '$\tilde{q}$'.

Using the same methodology that was used to construct the kinematic transformation matrix, the equilibrium transformation matrix is generated, in which it takes into account the anti-periodic constraints required for the static equilibrium of the lattice. For the four generic UCs of Fig. B.2, the static equilibrium

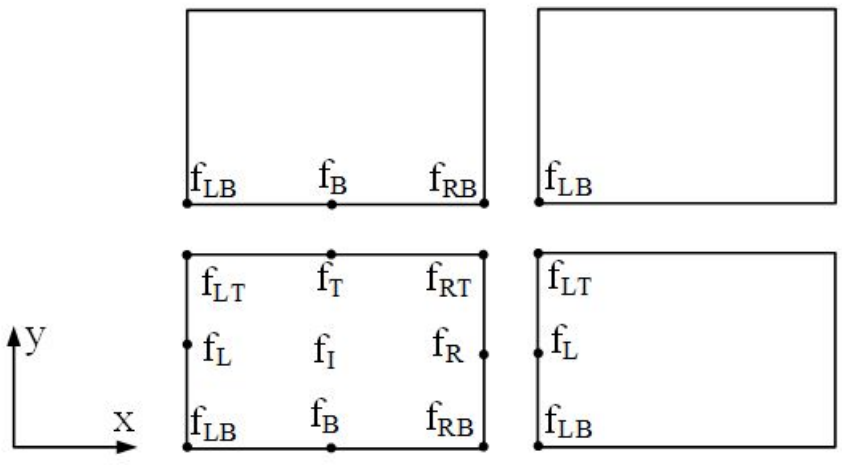

Figure B.2 The periodic equilibrium boundary conditions of a generic unit cell

relations can be expressed as follows:

$$f_R + f_L = 0; \quad f_T + f_B = 0; \quad f_{RT} + f_{LT} + f_{RB} + f_{LB} = 0; \tag{B.9}$$

Rearranging Eq. B.9 in matrix format leads to:

$$\begin{bmatrix} f_I \\ f_B \\ f_L \\ f_{LB} \end{bmatrix} = \begin{bmatrix} 1 & 0 & 0 & 0 & 0 & 0 & 0 & 0 & 0 \\ 0 & 1 & 1 & 0 & 0 & 0 & 0 & 0 & 0 \\ 0 & 0 & 0 & 1 & 1 & 0 & 0 & 0 & 0 \\ 0 & 0 & 0 & 0 & 0 & 1 & 1 & 1 & 1 \end{bmatrix} \begin{bmatrix} f_I \\ f_B \\ f_T \\ f_L \\ f_R \\ f_{LB} \\ f_{RB} \\ f_{LT} \\ f_{RT} \end{bmatrix}, \quad or \ \tilde{f} = \boldsymbol{T}^T f = 0 \tag{B.10}$$

with $\boldsymbol{T^T}$ being the transpose of the transformation matrix $\boldsymbol{T}$.

Appendix C

Closed-Form expressions of the effective strain gradient moduli

Applying the homogenization method described in section 2.2.2, the effective Cauchy and strain gradient moduli are obtained as closed-form expressions for the hexagonal and square unit cells as shown in tables Table C.1 and Table C.2 respectively (relying on Eq. 2.6 for the hexagonal UC and the same can be applied for the square UC).

Table C.1 Closed-from expressions of the effective properties of general hexagonal lattices.

Effective Moduli	Closed form expression
C_{11}	$\frac{AE\cos(\theta)\left[\cos^2(\theta)+\alpha\left(\sin^2(\theta)+2\beta_{eff}\right)\right]}{bL_{eff}\gamma_1(\beta+\sin(\theta))}$
C_{22}	$\frac{AE(\beta+\sin(\theta))\left[\sin^2(\theta)+\alpha\cos^2(\theta)\right]}{bL_{eff}\gamma_1\cos(\theta)}$
C_{12}	$\frac{AE\sin(2\theta)(1-\alpha)}{2bL_{eff}\gamma_1}$
C_{33}	$\frac{3EIL^2\left[\sin^2(\theta)+\beta^2+2\beta\sin(\theta)+4\beta^2\beta_{eff}^3\left(\sin^2(\theta)+\frac{\cos^2(\theta)}{\alpha}\right)+\gamma_2+\gamma_3\right]}{bh_{eff}^3\cos(\theta)(\beta+\sin(\theta))\left[\frac{1}{2}+\beta_{eff}^3\left(\sin^2(\theta)+\frac{\cos^2(\theta)}{\alpha}\right)\right]}$
A_{11}	$\frac{6EIL^2\cos^3(\theta)\left[\frac{1}{4}+\beta_{eff}^3\left(\sin^2(\theta)+\frac{\cos^2(\theta)}{\alpha}\right)\right]}{bh_{eff}^3(\beta+\sin(\theta))}$
A_{22}	$\frac{3EIL^2\cos(\theta)\left[10\sin(\theta)+10\beta(\beta+10\sin(\theta))+\beta_{eff}^3\gamma_4\right]}{bh_{eff}^3(\beta+\sin(\theta))}$
A_{33}	$\frac{AEL^2(\beta+\sin(\theta))\left[\alpha_1\gamma_5+\cos^2(\theta)\gamma_6\right]}{2bh_{eff}\cos(\theta)}$
A_{44}	$\frac{AEL^2(\beta+\sin(\theta))^3\left[\sin^2(\theta)+\alpha\cos^2(\theta)\right]}{4bL_{eff}\cos(\theta)}$

A_{55}	$\frac{AEL^2\cos^3(\theta)\left[\sin^2(\theta)+\alpha\cos^2(\theta)\right]}{bL_{eff}(\beta+\sin(\theta))}$
A_{66}	$\frac{48EIL^2(\beta+\sin(\theta))^4\left[\frac{1}{4}+\beta_{eff}^3\left(\sin^2(\theta)+\frac{\cos^2(\theta)}{\alpha}\right)\right]}{bh_{eff}^3(\sin(2\theta)+2\beta\cos(\theta))}$
A_{12}	$\frac{3EIL^2\cos^2(\theta)\left[1+2\beta_{eff}^3\left(\sin^2(\theta)+\frac{\cos^2(\theta)}{\alpha}\right)\right]}{bh_{eff}^3}$
A_{13}	$-\frac{6EIL^2\cos(\theta)\left[\frac{1}{4}(\beta+\sin(\theta))+\gamma_7\right]}{bh_{eff}^3}$
A_{16}	$\frac{12EIL^2\cos(\theta)\left[\frac{1}{4}+\beta_{eff}^3\left(\sin^2(\theta)+\frac{\cos^2(\theta)}{\alpha}\right)\right]}{bh_{eff}^3}$
A_{23}	$-\frac{6EIL^2(\beta+\sin(\theta))^2\left[\frac{1}{2}+\beta_{eff}^3\left(\sin^2(\theta)+\frac{\cos^2(\theta)}{\alpha}\right)\right]}{bh_{eff}^3}$
A_{24}	$\frac{AEL^2\cos(\theta)\gamma_8}{16bL_{eff}}$
A_{25}	$\frac{AEL^2\cos^3(\theta)[\sin(\theta)(1-\alpha)(2\beta+3\sin(\theta))+\alpha]}{2bL_{eff}(\beta+\sin(\theta))}$
A_{26}	$\frac{12EIL^2(\beta+\sin(\theta))^2\left[\frac{1}{2}+\beta_{eff}^3\left(\sin^2(\theta)+\frac{\cos^2(\theta)}{\alpha}\right)\right]}{bh_{eff}^3}$
A_{36}	$-\frac{12EIL^2(\beta+\sin(\theta))^2\left[\frac{1}{4}(\beta+\sin(\theta))+\gamma_6\right]}{bh_{eff}^3\cos(\theta)}$
A_{45}	$\frac{AEL^2(\beta+\sin(\theta))\left[\sin^2(\theta)+\alpha\cos^2(\theta)\right]}{2bL_{eff}}$

In this Table, b is the out-of-plane thickness of the unit cell, $A = bt$ is the cross-sectional area of the elements, and $I = \frac{1}{12}bt^3$ is the second moment of area of the elements. The intermediate parameters found in Table C.1 have the following expressions:

$$\alpha = \frac{12I}{AL_{eff}^2};\ \ \alpha_1 = \frac{3I}{Ah_{eff}^2}\ \ \beta_{eff} = \frac{h_{eff}}{L_{eff}};\quad \beta = \frac{h}{L};\quad h_{eff} = h - \frac{t(1-\sin\theta)}{\cos\theta};\quad L_{eff} = L - \frac{t}{2\cos\theta}$$

$$\gamma_1 = \left(1 + 2\beta_{eff}\sin^2(\theta)\right) + 2\alpha\beta_{eff}\cos^2(\theta)$$

$$\gamma_2 = 2\beta\beta_{eff}^3\sin(\theta)\left(\beta_{eff}^3 + 4\right) + \beta^2\beta_{eff}^6\left(\sin^4(\theta) + \frac{\cos^2(\theta)}{\alpha^2} + 2\sin^2(\theta)\cos^2(\theta)\right)$$

$$\gamma_3 = \beta_{eff}^6\left(\frac{4}{\alpha}\cos^2(\theta) + \sin^2(\theta)\right) + 2\beta_{eff}^3\left(1 - 3\sin^2(\theta) + 4\sin^2(\theta)\left(\sin^2(\theta) + \frac{\cos^2(\theta)}{\alpha}\right)\right)$$

$$\gamma_4 = \beta_{eff}^3\left(\frac{\cos^2(\theta)}{\alpha}\left(20\beta + 13\sin^2(\theta) + 8\beta^2\right) + 4\beta\sin(\theta)\left(5\sin^2(\theta) + 2\beta\sin(\theta)\right) + 1 + 13\sin^4(\theta) - 6\sin^2(\theta)\right)$$

$$\gamma_5 = \left(\sin^2(\theta) + 2\beta_{eff}^3\left(10\sin^4(\theta) - 12\sin^2(\theta) + 4 - 4\beta\sin(\theta)\cos(2\theta)\right) + \beta\left(2\sin(\theta) + \beta\left(1 + \beta_{eff}^3\sin^2(\theta)\right)\right)\right)$$

$$\gamma_6 = \cos^2(\theta)\left(4 + \beta^2\beta_{eff} + 4\beta\beta_{eff}\sin(\theta) + 5\beta_{eff}\sin^2(\theta)\right)$$

$$\gamma_7 = \beta\beta_{eff}^3\left(\sin^2(\theta) + \frac{\cos^2(\theta)}{\alpha}\right) + \beta_{eff}^3\sin(\theta)\left(\cos(2\theta) + \frac{2\cos^2(\theta)}{\alpha}\right)$$

$$\gamma_8 = 4\sin\theta\left((\alpha - 1)\left(2\beta^2 + 3\sin^2(\theta)\right) - \alpha\right) - 20\beta\sin^2(\theta) + 15\alpha\left(1 - 4\cos^2(\theta)\right) + \alpha\beta$$

Table C.2 Closed-from expressions of the effective properties of general square lattices.

Effective Moduli	$C_{11} = C_{22}$	C_{33}	$A_{11} = A_{44}$	$A_{22} = A_{33}$	$A_{55} = A_{66}$
Closed form expression	$\frac{AE}{bL_{eff}}$	$\frac{24EI}{bL_{eff}^3}$	$\frac{AEL^2}{4L_{eff}b}$	$\frac{3EIL^2}{L_{eff}^3b}$	$\frac{12EIL^2}{L_{eff}^3b}$

Appendix D

Comparison of the discrete homogenization method with another method

A comparison between the results obtained in the present discrete homogenization method and the one in literature by [202] was made. A summary of the method is exposed as follows:

1. The normal force N, the transverse force T and the moment M exerted on the beam extremities are expressed in the following expressions:

$$\begin{aligned} N_E^{\varepsilon b} &= k_l^b \left(e^b . \left(\mathbf{D}_{\mathbf{E}}^{\varepsilon} - \mathbf{D}_o^{\varepsilon} \right) \right) \\ N_o^{\varepsilon b} &= -N_E^{\varepsilon b} \\ T_E^{\varepsilon b} &= k_f^b \left(e^{b\perp} . \left(\mathbf{D}_{\mathbf{E}}^{\varepsilon} - \mathbf{D}_o^{\varepsilon} \right) - \frac{l_b^{\varepsilon}}{2} \left(\phi_{\mathbf{E}}^{\varepsilon} + \phi_o^{\varepsilon} \right) \right) \\ T_O^{\varepsilon b} &= -T_E^{\varepsilon b} \end{aligned} \tag{D.1}$$

$$\begin{aligned} M_E^{\varepsilon b} &= \frac{k_f^b l_b^{\varepsilon}}{6} \left(3 . e^{b\perp} . \left(\mathbf{D}_{\mathbf{E}}^{\varepsilon} - \mathbf{D}_o^{\varepsilon} \right) + l_b^{\varepsilon} \left(2\phi_E^{\varepsilon} + \phi_o^{\varepsilon} \right) \right) . e_3 \\ M_O^{\varepsilon b} &= \frac{k_f^b l_b^{\varepsilon}}{6} \left(-3 . e^{b\perp} . \left(\mathbf{D}_{\mathbf{E}}^{\varepsilon} - \mathbf{D}_o^{\varepsilon} \right) + l_b^{\varepsilon} \left(\phi_E^{\varepsilon} + 2\phi_o^{\varepsilon} \right) \right) . e_3 \end{aligned} \tag{D.2}$$

   wherein the subscripts E and O refer to the extremity and the origin nodes of the beam respectively and the superscript b refers to the beam. ϕ and $\mathbf{D}$ are the nodal microrotation and the displacement respectively and $l_b^{\varepsilon} = \varepsilon l_b$ is the length of the beam. e^b and $e^{b\perp}$ are the unit director and the normal unit vector respectively. $k_l^b = \frac{E^b A^{\varepsilon b}}{l_b^{\varepsilon}}$ and $k_f^b = \frac{12 E^b I^{\varepsilon b}}{\left(l_b^{\varepsilon} \right)^3}$ are respectively the beam tensile and flexural rigidities, with $I^{\varepsilon b}$ being the quadratic moment of the beam and $A^{\varepsilon b}$ the cross-sectional area

2. The asymptotic expansion of the geometric and kinematic variables of each beam is written in curvilinear coordinates, and next into Cartesian coordinates [205].

3. The equilibrium expressions of the beam forces and moments are expressed in virtual power form:

$$\begin{aligned}\sum_{\nu^i\in\mathbb{Z}^2}\sum_{b\in B_R}\left(T^b\overset{\bullet}{V}+N\overset{\bullet}{U}\right)=0\\ \sum_{\nu^i\in\mathbb{Z}^2}\sum_{b\in B_R}\left(M_O^b\cdot w_O^b+M_E^b\cdot w_E^b\right)=0\end{aligned}\tag{D.3}$$

With $\overset{\bullet}{U}$, and $\overset{\bullet}{V}$, virtual velocity field components and being the virtual rotation velocity.

4. The virtual power of internal forces over the elementary cell boundary nodes is written as :

$$\sum_{b\in B_R}\left(T_E\left(\overset{\bullet}{V}_E-\overset{\bullet}{V}_O\right)+N_E\left(\overset{\bullet}{U}_E-\overset{\bullet}{U}_O\right)\right)=0\tag{D.4}$$

After developing the expressions of $\left(\overset{\bullet}{V}_E-\overset{\bullet}{V}_O\right)$ and $\left(\overset{\bullet}{U}_E-\overset{\bullet}{U}_O\right)$ using Taylor series expansion, the continuous formulation of the virtual power is found to be:

$$\lim_{\varepsilon\to 0}P=\lim_{\varepsilon\to 0}\varepsilon^2\sum_b P_e=\int_\Omega P_e\tag{D.5}$$

Eq. D.5 will include three integrals of zero-order, first and second-order of ε, leading to Cauchy stress, coupling terms and second-order hyperstress tensors, respectively.

5. Comparing with the postulated second-order continuum then leads to the expression of the virtual power of internal forces:

$$P^i=\int_\Omega\left((\sigma-S\cdot\nabla)\cdot\nabla\right)\cdot\overset{\bullet}{\mathbf{D}}\,dV=\int_\Omega\left(F^q\cdot\left(\frac{\partial\overset{\bullet}{D}}{\partial x_q}\right)-H^{pq}\cdot\left(\frac{\partial^2\overset{\bullet}{D}}{\partial x_p\partial x_q}\right)\right)dV\tag{D.6}$$

The Cauchy stress σ and the hyperstress $\mathbf{S}$ can be calculated using Eq. D.6 as

$$\begin{aligned}\sigma&=(\sigma_{ij}e_i)\otimes e_q=F^q\otimes e_q\\ \mathbf{S}&=(S_{kqp}e_k)\otimes e_q\otimes e_p=H^{pq}\otimes e_q\otimes e_p\end{aligned}\tag{D.7}$$

in which the detailed expression of F^q and H^{pq} as well as the whole method can be found in [302]. Using the following constitutive law for a second-order continuum in Eq. D.8 the effective moduli are then determined.

$$\begin{aligned}\mathbf{\Sigma}_{ij}&=\mathbf{C}_{ijkl}:\mathbf{E}_{kl}+\mathbf{B}_{ijklm}\therefore\mathbf{K}_{klm}\\ \mathbf{S}_{ijk}&=\mathbf{B}_{ijkpq}{}^{\mathbf{T}}:\mathbf{E}_{pq}+\mathbf{A}_{ijkpqr}\therefore\mathbf{K}_{pqr}\end{aligned}\tag{D.8}$$

Appendix E

Quasi-periodic enriched Cauchy stress

This subsection introduces another post-processing scheme (top-bottom scheme) of the true strain gradient approach, which shows a link between the strain $\boldsymbol{E}$ and strain gradient term $(\boldsymbol{E} \otimes \nabla_x)$ from macro-scale computations. As well, it shows that the stress will depend on both, strain and strain gradient. Considering the quasi-periodic macrodomain as a first step for the full-field computations, allows the determination of the strain $\boldsymbol{E}$ across the boundaries of the UC of the quasi-periodic domain which differs from one UC to another. This difference is captured by the strain gradient term $(\boldsymbol{E} \otimes \nabla_x)$ that must be taken into consideration when accounting for the UC boundary conditions. Consequently, we show in subsequent developments that we will reach an enriched Cauchy medium starting from a quasi-periodic macrodomain Ω_η.

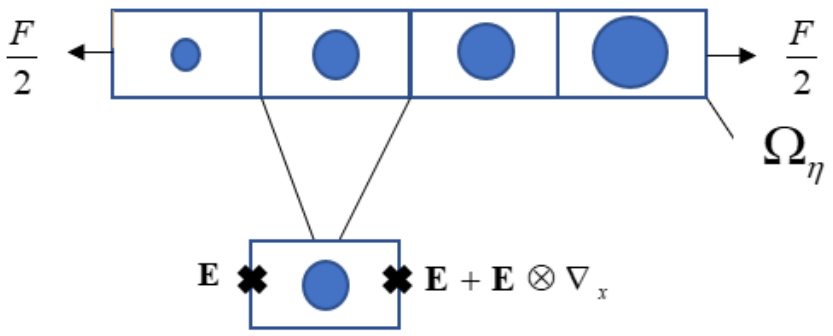

Figure E.1 Illustration showing the quasi-periodic macrodomain and an isolated UC with the macroscopic strain and strain gradient as kinematic loadings acting on it.

In order to set the stage, we evaluate the volume integral of the microscopic energy density in a

macroscopic quasi-periodic domain Ω_η:

$$\int_{\Omega_\eta} w_\mu\left(\boldsymbol{\varepsilon}\right)\,\mathrm{d}\Omega_\eta = \frac{1}{2}\int_{\Omega_\eta} \boldsymbol{\sigma} : \boldsymbol{\varepsilon}\,\mathrm{d}\Omega_\eta \tag{E.1}$$

At the macroscopic level, the strain is not constant throughout the domain, and there exists a strain gradient between two neighboring unit cells that accounts for this variation. Therefore, ($\boldsymbol{E}$, and $\boldsymbol{E}\otimes\nabla_x$) are considered to be the quasi-periodic kinematic boundary conditions applied on a UC extracted from the quasi-periodic domain. The microscopic strain is then assumed to be equal to the homogenized strain, which is an additive decomposition of the macrostrain and strain gradient (neglecting the fluctuating strain), $\boldsymbol{\varepsilon} = \boldsymbol{E} + \left(\boldsymbol{E}\otimes\nabla_x\right).\boldsymbol{y}$. Using Eq. 3.18 and inserting previous microstrain to macrostrain relation leads to the formulation of Eq. E.1 over the periodic macrodomain $\tilde{\Omega}_\eta$ as follows:

$$\int_{\Omega_\eta} w_\mu\left(\varepsilon\right)\,\mathrm{d}\Omega_\eta = \frac{1}{2}\int_{\widetilde{\Omega}_\eta} \left(\sigma : \mathbf{E} + \left(\sigma\otimes\mathbf{y}\right)\therefore\mathbf{E}\otimes\nabla_x\right)\det\left(\mathbf{A}\right)\,\mathrm{d}\widetilde{\Omega}_\eta \tag{E.2}$$

Before proceeding, a recall of the theorem mentioned in [303] will be useful in developing Eq. E.2; it states that for any $\widetilde{Y}$-periodic function Ψ, when $\eta\to 0$, the following integral relation holds:

$$\int_{\widetilde{\Omega}_\eta} \Psi\,\mathrm{d}\widetilde{\Omega}_\eta = \frac{1}{\left|\widetilde{Y}\right|}\int_{\widetilde{\Omega}}\int_{\widetilde{Y}} \Psi\,\mathrm{d}\widetilde{Y}\,\mathrm{d}\widetilde{\Omega} \tag{E.3}$$

Using Eq. 3.7, the quasi-periodic stress in Eq. E.2 can be expressed in terms of its periodic counterpart. Thus, we get a periodic function in the integral of Eq. E.2 which allows us to write, when $\eta\to 0$, according to [303] the following:

$$\begin{aligned}
&\int_{\Omega_\eta} w_\mu\left(\boldsymbol{\varepsilon}\right)\,\mathrm{d}\Omega_\eta = \frac{1}{2}\int_{\widetilde{\Omega}_\eta} \left(\left(\boldsymbol{A}^{-T}.\tilde{\boldsymbol{\sigma}}.\boldsymbol{A}^{T}\right) : \left(\boldsymbol{A}_M\boxtimes\boldsymbol{A}_M^{-T}\right) : \widetilde{\boldsymbol{E}} + \left(\left(\boldsymbol{A}^{-T}.\tilde{\boldsymbol{\sigma}}.\boldsymbol{A}^{T}\right)\otimes\boldsymbol{y}\right) : \left(\left(\boldsymbol{A}_M\boxtimes\boldsymbol{A}_M^{-T}\right) : \widetilde{\boldsymbol{E}}\right)\otimes\nabla_x\right)\det\left(\boldsymbol{A}\right)\,\mathrm{d}\widetilde{\Omega}_\eta \\
&\frac{1}{2}\int_{\widetilde{\Omega}_\eta} \left(\left(\boldsymbol{A}^{-T}.\tilde{\boldsymbol{\sigma}}.\boldsymbol{A}^{T}\right) : \left(\boldsymbol{A}_M\boxtimes\boldsymbol{A}_M^{-T}\right) : \widetilde{\boldsymbol{E}} + \left(\left(\boldsymbol{A}^{-T}.\tilde{\boldsymbol{\sigma}}.\boldsymbol{A}^{T}\right)\otimes\boldsymbol{y}\right) : \left(\left(\boldsymbol{A}_M\boxtimes\boldsymbol{A}_M^{-T}\right) : \widetilde{\boldsymbol{E}}\otimes\nabla_x\right)\right)\det\left(\boldsymbol{A}\right)\,\mathrm{d}\widetilde{\Omega}_\eta \\
&\overset{\eta\to 0}{=} \frac{1}{2}\int_{\widetilde{\Omega}} \left\langle\det\left(\boldsymbol{A}\right)\left(\boldsymbol{A}^{-T}.\tilde{\boldsymbol{\sigma}}.\boldsymbol{A}^{T}\right)\right\rangle_{\widetilde{Y}} : \left(\boldsymbol{A}_M\boxtimes\boldsymbol{A}_M^{-T}\right) : \widetilde{\boldsymbol{E}} + \left\langle\det\left(\boldsymbol{A}\right)\left(\left(\boldsymbol{A}^{-T}.\tilde{\boldsymbol{\sigma}}.\boldsymbol{A}^{T}\right)\otimes\boldsymbol{y}\right)\right\rangle_{\widetilde{Y}} : \left(\boldsymbol{A}_M\boxtimes\boldsymbol{A}_M^{-T}\right) : \widetilde{\boldsymbol{E}}\otimes\nabla_x\,\mathrm{d}\widetilde{\Omega} \\
&\overset{\eta\to 0}{=} \frac{1}{2}\int_{\widetilde{\Omega}} \left(\boldsymbol{A}_M\boxtimes\boldsymbol{A}_M^{-T}\right) : \left(\left\langle\det\left(\boldsymbol{A}\right)\left(\boldsymbol{A}^{-T}.\tilde{\boldsymbol{\sigma}}.\boldsymbol{A}^{T}\right)\right\rangle_{\widetilde{Y}} - \left\langle\det\left(\boldsymbol{A}\right)\left(\left(\boldsymbol{A}^{-T}.\tilde{\boldsymbol{\sigma}}.\boldsymbol{A}^{T}\right)\otimes\boldsymbol{y}\right)\right\rangle_{\widetilde{Y}}.\nabla_x\right) : \widetilde{\boldsymbol{E}}\,\mathrm{d}\widetilde{\Omega} \\
&\overset{\eta\to 0}{=} \frac{1}{2}\int_{\widetilde{\Omega}} \widetilde{\boldsymbol{\Sigma}}_{enrich} : \widetilde{\boldsymbol{E}}\,\mathrm{d}\widetilde{\Omega}
\end{aligned} \tag{E.4}$$

This leads to the formulation of an enriched Cauchy stress in the periodic domain $\widetilde{\boldsymbol{\Sigma}}_{enrich}$, when factoring out the macrostrain alone after integration by part:

$$\widetilde{\boldsymbol{\Sigma}}_{enrich} = \left(\boldsymbol{A}_M\boxtimes\boldsymbol{A}_M^{-T}\right) : \left(\left\langle\det\left(\boldsymbol{A}\right)\left(\boldsymbol{A}^{-T}.\tilde{\boldsymbol{\sigma}}.\boldsymbol{A}^{T}\right)\right\rangle_{\widetilde{Y}} - \left\langle\det\left(\boldsymbol{A}\right)\left(\left(\boldsymbol{A}^{-T}.\tilde{\boldsymbol{\sigma}}.\boldsymbol{A}^{T}\right)\otimes\boldsymbol{y}\right)\right\rangle_{\widetilde{Y}}.\nabla_x\right) \tag{E.5}$$

From Eq. E.4, and when $\eta\to 0$, one can move back to the macroscopic quasi-periodic domain Ω by

making a change of the macro unit cell averaging using the multiplicative factor $\det\left(\boldsymbol{A}_M^{-1}\right)$.

$$\begin{aligned}
&\text{Eq. } (E.4) \overset{\eta\to 0}{=} \frac{1}{2}\int_{\Omega} \det\left(\boldsymbol{A}_M^{-1}\right)\widetilde{\boldsymbol{\Sigma}}_{enrich} : \widetilde{\boldsymbol{E}}\ \mathrm{d}\Omega \\
&\overset{\eta\to 0}{=} \frac{1}{2}\int_{\Omega} \det\left(\boldsymbol{A}_M^{-1}\right)\widetilde{\boldsymbol{\Sigma}}_{enrich} : \left(\boldsymbol{A}_M^{-1}\boxtimes\boldsymbol{A}_M^{T}\right) : \boldsymbol{E}\ \mathrm{d}\Omega \\
&\overset{\eta\to 0}{=} \frac{1}{2}\int_{\Omega} \boldsymbol{\Sigma}_{enrich} : \boldsymbol{E}\ \mathrm{d}\Omega
\end{aligned} \tag{E.6}$$

Eq. E.6 leads to the formulation of quasi-periodic enriched Cauchy stress $\boldsymbol{\Sigma}_{enrich}$ in terms of $\widetilde{\boldsymbol{\Sigma}}_{enrich}$:

$$\boldsymbol{\Sigma}_{enrich} = \det\left(\boldsymbol{A}_M^{-1}\right)\widetilde{\boldsymbol{\Sigma}}_{enrich} : \left(\boldsymbol{A}_M^{-1}\boxtimes\boldsymbol{A}_M^{T}\right) \tag{E.7}$$

This scheme is considered as a variant of strain gradient approach in which the macro strain and macro strain gradients are linked and not treated as independent kinematic variables. This is a result of macroscopic computations in which the strain between one UC and another is accumulated from the generated strain gradient due to the microstructure grading.

Appendix F

Derivation of the expressions of piezoelectric static variables and moduli

To proceed in the determination of the piezoelectric moduli versus the macroscopic kinematic variables, the macroscopic stress and electric displacement are recalled from Eq. 4.17 and Eq. 4.18 and factorized for the macroscopic degrees of freedom $\left(\boldsymbol{E}, \boldsymbol{E_M^{elec}}\right)$ which leads to the following expressions :

$$\boldsymbol{\Sigma} = \frac{1}{2} \int_Y \left\{ \begin{array}{l} \left(\boldsymbol{E} + \boldsymbol{M}^{uE} \otimes \nabla_y : \boldsymbol{E} + \boldsymbol{M}^{uP} \otimes \nabla_y . \boldsymbol{E_M^{elec}}\right) : \boldsymbol{C} : \left(\boldsymbol{I}_4 + \boldsymbol{M}^{uE} \otimes \nabla_y\right) \\ + \left(\boldsymbol{I}_4 + \boldsymbol{M}^{uE} \otimes \nabla_y\right) : \boldsymbol{C} : \left(\boldsymbol{E} + \boldsymbol{M}^{uE} \otimes \nabla_y : \boldsymbol{E} + \boldsymbol{M}^{uP} \otimes \nabla_y . \boldsymbol{E_M^{elec}}\right) \\ - \left(\boldsymbol{E_M^{elec}} - \boldsymbol{M}^{PE}\left(\boldsymbol{y}\right) \otimes \nabla_y : \boldsymbol{E} - \boldsymbol{M}^{PP} \otimes \nabla_y . \boldsymbol{E_M^{elec}}\right) . \boldsymbol{a} . \left(-\boldsymbol{M}^{PE}\left(\boldsymbol{y}\right) \otimes \nabla_y\right) \\ - \left(-\boldsymbol{M}^{PE}\left(\boldsymbol{y}\right) \otimes \nabla_y\right) . \boldsymbol{a} . \left(\boldsymbol{E_M^{elec}} - \boldsymbol{M}^{PE} \otimes \nabla_y : \boldsymbol{E} - \boldsymbol{M}^{PP} \otimes \nabla_y . \boldsymbol{E_M^{elec}}\right) \\ -\boldsymbol{e}^T . \left(\boldsymbol{E_M^{elec}} - \boldsymbol{M}^{PE} \otimes \nabla_y : \boldsymbol{E} - \boldsymbol{M}^{PP} \otimes \nabla_y . \boldsymbol{E_M^{elec}}\right) : \left(\boldsymbol{I}_4 + \boldsymbol{M}^{uE} \otimes \nabla_y\right) \\ -\boldsymbol{e}^T . \left(-\boldsymbol{M}^{PE} \otimes \nabla_y\right) : \left(\boldsymbol{E} + \boldsymbol{M}^{uE} \otimes \nabla_y : \boldsymbol{E} + \boldsymbol{M}^{uP} \otimes \nabla_y . \boldsymbol{E_M^{elec}}\right) \\ -\boldsymbol{e} : \left(\boldsymbol{E} + \boldsymbol{M}^{uE} \otimes \nabla_y : \boldsymbol{E} + \boldsymbol{M}^{uP} \otimes \nabla_y . \boldsymbol{E_M^{elec}}\right) . \left(-\boldsymbol{M}^{PE} \otimes \nabla_y\right) \\ -\boldsymbol{e} : \left(\boldsymbol{I}_4 + \boldsymbol{M}^{uE} \otimes \nabla_y\right) . \left(\boldsymbol{E_M^{elec}} - \boldsymbol{M}^{PE} \otimes \nabla_y : \boldsymbol{E} - \boldsymbol{M}^{PP} \otimes \nabla_y . \boldsymbol{E_M^{elec}}\right) \end{array} \right\} dV_y$$

$$\boldsymbol{\Sigma} = \frac{1}{2}\int_Y \begin{pmatrix} \left(\boldsymbol{I}_4 + \boldsymbol{M}^{uE} \otimes \nabla_y\right)^T : \boldsymbol{C} : \left(\boldsymbol{I}_4 + \boldsymbol{M}^{uE} \otimes \nabla_y\right) \\ + \left(\boldsymbol{I}_4 + \boldsymbol{M}^{uE} \otimes \nabla_y\right) : \boldsymbol{C} : \left(\boldsymbol{I}_4 + \boldsymbol{M}^{uE} \otimes \nabla_y\right) \\ -\left(\boldsymbol{M}^{PE}(\boldsymbol{y}) \otimes \nabla_y\right)^T .\boldsymbol{a}. \left(\boldsymbol{M}^{PE}(\boldsymbol{y}) \otimes \nabla_y\right) \\ -\left(\boldsymbol{M}^{PE}(\boldsymbol{y}) \otimes \nabla_y\right) .\boldsymbol{a}. \left(\boldsymbol{M}^{PE}(\boldsymbol{y}) \otimes \nabla_y\right) \\ -\left(\boldsymbol{I}_4 + \boldsymbol{M}^{uE} \otimes \nabla_y\right)^T : \boldsymbol{e}^T . \left(-\boldsymbol{M}^{PE} \otimes \nabla_y\right) \\ -\boldsymbol{e}^T . \left(-\boldsymbol{M}^{PE} \otimes \nabla_y\right) : \left(\boldsymbol{I}_4 + \boldsymbol{M}^{uE} \otimes \nabla_y\right) \\ -\left(-\boldsymbol{M}^{PE} \otimes \nabla_y\right)^T .\boldsymbol{e} : \left(\boldsymbol{I}_4 + \boldsymbol{M}^{uE} \otimes \nabla_y\right) \\ -\boldsymbol{e} : \left(\boldsymbol{I}_4 + \boldsymbol{M}^{uE} \otimes \nabla_y\right) . \left(-\boldsymbol{M}^{PE} \otimes \nabla_y\right) \end{pmatrix} : \boldsymbol{E}\, dV_y$$

$$+ \frac{1}{2}\int_Y \begin{pmatrix} \left(\boldsymbol{M}^{uP} \otimes \nabla_y\right)^T : \boldsymbol{C} : \left(\boldsymbol{I}_4 + \boldsymbol{M}^{uE} \otimes \nabla_y\right) \\ + \left(\boldsymbol{I}_4 + \boldsymbol{M}^{uE} \otimes \nabla_y\right) : \boldsymbol{C} : \left(\boldsymbol{M}^{uP} \otimes \nabla_y\right) \\ -\left(\boldsymbol{I}_2 - \boldsymbol{M}^{PP} \otimes \nabla_y\right)^T .\boldsymbol{a}. \left(-\boldsymbol{M}^{PE}(\boldsymbol{y}) \otimes \nabla_y\right) - \left(-\boldsymbol{M}^{PE}(\boldsymbol{y}) \otimes \nabla_y\right) .\boldsymbol{a}. \left(\boldsymbol{I}_2 - \boldsymbol{M}^{PP} \otimes \nabla_y\right) \\ -\left(\boldsymbol{I}_4 + \boldsymbol{M}^{uE} \otimes \nabla_y\right)^T : \boldsymbol{e}^T . \left(\boldsymbol{I}_2 - \boldsymbol{M}^{PP} \otimes \nabla_y\right) \\ -\boldsymbol{e}^T . \left(-\boldsymbol{M}^{PE} \otimes \nabla_y\right) : \left(\boldsymbol{M}^{uP} \otimes \nabla_y\right) \\ -\left(-\boldsymbol{M}^{PE} \otimes \nabla_y\right)^T .\boldsymbol{e} : \left(\boldsymbol{M}^{uP} \otimes \nabla_y\right) \\ -\boldsymbol{e} : \left(\boldsymbol{I}_4 + \boldsymbol{M}^{uE} \otimes \nabla_y\right) . \left(\boldsymbol{I}_2 - \boldsymbol{M}^{PP} \otimes \nabla_y\right) \end{pmatrix} .\boldsymbol{E}_{\boldsymbol{M}}^{\boldsymbol{elec}}\, dV_y \tag{F.1}$$

$$\overline{\boldsymbol{D}} = \frac{1}{2}\int_Y \left\{ \begin{array}{l} \left(\boldsymbol{M}^{uP} \otimes \nabla_y\right) : \boldsymbol{C} : \left(\boldsymbol{E} + \boldsymbol{M}^{uE} \otimes \nabla_y : \boldsymbol{E} + \boldsymbol{M}^{uP} \otimes \nabla_y . \boldsymbol{E}_{\boldsymbol{M}}^{\boldsymbol{elec}}\right) \\ + \left(\boldsymbol{E} + \boldsymbol{M}^{uE} \otimes \nabla_y : \boldsymbol{E} + \boldsymbol{M}^{uP} \otimes \nabla_y . \boldsymbol{E}_{\boldsymbol{M}}^{\boldsymbol{elec}}\right) : \boldsymbol{C} : \left(\boldsymbol{M}^{uP} \otimes \nabla_y\right) \\ -\left(\boldsymbol{I}_2 - \boldsymbol{M}^{PP} \otimes \nabla_y\right) .\boldsymbol{a}. \left(\boldsymbol{E}_{\boldsymbol{M}}^{\boldsymbol{elec}} - \boldsymbol{M}^{PE} \otimes \nabla_y : \boldsymbol{E} - \boldsymbol{M}^{PP} \otimes \nabla_y . \boldsymbol{E}_{\boldsymbol{M}}^{\boldsymbol{elec}}\right) \\ -\left(\boldsymbol{E}_{\boldsymbol{M}}^{\boldsymbol{elec}} - \boldsymbol{M}^{PE} \otimes \nabla_y : \boldsymbol{E} - \boldsymbol{M}^{PP} \otimes \nabla_y . \boldsymbol{E}_{\boldsymbol{M}}^{\boldsymbol{elec}}\right) .\boldsymbol{a}. \left(\boldsymbol{I}_2 - \boldsymbol{M}^{PP} \otimes \nabla_y\right) \\ -\boldsymbol{e}^T . \left(\boldsymbol{E}_{\boldsymbol{M}}^{\boldsymbol{elec}} - \boldsymbol{M}^{PE} \otimes \nabla_y : \boldsymbol{E} - \boldsymbol{M}^{PP} \otimes \nabla_y . \boldsymbol{E}_{\boldsymbol{M}}^{\boldsymbol{elec}}\right) : \left(\boldsymbol{M}^{uP} \otimes \nabla_y\right) \\ -\boldsymbol{e}^T . \left(\boldsymbol{I}_2 - \boldsymbol{M}^{PP} \otimes \nabla_y\right) : \left(\boldsymbol{E} + \boldsymbol{M}^{uE} \otimes \nabla_y : \boldsymbol{E} + \boldsymbol{M}^{uP} \otimes \nabla_y . \boldsymbol{E}_{\boldsymbol{M}}^{\boldsymbol{elec}}\right) \\ -\boldsymbol{e} : \left(\boldsymbol{E} + \boldsymbol{M}^{uE} \otimes \nabla_y : \boldsymbol{E} + \boldsymbol{M}^{uP} \otimes \nabla_y . \boldsymbol{E}_{\boldsymbol{M}}^{\boldsymbol{elec}}\right) . \left(\boldsymbol{I}_2 - \boldsymbol{M}^{PP} \otimes \nabla_y\right) \\ -\boldsymbol{e} : \left(\boldsymbol{M}^{uP} \otimes \nabla_y\right) . \left(\boldsymbol{E}_{\boldsymbol{M}}^{\boldsymbol{elec}} - \boldsymbol{M}^{PE} \otimes \nabla_y : \boldsymbol{E} - \boldsymbol{M}^{PP} \otimes \nabla_y . \boldsymbol{E}_{\boldsymbol{M}}^{\boldsymbol{elec}}\right) \end{array} \right\} dV_y$$

$$\overline{\boldsymbol{D}} = \frac{1}{2}\int_Y \begin{pmatrix} \left(\boldsymbol{M}^{uP}\otimes\nabla_y\right) : \boldsymbol{C}\,(\boldsymbol{y}) : (\boldsymbol{I}_4 + \boldsymbol{M}^{uE}\otimes\nabla_y) + (\boldsymbol{I}_4 + \boldsymbol{M}^{uE}\otimes\nabla_y)^T : \boldsymbol{C} : \\ -\left(\boldsymbol{I}_2 - \boldsymbol{M}^{PP}\otimes\nabla_y\right).\boldsymbol{a}.\left(-\boldsymbol{M}^{PE}\otimes\nabla_y\right) - \left(-\boldsymbol{M}^{PE}\otimes\nabla_y\right)^T.\boldsymbol{a}.\left(\boldsymbol{I}_2 - \right. \\ -+\left(\boldsymbol{M}^{uP}\otimes\nabla_y\right)^T : \boldsymbol{e}^T.\left(-\boldsymbol{M}^{PE}\otimes\nabla_y\right) \\ -\boldsymbol{e}^T.\left(\boldsymbol{I}_2 - \boldsymbol{M}^{PP}\otimes\nabla_y\right) : \left(\boldsymbol{I}_4 + \boldsymbol{M}^{uE}\otimes\nabla_y\right) \\ -\left(\boldsymbol{I}_2 - \boldsymbol{M}^{PP}\otimes\nabla_y\right)^T.\boldsymbol{e} : \left(\boldsymbol{I}_4 + \boldsymbol{M}^{uE}\otimes\nabla_y\right) \\ -\boldsymbol{e}\left(\boldsymbol{M}^{uP}\otimes\nabla_y\right).\left(-\boldsymbol{M}^{PE}\otimes\nabla_y\right) \end{pmatrix}$$

$$+\frac{1}{2}\int_Y \begin{pmatrix} \left(\boldsymbol{M}^{uP}\otimes\nabla_y\right)\boldsymbol{C} : \left(\boldsymbol{M}^{uP}\otimes\nabla_y\right) + \left(\boldsymbol{M}^{uP}\otimes\nabla_y\right)^T : \boldsymbol{C} : \left(\boldsymbol{M}^{uP}\otimes\nabla_y\right) \\ -\left(\boldsymbol{I}_2 - \boldsymbol{M}^{PP}\otimes\nabla_y\right).\boldsymbol{a}.\left(\boldsymbol{I}_2 - \boldsymbol{M}^{PP}\otimes\nabla_y\right) - \left(\boldsymbol{I}_2 - \boldsymbol{M}^{PP}\otimes\nabla_y\right)^T.\boldsymbol{a}.\left(\boldsymbol{I}_2 - \boldsymbol{M}^{PP}\otimes\nabla_y\right) \\ -\left(\boldsymbol{M}^{uP}\otimes\nabla_y\right)^T : \boldsymbol{e}^T.\left(\boldsymbol{I}_2 - \boldsymbol{M}^{PP}\otimes\nabla_y\right) \\ -\boldsymbol{e}^T.\left(\boldsymbol{I}_2 - \boldsymbol{M}^{PP}\otimes\nabla_y\right) : \left(\boldsymbol{M}^{uP}\otimes\nabla_y\right) \\ -\left(\boldsymbol{I}_2 - \boldsymbol{M}^{PP}\otimes\nabla_y\right)^T.\boldsymbol{e} : \left(\boldsymbol{M}^{uP}\otimes\nabla_y\right) \\ -\boldsymbol{e} : \left(\boldsymbol{M}^{uP}\otimes\nabla_y\right).\left(\boldsymbol{I}_2 - \boldsymbol{M}^{PP}\otimes\nabla_y\right) \end{pmatrix} .\boldsymbol{E}_{\boldsymbol{M}}^{\boldsymbol{elec}}\, dV_y \tag{F.2}$$

By comparing Eq. F.1 and Eq. F.2 with the macroscopic constitutive law (Eq. 4.19), we obtain the expressions of $\boldsymbol{C}^{\text{hom}}$, $\boldsymbol{d}^{*,\text{hom}}$, and $\boldsymbol{a}^{\text{hom}}$ as follows:

$$\boldsymbol{C}^{\text{hom}} := \frac{1}{2}\int_Y \begin{pmatrix} \left(\boldsymbol{I}_4 + \boldsymbol{M}^{uE}\otimes\nabla_y\right)^T : \boldsymbol{C} : \left(\boldsymbol{I}_4 + \boldsymbol{M}^{uE}\otimes\nabla_y\right) + \left(\boldsymbol{I}_4 + \boldsymbol{M}^{uE}\otimes\nabla_y\right) : \boldsymbol{C} : \left(\boldsymbol{I}_4 + \boldsymbol{M}^{uE}\otimes\nabla_y\right) \\ -\left(\boldsymbol{M}^{PE}(\boldsymbol{y})\otimes\nabla_y\right)^T.\boldsymbol{a}.\left(\boldsymbol{M}^{PE}(\boldsymbol{y})\otimes\nabla_y\right) - \left(\boldsymbol{M}^{PE}(\boldsymbol{y})\otimes\nabla_y\right).\boldsymbol{a}.\left(\boldsymbol{M}^{PE}(\boldsymbol{y})\otimes\nabla_y\right) \\ -\left(\boldsymbol{I}_4 + \boldsymbol{M}^{uE}\otimes\nabla_y\right)^T : \boldsymbol{e}^T.\left(-\boldsymbol{M}^{PE}\otimes\nabla_y\right) - \boldsymbol{e}^T.\left(-\boldsymbol{M}^{PE}\otimes\nabla_y\right) : \left(\boldsymbol{I}_4 + \boldsymbol{M}^{uE}\otimes\nabla_y\right) \\ -\left(-\boldsymbol{M}^{PE}\otimes\nabla_y\right)^T.\boldsymbol{e} : \left(\boldsymbol{I}_4 + \boldsymbol{M}^{uE}\otimes\nabla_y\right) - \boldsymbol{e} : \left(\boldsymbol{I}_4 + \boldsymbol{M}^{uE}\otimes\nabla_y\right).\left(-\boldsymbol{M}^{PE}\otimes\nabla_y\right) \end{pmatrix} dV_y$$

$$\boldsymbol{e}^{\text{hom}} = \frac{1}{2}\int_Y \begin{pmatrix} \left(\boldsymbol{M}^{uP}\otimes\nabla_y\right) : \boldsymbol{C}\,(\boldsymbol{y}) : (\boldsymbol{I}_4 + \boldsymbol{M}^{uE}\otimes\nabla_y) + (\boldsymbol{I}_4 + \boldsymbol{M}^{uE}\otimes\nabla_y)^T : \boldsymbol{C} : \left(\boldsymbol{M}^{uP}\otimes\nabla_y\right) \\ -\left(\boldsymbol{I}_2 - \boldsymbol{M}^{PP}\otimes\nabla_y\right).\boldsymbol{a}.\left(-\boldsymbol{M}^{PE}\otimes\nabla_y\right) - \left(-\boldsymbol{M}^{PE}\otimes\nabla_y\right)^T.\boldsymbol{a}.\left(\boldsymbol{I}_2 - \boldsymbol{M}^{PP}\otimes\nabla_y\right) \\ -\left(\boldsymbol{M}^{uP}\otimes\nabla_y\right)^T : \boldsymbol{e}^T.\left(-\boldsymbol{M}^{PE}\otimes\nabla_y\right) \\ -\boldsymbol{e}^T.\left(\boldsymbol{I}_2 - \boldsymbol{M}^{PP}\otimes\nabla_y\right) : \left(\boldsymbol{I}_4 + \boldsymbol{M}^{uE}\otimes\nabla_y\right) \\ -\left(\boldsymbol{I}_2 - \boldsymbol{M}^{PP}\otimes\nabla_y\right)^T.\boldsymbol{e} : \left(\boldsymbol{I}_4 + \boldsymbol{M}^{uE}\otimes\nabla_y\right) \\ -\boldsymbol{e} : \left(\boldsymbol{M}^{uP}\otimes\nabla_y\right).\left(-\boldsymbol{M}^{PE}\otimes\nabla_y\right) \end{pmatrix} dV_y$$

$$\boldsymbol{a}^{\text{hom}} := \frac{1}{2}\int_Y \begin{pmatrix} \left(\boldsymbol{M}^{uP}\otimes\nabla_y\right)\boldsymbol{C} : \left(\boldsymbol{M}^{uP}\otimes\nabla_y\right) + \left(\boldsymbol{M}^{uP}\otimes\nabla_y\right)^T : \boldsymbol{C} : \left(\boldsymbol{M}^{uP}\otimes\nabla_y\right) \\ -\left(\boldsymbol{I}_2 - \boldsymbol{M}^{PP}\otimes\nabla_y\right).\boldsymbol{a}.\left(\boldsymbol{I}_2 - \boldsymbol{M}^{PP}\otimes\nabla_y\right) - \left(\boldsymbol{I}_2 - \boldsymbol{M}^{PP}\otimes\nabla_y\right)^T.\boldsymbol{a}.\left(\boldsymbol{I}_2 - \boldsymbol{M}^{PP}\otimes\nabla_y\right) \\ -\left(\boldsymbol{M}^{uP}\otimes\nabla_y\right)^T : \boldsymbol{e}^T.\left(\boldsymbol{I}_2 - \boldsymbol{M}^{PP}\otimes\nabla_y\right) - \boldsymbol{e}^T.\left(\boldsymbol{I}_2 - \boldsymbol{M}^{PP}\otimes\nabla_y\right) : \left(\boldsymbol{M}^{uP}\otimes\nabla_y\right) \\ -\left(\boldsymbol{I}_2 - \boldsymbol{M}^{PP}\otimes\nabla_y\right)^T.\boldsymbol{e} : \left(\boldsymbol{M}^{uP}\otimes\nabla_y\right) - \boldsymbol{e} : \left(\boldsymbol{M}^{uP}\otimes\nabla_y\right).\left(\boldsymbol{I}_2 - \boldsymbol{M}^{PP}\otimes\nabla_y\right) \end{pmatrix} dV_y \tag{F.3}$$

On the other hand these homogenized tensors can be written in terms of more compact localization operators (the strain localization operators $\left(\boldsymbol{Z^{uE}}, \boldsymbol{Z^{uP}}\right)$ and electric field localization operators $\left(\boldsymbol{Z^{PE}}, \boldsymbol{Z^{PP}}\right)$ where :

$$\left|\begin{array}{rl}
\boldsymbol{u}(\boldsymbol{y}) \otimes \nabla_y = & \left(\boldsymbol{u}^{\hom}(\boldsymbol{y}) + \tilde{\boldsymbol{u}}(\boldsymbol{y})\right) \otimes \nabla_y := \boldsymbol{E}(\boldsymbol{x}) + \boldsymbol{M}^{uE}(\boldsymbol{y}) \otimes \nabla_y : \boldsymbol{E}(\boldsymbol{x}) + \boldsymbol{M}^{uP}(\boldsymbol{y}) \otimes \nabla_y . \boldsymbol{E_M^{elec}}(\boldsymbol{x}) \\
& \equiv \boldsymbol{Z}^{uE}(\boldsymbol{y}) : \boldsymbol{E}(\boldsymbol{x}) + \boldsymbol{Z}^{uP}(\boldsymbol{y}) . \boldsymbol{E_M^{elec}}(\boldsymbol{x}) \\
\boldsymbol{Z}^{uE}(\boldsymbol{y}) = & \boldsymbol{I}_4 + \boldsymbol{M}^{uE} \otimes \nabla_y \\
\boldsymbol{Z}^{uP}(\boldsymbol{y}) = & \boldsymbol{M}^{uP} \otimes \nabla_y \\
\boldsymbol{E}^{elec} = & \boldsymbol{E_M^{elec}} + \tilde{\boldsymbol{E}}^{elec}(\boldsymbol{y}) = \boldsymbol{E_M^{elec}} - \boldsymbol{M}^{PE}(\boldsymbol{y}) \otimes \nabla_y : \boldsymbol{E}(\boldsymbol{x}) - \boldsymbol{M}^{PP}(\boldsymbol{y}) \otimes \nabla_y . \boldsymbol{E_M^{elec}}(\boldsymbol{x}) \\
& \equiv \boldsymbol{Z^{PE}}(\boldsymbol{y}) : \boldsymbol{E}(\boldsymbol{x}) + \boldsymbol{Z^{PP}}(\boldsymbol{y}) . \boldsymbol{E_M^{elec}}(\boldsymbol{x}) \\
\boldsymbol{Z^{PE}}(y) = & -\boldsymbol{M}^{PE}(\boldsymbol{y}) \otimes \nabla_y \\
\boldsymbol{Z^{PP}}(\boldsymbol{y}) = & \boldsymbol{I}_2 - \boldsymbol{M}^{PP}(\boldsymbol{y}) \otimes \nabla_y
\end{array}\right. \tag{F.4}$$

These expressions lead to the functional to be minimized, having the form of the following Lagrangian function:

$$\rightarrow L\left[\tilde{\boldsymbol{u}}, \tilde{\phi}\right] := \frac{1}{2} \int_Y \left\{ \begin{array}{l}
\left(\boldsymbol{Z^{uE}} : \boldsymbol{E} + \boldsymbol{Z^{uP}} . \boldsymbol{E_M^{elec}}\right) : \boldsymbol{C} : \left(\boldsymbol{Z}^{uE} : \boldsymbol{E} + \boldsymbol{Z}^{uP} . \boldsymbol{E_M^{elec}}\right) \\
- \left(\boldsymbol{Z^{PE}} : \boldsymbol{E} + \boldsymbol{Z^{PP}} . \boldsymbol{E_M^{elec}}\right) . \boldsymbol{a} . \left(\boldsymbol{Z^{PE}} : \boldsymbol{E} + \boldsymbol{Z^{PP}} . \boldsymbol{E_M^{elec}}\right) \\
- \boldsymbol{e}^T . \left(\boldsymbol{Z^{PE}} : \boldsymbol{E} + \boldsymbol{Z^{PP}} . \boldsymbol{E_M^{elec}}\right) : \left(\boldsymbol{Z^{uE}} : \boldsymbol{E} + \boldsymbol{Z^{uP}} . \boldsymbol{E_M^{elec}}\right) \\
- \boldsymbol{e} : \left(\boldsymbol{Z^{uE}} : \boldsymbol{E} + \boldsymbol{Z^{uP}} . \boldsymbol{E_M^{elec}}\right) . \left(\boldsymbol{Z^{PE}} : \boldsymbol{E} + \boldsymbol{Z^{PP}} . \boldsymbol{E_M^{elec}}\right)
\end{array} \right\} dV_y \tag{F.5}$$

which in turn leads to the formulation of stress and electric displacement versus the strain and electric

field localization operators as follows:

$$
\begin{aligned}
\boldsymbol{\Sigma} &= \underset{\tilde{\boldsymbol{u}},\tilde{\phi}\in H^1_{per}(Y)}{Min} \frac{\partial L\left[\tilde{\boldsymbol{u}},\tilde{\phi}\right]}{\partial E} \\
&= \frac{1}{2}\int_Y \left\{ \begin{array}{l}
\left(\boldsymbol{Z^{uE}}\right) : \boldsymbol{C} : \left(\boldsymbol{Z^{uE}} : \boldsymbol{E} + \boldsymbol{Z^{uP}}.\boldsymbol{E_M^{elec}}\right) + \left(\boldsymbol{Z^{uE}} : \boldsymbol{E} + \boldsymbol{Z^{uP}}.\boldsymbol{E_M^{elec}}\right) : \boldsymbol{C} : \left(\boldsymbol{Z^{uE}}\right) \\
-\left(\boldsymbol{Z^{PE}}\right).\boldsymbol{a}.\left(\boldsymbol{Z^{PE}} : \boldsymbol{E} + \boldsymbol{Z^{PP}}.\boldsymbol{E_M^{elec}}\right) - \left(\boldsymbol{Z^{PE}} : \boldsymbol{E} + \boldsymbol{Z^{PP}}.\boldsymbol{E_M^{elec}}\right).\boldsymbol{a}.\left(\boldsymbol{Z^{PE}}\right) \\
-\boldsymbol{e}^T.\left(\boldsymbol{Z^{PE}} : \boldsymbol{E} + \boldsymbol{Z^{PP}}.\boldsymbol{E_M^{elec}}\right) : \left(\boldsymbol{Z^{uE}}\right) - \boldsymbol{e}^T.\left(\boldsymbol{Z^{PE}}\right) : \left(\boldsymbol{Z^{uE}} : \boldsymbol{E} + \boldsymbol{Z^{uP}}.\boldsymbol{E_M^{elec}}\right) \\
-\boldsymbol{e} : \left(\boldsymbol{Z^{uE}} : \boldsymbol{E} + \boldsymbol{Z^{uP}}.\boldsymbol{E_M^{elec}}\right).\left(\boldsymbol{Z^{PE}}\right) - \boldsymbol{e} : \left(\boldsymbol{Z^{uE}}\right).\left(\boldsymbol{Z^{PE}} : \boldsymbol{E} + \boldsymbol{Z^{PP}}.\boldsymbol{E_M^{elec}}\right)
\end{array} \right\} dV_y \\
&= \frac{1}{2}\left(\int_Y \left\{ \begin{array}{l}
\left(\boldsymbol{Z^{uE}}\right) : \boldsymbol{C} : \boldsymbol{Z^{uE}} + \left(\boldsymbol{Z^{uE}}\right)^{\boldsymbol{T}} : \boldsymbol{C} : \boldsymbol{Z^{uE}} \\
-\left(\boldsymbol{Z^{PE}}\right).\boldsymbol{a}.\boldsymbol{Z^{PE}} - \left(\boldsymbol{Z^{PE}}\right)^T.\boldsymbol{a}.\boldsymbol{Z^{PE}} \\
-\left(\boldsymbol{Z^{uE}}\right)^T : \boldsymbol{e}^T.\left(\boldsymbol{Z^{PE}}\right) - \boldsymbol{e}^T.\left(\boldsymbol{Z^{PE}}\right) : \left(\boldsymbol{Z^{uE}}\right) \\
-\left(\boldsymbol{Z^{PE}}\right)^T.\boldsymbol{e} : \left(\boldsymbol{Z^{uE}}\right) - \boldsymbol{e} : \left(\boldsymbol{Z^{uE}}\right).\left(\boldsymbol{Z^{PE}}\right)
\end{array} \right\} dV_y \right) : \boldsymbol{E} \\
&+ \frac{1}{2}\left(\int_Y \left\{ \begin{array}{l}
\left(\boldsymbol{Z^{uE}}\right) : \boldsymbol{C} : \left(\boldsymbol{Z^{uP}}\right) + \left(\boldsymbol{Z^{uP}}\right)^T : \boldsymbol{C} : \left(\boldsymbol{Z^{uE}}\right) \\
-\left(\boldsymbol{Z^{PE}}\right).\boldsymbol{a}.\left(\boldsymbol{Z^{PP}}\right) - \left(\boldsymbol{Z^{PP}}\right)^T.\boldsymbol{a}.\left(\boldsymbol{Z^{PE}}\right) \\
-\left(\boldsymbol{Z^{uE}}\right)^T : \boldsymbol{e}^T.\left(\boldsymbol{Z^{PP}}\right) - \boldsymbol{e}^T.\left(\boldsymbol{Z^{PE}}\right) : \left(\boldsymbol{Z^{uP}}\right) \\
-\left(\boldsymbol{Z^{PE}}\right)^T.\boldsymbol{e} : \left(\boldsymbol{Z^{uP}}\right) - \boldsymbol{e} : \left(\boldsymbol{Z^{uE}}\right).\left(\boldsymbol{Z^{PP}}\right)
\end{array} \right\} dV_y \right) . \boldsymbol{E_M^{elec}}
\end{aligned}
\tag{F.6}
$$

$$
\begin{aligned}
\overline{\boldsymbol{D}} &= \underset{\tilde{\boldsymbol{u}},\tilde{\phi}\in H^1_{per}(Y)}{Min} \frac{\partial L\left[\tilde{\boldsymbol{u}},\tilde{\phi}\right]}{\partial \boldsymbol{E_M^{elec}}} \\
&= \frac{1}{2}\int_Y \left\{ \begin{array}{l}
\left(\boldsymbol{Z^{uP}}\right) : \boldsymbol{C} : \left(\boldsymbol{Z}^{uE} : \boldsymbol{E} + \boldsymbol{Z}^{uP}.\boldsymbol{E_M^{elec}}\right) + \left(\boldsymbol{Z^{uE}} : \boldsymbol{E} + \boldsymbol{Z^{uP}}.\boldsymbol{E_M^{elec}}\right) : C\left(\boldsymbol{y}\right) : \left(\boldsymbol{Z}^{uP}\right) \\
-\left(\boldsymbol{Z^{PP}}\right).\boldsymbol{a}.\left(\boldsymbol{Z^{PE}} : \boldsymbol{E} + \boldsymbol{Z^{PP}}.\boldsymbol{E_M^{elec}}\right) - \left(\boldsymbol{Z^{PE}} : \boldsymbol{E} + \boldsymbol{Z^{PP}}.\boldsymbol{E_M^{elec}}\right).\boldsymbol{a}.\left(\boldsymbol{Z^{PP}}\right) \\
-\boldsymbol{e}^T.\left(\boldsymbol{Z^{PE}} : \boldsymbol{E} + \boldsymbol{Z^{PP}}.\boldsymbol{E_M^{elec}}\right) : \left(\boldsymbol{Z^{uP}}\right) - \boldsymbol{e}^T.\left(\boldsymbol{Z^{PP}}\right) : \left(\boldsymbol{Z^{uE}} : \boldsymbol{E} + \boldsymbol{Z^{uP}}.\boldsymbol{E_M^{elec}}\right) \\
-\boldsymbol{e} : \left(\boldsymbol{Z^{uE}} : \boldsymbol{E} + \boldsymbol{Z^{uP}}.\boldsymbol{E_M^{elec}}\right).\left(\boldsymbol{Z^{PP}}\right) - \boldsymbol{e} : \left(\boldsymbol{Z^{uP}}\right).\left(\boldsymbol{Z^{PE}} : \boldsymbol{E} + \boldsymbol{Z^{PP}}.\boldsymbol{E_M^{elec}}\right)
\end{array} \right\} dV_y \\
&= \frac{1}{2}\left(\int_Y \left\{ \begin{array}{l}
\left(\boldsymbol{Z^{uP}}\right) : C\left(\boldsymbol{y}\right) : \left(\boldsymbol{Z}^{uE}\right) + \left(\boldsymbol{Z^{uE}}\right)^T : C\left(\boldsymbol{y}\right) : \left(\boldsymbol{Z}^{uP}\right) \\
-\left(\boldsymbol{Z^{PP}}\right).\boldsymbol{a}.\left(\boldsymbol{Z^{PE}}\right) - \left(\boldsymbol{Z^{PE}}\right)^T.\boldsymbol{a}.\left(\boldsymbol{Z^{PP}}\right) \\
-\left(\boldsymbol{Z^{uP}}\right)^T : \boldsymbol{e}^T.\left(\boldsymbol{Z^{PE}}\right) - \boldsymbol{e}^T.\left(\boldsymbol{Z^{PP}}\right) : \left(\boldsymbol{Z^{uE}}\right) \\
-\left(\boldsymbol{Z^{PP}}\right)^T.\boldsymbol{e} : \left(\boldsymbol{Z^{uE}}\right) - \boldsymbol{e} : \left(\boldsymbol{Z^{uP}}\right).\left(\boldsymbol{Z^{PE}}\right)
\end{array} \right\} dV_y \right) : \boldsymbol{E} \\
&+ \frac{1}{2}\left(\int_Y \left\{ \begin{array}{l}
\left(\boldsymbol{Z^{uP}}\right) : C\left(\boldsymbol{y}\right) : \left(\boldsymbol{Z}^{uP}\right) + \left(\boldsymbol{Z^{uP}}\right)^T : C\left(\boldsymbol{y}\right) : \left(\boldsymbol{Z}^{uP}\right) \\
-\left(\boldsymbol{Z^{PP}}\right).\boldsymbol{a}.\left(\boldsymbol{Z^{PP}}\right) - \left(\boldsymbol{Z^{PP}}\right)^T.\boldsymbol{a}.\left(\boldsymbol{Z^{PP}}\right) \\
-\left(\boldsymbol{Z^{uP}}\right)^T : \boldsymbol{e}^T.\left(\boldsymbol{Z^{PP}}\right) - \boldsymbol{e}^T.\left(\boldsymbol{Z^{PP}}\right) : \left(\boldsymbol{Z^{uP}}\right) \\
-\left(\boldsymbol{Z^{PP}}\right)^T.\boldsymbol{e} : \left(\boldsymbol{Z^{uP}}\right) - \boldsymbol{e} : \left(\boldsymbol{Z^{uP}}\right).\left(\boldsymbol{Z^{PP}}\right)
\end{array} \right\} dV_y \right) . \boldsymbol{E_M^{elec}}
\end{aligned}
\tag{F.7}
$$

F.1 Derivation of the expressions of flexoelectric moduli

When extending toward a flexoelectric media, the Lagrangian functional of the displacement and electric potential fluctuations after substituting the compact localization operators $(\boldsymbol{Z}^{uE}(\boldsymbol{y}), \boldsymbol{Z}^{uk}(\boldsymbol{y}), \boldsymbol{Z}^{uP}(\boldsymbol{y}), \boldsymbol{Z}^{uG_p}(\boldsymbol{y}), \boldsymbol{Z}^{Pk}(\boldsymbol{y}), \boldsymbol{Z}^{PG_P}(\boldsymbol{y}), \boldsymbol{Z}^{PE}(\boldsymbol{y}), \boldsymbol{Z}^{PP}(\boldsymbol{y}))$ is as follows:

$$
\begin{aligned}
L\left[\tilde{\boldsymbol{u}}, \tilde{\phi}\right] &:= \frac{1}{2}\int_Y \left\{\boldsymbol{\varepsilon} : \boldsymbol{C} : \boldsymbol{\varepsilon} - \boldsymbol{E}_{\boldsymbol{M}}^{\boldsymbol{elec}} . \boldsymbol{a} . \boldsymbol{E}_{\boldsymbol{M}}^{\boldsymbol{elec}} - \boldsymbol{e}^T . \boldsymbol{E}_{\boldsymbol{M}}^{\boldsymbol{elec}} : \boldsymbol{\varepsilon} - \boldsymbol{e} : \boldsymbol{\varepsilon} . \boldsymbol{E}_{\boldsymbol{M}}^{\boldsymbol{elec}}\right\} dV_y \\
&= \frac{1}{2}\int_Y \left\{\begin{array}{l}
\left(\boldsymbol{Z}^{\boldsymbol{uE}}(\boldsymbol{y}) : \boldsymbol{E}(\boldsymbol{x}) + \boldsymbol{Z}^{\boldsymbol{uk}}(\boldsymbol{y}) \therefore \boldsymbol{K}(\boldsymbol{x}) + \boldsymbol{Z}^{\boldsymbol{uP}}(\boldsymbol{y}) . \boldsymbol{E}_{\boldsymbol{M}}^{\boldsymbol{elec}}(\boldsymbol{x}) + \boldsymbol{Z}^{\boldsymbol{uG}_P}(\boldsymbol{y}) : \boldsymbol{G}_p(\boldsymbol{x})\right) : \boldsymbol{C}(\boldsymbol{y}) \\
: \left(\boldsymbol{Z}^{\boldsymbol{uE}}(\boldsymbol{y}) : \boldsymbol{E}(\boldsymbol{x}) + \boldsymbol{Z}^{\boldsymbol{uk}}(\boldsymbol{y}) \therefore \boldsymbol{K}(\boldsymbol{x}) + \boldsymbol{Z}^{\boldsymbol{uP}}(\boldsymbol{y}) . \boldsymbol{E}_{\boldsymbol{M}}^{\boldsymbol{elec}}(\boldsymbol{x}) + \boldsymbol{Z}^{\boldsymbol{uG}_P}(\boldsymbol{y}) : \boldsymbol{G}_p(\boldsymbol{x})\right) \\
- \left(\boldsymbol{Z}^{\boldsymbol{PP}}(\boldsymbol{y}) . \boldsymbol{E}_{\boldsymbol{M}}^{\boldsymbol{elec}}(\boldsymbol{x}) + \boldsymbol{Z}^{\boldsymbol{PE}}(\boldsymbol{y}) : \boldsymbol{E}(\boldsymbol{x}) + \boldsymbol{Z}^{\boldsymbol{PK}}(\boldsymbol{y}) \therefore \boldsymbol{K}(\boldsymbol{x}) + \boldsymbol{Z}^{\boldsymbol{PG}_P}(\boldsymbol{y}) : \boldsymbol{G}_p(\boldsymbol{x})\right) . \boldsymbol{a} \\
. \left(\boldsymbol{Z}^{\boldsymbol{PP}}(\boldsymbol{y}) . \boldsymbol{E}_{\boldsymbol{M}}^{\boldsymbol{elec}}(\boldsymbol{x}) + \boldsymbol{Z}^{\boldsymbol{PE}}(\boldsymbol{y}) : \boldsymbol{E}(\boldsymbol{x}) + \boldsymbol{Z}^{\boldsymbol{PK}}(\boldsymbol{y}) \therefore \boldsymbol{K}(\boldsymbol{x}) + \boldsymbol{Z}^{\boldsymbol{PG}_P}(\boldsymbol{y}) : \boldsymbol{G}_p(\boldsymbol{x})\right) \\
- \boldsymbol{e}^T . \left(\boldsymbol{Z}^{\boldsymbol{PP}}(\boldsymbol{y}) . \boldsymbol{E}_{\boldsymbol{M}}^{\boldsymbol{elec}}(\boldsymbol{x}) + \boldsymbol{Z}^{\boldsymbol{PE}}(\boldsymbol{y}) : \boldsymbol{E}(\boldsymbol{x}) + \boldsymbol{Z}^{\boldsymbol{PK}}(\boldsymbol{y}) \therefore \boldsymbol{K}(\boldsymbol{x}) + \boldsymbol{Z}^{\boldsymbol{PG}_P}(\boldsymbol{y}) : \boldsymbol{G}_p(\boldsymbol{x})\right) \\
: \left(\boldsymbol{Z}^{\boldsymbol{uE}}(\boldsymbol{y}) : \boldsymbol{E}(\boldsymbol{x}) + \boldsymbol{Z}^{\boldsymbol{uk}}(\boldsymbol{y}) \therefore \boldsymbol{K}(\boldsymbol{x}) + \boldsymbol{Z}^{\boldsymbol{uP}}(\boldsymbol{y}) . \boldsymbol{E}_{\boldsymbol{M}}^{\boldsymbol{elec}}(\boldsymbol{x}) + \boldsymbol{Z}^{\boldsymbol{uG}_P}(\boldsymbol{y}) : \boldsymbol{G}_p(\boldsymbol{x})\right) \\
- \boldsymbol{e} : \left(\boldsymbol{Z}^{\boldsymbol{uE}}(\boldsymbol{y}) : \boldsymbol{E}(\boldsymbol{x}) + \boldsymbol{Z}^{\boldsymbol{uk}}(\boldsymbol{y}) \therefore \boldsymbol{K}(\boldsymbol{x}) + \boldsymbol{Z}^{\boldsymbol{uP}}(\boldsymbol{y}) . \boldsymbol{E}_{\boldsymbol{M}}^{\boldsymbol{elec}}(\boldsymbol{x}) + \boldsymbol{Z}^{\boldsymbol{uG}_P}(\boldsymbol{y}) : \boldsymbol{G}_p(\boldsymbol{x})\right) \\
. \left(\boldsymbol{Z}^{\boldsymbol{PP}}(\boldsymbol{y}) . \boldsymbol{E}_{\boldsymbol{M}}^{\boldsymbol{elec}}(\boldsymbol{x}) + \boldsymbol{Z}^{\boldsymbol{PE}}(\boldsymbol{y}) : \boldsymbol{E}(\boldsymbol{x}) + \boldsymbol{Z}^{\boldsymbol{PK}}(\boldsymbol{y}) \therefore \boldsymbol{K}(\boldsymbol{x}) + \boldsymbol{Z}^{\boldsymbol{PG}_P}(\boldsymbol{y}) : \boldsymbol{G}_p(\boldsymbol{x})\right)
\end{array}\right\} dV_y
\end{aligned}
\tag{F.8}
$$

The flexoelectric constitutive law is obtained by taking the partial derivatives of the minimum macroscopic energy with respect to $\boldsymbol{E}, \boldsymbol{E}_{\boldsymbol{M}}^{\boldsymbol{elec}}, \boldsymbol{K}, \boldsymbol{G}_P$ to determine the stress, electric displacement, hyperstress, and higher gradient electric displacement respectively as follows:

$$
\begin{aligned}
\boldsymbol{\Sigma} &= \frac{\partial}{\partial \boldsymbol{E}}\left(\underset{\tilde{\boldsymbol{u}}, \tilde{\phi} \in H^1_{per}(Y)}{Min} L\left[\tilde{\boldsymbol{u}}, \tilde{\phi}\right]\right) \\
&\equiv \underset{\tilde{\boldsymbol{u}}, \tilde{\phi} \in H^1_{per}(Y)}{Min} \frac{\partial L\left[\tilde{\boldsymbol{u}}, \tilde{\phi}\right]}{\partial \boldsymbol{E}} = \frac{1}{2}\int_Y \left\{\begin{array}{l}
2\left(\boldsymbol{Z}^{\boldsymbol{uE}} : \boldsymbol{E} + \boldsymbol{Z}^{\boldsymbol{uk}} \therefore \boldsymbol{K} + \boldsymbol{Z}^{\boldsymbol{uP}} . \boldsymbol{E}_{\boldsymbol{M}}^{\boldsymbol{elec}} + \boldsymbol{Z}^{\boldsymbol{uG_P}} : \boldsymbol{G}_p\right) : \boldsymbol{C} : \boldsymbol{Z}^{\boldsymbol{uE}} \\
- \left(\boldsymbol{Z}^{\boldsymbol{PE}}\right) . \boldsymbol{a} . \left(\boldsymbol{Z}^{\boldsymbol{PP}} . \boldsymbol{E}_{\boldsymbol{M}}^{\boldsymbol{elec}} + \boldsymbol{Z}^{\boldsymbol{PE}} : \boldsymbol{E} + \boldsymbol{Z}^{\boldsymbol{PK}} \therefore \boldsymbol{K} + \boldsymbol{Z}^{\boldsymbol{PGp}} : \boldsymbol{G}_p\right) \\
- \left(\boldsymbol{Z}^{\boldsymbol{PP}} . \boldsymbol{E}_{\boldsymbol{M}}^{\boldsymbol{elec}} + \boldsymbol{Z}^{\boldsymbol{PE}} . \boldsymbol{E} + \boldsymbol{Z}^{\boldsymbol{PK}} \therefore \boldsymbol{K} + \boldsymbol{Z}^{\boldsymbol{PGp}} : \boldsymbol{G}_p\right) . \boldsymbol{a} . \left(\boldsymbol{Z}^{\boldsymbol{PE}}\right) \\
- \boldsymbol{e}^T . \left(\boldsymbol{Z}^{\boldsymbol{PP}} . \boldsymbol{E}_{\boldsymbol{M}}^{\boldsymbol{elec}} + \boldsymbol{Z}^{\boldsymbol{PE}} : \boldsymbol{E} + \boldsymbol{Z}^{\boldsymbol{PK}} \therefore \boldsymbol{K} + \boldsymbol{Z}^{\boldsymbol{PG}_P} : \boldsymbol{G}_p\right) : \left(\boldsymbol{Z}^{\boldsymbol{uE}}\right) \\
- \boldsymbol{e}^T . \left(\boldsymbol{Z}^{\boldsymbol{PE}}\right) : \left(\boldsymbol{Z}^{\boldsymbol{uE}} : \boldsymbol{E} + \boldsymbol{Z}^{\boldsymbol{uk}} \therefore \boldsymbol{K} + \boldsymbol{Z}^{\boldsymbol{uP}} . \boldsymbol{E}_{\boldsymbol{M}}^{\boldsymbol{elec}} + \boldsymbol{Z}^{\boldsymbol{uG}_P} : \boldsymbol{G}_p\right) \\
- \boldsymbol{e} : \left(\boldsymbol{Z}^{\boldsymbol{uE}} : \boldsymbol{E} + \boldsymbol{Z}^{\boldsymbol{uk}} \therefore \boldsymbol{K} + \boldsymbol{Z}^{\boldsymbol{uP}} . \boldsymbol{E}_{\boldsymbol{M}}^{\boldsymbol{elec}} + \boldsymbol{Z}^{\boldsymbol{uG}_P} : \boldsymbol{G}_p\right) . \left(\boldsymbol{Z}^{\boldsymbol{PE}}\right) \\
- \boldsymbol{e} : \left(\boldsymbol{Z}^{\boldsymbol{uE}}\right) . \left(\boldsymbol{Z}^{\boldsymbol{PP}} . \boldsymbol{E}_{\boldsymbol{M}}^{\boldsymbol{elec}} + \boldsymbol{Z}^{\boldsymbol{PE}} : \boldsymbol{E} + \boldsymbol{Z}^{\boldsymbol{PK}} \therefore \boldsymbol{K} + \boldsymbol{Z}^{\boldsymbol{PG}_P} : \boldsymbol{G}_p\right)
\end{array}\right\} dV_y
\end{aligned}
\tag{F.9}
$$

By the factorization of Eq. F.9, the stress tensor expresses versus the kinematic variables as:

$$
\begin{aligned}
\boldsymbol{\Sigma} = & \left(\frac{1}{2} \int_Y \left\{ \begin{array}{l} 2\left(\boldsymbol{Z}^{u\boldsymbol{E}}\right)^T : \boldsymbol{C} : \boldsymbol{Z}^{\boldsymbol{uE}} - \left(\boldsymbol{Z}^{\boldsymbol{PE}}\right) .\boldsymbol{a}. \boldsymbol{Z}^{\boldsymbol{PE}} - \left(\boldsymbol{Z}^{\boldsymbol{PE}}\right)^T .a. \left(\boldsymbol{Z}^{\boldsymbol{PE}}\right) \\ - \left(\boldsymbol{Z}^{\boldsymbol{uE}}\right)^{\boldsymbol{T}} : \boldsymbol{e}^T . \left(\boldsymbol{Z}^{\boldsymbol{PE}}\right) - \boldsymbol{e}^T . \left(\boldsymbol{Z}^{\boldsymbol{PE}}\right) : \boldsymbol{Z}^{\boldsymbol{uE}} - \left(\boldsymbol{Z}^{\boldsymbol{PE}}\right)^T .\boldsymbol{e} : \left(\boldsymbol{Z}^{u\boldsymbol{E}}\right) - \boldsymbol{e} : \left(\boldsymbol{Z}^{\boldsymbol{uE}}\right) .\boldsymbol{Z}^{\boldsymbol{PE}} \end{array} \right\} dV_y \right) : \boldsymbol{E} \\
& + \frac{1}{2} \left(\int_Y dV \left\{ \begin{array}{l} 2\left(\boldsymbol{Z}^{\boldsymbol{uk}}\right)^{\boldsymbol{T}} : \boldsymbol{C} : \boldsymbol{Z}^{\boldsymbol{uE}} - \left(\boldsymbol{Z}^{\boldsymbol{PE}}\right) .\boldsymbol{a}. \boldsymbol{Z}^{\boldsymbol{PK}} - \left(\boldsymbol{Z}^{\boldsymbol{PK}}\right)^T .\boldsymbol{a}. \boldsymbol{Z}^{PE} \\ - \left(\boldsymbol{Z}^{\boldsymbol{uE}}\right)^{\boldsymbol{T}} : \boldsymbol{e}^T . \left(\boldsymbol{Z}^{\boldsymbol{P}K}\right) - \boldsymbol{e}^T . \left(\boldsymbol{Z}^{\boldsymbol{P}E}\right) : \boldsymbol{Z}^{\boldsymbol{u}K} - \left(\boldsymbol{Z}^{\boldsymbol{PE}}\right)^T .\boldsymbol{e} : \left(\boldsymbol{Z}^{uK}\right) - \boldsymbol{e} : \left(\boldsymbol{Z}^{\boldsymbol{u}E}\right) .\boldsymbol{Z}^{\boldsymbol{P}K} \end{array} \right\} dV_y \right) \therefore \boldsymbol{K} \\
& + \frac{1}{2} \left(\int_Y \left\{ \begin{array}{l} 2\left(\boldsymbol{Z}^{\boldsymbol{uP}}\right)^T : \boldsymbol{C} : \boldsymbol{Z}^{\boldsymbol{uE}} - \left(\boldsymbol{Z}^{\boldsymbol{PE}}\right) .\boldsymbol{a}. \boldsymbol{Z}^{\boldsymbol{PP}} - \left(\boldsymbol{Z}^{\boldsymbol{PP}}\right)^T .\boldsymbol{a}. \boldsymbol{Z}^{\boldsymbol{PE}} \\ - \left(\boldsymbol{Z}^{\boldsymbol{uE}}\right)^{\boldsymbol{T}} : \boldsymbol{e}^T . \left(\boldsymbol{Z}^{PP}\right) - \boldsymbol{e}^T . \left(\boldsymbol{Z}^{\boldsymbol{P}E}\right) : \boldsymbol{Z}^{\boldsymbol{u}P} - \left(\boldsymbol{Z}^{\boldsymbol{PE}}\right)^T .\boldsymbol{e} : \left(\boldsymbol{Z}^{uP}\right) - \boldsymbol{e} : \left(\boldsymbol{Z}^{\boldsymbol{u}E}\right) .\boldsymbol{Z}^{\boldsymbol{P}P} \end{array} \right\} dV_y \right) .\boldsymbol{E}_{\boldsymbol{M}}^{\boldsymbol{elec}} \\
& + \frac{1}{2} \left(\int_Y \left\{ \begin{array}{l} 2\left(\boldsymbol{Z}^{\boldsymbol{uG}}\right)^T : \boldsymbol{C} : \boldsymbol{Z}^{\boldsymbol{uE}} - \left(\boldsymbol{Z}^{\boldsymbol{PE}}\right) .\boldsymbol{a}. \left(\boldsymbol{Z}^{\boldsymbol{PGp}}\right) - \left(\boldsymbol{Z}^{\boldsymbol{PGp}}\right)^T .\boldsymbol{a}. \boldsymbol{Z}^{\boldsymbol{PE}} \\ - \left(\boldsymbol{Z}^{\boldsymbol{uE^T}}\right) : \boldsymbol{e}^T . \left(Z^{PGp}\right) - \boldsymbol{e}^T . \left(\boldsymbol{Z}^{\boldsymbol{P}E}\right) : Z^{\boldsymbol{uG}_p} - \left(\boldsymbol{Z}^{\boldsymbol{PE}}\right)^T .\boldsymbol{e} : \left(Z^{\boldsymbol{uG}_p}\right) - \boldsymbol{e} : \left(\boldsymbol{Z}^{\boldsymbol{u}E}\right) .\boldsymbol{Z}^{\boldsymbol{PG}_p} \end{array} \right\} dV_y \right) : \boldsymbol{G}_p
\end{aligned}
\tag{F.10}
$$

Similarly, the electric displacement is written as follows:

$$
\begin{aligned}
\overline{\boldsymbol{D}} = & \frac{\partial}{\partial \boldsymbol{E}_{\boldsymbol{M}}^{\boldsymbol{elec}}} \left(\underset{\tilde{\boldsymbol{u}}, \tilde{\phi} \in H^1_{per}(Y)}{Min} L\left[\tilde{\boldsymbol{u}}, \tilde{\phi}\right] \right) \equiv \underset{\tilde{\boldsymbol{u}}, \tilde{\phi} \in H^1_{per}(Y)}{Min} \frac{\partial L\left[\tilde{\boldsymbol{u}}, \tilde{\phi}\right]}{\partial \boldsymbol{E}_{\boldsymbol{M}}^{\boldsymbol{elec}}} \\
= & \frac{1}{2} \int_Y dV_y \left\{ \begin{array}{l} \left(\boldsymbol{Z}^{\boldsymbol{uP}}\right) : \boldsymbol{C} : \left(\boldsymbol{Z}^{\boldsymbol{uE}}\right) + \left(\boldsymbol{Z}^{\boldsymbol{uE}}\right)^T : \boldsymbol{C} : \left(\boldsymbol{Z}^{\boldsymbol{uP}}\right) - \left(\boldsymbol{Z}^{\boldsymbol{PP}}\right) .\boldsymbol{a}. \left(\boldsymbol{Z}^{\boldsymbol{PE}}\right) - \left(\boldsymbol{Z}^{\boldsymbol{PE}}\right)^T .\boldsymbol{a}. \left(\boldsymbol{Z}^{\boldsymbol{PP}}\right) \\ - \boldsymbol{e}^T . \left(\boldsymbol{Z}^{\boldsymbol{PP}}\right) : \left(\boldsymbol{Z}^{\boldsymbol{uE}}\right) - \left(\boldsymbol{Z}^{\boldsymbol{uP}}\right)^T : \boldsymbol{e}^T . \left(\boldsymbol{Z}^{\boldsymbol{PE}}\right) - \boldsymbol{e} : \left(\boldsymbol{Z}^{\boldsymbol{uP}}\right) . \left(\boldsymbol{Z}^{\boldsymbol{PE}}\right) - \left(\boldsymbol{Z}^{\boldsymbol{PP}}\right)^T .\boldsymbol{e} : \left(\boldsymbol{Z}^{\boldsymbol{uE}}\right) \end{array} \right\} : \boldsymbol{E} \\
& + \frac{1}{2} \int_Y dV_y \left\{ \begin{array}{l} \left(\boldsymbol{Z}^{\boldsymbol{uP}}\right) : \boldsymbol{C} : \boldsymbol{Z}^{\boldsymbol{uk}} + \left(\boldsymbol{Z}^{\boldsymbol{uk}}\right)^T : \boldsymbol{C} : \left(\boldsymbol{Z}^{\boldsymbol{uP}}\right) - \left(\boldsymbol{Z}^{\boldsymbol{PP}}\right) .\boldsymbol{a}. \boldsymbol{Z}^{\boldsymbol{PK}} - \left(\boldsymbol{Z}^{\boldsymbol{PK}}\right)^T .\boldsymbol{a}. \boldsymbol{Z}^{\boldsymbol{PP}} \\ - \boldsymbol{e}^T . \left(\boldsymbol{Z}^{\boldsymbol{PP}}\right) : \left(\boldsymbol{Z}^{\boldsymbol{u}K}\right) - \left(\boldsymbol{Z}^{\boldsymbol{uP}}\right)^T : \boldsymbol{e}^T . \left(\boldsymbol{Z}^{\boldsymbol{P}K}\right) - \boldsymbol{e} : \left(\boldsymbol{Z}^{\boldsymbol{uP}}\right) . \left(\boldsymbol{Z}^{\boldsymbol{P}K}\right) - \left(\boldsymbol{Z}^{\boldsymbol{PP}}\right)^T .\boldsymbol{e} : \left(\boldsymbol{Z}^{\boldsymbol{u}K}\right) \end{array} \right\} \therefore \boldsymbol{K} \\
& + \frac{1}{2} \int_Y dV_y \left\{ \begin{array}{l} \left(\boldsymbol{Z}^{\boldsymbol{uP}}\right) : \boldsymbol{C} : \boldsymbol{Z}^{\boldsymbol{uP}} + \left(\boldsymbol{Z}^{\boldsymbol{uP}}\right)^T : \boldsymbol{C} : \boldsymbol{Z}^{\boldsymbol{uP}} - \boldsymbol{Z}^{\boldsymbol{PP}} .\boldsymbol{a}. \boldsymbol{Z}^{\boldsymbol{PP}} \\ - \left(\boldsymbol{Z}^{\boldsymbol{PP}}\right)^T .\boldsymbol{a}. \boldsymbol{Z}^{\boldsymbol{PP}} - \boldsymbol{e}^T . \left(\boldsymbol{Z}^{\boldsymbol{PP}}\right) : \left(\boldsymbol{Z}^{\boldsymbol{u}P}\right) \\ - \left(\boldsymbol{Z}^{\boldsymbol{uP}}\right)^T : \boldsymbol{e}^T . \left(\boldsymbol{Z}^{\boldsymbol{P}P}\right) - \boldsymbol{e} : \left(\boldsymbol{Z}^{\boldsymbol{uP}}\right) . \left(\boldsymbol{Z}^{\boldsymbol{P}P}\right) - \left(\boldsymbol{Z}^{\boldsymbol{PP}}\right)^T .\boldsymbol{e} : \left(\boldsymbol{Z}^{\boldsymbol{u}P}\right) \end{array} \right\} .\boldsymbol{E}_{\boldsymbol{M}}^{\boldsymbol{elec}} \\
& + \frac{1}{2} \int_Y dV_y \left\{ \begin{array}{l} \left(\boldsymbol{Z}^{\boldsymbol{uP}}\right) : \boldsymbol{C} : \boldsymbol{Z}^{\boldsymbol{uG}_P} + \left(\boldsymbol{Z}^{\boldsymbol{uG}_P}\right)^T : \boldsymbol{C}\left(\boldsymbol{y}\right) : \boldsymbol{Z}^{\boldsymbol{uP}} - \boldsymbol{Z}^{\boldsymbol{PP}} .\boldsymbol{a}. \boldsymbol{Z}^{\boldsymbol{PG}_P} \\ - \left(\boldsymbol{Z}^{\boldsymbol{PG}_P}\right)^T .\boldsymbol{a}. \boldsymbol{Z}^{\boldsymbol{PP}} - \boldsymbol{e}^T . \left(\boldsymbol{Z}^{\boldsymbol{PP}}\right) : \left(\boldsymbol{Z}^{\boldsymbol{uG}_P}\right) - \left(\boldsymbol{Z}^{\boldsymbol{uP}}\right)^T : \boldsymbol{e}^T . \left(\boldsymbol{Z}^{\boldsymbol{PG}_P}\right) \\ - \boldsymbol{e} : \left(\boldsymbol{Z}^{\boldsymbol{uP}}\right) . \left(\boldsymbol{Z}^{\boldsymbol{PG}_P}\right) - \left(\boldsymbol{Z}^{\boldsymbol{PP}}\right)^T .\boldsymbol{e} : \left(\boldsymbol{Z}^{\boldsymbol{uG}_P}\right) \end{array} \right\} : \boldsymbol{G}_p
\end{aligned}
\tag{F.11}
$$

As to higher gradient effects, the hyperstress is derived as follows:

$$
\begin{aligned}
\boldsymbol{S} &:= \frac{\partial}{\partial \boldsymbol{K}} \left(\underset{\tilde{\boldsymbol{u}},\tilde{\phi}\in H^1_{per}(Y)}{Min} L\left[\tilde{\boldsymbol{u}},\tilde{\phi}\right] \right) \equiv \underset{\tilde{\boldsymbol{u}},\tilde{\phi}\in H^1_{per}(Y)}{Min} \frac{\partial L\left[\tilde{\boldsymbol{u}},\tilde{\phi}\right]}{\partial \boldsymbol{K}} \\
&= \frac{1}{2}\int_Y dV_y \begin{Bmatrix} \left(\boldsymbol{Z^{uk}}\right) : \boldsymbol{C} : \boldsymbol{Z^{uE}} + \left(\boldsymbol{Z^{uE}}\right)^T : \boldsymbol{C} : \boldsymbol{Z^{uk}} - \boldsymbol{Z^{PK}}.\boldsymbol{a}.\boldsymbol{Z^{PE}} - \left(\boldsymbol{Z^{PE}}\right)^T.\boldsymbol{a}.\boldsymbol{Z^{PK}} \\ -\boldsymbol{e}^T.\left(\boldsymbol{Z^{PK}}\right) : \left(\boldsymbol{Z^{uE}}\right) - \left(\boldsymbol{Z^{uK}}\right)^T : \boldsymbol{e}^T.\left(\boldsymbol{Z^{PE}}\right) \\ -\boldsymbol{e} : \left(\boldsymbol{Z^{uK}}\right).\left(\boldsymbol{Z^{PE}}\right) - \left(\boldsymbol{Z^{PK}}\right)^T.\boldsymbol{e} : \left(\boldsymbol{Z^{uE}}\right) \end{Bmatrix} : \boldsymbol{E} \\
&\frac{1}{2}\int_Y dV_y \begin{Bmatrix} \left(\boldsymbol{Z^{uk}}\right) : \boldsymbol{C} : \boldsymbol{Z^{uk}} + \left(\boldsymbol{Z^{uk}}\right)^T : \boldsymbol{C} : \boldsymbol{Z^{uk}} - \boldsymbol{Z^{PK}}.\boldsymbol{a}.\boldsymbol{Z^{PK}} - \left(\boldsymbol{Z^{PK}}\right)^T.\boldsymbol{a}.\boldsymbol{Z^{PK}} \\ -\boldsymbol{e}^T.\left(\boldsymbol{Z^{PK}}\right) : \left(\boldsymbol{Z^{uK}}\right) - \left(\boldsymbol{Z^{uK}}\right)^T : \boldsymbol{e}^T.\left(\boldsymbol{Z^{PK}}\right) \\ -\boldsymbol{e} : \left(\boldsymbol{Z^{uK}}\right).\left(\boldsymbol{Z^{PK}}\right) - \left(\boldsymbol{Z^{PK}}\right)^T.\boldsymbol{e} : \left(\boldsymbol{Z^{uK}}\right) \end{Bmatrix} \therefore \boldsymbol{K} \\
&\frac{1}{2}\int_Y dV_y \begin{Bmatrix} \left(\boldsymbol{Z^{uk}}\right) : \boldsymbol{C} : \boldsymbol{Z^{uP}} + \left(\boldsymbol{Z^{uP}}\right)^T : \boldsymbol{C} : \boldsymbol{Z^{uk}} - \boldsymbol{Z^{PK}}.\boldsymbol{a}.\boldsymbol{Z^{PP}} - \left(\boldsymbol{Z^{PP}}\right)^T.\boldsymbol{a}.\boldsymbol{Z^{PK}} \\ -\boldsymbol{e}^T.\left(\boldsymbol{Z^{PK}}\right) : \left(\boldsymbol{Z^{uP}}\right) - \left(\boldsymbol{Z^{uK}}\right)^T : \boldsymbol{e}^T.\left(\boldsymbol{Z^{PP}}\right) \\ -\boldsymbol{e} : \left(\boldsymbol{Z^{uK}}\right).\left(\boldsymbol{Z^{PP}}\right) - \left(\boldsymbol{Z^{PK}}\right)^T.\boldsymbol{e} : \left(\boldsymbol{Z^{uP}}\right) \end{Bmatrix} .\boldsymbol{E^{elec}_M} \\
&\frac{1}{2}\int_Y dV_y \begin{Bmatrix} \left(\boldsymbol{Z^{uk}}\right) : \boldsymbol{C} : \boldsymbol{Z^{uG}} + \left(\boldsymbol{Z^{uG}}\right)^T : \boldsymbol{C} : \boldsymbol{Z^{uk}} - \boldsymbol{Z^{PK}}.\boldsymbol{a}.\boldsymbol{Z^{PGp}} - \left(\boldsymbol{Z^{PGp}}\right)^T.\boldsymbol{a}.\boldsymbol{Z^{PK}} \\ -\boldsymbol{e}^T.\left(\boldsymbol{Z^{PK}}\right) : \left(\boldsymbol{Z^{uG_P}}\right) - \left(\boldsymbol{Z^{uK}}\right)^T : \boldsymbol{e}^T.\left(\boldsymbol{Z^{PG_P}}\right) \\ -\boldsymbol{e} : \left(\boldsymbol{Z^{uK}}\right).\left(\boldsymbol{Z^{PG_P}}\right) - \left(\boldsymbol{Z^{PK}}\right)^T.\boldsymbol{e} : \left(\boldsymbol{Z^{uG_P}}\right) \end{Bmatrix} : \boldsymbol{G}_p
\end{aligned}
\tag{F.12}
$$

Also, the higher gradient electric displacement second order tensor can be obtained as follows:

$$
\begin{aligned}
\boldsymbol{R} &:= \frac{\partial}{\partial \boldsymbol{G}_p} \left(\underset{\tilde{\boldsymbol{u}},\tilde{\phi}\in H^1_{per}(Y)}{Min} L\left[\tilde{\boldsymbol{u}},\tilde{\phi}\right] \right) \equiv \underset{\tilde{\boldsymbol{u}},\tilde{\phi}\in H^1_{per}(Y)}{Min} \frac{\partial L\left[\tilde{\boldsymbol{u}},\tilde{\phi}\right]}{\partial \boldsymbol{G}_p} \\
&= \frac{1}{2}\int_Y dV_y \begin{Bmatrix} \left(\boldsymbol{Z^{uG_P}}\right) : \boldsymbol{C} : \boldsymbol{Z^{uE}} + \left(\boldsymbol{Z^{uE}}\right)^T : \boldsymbol{C} : \boldsymbol{Z^{uG_p}} - \boldsymbol{Z^{PG_p}}.\boldsymbol{a}.\boldsymbol{Z^{PE}} - \left(\boldsymbol{Z^{PE}}\right)^T.\boldsymbol{a}.\boldsymbol{Z^{PG_p}} \\ -\boldsymbol{e}^T.\left(\boldsymbol{Z^{PG_P}}\right) : \left(\boldsymbol{Z^{uE}}\right) - \left(\boldsymbol{Z^{uG_P}}\right)^T : \boldsymbol{e}^T.\left(\boldsymbol{Z^{PE}}\right) \\ -\boldsymbol{e} : \left(\boldsymbol{Z^{uG_P}}\right).\left(\boldsymbol{Z^{PE}}\right) - \left(\boldsymbol{Z^{PG_P}}\right)^T.\boldsymbol{e} : \left(\boldsymbol{Z^{uE}}\right) \end{Bmatrix} : \boldsymbol{E} \\
&+ \frac{1}{2}\int_Y dV_y \begin{Bmatrix} \boldsymbol{Z^{uG_p}} : \boldsymbol{C} : \boldsymbol{Z^{uk}} + \left(\boldsymbol{Z^{uk}}\right)^T : \boldsymbol{C} : \boldsymbol{Z^{uG_p}} - \boldsymbol{Z^{PG_p}}.\boldsymbol{a}.\boldsymbol{Z^{PK}} - \left(\boldsymbol{Z^{PK}}\right)^T.\boldsymbol{a}.\boldsymbol{Z^{PG_p}} \\ -\boldsymbol{e}^T.\left(\boldsymbol{Z^{PG_p}}\right) : \left(\boldsymbol{Z^{uK}}\right) - \left(\boldsymbol{Z^{uG_p}}\right)^T : \boldsymbol{e}^T.\left(\boldsymbol{Z^{PK}}\right) \\ -\boldsymbol{e} : \left(\boldsymbol{Z^{uG_p}}\right).\left(\boldsymbol{Z^{PK}}\right) - \left(\boldsymbol{Z^{PG_p}}\right)^T.\boldsymbol{e} : \left(\boldsymbol{Z^{uK}}\right) \end{Bmatrix} \therefore \boldsymbol{K} \\
&+ \frac{1}{2}\int_Y dV_y \begin{Bmatrix} \boldsymbol{Z^{uG_p}} : \boldsymbol{C} : \boldsymbol{Z^{uP}} + \left(\boldsymbol{Z^{uP}}\right)^T : \boldsymbol{C} : \boldsymbol{Z^{uG_p}} - \boldsymbol{Z^{PG_p}}.\boldsymbol{a}.\boldsymbol{Z^{PP}} - \left(\boldsymbol{Z^{PP}}\right)^T.\boldsymbol{a}.\boldsymbol{Z^{PG_p}} \\ -\boldsymbol{e}^T.\left(\boldsymbol{Z^{PG_p}}\right) : \left(\boldsymbol{Z^{uP}}\right) - \left(\boldsymbol{Z^{uG_p}}\right)^T : \boldsymbol{e}^T.\left(\boldsymbol{Z^{PP}}\right) \\ -\boldsymbol{e} : \left(\boldsymbol{Z^{uG_p}}\right).\left(\boldsymbol{Z^{PP}}\right) - \left(\boldsymbol{Z^{PG_p}}\right)^T.\boldsymbol{e} : \left(\boldsymbol{Z^{uP}}\right) \end{Bmatrix} .\boldsymbol{E^{elec}_M} \\
&+ \frac{1}{2}\int_Y dV_y \begin{Bmatrix} \boldsymbol{Z^{uG_p}} : \boldsymbol{C} : \boldsymbol{Z^{uG_p}} + \left(\boldsymbol{Z^{uG_p}}\right)^T : \boldsymbol{C} : \boldsymbol{Z^{uG_p}} - \boldsymbol{Z^{PG_p}}.\boldsymbol{a}.\boldsymbol{Z^{PG_p}} - \left(\boldsymbol{Z^{PG_p}}\right)^T.\boldsymbol{a}.\boldsymbol{Z^{PG_p}} \\ -\boldsymbol{e}^T.\left(\boldsymbol{Z^{PG_p}}\right) : \left(\boldsymbol{Z^{uG_P}}\right) - \left(\boldsymbol{Z^{uG_p}}\right)^T : \boldsymbol{e}^T.\left(\boldsymbol{Z^{PG_P}}\right) \\ -\boldsymbol{e} : \left(\boldsymbol{Z^{uG_p}}\right).\left(\boldsymbol{Z^{PG_P}}\right) - \left(\boldsymbol{Z^{PG_p}}\right)^T.\boldsymbol{e} : \left(\boldsymbol{Z^{uG_P}}\right) \end{Bmatrix} : \boldsymbol{G}_p
\end{aligned}
\tag{F.13}
$$

Appendix G

Comparison of the proposed homogenization approach with the literature

A comparison between the results obtained in our variational approach and the analytical model in [262] was made. The materials used were $BaTiO_3$ for the fiber and PZT-5H for the matrix with their properties presented in Table G.1.

Table G.1 Mechanical and electrical properties of the two piezoelectric materials within the unit cell of the composite material

	C_{11}(GPa)	C_{33}(GPa)	C_{12}(GPa)	C_{13}(GPa)	d^*_{31}(C/m^2)	d^*_{33}(C/m^2)	a_{11}(nF/m)	a_{33}(nF/m)
$BaTiO_3$	166	162	77	78	-4.4	18.6	11.2	12.6
PZT-5H	126	117	55	53	-6.5	23.3	15.1	13

Fig. G.1 shows the variation of different homogenized piezoelectric and dielectric moduli as a function of volume fraction of the inclusion. The blue curves corresponds to the results obtained using the variational approach and the red ones correspond to the results obtained in the literature [262] .Fig. G.1 shows a good agreement between the results obtained using the variational approach and the results in [262] for the dielectric and piezoelectric coefficients with a maximum relative error for the piezoelectric coefficients (d^{*hom}_{31} and d^{*hom}_{33}) of around 3%, and for the dielectric coefficient (permittivity) around 1%.

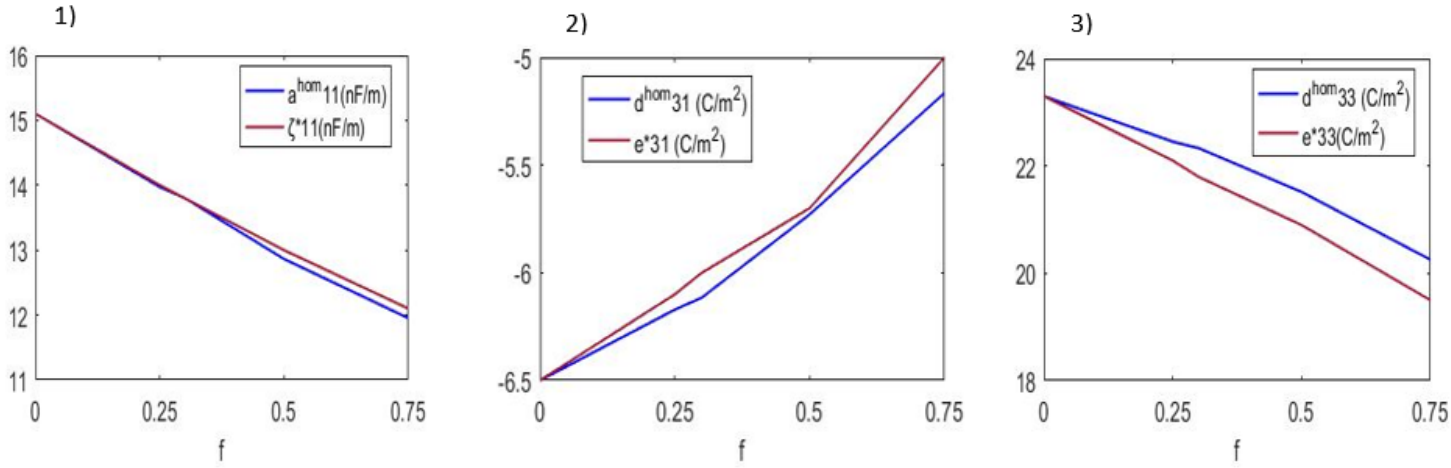

Figure G.1 Variation of the 1) dielectric coefficient, 2) and 3) piezoelectric coefficients as a function of the volume fraction. Red corresponds to the results in literature [260], blue corresponds to the results using the variational approach.

Appendix H

Components of the Π matrix in the wave propagation analysis

The components of the wave motion matrix Π with homogenized flexoelectric parameters are as follows:

$$\Pi_{11} = -C_{11}k^2{}_x - A_{11}k^4{}_x - \frac{1}{2}C_{33}k^2{}_y - \frac{1}{2}A_{66}k^4{}_y + w^2(\rho + n^2(k^2{}_x + k^2{}_y))$$
$$- \frac{1}{2}(A_{56} + A_{65})k_x k^3{}_y - \frac{1}{2}A_{55}k^2{}_x k^2{}_y - A_{12}k^3{}_x k_y + iB_{12}k^2{}_x k_y$$
$$\Pi_{12} = -(A_{13} + \frac{1}{2}A_{55})k_x{}^3 k_y - \frac{1}{2}(2A_{14} + A_{56} + A_{65})k_x{}^2 k^2{}_y$$
$$- (C_{12} + \frac{1}{2}C_{33})k_x k_y + i(B_{13} - B_{21})k^2{}_x k_y + iB_{14}k_x k^2{}_y - \frac{1}{2}A_{66}k_x k^3{}_y$$
$$\Pi_{13} = -H_{11}k_x{}^4 - d^*_{11}k_x{}^2 - d^*_{23}k_y{}^2 + ie_{11}k_x{}^3 - d^*_{21}k_x k_y + ie_{12}k_x k_y{}^2$$
$$+ i(e_{13} - F_{21})k_x{}^2 k_y - H_{12}k_x{}^2 k^2{}_y - H_{13}k_x{}^3 k_y$$
$$\Pi_{21} = -(C_{21} + \frac{1}{2}C_{33})k_x k_y - (A_{31} + \frac{1}{2}A_{55})k^3{}_x k_y - (A_{32} + A_{41} + \frac{1}{2}A_{56})k_x{}^2 k^2{}_y$$
$$- A_{42}k_x k^3{}_y + i(B_{22} + \frac{1}{2}B_{36} - B_{14})k_x k_y{}^2 + i(B_{21} - B_{13})k^2{}_x k_y$$
$$\Pi_{22} = -\frac{1}{2}C_{33}k^2{}_x - \frac{1}{2}A_{55}k^4{}_x - C_{22}k^2{}_y - A_{44}k^4{}_y + w^2(\rho + n^2(k^2{}_x + k^2{}_y))$$
$$- (A_{34} + A_{43})k_x k^3{}_y - A_{33}k^2{}_x k^2{}_y - \frac{1}{2}A_{56}k^3{}_x k_y + \frac{1}{2}iB_{36}k^2{}_x k_y$$
$$\Pi_{23} = -d^*_{22}k_y{}^2 - H_{42}k_y{}^4 + i(e_{22} - F_{24})k_y{}^3 - (d^*_{23} + d^*_{12})k_x k_y - (H_{33} + H_{41})k_x{}^2 k^2{}_y$$
$$- H_{31}k_x{}^3 k_y - (H_{32} + H_{43})k_x k^3{}_y + i(e_{23} + e_{32} - F_{23})k_x k_y{}^2 + i(e_{33} + e_{21})k^2{}_x k_y$$
$$\Pi_{31} = -H_{11}k_x{}^4 - d^*_{11}k_x{}^2 - \frac{1}{2}d^*_{23}k_y{}^2 - \frac{1}{2}ie_{32}k_y{}^3 - ie_{11}k_x{}^3 - d^*_{21}k_x k_y$$
$$+ i(F_{22} - \frac{1}{2}e_{33} - e_{12})k_x k_y{}^2 + i(F_{21} - e_{23})k_x{}^2 k_y - (H_{12} + H_{23})k_x{}^2 k^2{}_y - (H_{13} + H_{21})k_x{}^3 k_y - H_{22}k_x k^3{}_y$$
$$\Pi_{32} = -H_{42}k_y{}^4 - d^*_{22}k_y{}^2 + i(F_{24} - e_{22})k_y{}^3 - (d^*_{12} + \frac{1}{2}d^*_{23})k_x k_y + i(F_{23} - \frac{1}{2}e_{32} - e_{23})k_x k_y{}^2$$
$$- i(\frac{1}{2}e_{33} + e_{21})k_x{}^2 k_y - (H_{33} + H_{41} + \frac{1}{2}H_{52})k_x{}^2 k^2{}_y - H_{31}k_x{}^3 k_y - (H_{32} + H_{43})k_x k_y{}^3$$
$$\Pi_{33} = -a_{11}k^2{}_x - N_{11}k^4{}_x - a_{22}k^2{}_y - N_{22}k^4{}_y - N_{23}k_x k^3{}_y - (N_{12} + N_{33} + N_{21})k^2{}_x k^2{}_y - (N_{13} + N_{31})k^3{}_x k_y \quad \text{(H.1)}$$